Sodium channel-dependent intrinsic plasticity in cerebellar stellate cells

By

RYAN P.D. ALEXANDER

December 2019

Integrated Program in Neuroscience

McGill University

(Montreal, CANADA)

A thesis submitted to the Faculty of Graduate and Postdoctoral Studies in partial fulfillment of the requirement of the degree of

DOCTOR OF PHILOSOPHY

We are a way for the cosmos to know itself.

- Carl Sagan

ABSTRACT

Cerebellar molecular layer interneurons (MLIs) provide dynamic feedforward inhibition onto Purkinje cells which constitute the sole output of the cerebellar cortex. MLI-mediated inhibition has recently been demonstrated to drive modulation of the vestibulo-ocular reflex and rhythmic oromotor behaviour, though their specific roles in broader cerebellar behaviours are still relatively mysterious. Since MLI activity is critical to the regulation of Purkinje cell output, the mechanisms by which MLIs fine-tune their intrinsic excitability on both short-term and long-term time scales is of unique importance to decipher. An added complication to studying the ionic basis of action potential firing in MLIs is the instability of their membrane excitability during patch clamp electrophysiological investigation. Although reported in cell-attached recording, an explanation for why these cells exhibit changes in firing behaviour during whole-cell recording remains elusive. This thesis is a study of how and why these changes occur, and demonstrates that important neurophysiological insights can be made through the investigation and explanation of measurement-induced phenomena.

We first sought to characterize the action potential phenotype and identify the ion channel basis for these changes. Through patch clamp recording of stellate cells in acute slices of cerebellar vermis we found that action potential frequency increased over tens of minutes from the moment of patch breakthrough into whole-cell configuration. This behaviour was underpinned by a gradual hyperpolarization of spike threshold over time, as opposed to changes in passive membrane properties like input resistance or resting membrane potential. Using the combined approaches of Hodgkin-Huxley modeling of action potential firing and isolated study of individual voltage-dependent ionic conductances in voltage clamp, we demonstrated that the

primary driver of the time-dependent threshold decrease is a hyperpolarization of voltage-gated sodium channel gating properties. We also observed shifts in the gating of A-type potassium channels, but this served to further increase firing rates by shortening intervals between action potentials rather than affecting spike threshold.

We next wanted to uncover the distinct intracellular signaling events that gave rise to shifts in channel gating. Calcium chelation experiments showed that this process occurred before breakthrough and was calcium-dependent. Following the patch-induced calcium rise, various protein kinases are activated which are the ultimate effectors of threshold hyperpolarization and channel modulation. Next, we investigated whether stellate cells could use this plasticity in a more physiologically-relevant context. First, we showed that using minimally-invasive cell-attached recording a stable level of basal activity could be achieved. We then showed that stimulating NMDA receptors caused a long-lasting upregulation of action potential firing similar to what previously was invoked by patch clamp itself. Finally, we demonstrated that this firing rate plasticity relied on the same intracellular signaling molecules as those driving threshold hyperpolarization during whole-cell recording. Taken together, these findings provide compelling evidence for a new mechanism of long-term firing rate control in MLIs.

Overall, two principal conclusions can be derived from my results. First, cerebellar stellate cells experience a coordinated re-adjustment of two voltage-gated ion channel families that causes long-lasting excitability change during patch clamp investigation. Second, the signaling events induced by patch recording serve the same purpose when activated by physiological means and constitute a novel form of intrinsic plasticity in cerebellar MLIs.

ABRÉGÉ

Les interneurones de couche moléculaire cérébelleuse (MLI) fournissent une inhibition dynamique directe des cellules de Purkinje, qui constituent le seul produit de sortie du cortex cérébelleux. Il a récemment été démontré que l'inhibition à médiation MLI induisait la modulation du réflexe vestibulo-oculaire et du comportement rythmique ou moteur, bien que leurs rôles spécifiques dans les comportements cérébelleux plus larges soient encore relativement mystérieux. Etant donné que l'activité de la MLI est essentielle à la régulation de la production cellulaire de Purkinje, il est essentiel de déchiffrer les mécanismes par lesquels les MLI ajustent leur excitabilité intrinsèque à des échelles de temps à court et à long terme. L'instabilité de l'excitabilité de leur membrane lors de l'enregistrement électrophysiologique par patch clamp constitue une complication supplémentaire lors de l'étude de la base ionique de potentiel d'action à la décharge dans les MLI. Bien que caractérisé par un enregistrement attaché à une cellule moins invasif, une explication de la raison pour laquelle ces cellules subissent des changements de comportement de tir au cours de l'enregistrement de cellules entières reste difficile à atteindre. Ma thèse étudie exactement comment et pourquoi ces changements se produisent et démontre que des informations neurophysiologiques importantes peuvent être obtenues grâce à la recherche et à l'explication de phénomènes induits par l'observation.

Nous avons d'abord cherché à caractériser le phénotype de potentiel d'action spécifique qui se présente et à identifier la base moléculaire de ces changements. Grâce à une étude électrophysiologique par patch clamp de cellules étoilées dans des tranches aiguës de vermis cérébelleux, nous avons constaté que la fréquence du potentiel d'action augmentait en quelques dizaines de minutes à partir du moment où le patch apparaissait dans la configuration à cellules

entières. Ce comportement était sous-tendu par une hyperpolarisation progressive du seuil des pointes dans le temps, par opposition aux modifications des propriétés de la membrane passive telles que la résistance d'entrée ou le potentiel de membrane au repos. Par les approches combinées de la modélisation de Hodgkin-Huxley et de l'étude isolée de conductances ioniques dépendantes de la tension individuelles à l'aide de la pince de tension, nous avons démontré que le principal facteur de la diminution du seuil dépendant du temps est une hyperpolarisation des propriétés de déclenchement des canaux sodiques dépendants du voltage. Nous avons également observé des changements dans les propriétés de déclenchement des canaux potassiques de type A, mais cela a permis d'augmenter encore la cadence de tir en raccourcissant les intervalles entre les potentiels d'action plutôt qu'en affectant le seuil des pointes.

Nous avons ensuite voulu découvrir les événements de signalisation intracellulaires distincts qui ont entraîné des changements dans la synchronisation de canal. Des expériences avec des chélateurs de calcium ont montré que ce processus se produit avant la percée et est entièrement dépendant du calcium. Suite à l'élévation du calcium induite par le patch, différentes protéines kinases sont activées, lesquelles sont les effecteurs ultimes de l'hyperpolarisation à seuil et de la modulation de canal. Nous voulions ensuite déterminer si les cellules étoilées pourraient utiliser cette plasticité dans un contexte plus pertinent sur le plan physiologique. Tout d'abord, nous avons montré que l'utilisation d'un enregistrement attaché à une cellule peu invasif pouvait atteindre un niveau d'activité basale stable. Nous avons ensuite montré que la stimulation des récepteurs NMDA provoquait une régulation à la hausse durable du potentiel d'action semblable à celle précédemment invoquée par le patch clamp lui-même. Enfin, nous avons démontré que cette plasticité de la cadence de tir reposait sur les mêmes

molécules de signalisation intracellulaires que celles de l'hyperpolarisation à seuil déterminant lors de l'enregistrement de cellules entières. Pris ensemble, ces résultats fournissent des preuves convaincantes d'un nouveau type de plasticité intrinsèque dans les MLI cérébelleux.

Globalement, deux conclusions principales peuvent être tirées de mes résultats. Premièrement, les cellules étoilées cérébelleuses subissent un réajustement coordonné du comportement de déclenchement de multiples familles de canaux ioniques voltage-dépendants, ce qui provoque un changement d'excitabilité durable pendant l'investigation par patch clamp. Deuxièmement, les événements de signalisation induits par l'enregistrement de patchs ont le même objectif lorsqu'ils sont activés par des moyens physiologiques et constituent une nouvelle forme de plasticité intrinsèque dans les MLI cérébelleux.

TABLE OF CONTENTS

PART II: EXPERIMENTAL SECTION

PART III: GENERAL DISCUSSION

PART IV: APPENDICES

LIST OF FIGURES

Chapter 2

LIST OF TABLES

LIST OF ABBREVIATIONS

4-AP	4-aminopyridine
ACSF	artificial cerebrospinal fluid
AHP	afterhyperpolarization
-AM	acetoxymethyl ester
AMPA	α-amino-3-hydroxy-5-methyl-4-isoxazolepropionic acid
AP	action potential
BAPTA	1,2-Bis(2-aminophenoxy)ethane-N,N,N′,N′-tetraacetic acid tetrakis
BC	basket cell
CaMKII	Ca^{2+}-/calmodulin-dependent kinase II
Cav	voltage-gated calcium channel
CF	climbing fiber
CTD	C-terminal domain
CNS	central nervous system
ESPC	excitatory postsynaptic current
EPSP	excitatory postsynaptic potential
GABA	γ-aminobutyric acid
GC	granule cell
GoC	Golgi cell
HCN	hyperpolarization-activated cyclic nucleotide-gated channel
I_A	A-type potassium current
I_{Ca}	calcium current
I_h	hyperpolarization-activated current
I_K	delayed-rectifier potassium current
I_{Na}	sodium current
I_T	T-type calcium current

IPSC	inhibitory postsynaptic current
IPSP	inhibitory postsynaptic potential
KCa	calcium-activated potassium channel
KChIP	potassium channel-interacting protein
Kv	voltage-gated potassium channel
LTD	long-term depression
LTP	long-term potentiation
mGluR	metabotropic glutamate receptor
MLI	molecular layer interneuron
Nav	voltage-gated sodium channel
NMDA	N-methyl-D-aspartate
PF	parallel fiber
PC	Purkinje cell
PKA	cAMP-dependent protein kinase, or protein kinase A
PKC	protein kinase C
PV	parvalbumin
RMP	resting membrane potential
SC	stellate cell
SEM	standard error of the mean
TEA	tetraethylammonium
TTX	tetrodotoxin
UBC	unipolar brush cell
$V_{1/2}$	voltage at half-maximum
VGIC	voltage-gated ion channel

ACKNOWLEDGEMENTS

I begin by thanking my supervisor Derek, whose support has been always felt and appreciated, and whose academic insight has been critical for the success of my research. He's never been one to shy away from tough problems, and I hope to emulate that courage going forward. His encouragement of an informal atmosphere of camaraderie and discussion has made the lab environment fun and kept the science juices flowing. Through his encouragements I was able to present my work at many conferences both local and international, including in California and Switzerland, which have been some of the highlights of my doctorate. His collaborative knack led to some extremely fruitful academic partnerships, which I benefited from greatly. He could also always be counted on to mosey into the student room at around 4:45 on a Friday asking if anyone is up for a beer. Capping off the week in this way is a tradition begun long before I started in the lab, and I hope it continues long after I leave.

I would like to thank the members of my advisory committee, Drs. Ellis Cooper, Philippe Séguéla, and Alanna Watt, as well as my IPN mentor, Dr. Jesper Sjöström. They could all be counted on to ask great questions and provide important insight during committee meetings and seminars. Their feedback was instrumental in steering and shaping my work.

I must also thank my collaborators, Dr. Anmar Khadra and his lab members both current and former: Vasu Sareen, Dr. John Mitry, and Dr. Saeed Farjani. Without their valuable contributions this thesis would look strikingly different and would be worse for it. Their work brought a unique perspective that has changed the way I think about neuronal dynamics, at times challenging but always rewarding.

I owe a huge debt to the incredible group of labmates I've shared space with over these 6 years. Input during practice talks and data clubs, the swirling chatter of the student room, and heady chats during social outings and out-of-town trips had a large impact on my life and work that is impossible to overstate. To Niklas, Sara, Alek, Alexia, Karelle, Jihane, Frédérique, Kaitlin, Rafael, Tian, thank you, it was great getting to know you all. *Mike*, your sense of humour and initial kickstart of my stellate cell patching experience are much appreciated. *Marika*, your bright presence and work ethic were welcome additions to the lab environment. *Patricia*, your technical prowess was endlessly inspiring to me. I'll also never forget your infamous spermine permeation graphic… *Bryan*, you were the grumpy and jaded experimentalist when I first joined the lab. Your insight inevitably increased the quality of a project, and your input forced me to raise my game. *Hugo*, a true innovator, it was inspiring to just hear about your ideas. Can't wait until eNuvio blows up. *Lois*, your endless optimism and unique narrative insight were incredibly memorable, thanks for being my occasional cheerleader. *Kat*, the in-house Danish connection, I hope to once again argue about Spotify playlists in person. *Martina*, the goodwill advocate of the lab, you are sincerely missed. Your presence had a notable positive impact on everyone, I'll see you in Sicily (or London!) someday soon. *Brent*, the lab 'superstar', the quality of your work both at the bench or on the page speaks for itself and was easy to admire. On top of that, it was great hashing through recent papers or chuckling at news stories with you in the student room. *Mark*, a harsh scientific critic but invaluable voice to have in the room, I learned a great deal from your technical expertise and all-around practical sense.

And now to the most recent long-term Bowie lab incarnation: *Amanda*, you joined the lab at an interesting and transitionary time but hit the ground running. I can't wait for your

accomplishments to be fully realized, you've got a bright future ahead of you. *Edward*, the jack-of-all-trades, you were always up for a challenge and always able to get things to work. I can't believe you're still only a MSc student… UBC is lucky to have you. *Adamo*, the resident contrarian, you shook things up from the moment you joined. You've got an incredible natural ability and intellect that will take you far. I'm going to miss laughing at the *Scientific Reports* table of contents with you… Finally, *Erik*, my faithful compadre and international travel companion. I've overlapped with you the longest and we've shared many highs and lows. Our love of *The Office* and comic book movies led into serious talks about our respective projects and lives. I've learned more than I banked on about Canadian historical esoterica, but it's been a blessing having you as a colleague and friend.

An additional thank you goes also to those that shared our student room from the Münter lab, in particular Felix and Sandra. *Sandra*, you were inspiring on an academic level and a force for good within this shared space. I can't wait to get your official Berlin tour one day.

Finally, I'm eternally grateful for the constant support from my friends and family outside of the lab. In no particular order, Ryan B, Alex, Jeremy, Ryan T, Nathan, Jared, Peter, Chris, Phil, and Ricky, thank you. Mom, Dad, Megan, Opa, Oma, Patti, Karlee, and Karsen, you guys are my biggest fans and this wouldn't have been possible without you. A special acknowledgement goes to Lindsey who has seen me after good days and bad, thank you for being my foundation.

CONTRIBUTION TO ORIGINAL KNOWLEDGE

I. I report a patch clamp-induced excitability increase in cerebellar stellate cells

II. I found that the excitability increase is driven by hyperpolarization of spike threshold

III. I found that A-type potassium channels undergo large symmetric shifts in voltage-dependence of activation and inactivation, but that this has no effect on spike threshold

IV. I found that A-type potassium current shifts are absent in excised nucleated patches

V. I found that delayed rectifer potassium currents exhibit stable properties during patch clamp investigation

VI. I found that shifts in sodium channel gating properties, and not surface expression, underlie threshold hyperpolarization

VII. I found that threshold hyperpolarization in stellate cells is initiated before breakthrough into whole-cell configuration

VIII. I found that threshold hyperpolarization is calcium-dependent

IX. I found that threshold hyperpolarization is mediated by PKA and CaMKII

X. I found that shifts in sodium channel properties are influenced by calcium and CaMKII

XI. I found that stable basal excitability can be achieved using loose-seal cell-attached recording

XII. I found that NMDA receptor stimulation causes an upregulation of spontaneous firing frequency in a calcium- and CaMKII-dependent manner

CONTRIBUTION OF AUTHORS

This thesis is written in a manuscript-based format, as outlined in the McGill guidelines. The body of the thesis is composed of two chapters, the first being a published manuscript and the second which will be submitted for publication in a similar form. All manuscripts are co-authored, and a detailed description of authors' contributions follows below, as required by McGill guidelines.

In addition to the two results chapters, I have included one publication as an appendix that I appeared as a co-author. Although not explicitly related to the questions of my main project, I am proud of the work and believe it gives a fuller picture of the productivity during my thesis time.

Chapter 1: "Cerebellar stellate cell excitability is coordinated by shifts in the gating behavior of voltage-gated Na^+ and A-type K^+ channels" was published in eNeuro in April 2019 as **Alexander, R.P.D., Mitry, J., Sareen, V., Khadra, A., & Bowie, D. (2019). Cerebellar stellate cell excitability is coordinated by shifts in the gating behavior of voltage-gated Na^+ and A-type K^+ channels. *eNeuro*, 6(3).** For this work, I generated and analyzed the entirety of the data present in Figures 1.1, 1.2, 1.3, 1.4, 1.7, 1.8, 1.9, and 1.10. I also contributed to some analysis in Figures 1.5, 1.6, and 1.11. J. Mitry generated and analyzed data in Figures 1.5, 1.6, and 1.11. I along with D. Bowie conceived the project. V. Sareen and A. Khadra were responsible for generating the first version of the Hodgkin-Huxley model, while J. Mitry heavily refined the code and performed the majority of the simulations. D. Bowie and I drafted the manuscript with significant input from A. Khadra throughout the modeling sections.

Chapter 2: "NMDA receptor signaling to voltage-gated Na^+ channels mediates intrinsic plasticity in cerebellar stellate cells" has not been submitted for publication at the time of this thesis. For this work I generated and analyzed data for all figures. D. Bowie and I conceived the project and interpreted results. I wrote the manuscript in its current form.

Appendix I

Dawe, G.B., Kadir, M.F., Venskutonytė, R., Perozzo, A.M., Yan, Y., Alexander, R.P.D., Navarrete, C., Santander, E.A., Arsenault, M., Fuentes, C., Aurousseau M.R.P., Frydenvang, K., Barrera, N.P., Kastrup, J.S., Edwardson, J.M., Bowie, D. Nanoscale Mobility of the Apo State and TARP Stoichiometry Dictate the Gating Behavior of Alternatively Spliced AMPA Receptors. ***Neuron*****. 2019 Jun 5;102(5):976.**

For this work I generated and analyzed the data in Figure 7 and contributed some data to Figure 8 and Table S5. I was also involved in the interpretation of results and finalization of the manuscript.

PART I

REVIEW OF THE LITERATURE

1 CEREBELLAR PHYSIOLOGY

1.1 The cerebellar cortex: anatomy and cell types

The cerebellar cortex is one of the most heavily studied and highly characterized sub-organs in neuroanatomy. From Jan Purkyně's first description of the intricate dendritic arborizations of his namesake cell in 1837, to Santiago Ramón y Cajal and Camillo Golgi's meticulous silver nitrate stainings depicting the layered regularity of its sparsely labelled cells in the late 19th century (Sotelo, 2011), to Sanford Palay and Victoria Chan-Palay's early ultrastructural investigations with electron microscopy in the 1970s (Palay & Chan-Palay, 1974), the cerebellar cortex has enjoyed much academic focus. Based on much of these neuroanatomical observations, a generalized circuit pathway was proposed by John Eccles and Masao Ito in the 1960s (Eccles, 1967), and further crystallized into a computational model by David Marr and James Albus a few years later (Marr, 1969; Albus, 1971).

Looking at a slice of the mammalian cerebellum from the sagittal aspect, around the dense white matter bundles in the core of the sample, three layers of neural tissue with distinct microstructural elements are clearly visible (Figure R.1). Nearest to the white matter is the granule layer which is composed almost entirely of granule cell bodies, but also contains Golgi and unipolar brush cells. The granule layer is home to one of the two major inputs to the cerebellar cortex, the mossy fibers. Mossy fibers are glutamatergic and project from a diverse array of precerebellar nuclei including the spinal cord and medullary pathways, vestibular and auditory systems, as well as the reticular and pontine nuclei, which are more closely connected to the cerebral cortex (Ito & Itō, 1984). Neighbouring the granule layer is a single cell-thick sheet of Purkinje cell bodies which comprise the Purkinje layer. Purkinje cell dendrites extend

superficially towards the pia mater, scaffolded by the projections of Bergmann glia. Purkinje cell arbourizations are virtually planar, each having a dendritic extent of ~200 µM (Stuart *et al.*, 2016) while only being ~7 µM wide (Mukamel *et al.*, 2009). Each Purkinje cell is contacted by a single climbing fiber axon, which is the second major input to the cerebellar cortex. Climbing fiber axons project from the inferior olive, a medullary nucleus situated directly below the superior olivary nucleus. The inferior olive receives multimodal sensory information from a number of sources including auditory, visual, vestibular and proprioceptive systems (Ito & Itō, 1984).

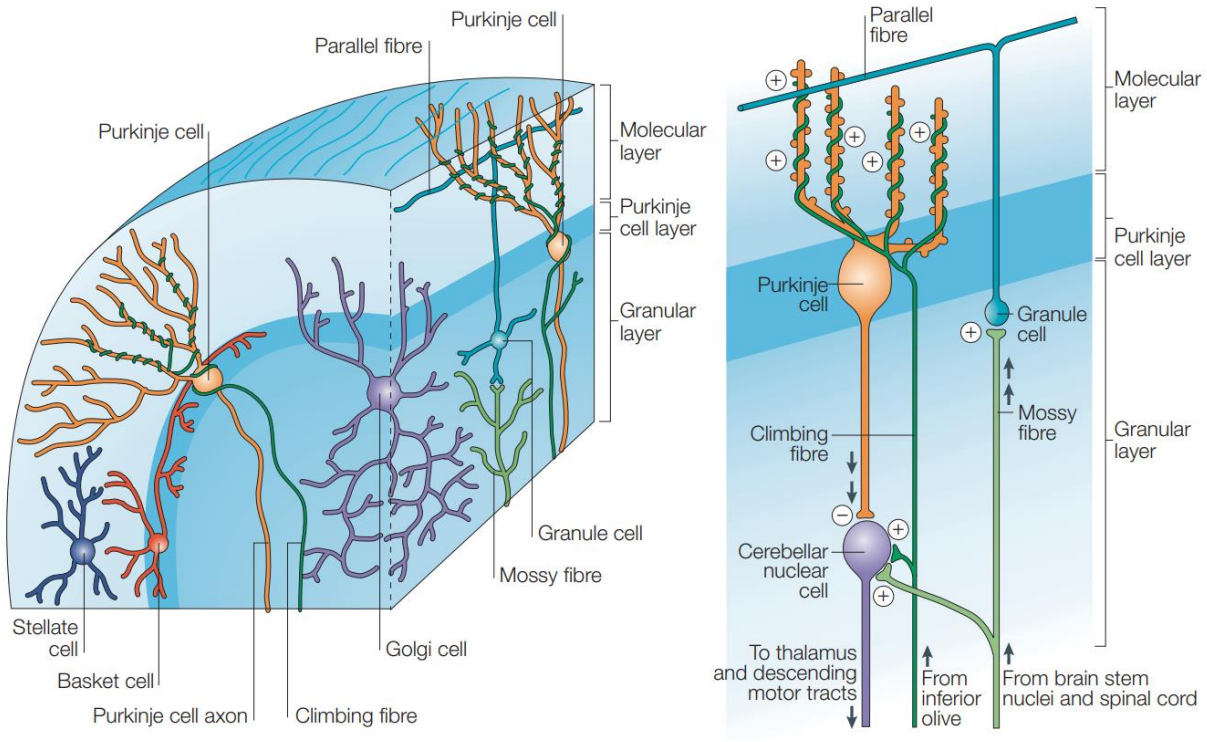

Figure R.1 Cerebellar cortex anatomy and microcircuitry
(left) Cartoon illustrating the major cell types and layers of the cerebellar cortex. Generalized topography is also depicted here, with cell types placed where they are usually found (ie. stellate cells more superficial than basket cells). (right) Diagram of the two major afferent inputs, the climbing and mossy fibers, and their cellular targets. Efferent output of this region is mediated solely by Purkinje cells whose first synapse is onto cells of the deep cerebellar nuclei. Valence of synaptic signal is depicted as (+) for excitatory and (-) for inhibitory. Used with permission from Apps & Garwicz (2005).

Granule cells send their axons past the Purkinje layer to bisect and extend orthogonally in the transverse plane. These axons constitute what become the main excitatory inputs in the

molecular layer, the parallel fibers, which release the neurotransmitter glutamate onto Purkinje cell dendrites and the main inhibitory neurons of this region, molecular layer interneurons (MLIs). MLIs are subdivided into two classes based on size, location, membrane properties, and efferent targeting. Basket cell somata are relatively larger at ~15 µm in diameter (O'Donoghue *et al.*, 1989) and have lower input resistances (Southan & Robertson, 1998). In terms of location, they are found almost exclusively within the lower one-third of the molecular layer (Ramon y Cajal, 1911; Palay & Chan-Palay, 1974) and form GABAergic connections with the somata and proximal dendrites of Purkinje neurons where they encapsulate the entire cell body with their giant 'pinceau' synaptic apparatus. Stellate cells, in contrast, are located in the outer two-thirds of the molecular layer (Ramon y Cajal, 1911; Palay & Chan-Palay, 1974), are smaller in diameter at 8 – 9 µm (Llano & Gerschenfeld, 1993b), and have higher input resistances (Llano & Gerschenfeld, 1993b). Dictated by their location, their projections instead primarily target distal Purkinje dendrites and other MLIs.

Other cell types in the cerebellar cortex include Golgi cells, which are large GABAergic interneurons found in the granule layer that primarily inhibit granule cells with their widely ramified axonal plexus (D'Angelo *et al.*, 2013). Lugaro cells are another type of GABAergic inhibitory interneuron situated in the Purkinje layer directly below Purkinje somata. They have been shown to receive information from Purkinje axon collaterals and transmit inhibition mainly to MLIs (Laine & Axelrad, 1998) and Golgi cells (Dieudonne & Dumoulin, 2000). Unipolar brush cells are glutamatergic interneurons located in the granule layer. These neurons act as amplifiers of vestibular input by enhancing mossy fiber-mediated excitation onto granule cells and other unipolar brush cells (Dino *et al.*, 2001; Nunzi *et al.*, 2001).

Aside from the mossy and climbing fibers, the cerebellar cortex also receives cholinergic and monoaminergic inputs in the form of diffuse, paracrine release zones in all three layers that serve diverse neuromodulatory functions (Schweighofer *et al.*, 2004). Serotonergic tracts deriving primarily from the medullary and pontine reticular formation have been demonstrated to project into and modulate all parts of circuitry in the cerebellar cortex (Kerr & Bishop, 1991). For example, serotonin causes an increase in Lugaro cell activity which in turn feeds-forward an increased inhibitory drive onto Golgi cells (Dieudonne & Dumoulin, 2000). Serotonin has also been shown to induce a long-lasting facilitation of GABAergic synaptic responses in Purkinje cells (Mitoma & Konishi, 1999). Noradrenergic inputs from the locus coeruleus have this same effect on inhibitory Purkinje synapses (Mitoma & Konishi, 1999), while also projecting into the molecular layer and causing an increased spontaneous spike discharge in basket (Saitow & Konishi, 2000) and stellate cells (Kondo & Marty, 1998). Norepinephrine causes an increase in presynaptic release probability at MLI-MLI synapses (Llano & Gerschenfeld, 1993a; Kondo & Marty, 1997), and can also mediate a switch in glutamatergic receptor subunit composition in response to a fear-inducing stimulus (Liu *et al.*, 2010). Cholinergic projections from various brainstem nuclei (Jaarsma *et al.*, 1997) have been shown to cause a long-term enhancement of glutamatergic synapses on Purkinje cells, apparently mediated by muscarinic acetylcholine receptors (Andre *et al.*, 1993). Dopaminergic inputs to the cerebellar cortex have been observed by many groups (Alder & Barbas, 1995; Melchitzky & Lewis, 2000; Schweighofer *et al.*, 2004) but their role is more mysterious.

After this broad overview of the basic anatomy and innervation in the cerebellar cortex, I will now address the physiology of the MLIs in greater detail as the majority of this thesis is focused specifically on this cell type.

1.2 Molecular layer interneuron physiology

1.2.1 Synaptic regulation

As discussed above, MLIs are situated in the molecular layer of the cerebellar cortex and can be subdivided into two groups: basket (BC) and stellate cells (SCs). In addition to the monoaminergic innervation described earlier, inputs to MLIs consist primarily of excitatory parallel fiber (PF) synapses and MLI-MLI GABAergic synapses (Jorntell *et al.*, 2010). A somewhat unique feature of SCs is that their high input resistances allow them to be significantly influenced by quantal events, both excitatory and inhibitory (Carter & Regehr, 2002). In this way, reliable spiking can be evoked by only a few coincident excitatory postsynaptic potentials (EPSPs), and single inhibitory postsynaptic potentials (IPSPs) dramatically suppress or sharpen responses to EPSPs. SC excitatory synapses are also constructed in such a way to respond to high levels of activity in afferent PFs. They express NMDA receptors at extrasynaptic sites outside of the traditional postsynaptic complex (Clark & Cull-Candy, 2002) that are selectively activated by glutamate spillover caused by high frequency release, demonstrated by their notable sensitivity to glutamate reuptake inhibition (Figure R.2) (Carter & Regehr, 2000). The second type of excitatory input to MLIs is also mediated through glutamate spillover, but in this case from climbing fibers (CFs) (Szapiro & Barbour, 2007; Coddington *et al.*, 2013). CF-mediated excitatory postsynaptic currents (EPSCs) have a distinct signature compared to those from PFs in that they

exhibit paired-pulse depression instead of facilitation in the first few hundred milliseconds post-stimulation (Figure R.2) (Szapiro & Barbour, 2007).

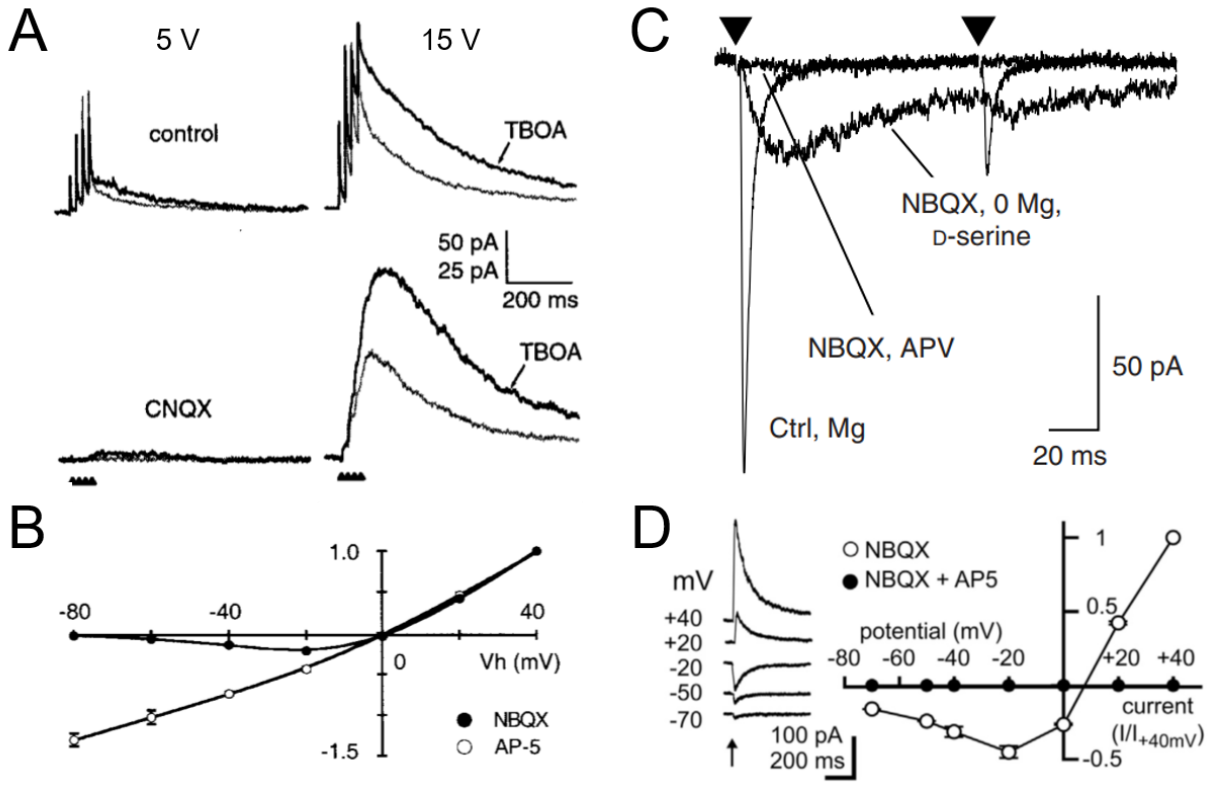

Figure R.2 Molecular layer interneurons express functional NMDA receptors that are located extrasynaptically
(A) High frequency parallel fiber stimulation in the presence of CNQX reveals NMDA receptor-mediated EPSCs at stronger stimulus intensities. Blocking glutamate reuptake with TBOA increases NMDA receptor component, suggesting extrasynaptic location. (B) APV-sensitive EPSCs are strongly inwardly rectifying. (C) Climbing fiber stimulation elicits NBQX-sensitive currents that exhibit paired-pulse depression. EPSCs evoked in the presence of NBQX, 0 Mg, and D-serine are slowly decaying, consistent of NMDA receptors. (D) Climbing fiber EPSCs in the presence of NBQX are strongly inwardly rectifying and APV-sensitive. Used with permission from Clark & Cull-Candy (2002), Carter & Regehr (2000), Szapiro & Barbour (2007), and Coddington *et al*. (2013).

The primary source of inhibitory input onto MLIs is afferent projections from other MLIs. Phasic GABAergic events in cerebellar stellate cells are relatively large and frequent, and miniature inhibitory postsynaptic currents (mIPSCs) can reach hundreds of picoamps in amplitude (Llano & Gerschenfeld, 1993b). Although very stereotypical in terms of activation kinetics, there is a large variation in mIPSC amplitude within individual SCs, which can be

explained by a variable number of postsynaptic GABA receptors receiving synaptic quanta (Nusser *et al.*, 1997). The molecular composition of $GABA_A$ receptors was assumed to be constant across all synapses in SCs as containing α1, β2 and γ2 based on proportion of immunolabelled subunits (Somogyi *et al.*, 1996) and preferential stoichiometry of recombinant receptors (Tretter *et al.*, 1997). However, more recently it has been shown that SCs can drive α3-containing receptors into synapses under certain conditions, specifically by elevating cytosolic reactive oxygen species (Accardi *et al.*, 2014). These receptors give rise to mIPSCs with smaller amplitudes and slower decay kinetics, demonstrating the diversity of inhibitory signaling utilized by MLIs. Another type of inhibitory information transfer in MLIs is through GABAergic autapses (Pouzat & Marty, 1998, 1999). These autoreceptor synapses receive innervation via MLI axon collaterals providing feedback onto themselves, which affords a strong degree of firing rate control (Mejia-Gervacio & Marty, 2006).

MLIs also receive GABAergic input via tonic inhibition arising from stochastic openings of high-affinity extrasynaptic $GABA_A$ receptors, which are outside of the direct apposition of pre- and postsynaptic zones. These receptors are therefore highly subject to the level of GABA transmitter in the extracellular space, which is tightly regulated by the GABA transporters GAT1 and GAT3 on neurons and glia, respectively (Farrant & Nusser, 2005). Tonic inhibition, although heavily studied in cerebellar granule cells (Brickley *et al.*, 2001; Duguid *et al.*, 2012), does not play a large role in MLIs, although some reports link it to spiking pattern (Hausser & Clark, 1997).

1.2.2 Circuit dynamics

The primary role of MLIs in the cerebellar cortex is ultimately to inhibit Purkinje cells, which constitute the sole output of this region. The release of GABA from their presynaptic

terminals, a process normally accomplished through traditional AP-driven transmitter exocytosis, is subject to a variety of regulatory controls. Release of transmitter from MLI terminals can be suppressed via retrograde signaling following postsynaptic Ca^{2+} entry in Purkinje cells (Llano *et al.*, 1991; Vincent *et al.*, 1992) through a process known as depolarization-induced suppression of inhibition (DSI). This signal, although first believed to be acting via metabotropic glutamate receptors (mGluRs) (Glitsch *et al.*, 1996), was discovered to be retrograde endocannabinoid diffusion across the synaptic cleft which bind to CB1 receptors on the MLI terminal, causing membrane hyperpolarization and suppression of vesicle fusion (Kreitzer & Regehr, 2001; Yoshida *et al.*, 2002). Presynaptic mGluRs were still proposed to affect GABA release at the MLI-Purkinje cell synapse (Llano & Marty, 1995), but this could in fact still be due to cannabinoid-mediated DSI (Galante & Diana, 2004). Physiological DSI acts using the endocannabinoid 2-AG (Szabo *et al.*, 2006) whose primary effect is (probably) a reduction of presynaptic P/Q-type voltage-gated Ca^{2+} channel activity (Diana & Marty, 2003, 2004).

MLI terminals also possess presynaptic NMDA receptors that serve to increase GABA release probability (Glitsch & Marty, 1999). In fact, a strengthening mechanism known as depolarization-induced potentiation of inhibition (DPI) was demonstrated to rely on glutamate binding to presynaptic NMDA receptors (Duguid & Smart, 2004; Liu & Lachamp, 2006). This was further shown to increase the size (Fiszman *et al.*, 2005) and release probability of GABA in a protein kinase A (PKA)-dependent manner (Lachamp *et al.*, 2009). Although demonstrated by many groups, other studies have failed to identify any role for presynaptic NMDA receptors at this synapse (Christie & Jahr, 2008; Pugh & Jahr, 2011). GABA release from MLI terminals is further regulated by presynaptic AMPA receptors that paradoxically reduce Ca^{2+} flux through

voltage-gated calcium channels (Rusakov *et al.*, 2005), and thus suppress release (Satake *et al.*, 2000). This process is present at earlier developmental timepoints and is likely more relevant to immature cerebellar interneurons (Liu, 2007). Similar to the action of presynaptic NMDA receptors, presynaptic AMPA receptors also affect the size of the terminals themselves (Fiszman *et al.*, 2007). GABA release can also be regulated by presynaptic $GABA_B$ receptors (Mann-Metzer & Yarom, 2002b), alpha adrenergic receptors (Hirono & Obata, 2006), and neuropeptide Y receptors (Dubois *et al.*, 2012), which showcases the incredible convergence of regulatory mechanisms that fine-tune inhibition on Purkinje cells.

As discussed earlier, CFs mediate a second type of excitatory input to MLIs exclusively via glutamate spillover (Szapiro & Barbour, 2007; Coddington *et al.*, 2013). Aside from communicating indirectly with MLIs, a single CF makes hundreds of synaptic contacts with the Purkinje cell it innervates (Palay & Chan-Palay, 1974), contributing to a robust EPSP response and somatically-generated complex spike (Eccles, 1967). CF-mediated feedforward inhibition through MLIs impacts downstream Purkinje cell activity by favouring post-complex spike pauses in tonic spike output, which are thought to be important for Purkinje cell synchronization (Mathews *et al.*, 2012; Coddington *et al.*, 2013). Complex spikes are accompanied by widespread Ca^{2+} influx in Purkinje dendrites (Rancz & Hausser, 2006; Otsu *et al.*, 2014) which is the biochemical substrate for tuning the strength of neighbouring PF inputs (Ito & Kano, 1982; Konnerth *et al.*, 1992). Aside from their involvement in shaping Purkinje cell activity via CF-mediated feedforward inhibition, MLIs can influence postsynaptic strength of CF-mediated responses in Purkinje cells directly. With the help of targeted genetic control of MLIs (Amat *et al.*, 2017), the role of concomitant inhibitory input on CF-mediated Purkinje depolarization has been revealed. MLI output directly suppresses

CF-evoked dendritic Ca^{2+} signals in Purkinje cells (Gaffield *et al.*, 2018; Rowan *et al.*, 2018), which actively controls the valence of PF plasticity depending on the level of MLI activity (Rowan *et al.*, 2018).

1.2.3 Role *in vivo*

Surprisingly little known is about how MLIs contribute to behaviour in an *in vivo* context. MLI activity has long been linked to cutaneous stimulation (Armstrong & Rawson, 1979), and their receptive fields were mapped in the C3 cerebellar cortex using cutaneous stimulation of forelimbs in cats (Ekerot & Jorntell, 2001; Jorntell & Ekerot, 2002, 2003). One study demonstrated a upregulation of inhibitory input onto Purkinje cells following fear conditioning (Scelfo *et al.*, 2008), suggesting that long-term modifications of MLI-Purkinje synapses were somehow representing the memory. Similarly, other studies have suggested that MLIs underlie the learned eyeblink response, which is another type of classical conditioning that relies on the cerebellum (Attwell *et al.*, 2002; Cooke *et al.*, 2004). More recently, MLI activity has been directly tied to the vestibulo-ocular reflex which functions to compensate for head movement by producing eye movement in the opposite direction, thus stabilizing images on the retina (Wulff *et al.*, 2009; Rowan *et al.*, 2018). Furthermore, multiple groups have demonstrated using genetically-targeted expression of Ca^{2+} indicators specifically in MLIs that their activity encodes movement rate of oromotor behavior (Astorga *et al.*, 2017; Gaffield & Christie, 2017). Aside from these scattered studies, the specific role of MLIs has been inferred through their effects on Purkinje cell firing output (Ozden *et al.*, 2012; ten Brinke *et al.*, 2015; Jelitai *et al.*, 2016).

2 THE NEURONAL ACTION POTENTIAL

The action potential (AP) is the fundamental signaling unit used by excitable tissue to communicate across distance. The AP relies on the electrochemical gradient across the plasma membrane and temporally regimented openings of distinct ion channels to allow flux of ions giving rise to membrane currents. With respect to the nervous system, the ionic basis of the action potential in the squid giant axon was demonstrated to arise from a transient inward flux of Na^+ ions followed by a delayed, non-inactivating, rectifying K^+ conductance, each mediated by their respective ion channel subfamily, each selective for their preferred ion species, and each activated by sufficient depolarization of the membrane potential (Hodgkin & Huxley, 1952). Before the modern acute slice preparation or the dissociated neuronal electrophysiology experiments pioneered in the 1980s, it was assumed by the field that neurons of the central nervous system fulfilled a 'Platonic' role and were simple threshold elements within the larger circuit (Llinas, 1988), as had been described in spinal motoneurons (Coombs *et al.*, 1955). In the decades since, a complement of over a dozen voltage-gated ion channel subtypes, not to mention unique and region-typical membrane specializations, afford an incredible diversity of signaling in the central nervous system (Bean, 2007). The main voltage-dependent ionic conductances that neurons engage during AP firing include members of voltage-gated sodium channel (Nav), voltage-gated potassium channel (Kv), voltage-gated calcium channel (Cav), and calcium-activated potassium channel (KCa) subfamilies, as well as the I_h current mediated through hyperpolarization-activated cyclic nucleotide-gated channels (HCN). The anatomy of an action potential, at least when examining it as a change in membrane voltage over time, consists of a few core components that are summarized in Figure R.3.

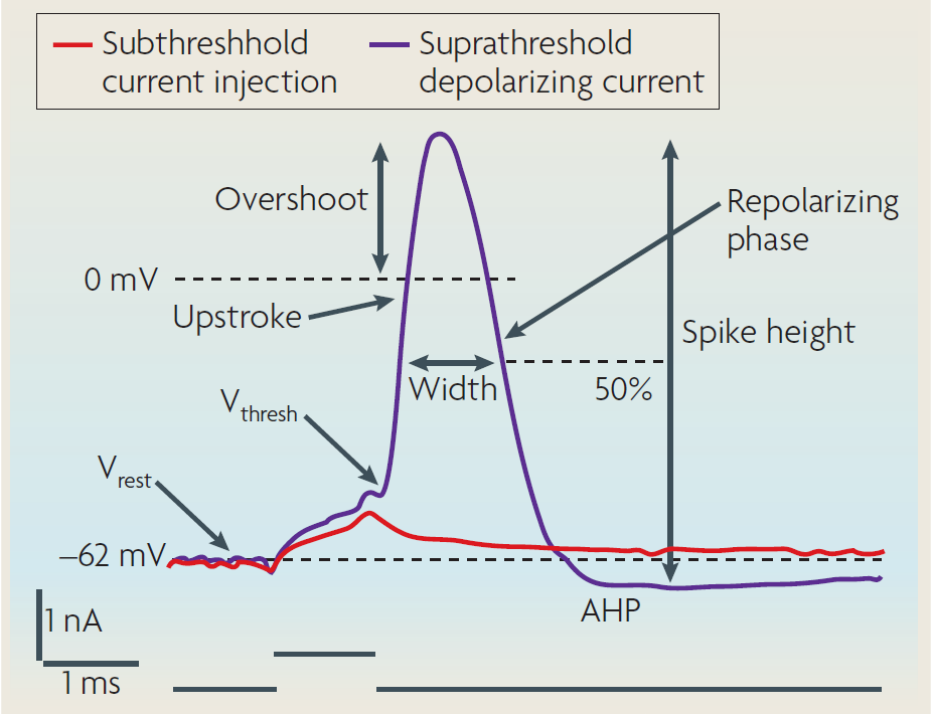

Figure R.3 Prototypical neuronal action potential
Voltage response over time of a neuron responding to either a suprathreshold (purple) or subthreshold (red) current injection. An action potential is elicited only if membrane potential reaches a certain threshold (V_{thresh}). The terms depict various main features found across most neurons in the nervous system. Reproduced with permission from Bean (2007).

2.1 Ionic mechanisms of firing

2.1.1 Voltage-dependent sodium currents

Nav channels can be subdivided into the nine different isoforms Nav1.1 – Nav1.9, four of which are dominant in the CNS: Nav1.1, Nav1.2, Nav1.3 and Nav1.6 (Ahern *et al.*, 2016). There are three main types of Na^+ currents, each having a specific role in regulating neuronal excitability. When Nav channels on a neuronal membrane experience coherent activation, either in response to a step current pulse during an electrophysiological experiment or as a result of synaptically-driven suprathreshold membrane depolarization, the resulting Na^+ current is massive and elicited in an all-or-none fashion. Nav channel activation drives the upstroke of the

consequent action potential, quickly depolarizing the membrane potential toward 0 mV (Figure R.3). Because of this rapid depolarization, Nav channels then undergo voltage-dependent inactivation, closing them to subsequent ion flux. Different types of neurons exhibit differences in Nav gating kinetics (Martina & Jonas, 1997), which are important properties involved in conferring the differences in AP shapes and firing rates between such neurons. Another type of Na^+ current that has a large role in contributing to rapid AP discharges is the resurgent current. First discovered in cerebellar Purkinje neurons, this current arises when the neuron rapidly repolarizes after strong depolarization and Nav channels quickly switch between inactivated and closed states (Raman & Bean, 1997, 2001). It relies on a voltage-dependent blocking particle distinct from the inactivation lid that relieves upon repolarization, thereby allowing a transient Na^+ flux before channels settle into a deactivated state. This particle is likely a cytoplasmic portion of the Nav channel auxiliary subunit β4 (Grieco *et al.*, 2005), although there is some debate in the field (Yan *et al.*, 2014). It has been identified in at least ten neuronal subtypes and in each case establishes opposition to the AP refractory period, thus allowing for quicker subsequent spikes and higher overall firing rates (Khaliq *et al.*, 2003; Lewis & Raman, 2014). The last type of Na^+ current that has been identified in central neurons is the non-inactivating or persistent current. This current was originally identified in both hippocampal pyramidal neurons (Hotson *et al.*, 1979) and cerebellar Purkinje cells (Llinas & Sugimori, 1980) and produces prolonged, small amplitude plateau potentials following APs. Single channel recordings from neocortical pyramidal neurons revealed that the persistent current could be explained by stochastic, low probability reopenings of single Nav channels after inactivation had occurred (Alzheimer *et al.*, 1993), suggesting it follows a distinct gating mode from the typical fast activation discussed earlier. This

conductance is only 0.5 – 5% of peak transient sodium current but has substantial contribution at subthreshold potentials before spikes are initiated, during the interspike interval, as well as to setting resting membrane potential, though in a compartment-dependent manner (Crill, 1996; Hu & Bean, 2018). The persistent Na^+ current is thought to be a critical factor in generating and maintaining repetitive AP firing and neural oscillatory behavior (Llinas, 1988).

2.1.2 Voltage-dependent potassium currents

With respect to the roles of voltage-dependent K^+ channels in regulating AP firing in central neurons, the situation is considerably more complex than that of the squid giant axon and its single contributing outward conductance. Kv channels have been divided into twelve subfamilies (Kv1 – Kv12), with more than thirty distinct isoforms collectively (Gutman *et al.*, 2005). The nomenclature is less helpful when attempting to ascribe a role for an individual channel subtype on an excitable membrane, since there is significant overlap between subfamilies with respect to the profiles of currents mediated. This is further complicated by the extra layer(s) of regulation that Kv channels are subject to, and depending on the membrane microenvironment, the gating behaviour of a given Kv isoform cannot necessarily be predicted solely based on its molecular identity. For example, activation and inactivation properties of Kv channels can be completely transformed based on heteromerization with 'modifier' subunits (eg. Kv5s), association with auxiliary proteins like β subunits and KChIPs, as well as by membrane lipid composition (Coetzee *et al.*, 1999; Oliver *et al.*, 2004; Gutman *et al.*, 2005). In the context of neuronal AP firing, two main types of fast-activating K^+ currents have significant contributions during single spikes: first, the non-inactivating current through some Kv1 and Kv3 channels, and

second, the fast-inactivating A-type current mediated primarily by Kv1.4, the remaining Kv3s, and various Kv4 isoforms (Bean, 2007).

Kv3 channels seem to be specialized to participate in neuronal AP firing since their voltage-dependence of activation is sufficiently right-shifted, causing them to open only near upstroke peaks (Rudy & McBain, 2001). In this way, they activate rapidly and robustly during the repolarizing phase and have a substantial effect on narrowing spike width (Figure R.3). The so-called fast-spiking inhibitory neurons of the hippocampus and neocortex rely on these channels to generate their characteristic high frequency firing rates, and accordingly demonstrate a high expression of Kv3 mRNA transcripts (Weiser *et al.*, 1995). Interestingly, blocking these channels with 4-aminopyridine or tetraethylammonium results in lower firing rates (Erisir *et al.*, 1999), a puzzling effect considering that removing a hyperpolarizing conductance should logically result in greater membrane depolarization. However, blocking Kv3 activity causes the afterhyperpolarization phase (AHP; Figure R.3) following individual APs to be reduced, which likely results in either slower recovery of Nav channels from inactivation or less activation of resurgent Na^+ current, both of which would lead to greater latencies in firing subsequent APs (Fernandez *et al.*, 2005; Akemann & Knopfel, 2006). The A-type current also contributes to the AP repolarizing phase and elimination of the these Kv subunits via genetic approaches or pharmacology yields substantial spike broadening (Kim *et al.*, 2005). A-type currents also shape neuronal firing through frequency-dependent spike broadening in trains of APs during prolonged depolarization. The A-type current is also active at subthreshold voltages and serves to increase latency before the spike is initiated (Connor & Stevens, 1971; Kim *et al.*, 2005; Molineux *et al.*, 2005).

The other main type of Kv channel involved in regulating neuronal AP firing is the Kv7 family, also known as KCNQ channels (Jentsch, 2000). These channel proteins mediate what is known as the M-current, identified in frog sympathetic nerve tissue long before the molecular cloning revolution as the outward conductance downstream of muscarinic acetylcholine receptor activation (Brown & Adams, 1980). Kv7 channels activate and deactivate slowly, thus serving as an inhibitory brake during sustained periods of neuronal activity rather than contributing significantly to the repolarization of individual APs. Pharmacological inhibition of the M-current using XE-991 or linopirdine generally results in increased spontaneous and step-evoked AP firing (Lawrence *et al.*, 2006). Kv7 channels have a large contribution to setting resting membrane potential (in some neurons) which further adds to their regulatory control over intrinsic excitability (Hu & Bean, 2018).

2.1.3 Voltage-dependent calcium currents

Neurons typically express at least four of a variety of different subtypes of Cav channels, specifically the high-voltage-activated L-type channels Cav1.2 and Cav1.3, the P/Q-type Cav2.1, the N-type Cav2.2, and the R-type Cav2.3, as well as the low-voltage-activated T-type channels Cav3.1, Cav3.2 and Cav3.3 (Catterall, 2011). Cav channels contribute little to the upstroke of the typical central AP since their activation kinetics are generally much slower than Nav channels (Bean, 2007). They instead shape APs indirectly through the activation of KCa channels, regulate firing by acting at subthreshold membrane voltages during interspike intervals, and influence pacemaking behaviour (Bean, 2007; Cain & Snutch, 2010). For example, Cav1.3 has been demonstrated to play a crucial role in generating the subthreshold oscillations necessary for the rhythmic spontaneous firing in neurons of substantia nigra (Nedergaard *et al.*, 1993; Chan *et al.*,

2007). The authors showed that although the main sodium-dependent spikes were eliminated upon inclusion of the Nav channel blocker tetrodotoxin (TTX), the slow rhythmic oscillations persisted until the L-type-specific pharmacological inhibitor nifedipine was applied to the midbrain tissue, a treatment that ceased all activity in these neurons.

Similarly, T-type channels also play a large role in regulating firing modes of central neurons. Because of their relatively hyperpolarized and overlapped activation and inactivation curves, their 'window' or steady-state current is quite prominent at typical neuronal resting voltages (Cain & Snutch, 2010), and are thus heavily involved in setting intrinsic excitability (Chevalier *et al.*, 2006). In thalamocortical neurons their contribution to low threshold spikes are critical in generating the bursting rhythms typical of this region (Zamponi *et al.*, 2015). The underlying mechanism for this oscillatory behavior relies on initial membrane hyperpolarization which relieves a greater fraction of these channels from inactivation than available at rest, allowing effective facilitation of subsequent depolarization in a phenomenon known as rebound bursting (McCormick & Huguenard, 1992). T-type channels have also been demonstrated to form complexes with A-type K^+ channels (Kv4) on neuronal membranes in the cerebellum (Anderson *et al.*, 2010b). Ca^{2+} flux through Cav3s binds to the KChIP auxiliary subunits in close association with pore-forming Kv4 channels (Anderson *et al.*, 2010a). This has been shown to affect Kv4 gating properties and regulate the excitability of cerebellar stellate and granule cells (Anderson *et al.*, 2013; Heath *et al.*, 2014).

2.1.4 Calcium-activated potassium currents

Cav2.1 and Cav2.2 are involved in regulating neuronal AP firing mainly through the association with the large conductance KCa (BK) channels, whereby their Ca^{2+} influx is required for sufficient activation of these K^+ channels (Berkefeld *et al.*, 2010). BK channels are activated physiologically by local increases in cytosolic Ca^{2+} concentrations above 10 µM, but also through membrane depolarization-induced movement of their S2-4 segments (Ma *et al.*, 2006), requiring both for robust activation (Cui *et al.*, 1997). These channels form macromolecular complexes (Berkefeld *et al.*, 2006) that are often found localized together in neuronal membranes (Marrion & Tavalin, 1998) to provide efficient Ca^{2+}-driven, K^+-mediated hyperpolarizing influence during the repolarizing phase of the AP as well as the fast phase of the AHP (Lancaster & Nicoll, 1987; Storm, 1987a). The effect of BK channels on shaping the AP in neurons can be visualized by either blocking them directly with the selective pharmacological inhibitor iberiotoxin or blocking their associated Cav subunit, where in each case a broadening of individual APs is produced (Shao *et al.*, 1999; Goldberg & Wilson, 2005). This can be demonstrated in neurons firing trains of APs as well, where spikes later in the depolarizing pulse are broader than those near the start, a phenomenon driven by the gradual inactivation of BK channels over hundreds of milliseconds. Spike broadening during prolonged firing can be occluded by either chelating Ca^{2+} inside the cell or removing Ca^{2+} from the extracellular media (Storm, 1987b; Shao *et al.*, 1999). The small conductance calcium-activated potassium (SK) channel is another type of KCa channel with a relatively smaller single channel conductance and higher sensitivity to Ca^{2+} ion concentration at 100 – 400 nM (Sah, 1996). These channels are expressed as the four distinct isoforms SK1-4, where only SK1-3 are expressed in the central nervous system (Berkefeld *et al.*, 2010). SK channels have been demonstrated to be important to various forms of synaptic plasticity and

signal integration in the dendrites of CA1 pyramidal neurons (Stackman *et al.*, 2002; Cai *et al.*, 2004; Hammond *et al.*, 2006), but they are also a critical in regulating the firing of somatic APs (Pedarzani *et al.*, 2001; Wolfart *et al.*, 2001; Edgerton & Reinhart, 2003). SK channels are insensitive to voltage and are generally thought to underlie the apamin-sensitive intermediate component of the spike AHP in central neurons (Sah, 1996).

2.1.5 Hyperpolarization-activated currents

The hyperpolarization-activated I_h is a current mediated by HCN channels and appears to be a ubiquitous feature of excitable membranes (Pape, 1996). HCN channels have mixed Na^+-K^+ permeability, producing a negative reversal potential in neuronal membranes (-20 – -50 mV) and thus mediate strong inward currents upon activation at subthreshold voltages (Maccaferri *et al.*, 1993; Maccaferri & McBain, 1996). Because of its depolarizing influence near resting membrane potential, these currents have been described as a central pacemaking conductance in neurons that fire spontaneously. The I_h can be blocked by Cs^+ and the HCN-selective inhibitor ZD7288, and applying these agents to neurons both result in reduced intrinsic excitability and firing rates (Maccaferri *et al.*, 1993; Maccaferri & McBain, 1996). This conductance also participates in setting the resting membrane potential in many neurons, contributing about +5 mV overall (Gasparini & DiFrancesco, 1997; Hu & Bean, 2018), as well having a critical role in signal propagation and integration in dendrites (Magee, 1998; Stuart & Spruston, 1998; Magee, 1999).

2.1.6 Morphological factors

Since neurons are highly ramified structures with a significant degree of functional compartmentalization, morphological specializations play a critical role in the generation and

modulation of electrical activity. The voltage-gated ion channels described in the previous section exhibit highly localized expression on neuronal membranes in order to produce the desired output. One such region is known as the axon initial segment (AIS) and is generally thought of as being the site of AP initiation, and consequently the properties of this region confer a lower threshold for spike generation (Palmer & Stuart, 2006; Meeks & Mennerick, 2007; Kole *et al.*, 2008). This can be contrasted with the notion of spike initiation zones in general, which would also include sites on dendrites in neurons that fire dendritic APs (Larkum *et al.*, 2001). The AIS is a 20 – 60 μM long domain at the interface of the proximal axon and neuronal soma enriched in voltage-gated ion channels and unique cytoskeletal elements (Huang & Rasband, 2018). The master regulator is an intracellular scaffolding protein called ankyrin G and all AIS components interact with this molecule either directly or indirectly. Since spike initiation depends on Nav channels, a defining feature of the AIS is a high density of these channels which bind directly to and are clustered by ankyrin G (Garrido *et al.*, 2003; Kole *et al.*, 2008). Nav1.1, Nav1.2, and Nav1.6 are the primary sodium channel isoforms expressed at the AIS, and they exhibit non-overlapping and neuronal subtype-specific expression patterns (Figure R.4) (Lorincz & Nusser, 2008). This specialized molecular composition in the AIS serves a crucial function in determining spike initiation location and setting spike threshold (Hu *et al.*, 2009; Kress *et al.*, 2010). βIV spectrin is another protein specifically enriched in the AIS that interacts with ankyrin G and binds it to the actin cytoskeleton, thus stabilizing the entire complex within the membrane (Huang & Rasband, 2018). Particular potassium channel subunits like members of the Kv1 and Kv7 families are also present in the AIS, through either direct interaction with ankyrin G or indirectly by association with the scaffolding protein postsynaptic density-93 (Pan *et al.*, 2006; Ogawa *et al.*, 2008).

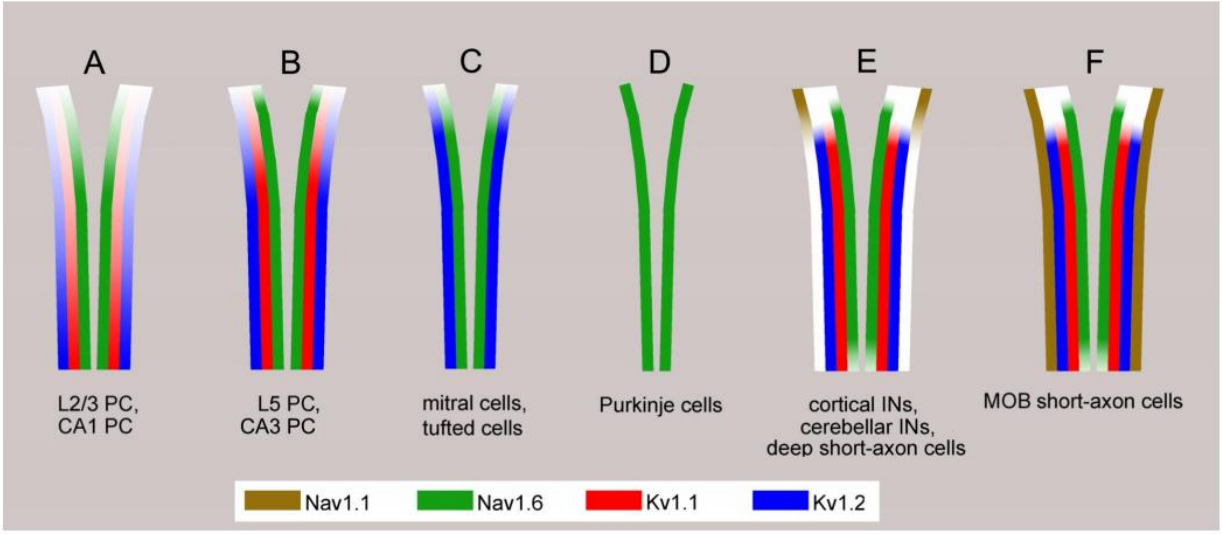

Figure R.4 Differential Nav and Kv channel expression patterns at the axon initial segment
Summary cartoon of immunohistochemical investigation of two types of Nav and two types of Kv. Relative location of AIS was determined using co-staining with ankyrin-G. Used with permission from Lorincz & Nusser (2008).

There is a large diversity of AIS geometry across central neurons. Because of resistive coupling between axon and soma, it has been argued that more distant AIS means lower spike initiation threshold (Brette, 2013; Kole & Brette, 2018). Briefly, this is due to the somatodendritic compartment acting as a current sink for Na^+ flux through Nav in the AIS membrane, where most of it escapes as capacitive current across the relatively larger membrane. Further distance provides greater axial resistance between the AIS and soma, thereby allowing less Na^+ current to influence local potential, thereby reducing AP threshold in this region. Although this is a relatively simple theoretical framework for predicting the electrical impact of AIS location and geometry on firing behavior which has been demonstrated experimentally in some neurons (Kuba, 2012; Meza *et al.*, 2018), there is contrary evidence suggesting that, at best, the situation is more complicated (eg. (Moubarak *et al.*, 2019)).

Aside from AIS properties, neuronal AP firing is also influenced by dendritic excitability. Bursting activity in neocortical pyramidal neurons is critically dependent on dendritic Cav

channels that are recruited during somatic APs due to backpropagation (Stuart *et al.*, 1997; Williams & Stuart, 1999). This represents another layer of regulatory control on neuronal AP output that relies on morphological considerations.

2.2 Regulation of AP firing in the cerebellum

The previous section provided a generic overview to the ionic mechanisms contributing to AP firing in central neurons, and now I will focus more specifically on the cerebellum. This section will take three neurons in the cerebellar cortex as examples, all intrinsically active at rest, and showcase the ionic mechanisms discussed in the previous section and how they are utilized in my region of interest. Following that will be a more thorough overview on what exactly is known about the way MLIs fire APs and how they regulate their ability to do so.

2.2.1 Purkinje cells

One of the most extensively studied neurons of the CNS, the firing behaviour of cerebellar Purkinje cells has intrigued neuroscientists for decades. Purkinje cells are intrinsically active *in vivo* (Latham & Paul, 1971) as well as after acute isolation at room temperature *in vitro* (Raman & Bean, 1999b, a), with spontaneous tonic firing rates ranging from 5 – 200 Hz. With such high spontaneous activity as well as incredible spike regularity in the absence of synaptic input (Raman & Bean, 1999a), there has been a concerted effort to define the ionic mechanisms underlying this firing behaviour. Although earlier evidence suggested otherwise (Clark *et al.*, 2005), Purkinje cell APs are evoked at the AIS (Khaliq & Raman, 2006). This is due to a high density and pure population of Nav1.6 sodium channels (Lorincz & Nusser, 2008), incidentally first discovered and characterized in this cell type (Raman *et al.*, 1997). Raman & Bean performed key voltage clamp

recordings in dissociated Purkinje cell somata where, using the dynamic clamp approach, AP train-shaped voltage commands were injected in order to examine and pharmacologically dissect active voltage-dependent conductances during spiking (Figure R.5) (Raman & Bean, 1999a). They found inward currents were predominantly due to TTX-sensitive Na^+ flux, and outward currents were both Ca^{2+}-dependent and -independent TEA-sensitive K^+ currents. Although AP-derived voltage commands evoked Cav channel activation, mostly P/Q-type, this was entirely occluded under physiological conditions by outward Ca^{2+}-activated K^+ current, probably through BK channels (Womack & Khodakhah, 2002b). A key factor in generating such high spontaneous firing rates is the fast activating, fast deactivating TEA-sensitive K^+ current, probably mediated by Kv3.3 (Akemann & Knopfel, 2006). Akemann & Knopfel found that genetic deletion of this subunit reduced spontaneous Purkinje firing by roughly a third, which could be rescued by inserting artificial Kv3 currents in knockout mice using dynamic clamp. Another important current property for yielding high firing ability is the presence of resurgent Na^+ currents immediately following individual spikes, as well as significant persistent Na^+ current during interspike intervals (Figure R.5) (Raman & Bean, 1999a; Khaliq *et al.*, 2003). These properties, along with the lack of subthreshold K^+ currents (Figure R.5), keeps the depolarizing influence strong and allows subsequent spikes to be efficiently generated. The authors also contrast the spontaneous firing ability of Purkinje cells with other pacemaking neurons throughout the brain in that they do not rely on the I_h current in any significant way (Raman & Bean, 1999a). Other groups have observed a form of firing bistability in Purkinje neurons in acute slice after blockade of I_h, and have argued that its activity preserves tonic firing behaviour during periods of strong inhibition as well as affecting integrative properties (Williams *et al.*, 2002; Nolan *et al.*, 2003).

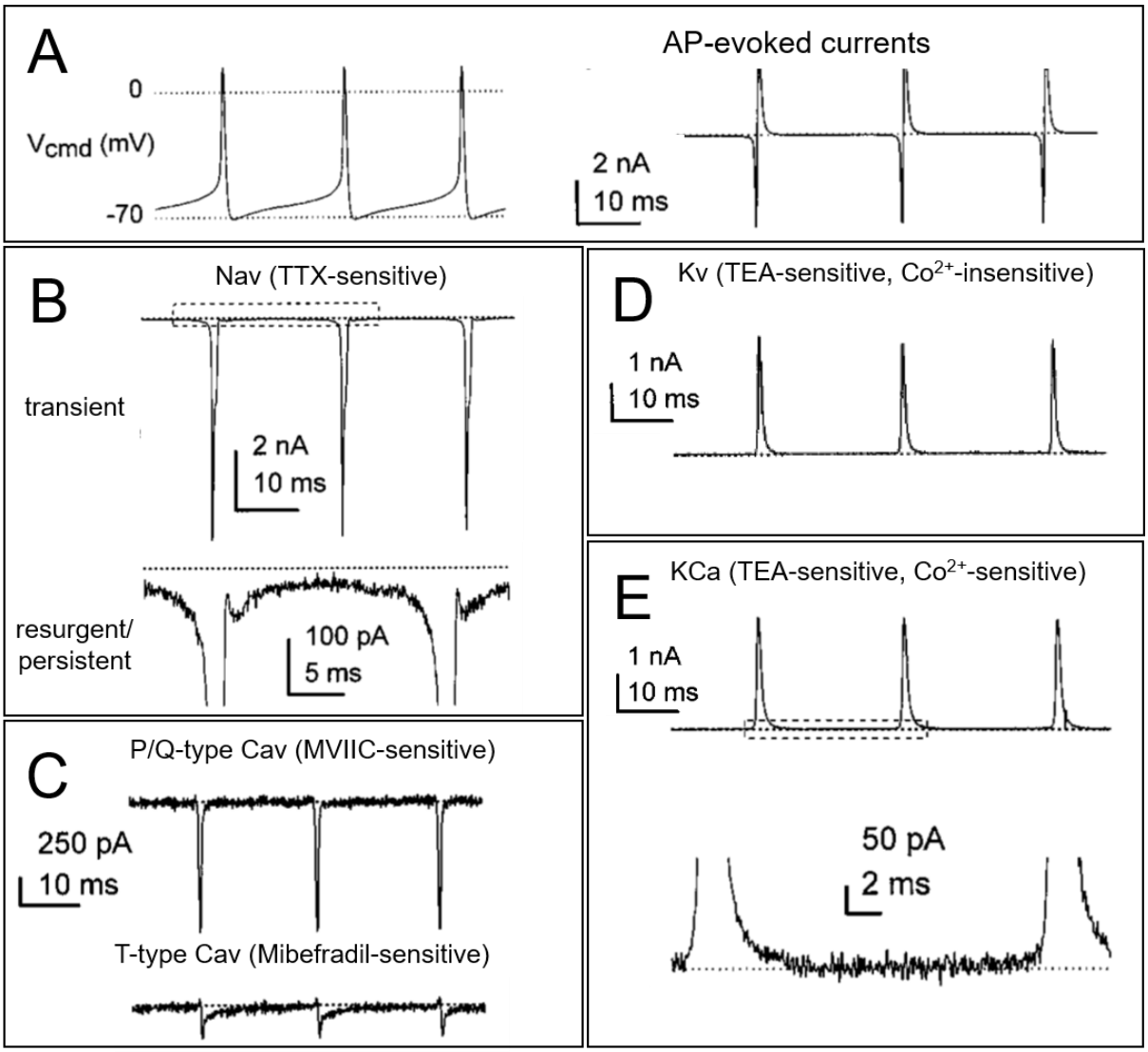

Figure R.5 Ionic components of spontaneous action potential firing in Purkinje cells
(A) (left) Voltage command constructed from typical spontaneous APs in dissociated Purkinje neurons. (right) Currents evoked from AP-derived command protocol injected via dynamic clamp in blocker-free saline. (B) Large transient sodium currents revealed after TTX application and leak subtraction. Note the resurgent bump after the main inward spike, as well as the substantial current flux during the interspike interval. (C) Two predominant calcium current subtypes carrying some inward current during spontaneous firing. (D,E) The main conductances contributing to the overall fast repolarization are both TEA-sensitive, but one being a calcium-independent Kv current, while the other is calcium-dependent and blocked by the broad spectrum Cav channel blocker cobalt. Note the lack of subthreshold outward current during the interspike interval. Used with permission from Raman & Bean (1999).

Apart from tonic AP firing, Purkinje cells also exhibit bursting behaviour, commonly seen during strong depolarizing stimulation but also occurring spontaneously (Womack & Khodakhah, 2002a), that relies on slightly different ionic mechanisms. In dissociated Purkinje neurons,

Swensen & Bean identify that Cav channels, including Cav-dependent activation of BK and SK channels, are important regulators of bursting activity (Swensen & Bean, 2003). Specifically, the slow inactivating T-type Cav channels mediate most of the Ca^{2+} current during the burst duration, as the P/Q-type channels inactivate too quickly and are thus again occluded by fast outward K^+ flux. BK and especially SK channels are important in controlling burst duration, and pharmacological inhibition of these channels dramatically prolongs this activity. Another important factor involved in Purkinje cell bursting is the electrical impact of its extensive dendritic arbour, which the previous study has eliminated during cell isolation procedure. Womack & Khodakhah have argued that Na^+ spikes in the Purkinje soma reverberate into the dendritic compartment and engage P/Q-type Cav channels, whose coherent activation results in a dendritic Ca^{2+} spike which serves to terminate the burst (Womack & Khodakhah, 2004). Kv3 channels have also been demonstrated to be a necessary conductance during bursting, which act in concert with BK channels to robustly repolarize following somatic Na^+ and dendritic Ca^{2+} spike discharge (McKay & Turner, 2004).

2.2.2 Unipolar brush cells

Unipolar brush cells (UBCs) are glutamatergic interneurons in the cerebellar granule layer primarily associated with the processing of vestibular input (Mugnaini *et al.*, 2011). These neurons fire spontaneously both *in vitro* and *in vivo* at frequencies ranging from 5 – 35 Hz (Simpson *et al.*, 2005; Russo *et al.*, 2007; Russo *et al.*, 2008). Intrinsic firing in these cells has been demonstrated to depend on a persistent Na^+ current and the activity of a mixed cationic transient receptor potential (TRP)-like conductance, with little contribution of I_h (Russo *et al.*, 2007). This is under further dynamic control by mGluR2 activity, which upregulates an inward rectifier K^+

conductance, probably GIRK2, and serves to lower firing rates (Russo *et al.*, 2008; Mugnaini *et al.*, 2011). UBCs also possess Nav channels able to produce the resurgent Na^+ current which further promotes their high frequency firing ability (Afshari *et al.*, 2004). UBCs express two types of Cav channels which have distinct roles and yield bimodal firing patterns. First, the combined action of L-type Cav and BK channels produces tonic firing at relatively low levels of depolarizing input, whereas T-type Cav channels contribute more to burst firing following sufficient hyperpolarization to relieve these channels from steady-state inactivation (Diana *et al.*, 2007).

2.2.3 Golgi cells

Cerebellar Golgi cells (GoCs) are GABAergic interneurons that act as the sole source of inhibition in the granule layer of the cerebellar cortex (Crowley *et al.*, 2009) and are critically important in motor control (Watanabe *et al.*, 1998). GoCs, like MLIs, have relatively high input resistances of ~500 MΩ and are intrinsically active in the absence of ionotropic synaptic input and metabotropic effects from mGluR and $GABA_B$ activation (Forti *et al.*, 2006). Forti and colleagues characterized the main conductances involved in this pacemaking activity. They demonstrated that subthreshold activity of persistent Na^+ current and depolarizing influence of I_h at resting membrane potentials to be the primary drivers of autorhythmicity in GoCs. They argue that the M-current mediated by Kv7 channels should be active at rest in GoCs and show that its activation by retigabine reduces step-evoked firing rate, but also show that the antagonist XE-991 has no effect on spontaneous AP frequency. The authors state that this must mean GoCs express XE-991-insensitive Kv7 channels, although I would argue that they simply do not contribute substantially during tonic firing. Retigabine has a very mild effect on evoked firing, so the M-current in GoCs may only be relevant during periods of robust and sustained excitatory

input. Both BK and SK Ca^{2+}-activated K^+ channels have a role in maintaining tonic spike precision as opposed to their minor effect on regulating AP frequency (Forti *et al.*, 2006; Cheron *et al.*, 2009). Rudolph and colleagues shed more light on the types of channels GoCs use to regulate their excitability, specifically the compartment-dependency of their action (Rudolph *et al.*, 2015). They showed that Golgi dendrites express R- and T-type Cav channels that activate upon somatic Na^+ spike invasion, thereby boosting excitatory synaptic inputs and promoting burst firing. Conversely, N-type Cav channels were enriched on the somatic membrane and were important in maintaining tonic spiking pattern. The authors demonstrated that blockade of N-type channels with ω-conotoxin GVIA induced oscillatory, high frequency firing in GoCs, an effect that was replicated by inhibition of both BK and SK channels, as well as strong intracellular Ca^{2+} buffering.

2.3 MLI firing regulation

Like the neurons of the previous section, MLIs are intrinsically active in the absence of synaptic input. Spontaneous firing rates in mammalian cerebellar SCs have been measured both *in vivo* and *in vitro* to be between 5 – 30 Hz (Armstrong & Rawson, 1979; Midtgaard, 1992; Hausser & Clark, 1997; Carter & Regehr, 2002; Jorntell & Ekerot, 2003; Beierlein & Regehr, 2006; Liu *et al.*, 2011; Liu *et al.*, 2014). Interestingly, they exhibit irregular spiking patterns in the presence of spontaneous inhibitory transmission, which switches to a highly regular mode upon $GABA_A$ receptor blockade (Hausser & Clark, 1997). Although not to the same extent as Purkinje cells or mossy fiber boutons, MLIs are fast-spiking and can evoke discrete APs at rates up to ~100 Hz upon sufficient depolarization (Rowan *et al.*, 2014). They do not fire true bursts, so their firing regime is simple tuning of tonic spiking. What are the mechanisms controlling their membrane excitability and firing behaviour?

2.3.1 Channels

MLIs express non-overlapping patterns of two Nav isoforms at their AIS. Specifically, Nav1.6 is located throughout most of the central and distal AIS, whereas there is a relatively smaller patch of Nav1.1 at the proximal portion (see Figure R.4) (Lorincz & Nusser, 2008). In their definitive immunohistochemical characterization, Lorincz & Nusser speculated that the presence of both isoforms in their specific pattern could be present in order to overcome the high spike threshold burden conferred to the AIS by the high density of both Kv1.1 and Kv1.2. The authors could have been contrasting the MLIs with the Purkinje cell where the only investigated channel found in the AIS is Nav1.6. Since both neurons are high-firing, this may have led the authors to think an 'extra' Na^+ conductance would be necessary to confer these properties against the influence of Kv activity. As described earlier, Purkinje cells express an abundance of Kv3 channels which provide the main repolarization during high frequency firing instead of Kv1 (McKay & Turner, 2004; Akemann & Knopfel, 2006), so clearly Nav1.1 must be fulfilling another role. Since different Nav isoforms are differentially regulated by various intracellular signaling pathways (Scheuer, 2011), the distinct presence of Nav1.1 at the proximal AIS may be of importance only upon the induction of its preferential cascade. Lorincz & Nusser further reported that the somatodendritic compartment of cerebellar MLIs is virtually absent of Nav channels (Lorincz & Nusser, 2008). In functional terms, the persistent Na^+ current is substantial in MLIs and has been suggested to contribute to highly variable and 'jittery' spike trains in response to synaptic input (Mann-Metzer & Yarom, 2002a).

Cerebellar SCs express a variety of Cav channels on somatic and dendritic membranes (Molineux *et al.*, 2005), but also on their axonal varicosities where AP-dependent Ca^{2+} flux causes

GABA release (Llano *et al.*, 1997; Forti *et al.*, 2000). Christie & Jahr demonstrated that Ca^{2+} transients here can also be achieved via passive electrotonic spread following dendritic stimulation (Christie & Jahr, 2008), which has also been demonstrated following GABAergic input to rely on Nav channels (de San Martin *et al.*, 2015). Conversely, somatic APs in SCs also invade their own dendrites in a Nav-independent manner, instead relying on Cav channel activation, and ultimately influencing dendritic signal integration (Myoga *et al.*, 2009). Both of these mechanisms depend on compact dendrites and membranes with long length constants. Myoga and colleagues demonstrated that somatic activation of distant Cav is mostly present in immature animals whose neuronal morphology and channel composition allow for it, compared to the relatively leakier dendritic membranes of older animals. Cav channels, probably Cav1 and Cav3 subtypes, also contribute to supralinear integration of dendritic Ca^{2+}, but not voltage, yielded from PF input, which leads to presynaptic release suppression (Tran-Van-Minh *et al.*, 2016) through retrograde endocannabinoid signaling (Myoga *et al.*, 2009).

Cav channels promote MLI hyperpolarization by acting in concert with KCa channels, as is the case for the other cerebellar neurons overviewed in the previous section. Pharmacological blockade of BK channels with iberiotoxin broadens individual APs in spontaneously firing SCs, but paradoxically has no effect on spike rate (Liu *et al.*, 2011). SC membrane excitability is also controlled by the interaction of T-type Ca^{2+} and A-type K^{+} channels, a mechanism extensively investigated by Ray Turner and his lab. Kv4.2 and Kv4.3 subunits associate with the intracellular interacting protein KChIP3 in the SC somatodendritic compartment (Anderson *et al.*, 2010a; Anderson *et al.*, 2010b). KChIPs have EF-hand motifs that allow binding of free Ca^{2+} ions, thus acting as a Ca^{2+} sensor for Kv4 channels. Kv4 channels form complexes with Cav3.2 and Cav3.3 in

SC membranes, and upon activation, Ca^{2+} flux causes a KChIP-mediated depolarizing shift in the steady-state availability of Kv4-mediated A-type K^+ current (Figure R.6) (Molineux *et al.*, 2005; Anderson *et al.*, 2010a; Anderson *et al.*, 2013). Since there is no effect on voltage-dependence of activation, the A-type window current expands and its contribution to subthreshold current during interspike intervals is substantially increased.

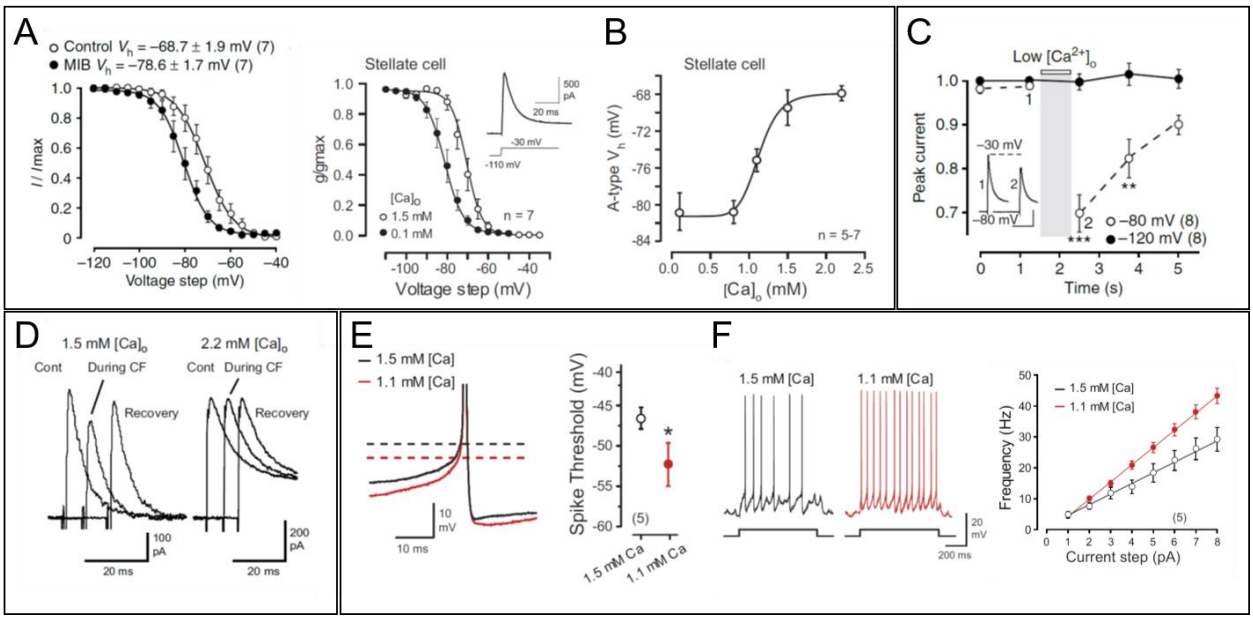

Figure R.6 Cav3-Kv4 complex regulates excitability in stellate cells by sensing extracellular calcium
(A) Steady-state inactivation of A-type K^+ current in SCs shifts ~-10 mV in the presence of T-type Cav blocker Mibefradil (MIB) or reduced external Ca^{2+} concentration. (B) A-type $V_{1/2}$ inactivation is dependent on extracellular Ca^{2+} and can be tuned based on concentration. (C) Brief exposure to low external Ca^{2+} causes a brief reduction in peak A-type current (due to $V_{1/2}$ shift) that subsides after a few seconds. (D) Reductions in extracellular Ca^{2+} produced by climbing fiber stimulation can cause this same brief A-type suppression, but this can be occluded by increasing baseline concentration. (E,F) Physiologically-relevant decrease in extracellular Ca^{2+} significantly decreases spike threshold and increases AP output. Used with permission from Anderson *et al*. (2010) and Anderson *et al*. (2013).

Accordingly, blockade of KChIP regulation increases the gain of step-evoked AP frequency in SCs (Anderson *et al.*, 2010a). This Cav3-Kv4 interaction also produces a biphasic profile in the dependency of spike latency on holding potential during a current step protocol, where a dramatic increase in latency occurs around -72 mV (Molineux *et al.*, 2005). The authors argue that this mechanism has implications for the probability of postsynaptic input evoking an AP

during periods of sustained inhibition. Another role of the Cav3-Kv4 complex is to respond to fluctuations in extracellular Ca^{2+} concentration arising from synaptic activity (Anderson *et al.*, 2013). Anderson and colleagues demonstrate that physiologically-relevant decreases in extracellular Ca^{2+} concentration (~-0.4 mM) cause a concurrent upregulation of SC firing gain, based in a hyperpolarizing shift in A-type availability (Figure R.6). This increase in SC excitability maintains spontaneous inhibitory charge transfer onto Purkinje cells, which the authors argue is an important homeostatic control during periods of prolonged afferent activity.

Cerebellar MLIs express Kv1 and Kv3 subunits at distinct sites. Early electrophysiological and immunohistochemical work demonstrated that BC presynaptic pinceau contain a high density of α-dendrotoxin (DTX)-sensitive Kv1 channels, which were almost absent in the soma (Wang *et al.*, 1994; Southan & Robertson, 1998, 2000). Application of DTX resulted in a dramatic increase in sIPSCs recorded postsynaptically from Purkinje cells (Southan & Robertson, 1998) and a broadening of APs recorded in the BC terminal but not soma (Begum *et al.*, 2016), both of which agree with previous immunostaining of Kv1.1 and Kv1.2 at the MLI AIS (Lorincz & Nusser, 2008). Contrary to these findings, another study found that DTX, although leading to the increased Purkinje cell sIPSC rate observed previously, had no effect on AP-evoked axonal Ca^{2+} entry (Tan & Llano, 1999). Later work demonstrated that although Kv1 channels have no effect on actual AP broadening or GABA release from the BC pinceau, they still serve to regulate Purkinje firing via nonsynaptic ephaptic inhibition, where the electric field surrounding the AIS is modulated to decrease the likelihood of 'postsynaptic' Na^{+} channel activation (Blot & Barbour, 2014; Kole *et al.*, 2015). Otherwise, it is still mostly unclear how/if Kv1 subunits play a part in controlling GABA release from BC terminals.

The role of axonal Kv channels in cerebellar SCs has been studied in great detail by the lab of Jason Christie. Using 2-photon imaging of voltage-sensitive dye loaded into SCs via patch electrodes, Rowan and colleagues find that Kv1-selective blocker DTX broadens AP-mediated fluorescence transients at the AIS but not at presynaptic boutons, whereas the inverse is true for Kv3-selective gating modulator BDS-I (Rowan *et al.*, 2014). Consistent with these findings, DTX slows somatically-evoked spike rate while BDS-I limits the Ca^{2+} entry into SC terminals and thus reduces postsynaptic IPSC amplitudes. The authors argue that there is a mutually exclusive differential expression pattern of Kv1 and Kv3 subunits in the AIS and axonal varicosities, respectively, each controlling distinct aspects of SC excitability and release properties. Furthermore, SC boutons have highly variable spike durations, even between neighbouring boutons along the same stretch of axon, that depend on Kv3 density (Rowan *et al.*, 2016). The authors argue that this local heterogeneity allows for synapse-specific adaptive control and contributes to an overall flexibility in neural circuit dynamics. In agreement with the strong electrotonic coupling between SC compartments observed in previous studies (Christie & Jahr, 2008; Myoga *et al.*, 2009; Christie *et al.*, 2011; de San Martin *et al.*, 2015), Rowan & Christie show that somatic depolarization spreads effectively into the axon (Rowan & Christie, 2017). This passive depolarization broadens AP durations in boutons by pre-inactivating Kv3.4 (and not Kv3.1), and functions to provide short-term potentiation of release, in what they term analog facilitation. These studies provide great insight into the mechanisms by which cerebellar SCs tune their output using differential and compartment-specialized expression of Kv subunits.

HCN channels are expressed in MLIs (Moosmang *et al.*, 1999) and the I_h current has been demonstrated to have an impact on membrane excitability in a compartment-dependent

manner. Blockade using extracellular Cs^+ switched MLI firing type from tonic to oscillatory (Mann-Metzer & Yarom, 2002a), in much the same way that ZD7288 induces membrane bistability in Purkinje cells (Williams *et al.*, 2002). There appears to be developmental regulation of HCN channel expression, since their effect on membrane potential in juvenile animals (Mejia-Gervacio & Marty, 2006) is lost at maturity (Rowan *et al.*, 2016). Interestingly, influence of I_h at BC terminals is still intact in mature animals and its blockade reduces sIPSC frequency and amplitude recorded from Purkinje cells (Southan *et al.*, 2000).

2.3.2 Passive properties

Cerebellar MLIs have other properties that contribute to firing rate control and general excitability aside from differential localization of the voltage-gated ion channels involved in AP generation. As outlined in the previous section, SC membranes exhibit large length constants, allowing for the passive spread of potential from dendrites to soma (Christie & Jahr, 2008), soma to AIS and axon (Christie *et al.*, 2011; Rowan & Christie, 2017), soma to dendrites (Myoga *et al.*, 2009), and axonal varicosities further along the axon (de San Martin *et al.*, 2015). Essentially what this means is that there is a low degree of strict functional compartmentalization in MLIs since membrane potential changes in one part of the neuron can easily invade others, thereby affecting strength of inputs onto dendrites, spike likelihood at the AIS, and release probability inside individual presynaptic boutons. This property is showcased in the study by Carter & Regehr where they use dynamic clamp to inject stereotypical synaptic quantal inputs and investigate the effect on firing pattern in SCs (Carter & Regehr, 2002). They find that individual quanta can reliably induce or prevent APs depending on the valence of the input, which they attribute to small size, electrical compactness, and high input resistance. All of these features in SCs are in

place to provide reliable feedforward inhibition onto their downstream targets, primarily Purkinje cells but also other MLIs.

2.3.3 Calcium buffering

Since activation of plasma membrane Cav channels leads to a 10 – 100 fold increase in free cytosolic Ca^{2+} upon depolarization (Schwaller *et al.*, 2002; Bastianelli, 2003), another factor that plays role in excitability regulation is the presence and relative abundance of endogenous Ca^{2+} buffering proteins. There are three main versions expressed by cerebellar neurons and exhibit a high degree of developmental regulation (Schwaller *et al.*, 2002). Calretinin is expressed by essentially all cerebellar cell types to varying levels, but its function in MLIs is not particularly important (Bastianelli, 2003). Calbindin-D28k is the primary buffering protein in Purkinje cells but is not expressed in MLIs. Parvalbumin (PV) is also expressed by Purkinje cells, but it fulfills the primary Ca^{2+} buffering role in MLIs. PV is a relatively slow Ca^{2+} buffer with a dissociation rate of about 1 s^{-1}, and has been estimated to be found in MLI cytoplasm at a concentration of 0.6 – 1.0 mM (Caillard *et al.*, 2000; Schwaller *et al.*, 2002). One main result of the absence of PV in knockout mice is the conversion of presynaptic depression into facilitation at MLI-Purkinje GABAergic synapses (Caillard *et al.*, 2000). This is presumably due to the accumulation of residual terminal Ca^{2+} after initial release that potentiates release upon subsequent stimulation. The impact of PV on basal firing rates is unclear however. A previous study in cerebellar granule cells demonstrated that a calretinin knockout resulted in a substantial increase in spontaneous firing (Gall *et al.*, 2003), so whether the same is true for MLIs is not known. The same would theoretically be true for a PV knockout, since longer durations of free Ca^{2+} able to access binding sites on KCa channels would provide more complete activation of these channels to narrow spikes and increase AHP,

which should result in quicker overall AP rates. Their ability to fire at such high frequencies also does not have to depend on presence of Ca^{2+} buffers, since similar PV-expressing interneurons in the hippocampus still demonstrate fast-spiking even in the absence of PV (Schwaller *et al.*, 2002) and probably rely on distinct Nav and Kv specializations instead (Hu & Jonas, 2014; Hu *et al.*, 2018).

2.3.4 Electrical coupling

Another interesting property of MLIs is their tendency to be electrically coupled in inhibitory networks. This is accomplished though expression of Connexin 36 and their formation of interneuronal pores called gap junctions (Alcami & Marty, 2013). These electrical synapses allow a certain amount of potential change in a presynaptic neuron to be exerted onto its postsynaptic partner. Electrophysiological recordings have revealed that roughly 40% of MLI pairs are electrically connected (Mann-Metzer & Yarom, 1999). On average, ~10% of the voltage influence is transmitted to the postsynaptic MLI during sustained somatic hyperpolarizations, and ~0.5% during AP-mediated depolarizations (Alcami & Marty, 2013; Rieubland *et al.*, 2014). This electrical coupling serves to synchronize activity in nearby MLIs into a cohesive network, amplifying spatial convergence of inhibitory drive onto Purkinje cells (Kim *et al.*, 2014).

3 ION CHANNEL REGULATION

Pore-forming subunits of voltage-gated channels, though responsible for ion conduction, are nevertheless partnered with a wide array of interacting molecules and subjected to many levels of structural and chemical regulation. Many of these reactions and manipulations result in a fine-tuning of functional gating output, whether through trafficking of the constructed channels

to the membrane surface, clustering at a desired site, or tweaking voltage-sensitivities of channel complexes. In the next section, some of these control mechanisms will be overviewed, with specific attention paid to the particular Nav, Kv, and Cav channels that are important to AP firing in cerebellar MLIs.

3.1 Nav channels

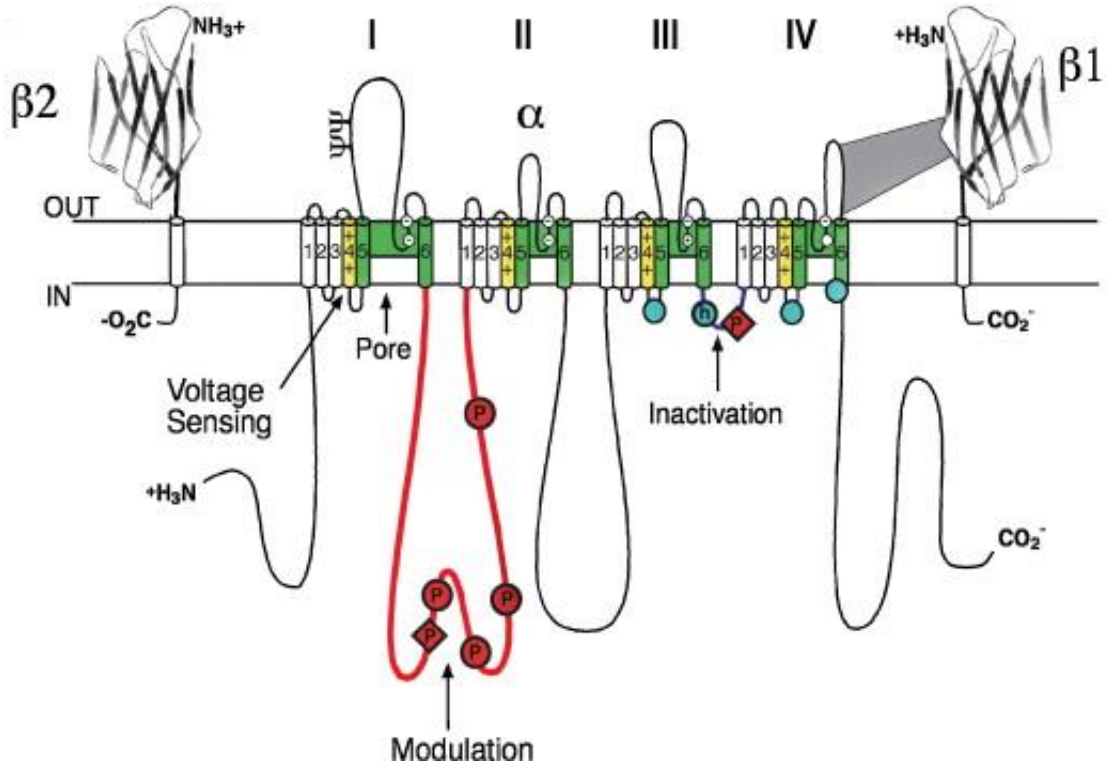

Figure R.7 General topology of Nav channel alpha subunit
Generic topology diagram of a stereotypical sodium channel polypeptide embedded in the plasma membrane. Domains I – IV constitute the four subunits of the pseudotetrameric tertiary structure. Each domain consists of six transmembrane segments S1 – S6, with the voltage-sensitive positive charges (+) concentrated on each S4. The canonical phosphorylation sites (P) are also depicted, mostly on the DI-DII cytoplasmic linker, as well as near the inactivation gate (h) between DIII and DIV. β1 and β2 are also shown with their single transmembrane regions. Possible glycosylation sites are also located on the extracellular S5-S6 linker on DI (Ψ). Reproduced with permission from Yu & Catterall (2003).

Nav channels are single polypeptides stretches, each with an intracellular N-terminus, four repeating domains (DI-DIV) containing six transmembrane segments (S1-S6) each, and a cytoplasmic C-terminal domain (CTD) (Figure R.7) (Catterall, 2000). S5/S6 of each domain are the

pore-lining regions, while S1-S4 segments constitute voltage sensor domains and translocate in an extracellular direction upon membrane depolarization, aided by critical positively-charged residues on S4 segments. The extracellular segment-segment linkers are generally thought of as binding regions for β subunits, while the intracellular domain-domain linkers, as well as the CTD, are enriched in residues important for cytoplasmic regulators.

3.1.1 β subunits

Neuronal Nav channels were first purified as pore-forming α subunits weighing ~260 kDa, in complex with two smaller auxiliary β subunits of 30 – 40 kDa (Figure R.7) (Catterall, 2017). β subunits are found in five different isoforms: β1 and its splice variant β1B, followed by β2, β3, and β4 (O'Malley & Isom, 2015). Each α subunit interacts with two β subunits, either a β1 or β3 covalently, and either a β2 or β4 through disulfide bridges. Heterologous co-expression of α and β subunits demonstrates the impact of these protein-protein interactions on channel function. For example, expression of Nav1.2 with both β1 and β2 in *Xenopus* oocytes yielded larger peak current densities, hyperpolarized shifts in channel availability, and rapid inactivation compared to α subunits expressed alone (Isom *et al.*, 1995). Co-expression of β1 or β3 with Nav1.3 in Chinese hamster ovary (CHO) cells resulted in a negative shift of steady-state inactivation, but no effect on rate of inactivation (Meadows *et al.*, 2002). Co-expression of β4 with Nav1.1 in human embryonic kidney (HEK) 293 cells resulted in a negative shift in voltage-dependence of activation as well as an increase in persistent current (Aman *et al.*, 2009). These effects are not consistent across all cell types, expression systems, or Nav isoforms, so the best way to determine the functional impact of a particular β subunit is to study it in a neuronal context. Well-known to be associated with Nav1.6 in cerebellar Purkinje cells, β4 was theorized to provide the cytoplasmic

factor necessary for an open channel block mechanistic explanation of the resurgent Na^+ current (Grieco *et al.*, 2005). However, later work demonstrated that Purkinje-specific genetic deletion of β4 greatly attenuated resurgent current but did not eliminate it (Ransdell *et al.*, 2017). Neurons lacking β4 also exhibited negatively-shifted voltage-dependence of activation as well as greatly reduced persistent current. Although apparently not entirely responsible for the resurgent current, β4 in Purkinje cells clearly has an important modulatory role on Nav function, thus demonstrating the importance of β subunit regulation of Nav in neurons.

3.1.2 Spectrins and fibroblast growth factors

As discussed earlier, βIV spectrin is a critical structural element in the neuronal AIS. This protein has been shown to directly regulate Nav channel function in a Ca^{2+}/calmodulin-dependent kinase (CaMKII)-dependent manner. In cardiomyocytes from mutant animals containing disrupted βIV spectrin, Nav channels exhibited depolarizing shifts in steady-state inactivation as well as reduced persistent current, which resulted in abnormal cardiac excitability (Hund *et al.*, 2010). βIII spectrin is another member of this protein subfamily and has been shown to regulate Purkinje cell dendritogenesis. Elimination of βIII spectrin in Purkinje cells also caused a reduction in both transient and resurgent Na^+ currents, an effect that can be recapitulated in HEK 293 cells (Perkins *et al.*, 2010; Clarkson *et al.*, 2014). Intracellular fibroblast growth factors (FGFs) are another family of proteins that interact with the AIS and regulate Nav channel function in neurons (Xiao *et al.*, 2013). In HEK cells, co-expression with FGF14 reduced Nav1.5 current density but increased current for Nav1.1 (Lou *et al.*, 2005). Depending on the splice variant, it can either depolarize or hyperpolarize channel availability of both Nav1.1 and Nav1.5. For example, FGF14-1a depolarized channel availability of Nav1.5 while FGF14-1b had the opposite effect. In

contrast, both splice forms had a depolarizing effect on Nav1.1 channel availability co-expressed in HEK cells (Lou *et al.*, 2005). In hippocampal neurons, both FGF14 variants increased current density and hyperpolarized voltage-dependence of activation. Furthermore, FGF14 variants, especially 1b, heavily reduced current density of both Nav1.2 and Nav1.6, while all splice variants hyperpolarized channel availability, although to varying degrees (Laezza *et al.*, 2009). Further work demonstrated that concerted effort by FGF13 and FGF14 controls Nav localization based on neuronal polarity (Pablo *et al.*, 2016). FGF13 binds to Nav channels and limited their somatodendritic expression in hippocampal neurons, while FGF14 clustered Nav channels directly at the AIS. This is corroborated by electrophysiological evidence showing that knockdown of FGF13 increased Na^+ current density, whereas FGF14 knockdown sharply reduced it (Pablo *et al.*, 2016). Lastly, FGF14 has been shown to regulate the resurgent current in Purkinje cells where it also substantially depolarized Nav channel availability (Yan *et al.*, 2014). Although these proteins have been shown to bind directly to the Nav α subunit, it is possible that they are exerting at least some of their modulatory impact indirectly by manipulation of one or more β subunits.

3.1.3 Kinases

Nav1.1, Nav1.2, and Nav1.3 are the three original Nav subunits identified in the brain and exhibit similar regulation by protein kinases (Scheuer, 2011). Biochemical studies revealed the major serine phosphorylation sites for adenosine 3',5'-monophosphate (cAMP)-dependent protein kinase (PKA) on the intracellular DI-DII loop (Figure R.7) (Rossie & Catterall, 1987, 1989). Activated PKA in *Xenopus* oocytes reduced current density of both recombinantly expressed Nav1.1 and Nav1.2 in a DI-DII loop-dependent manner (Gershon *et al.*, 1992; Smith & Goldin,

1998). Protein kinase C (PKC) activation reduced current density of rat Nav1.2 expressed in CHO cells, and also slowed inactivation kinetics (Numann *et al.*, 1991). This effect depended on phosphorylation of serine 1506, which is located on the inactivation gate in loop DIII-DIV (West *et al.*, 1991). Interestingly, serine 1506 must be phosphorylated by PKC before PKA can exert its effects on Nav1.2, demonstrating convergent regulation by these two kinases (Li *et al.*, 1993). PKA and PKC both caused an increase in Nav slow inactivation, a gating process consisting of a gradual drift toward a refractory state distinct from fast inactivation that occurs over seconds rather than milliseconds. This kinase regulation of slow inactivation depended on asparagine 1466 on the DIII-S6 segment of Nav1.2 (Chen *et al.*, 2006). Although most of this pioneering work focused on rat Nav1.2, there are phosphorylation sites unique to Nav1.1 (still mostly on the DI-DII loop) (Berendt *et al.*, 2010) that leave open questions regarding differences in subunit-specific effects relating to channel function and neuronal excitability.

Nav1.6 current density is also mildly reduced by PKA and PKC activity, though not nearly to the degree of Nav1.2 (Chen *et al.*, 2008). Instead, Nav1.6 is more strongly regulated by p38 mitogen-activated protein kinase (MAPK). Activation of MAPK in ND7/23 cells transfected with Nav1.6 reduced Na^+ current through a mechanism dependent on serine 553 on the DI-DII loop (Wittmack *et al.*, 2005). The Nav1.6-FGF14 complex is also subject to regulation by glycogen synthase kinase 3 (GSK3) and casein kinase 2 (CK2), and their activation resulted in increased FGF14 association, increased transient Na^+ current, and depolarized channel availability (Shavkunov *et al.*, 2013; Hsu *et al.*, 2016).

Returning to Nav1.2, this subunit is also regulated by tyrosine phosphorylation through Fyn kinase, one of the Src family tyrosine kinases expressed in the brain (Ahn *et al.*, 2007). Co-expression with Fyn kinase increased inactivation rate of Nav1.2 as well as negatively shifted its channel availability. Tyrosine residues within Src homology 3 (SH3) domains on the DI-DII as well as the DIII-DIV loops are required for this effect. Nav1.1 lacks this SH3 domain and is thus unaffected by Fyn kinase (Beacham *et al.*, 2007).

With respect to CaMKII phosphorylation of Nav channels, most of the effort has been on the dominant cardiac isoform Nav1.5 where it causes a hyperpolarizing shift in steady-state availability (Wagner *et al.*, 2006). However, a handful of recent studies suggest that CaMKII could have an important role in brain Nav modulation. First, CaMKII has been demonstrated to work in concert with FGF12 to negatively shift voltage-dependence of activation in Nav1.2 channels, as well as to promote basal current density in HEK 293 cells (Wildburger *et al.*, 2015). Second, activated CaMKII increased persistent current in epilepsy-related Nav1.2 mutants expressed in HEK 293 cells, as well as depolarized channel availability (Thompson *et al.*, 2017). Third, CaMKII activity increased calmodulin (CaM) binding to the Nav1.1 CTD IQ motif, although its functional impact remains unclear (Li *et al.*, 2018). In addition, CaMKII regulation does not have to be on the α subunit itself to confer modulation onto Nav gating behaviour. For example, in cardiomyocytes CaMKII requires βIV spectrin in order to confer its hyperpolarizing effect on channel availability (Hund *et al.*, 2010). Taken together, these findings demonstrate how much there still is left to learn about kinase regulation of brain Nav channels, in particular Nav1.1 and Nav1.6. Furthermore, CaMKII is a relatively understudied phosphorylating agent in the context of brain Nav.

3.2 Kv channels

Neuronal Kv channels are homo- or heterotetramers composed of four domain-like subunits, each with six transmembrane segments and ~80 kDa in size (Pongs & Schwarz, 2010). The S1-S4 segments again function as the voltage-sensing domain. Although there is an abundance of important regulatory mechanisms that affect KCa and leak channels, this section will focus primarily on subfamilies that will be discussed in later parts of this thesis, specifically, Kv1, Kv3, Kv4, and Kv7 proteins.

3.2.1 β subunits

Original purification studies found Kv1 subunits always in complex with another protein weighing ~40 kDa in a 1:1 stoichiometry (Pongs & Schwarz, 2010). It was suggested that native Kv1 channels were octameric macromolecules consisting of four transmembrane α subunits and four cytoplasmic β subunits, which was later confirmed in the first crystal structure of this complex (Long *et al.*, 2005a). Kvβ subunits are expressed as three main isoforms, Kvβ1, Kvβ2, and Kvβ3, and further diversity is afforded through alternative splicing of its N-terminal domain. The N-termini of the α subunits interact with each other upon tetramerization and protrude intracellularly to provide a docking platform for the β subunits, also already tetramerized (Gulbis *et al.*, 1999; Sokolova *et al.*, 2001; Long *et al.*, 2005b). Co-expression of Kvβ subunits with Kvα resulted in increased surface expression and larger currents in heterologous systems (Accili *et al.*, 1997), and they also have a role in targeting to specific neuronal compartments (Gu *et al.*, 2006). In terms of functional effects, it was demonstrated that the N-terminal domain of the Kvβ subunit could act like an inactivation gate, swinging into the Kv pore to occlude ion flux (Heinemann *et al.*, 1995; Heinemann *et al.*, 1996). This essentially would convert a non- or very slowly-

inactivating current response into a relatively rapidly decaying one; for example, Kv1.1 co-expressed with Kvβ1 (Heinemann *et al.*, 1994; Rettig *et al.*, 1994). The other consequence of Kvβ interaction is a negative shift in voltage-dependence of activation on their Kv1 counterparts. For example Kvβ2 shifted the $V_{1/2}$ activations of Kv1.4 and Kv1.5 ~10 mV more hyperpolarized (Heinemann *et al.*, 1996).

The main effects of Kvβ subunits on Kv1 channels appear to be increased current density, facilitation of N-type or 'fast' inactivation, and negatively-shifted voltage dependence of activation, although these are highly dependent on both the specific α and β subunit involved (Pongs & Schwarz, 2010). In neurons, Kv1 subunits are strategically positioned at the AIS to control AP threshold and duration (Figure R.4) (Lorincz & Nusser, 2008), so any modulation of Kv1 gating would be expected to have a profound effect on neuronal function. To this end, electrophysiological investigation of neurons in Kvβ knockout mice has revealed decreased A-type current, increased neuronal excitability, and animals that are more susceptible to seizures (Giese *et al.*, 1998). However, even in Kvβ1/Kvβ2 double knockout mice Kv1 expression at cerebellar BC terminals was preserved, so there are clearly additional forms of regulation on Kv1 function in neurons (Connor *et al.*, 2005).

3.2.2 KChIP and DPPL proteins

Potassium channel interacting proteins (KChIPs) interact exclusively with Kv4 subunits and confer a wide array of functional effects. Unlike Kvβs, KChIPs purify as monomers without tetramerizing, but still associate with Kv4 subunits with a 1:1 stoichiometry (Pongs & Schwarz, 2010). There are four known KChIP genes (KChIP1-4) that encode a large number of alternatively

spliced isoforms. In contrast to Kvβs, structural contact between KChIPs and Kv4s is complex and intricate, with the KChIP molecules spread laterally outward parallel to the plasma membrane, forming many interaction sites with the α subunit N-termini (Kim *et al.*, 2004; Callsen *et al.*, 2005; Wang *et al.*, 2007). Generally, KChIPs affect Kv4 function by increasing surface expression, slowing N-type inactivation rate, and speeding recovery from inactivation, although this varies greatly between KChIP isoforms (Pongs & Schwarz, 2010). For example, KChIP4 had only marginal effects on current density and recovery rate, while KChIP1 increased peak Kv4 current by more than ten-fold (An *et al.*, 2000; Jerng & Pfaffinger, 2008). KChIPs contain EF-hand motifs and early studies demonstrated that Ca^{2+} concentration could manipulate the regulatory ability of KChIP on Kv4 function (An *et al.*, 2000; Patel *et al.*, 2002). Ca^{2+}-dependent, KChIP-mediated modulation of Kv4 gating in a physiological context was first demonstrated in MLIs where activation of nearby T-type Cav channels acted as the source of Ca^{2+} to shift steady-state Kv4 availability (Anderson *et al.*, 2010a).

Dipeptidyl peptidase-like proteins (DPPLs) are the other main accessory subunit found with native Kv4s, and together with KChIPs, they constitute the full multimeric channel protein complex found on membranes of excitable cells. Two families of DPPLs have been characterized, DPP6 and DPP10, each containing a single short transmembrane segment and large extracellular CTD (Nadal *et al.*, 2003; Jerng *et al.*, 2005). Unlike the Kv accessory subunits discussed so far, DPPL proteins form dimers and preferentially associate with Kv4s in a 2:4 stoichiometry (DPPL:Kv4) (Kitazawa *et al.*, 2015). Heterologous expression of DPPLs increased surface expression of Kv4s as well as modulated channel gating, specifically by speeding inactivation and hyperpolarizing steady-state activation and inactivation properties (Nadal *et al.*, 2003; Jerng *et*

al., 2005; Jerng *et al.*, 2007). Interestingly, co-expression of Kv4, DPPL, and KChIP yielded A-type K^+ currents with properties most resembling those found in native neurons (Amarillo *et al.*, 2008), providing further support for it being an accurate depiction of the Kv4 channel complex found in physiology.

3.2.3 KCNE proteins

Minimal K^+ channel protein (MinK, or KCNE1) and MinK-related peptides (MiRPs, or KNCE2-5) are small membrane-spanning proteins usually associated with the Kv7 channel family. KCNE subunits bind to Kv7 channels with a 2:4 stoichiometry (KCNE:Kv7) but their structural association sites are relatively unclear (Morin & Kobertz, 2008). The KCNE structure suggests that it wedges in between Kv7 voltage-sensing domains in the membrane (Kang *et al.*, 2008), and recent work has shown that extracellular residues on the KCNE3 N-terminus interact with positively charged residues in the Kv7.1 S4 voltage-sensor (Barro-Soria *et al.*, 2015). KCNE1 and KCNE3 have dramatically opposing effects on the gating of Kv7.1. Co-expressed KCNE3 potentiated Kv7 current density by ~10-fold while stabilizing its open conformation, essentially converting Kv7.1 into a voltage-independent channel (Schroeder *et al.*, 2000). KCNE1, while also increasing Kv7 current density, seemed to stabilize the closed conformation of the channel, slowing activation kinetics and shifting its voltage-dependency ~20 mV more depolarized (Barhanin *et al.*, 1996; Sanguinetti *et al.*, 1996). As opposed to other Kv auxiliary subunits, KCNEs are more promiscuous, having been demonstrated to associate with and modulate gating of Kv1, Kv2, Kv4, and Kv11 isoforms (Abbott & Goldstein, 2002; McCrossan & Abbott, 2004). Interestingly, KNCEs also regulate Kv3 function, which is of importance to cerebellar neurons, including MLIs, where these channels are important for fast-spiking behaviour (see Section 2.3.1).

In CHO cells, co-expression with KCNE1-3 caused a slowing of activation and deactivation kinetics of both Kv3.1 and Kv3.2, as well as a hyperpolarized activation profile (Lewis *et al.*, 2004). KCNE1 and KCNE2 have also been shown to act as a retention signal for Kv3.3 and Kv3.4, and co-expression demonstrated a complete inhibition of surface expression (Kanda *et al.*, 2011a). This retention was only present for homomeric channels, however, and co-expression with Kv3.1 allowed functional heteromeric Kv3.1/Kv3.4/KCNE channel complexes onto the surface (Kanda *et al.*, 2011b). The authors argued that KCNEs are a mechanism for neurons to dynamically modulate Kv3 channels to fulfill other roles than repolarization during fast-spiking.

3.2.4 Kinases

Due to the massive combinatorial complexity of Kv subunits, ascribing definitive and relevant phosphorylation effects on Kv channel function has been particularly challenging, especially compared to the single polypeptide channels like Nav and Cav (Park *et al.*, 2008). This next section outlines several examples of specific phosphorylation events that modulate activation and inactivation profiles, single-channel conductance, and surface expression of neuronal Kv subtypes.

First, phosphorylation can regulate inactivation kinetics of various Kv subtypes. PKA-mediated phosphorylation state controls N-type inactivation of Drosophila *Shaker* channels (Kv1-type) expressed in *Xenopus* oocytes in a manner dependent on the CTD (Drain *et al.*, 1994). Applying phosphatase to patches containing *Shaker* substantially slowed inactivation kinetics, an effect that could be occluded through inclusion of active PKA in the recording pipette. In another study, PKC-mediated phosphorylation of the N-terminus of Kv3.4 channels eliminated N-type

inactivation completely (Covarrubias *et al.*, 1994). Slowing of N-type inactivation has also been observed in Kv1.4 expressed in HEK 293 cells following treatment with constitutively active CaMKII (Roeper *et al.*, 1997). Second, kinase activity can also affect surface expression of Kv channels. Kv1.2 surface expression in *Xenopus* oocytes is upregulated by PKA (Huang *et al.*, 1994) and downregulated by tyrosine kinase (Huang *et al.*, 1993). Kv1.1 is upregulated by PKA through phosphorylation of a conserved site on the CTD (Levin *et al.*, 1995), while Kv3.1 is downregulated by PKC in HEK 293 cells (Critz *et al.*, 1993). Third, kinase activity regulates voltage-dependence of activation and steady-state inactivation of Kv channels. Kv2.1 is maintained at a high resting phosphorylation state in mammalian neurons and potentiating the phosphatase calcineurin induces hyperpolarizing shifts in activation properties (Park *et al.*, 2006). Kv4 channels exhibit depolarizing shifts in both activation and inactivation following stimulation of either PKA or PKC in CA1 pyramidal neurons (Hoffman & Johnston, 1998). However, this effect requires presence of the ancillary subunit KChIP3, since expression of Kv4 alone in *Xenopus* oocytes lacks PKA-mediated regulation (Schrader *et al.*, 2002). This finding demonstrates an important factor in kinase regulation of Kv channels, that the specific functional consequence of phosphorylation might depend entirely on the expression system or macromolecular complex the Kv is situated in. In the previous study, although the KChIP3 was shown to be phosphorylated by PKA, this site was apparently not important for functional modulation of Kv4. Instead phosphorylation of Kv4 itself only modulated gating in the presence of KChIP3, demonstrating that the conformational changes induced by the presence of the ancillary subunit were required to make Kv4 susceptible to PKA-mediated effects (Schrader *et al.*, 2002). This demonstrates the complexity of overlapping and sometimes redundant or silent regulatory processes that affect Kv function.

Native ion channels are embedded in membranes with partner proteins that help them reach their intended location and tailor their function to produce a desired neuronal output. These channel complexes are further tuned by posttranslational modifications like phosphorylation by a suite of endogenous protein kinases to adjust gating behaviour dynamically. How do the specific regulatory mechanisms manifest in the neuronal context to influence AP firing over varying lengths of time?

4 INTRINSIC PLASTICITY

In the most fundamental terms, neurons are signal generation and relay elements, converting external stimulus information into response action. What neurons actually do is far more complex, and a critical part of that complexity is the ability to modify their output based on previous inputs. This is generally known as neuronal plasticity and can be divided into two general categories. Synaptic plasticity occurs locally at individual synapses to strengthen or weaken the responsiveness of that synapse to subsequent input. This can be accomplished presynaptically by changing the probability of transmitter release, or postsynaptically by modifying the number of accessible receptors or modulating the activity of the receptors already present on the membrane. A famous example of synaptic plasticity is the NMDA receptor-mediated insertion of AMPA receptors in the postsynaptic membranes of hippocampal CA1 pyramidal neurons known as long-term potentiation (LTP) (Malenka & Nicoll, 1999). The second category is called plasticity of intrinsic excitability, or intrinsic plasticity, and relies instead on modulation of voltage-gated ion channels. This can be expressed functionally in at least three different ways: local modulation of voltage-gated channels near the synaptic input to amplify or attenuate the EPSP; modulation of AP threshold to make the neuron more likely to fire in response to the same EPSP; and

modulation of resting membrane potential to bring the baseline itself closer to AP threshold, which increases likelihood of firing to the same input (Figure R.8) (Debanne *et al.*, 2019). These last two types can be thought of as globally acting since they affect all inputs equally. Although intrinsic plasticity is a term generally used for longer time scales, there are many important examples of dynamic, activity-dependent changes in voltage-gated ion channel activity that affect input strength and AP likelihood over the short-term.

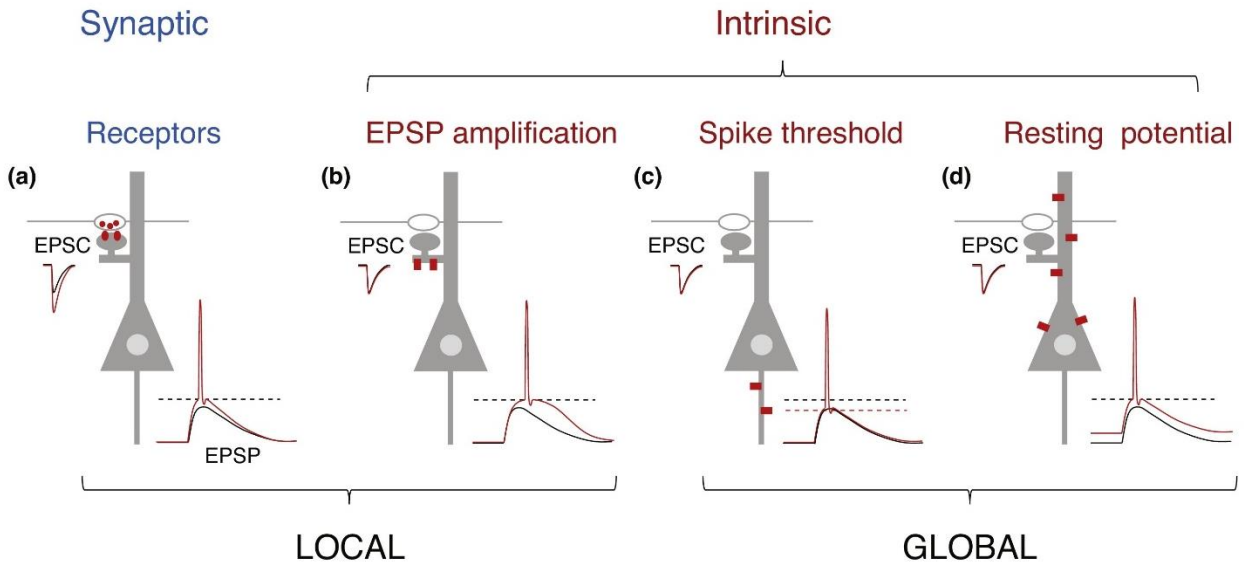

Figure R.8 Local vs. global action of plasticity mechanisms
Synaptic plasticity acts locally at individual synapses to increase the strength of subsequent EPSCs, causing an increased likelihood of postsynaptic AP. Intrinsic plasticity can act either locally or globally. (B) Local potentiation of dendritic voltage-gated channels near to the synaptic input causes strengthened EPSP propagation and increases chances for postsynaptic AP. (C) Global intrinsic plasticity can act at the AIS to decrease threshold of APs to the same level of subsequent input. (D) Raising the RMP throughout the neuron has a similar effect since all subsequent inputs have a greater chance to elicit an AP because the baseline potential is closer to threshold. Reproduced with permission from Debanne *et al.* (2019).

4.1 Short-term intrinsic plasticity

This kind of regulation can act either local to a specific synapse or more globally to reset AP threshold for the entire neuron. Commonly invoked by metabotropic signaling, this type of regulation has been observed throughout the brain, usually relies on intracellular protein kinases,

and shifts voltage-gated channel activity on the time scale of seconds or tens of seconds. In rat striatal neurons, activation of D1 and D2 dopamine receptors caused a ~70% reduction in peak Na^+ current evoked from -70 mV, which ultimately resulted in an increased AP threshold and reduced excitability (Surmeier *et al.*, 1992; Schiffmann *et al.*, 1995). Dopamine receptor stimulation induced a PKA-mediated hyperpolarizing shift in steady-state inactivation, causing less channels to be available for activation at resting membrane potential. A similar mechanism was observed in pyramidal neurons of rat prefrontal cortex (PFC), where both dopamine and D1/D5 receptor agonist application caused a sharp reduction in peak Na^+ current, likely through Nav1.2 (Maurice *et al.*, 2001). In striatal cholinergic neurons, D2 dopamine receptor activation reduced pacemaking activity by enhancing Nav channel entry into a slow-inactivated state (Maurice *et al.*, 2004). Slow inactivation is induced effectively during repetitive spiking, meaning multiple spike trains will ultimately lead to reduced firing rates and spike failures (Fleidervish *et al.*, 1996). Reducing Nav channel availability by potentiating slow inactivation can also be invoked through serotonergic receptor stimulation and PKC activity. Applying a 5-hydroxytryptamine (5-HT) type 2 receptor agonist to PFC pyramidal neurons enhanced Nav slow inactivation which resulted in attenuated backpropagating dendritic APs and a curtailed ability to sustain firing (Carr *et al.*, 2002; Carr *et al.*, 2003).

A-type K^+ current in dendrites of pyramidal neurons is also subject to short-term intrinsic plasticity. This current is important for signal propagation and integration in dendrites (Hoffman *et al.*, 1997) and can be tuned dynamically by PKA and PKC to affect the strength of dendritic attenuation (Hoffman & Johnston, 1998). Physiological induction can be achieved by stimulation of either β-adrenergic or muscarinic acetylcholine receptors, which causes a PKA/PKC-dependent

depolarizing shift in A-type voltage-dependence of activation, reducing its impact on the membrane potential and resulting in increased backpropagating AP amplitudes (Hoffman & Johnston, 1999). The effect of PKA and PKC was later found to converge on MAPK-mediated phosphorylation of dendritic Kv4.2, thus demonstrating the common pathway underlying dendritic AP amplification (Yuan *et al.*, 2002).

4.2 Long-term intrinsic plasticity

Long-term neuronal plasticity has driven considerable interest from neuroscientists due to its apparent fulfillment of criteria for a cellular and molecular substrate of memory. As mentioned previously, efforts have largely focused on changes to synapse strength such as LTP and LTD; however, persistent activity-dependent modulation of intrinsic excitability has been intriguing for some, with David Linden calling it “the other side of the engram” (Zhang & Linden, 2003). Early mammalian experiments linking memory acquisition to observable changes in neuronal excitability came from studies of eyeblink conditioning in rabbits. Disterhoft and colleagues trained rabbits in an eyeblink conditioning paradigm and observed a decrease of AHP amplitude in CA1 and CA3 pyramidal neurons in hippocampal slices prepared 1 day post-training, but not after 7 days (Disterhoft *et al.*, 1986; Coulter *et al.*, 1989; de Jonge *et al.*, 1990). Voltage clamp investigation revealed a reduced KCa current that was responsible for the decrease in AHP and demonstrated that there was a cell-specific lability in membrane conductances underlying the acquisition of this behaviour (Sanchez-Andres & Alkon, 1991). In a similar set of findings, Barkai and colleagues found that following an odour discrimination paradigm, pyramidal cells in layer II piriform cortex in trained rats exhibited reduced post-AP train AHPs compared to naïve rats (Saar *et al.*, 1998). This property was present in slices harvested 1 – 3 days post-training but

not after 5 – 7 days. The authors found that cholinergic activation of intracellular PKC during learning caused a reduction in KCa current (Saar *et al.*, 2001; Seroussi *et al.*, 2002). These studies showed that there is a discernable excitability signature associated with learning a particular behavioural task, but what are the molecular underpinnings of these changes?

Pioneering work from Gina Turrigiano demonstrated that even neurons *in vitro* are designed to regulate their excitability based on a homeostatic response to changes in their environment (Turrigiano *et al.*, 1994). Cultured neocortical pyramidal neurons exhibited increased step-evoked AP firing after two days of TTX-induced activity deprivation, which relied on increased transient Na^+ current, reduced TEA-sensitive delayed rectifier K^+ current, but not changes to A-type K^+ current or Ca^{2+} current (Desai *et al.*, 1999). These findings were replicated in organotypic hippocampal slices by applying glutamate receptor antagonists kynurenate or CNQX (Karmarkar & Buonomano, 2006; Cudmore *et al.*, 2010), and could also be induced through sensory deprivation of barrel and primary visual cortices (Maffei & Turrigiano, 2008; Milshtein-Parush *et al.*, 2017). Conversely, network over-excitability can also cause plastic changes to voltage-gated ion channel activity on the membrane. One study observed increased production and clustering of Kv2.1 in hippocampal pyramidal neurons following long-term seizures in the kainite epilepsy model (Misonou *et al.*, 2004). The protein phosphatase calcineurin was responsible for this potentiation, which also produced a gain-of-function hyperpolarizing shift in voltage-dependence of activation in the K^+ current resulting in greater excitability suppression. The central idea of chronic hypo- or hyperactivity causing up- or downregulation of membrane excitability is a strong example of what is known as homeostatic plasticity, an important type of intrinsic plasticity. The induction relies on chronic changes in general network activity that forces

neurons to adjust their own activity to compensate for long-lasting periods of strong input and is a slow process of channel turnover on the membrane. There are other examples of activity-dependent intrinsic excitability that instead occur quickly after a brief synaptic or otherwise physiological stimulus.

In the presence of a muscarinic acetylcholine receptor agonist, layer V neurons of the entorhinal cortex exhibit persistent upregulation of basal firing upon a brief depolarizing current injection (Egorov *et al.*, 2002). This effect was graded based on the duration of stimulus and depended on intracellular Ca^{2+} dynamics. In acute slices of rat visual cortex, repeated 500 ms depolarizing pulses to layer V pyramidal neurons were also able to induce an upregulation of step-evoked AP firing in a Ca^{2+}- and PKA-dependent manner (Cudmore & Turrigiano, 2004). Layer V cortical pyramidal neurons also upregulate their firing behaviour for tens of minutes in response to transient mGluR1/5 stimulation through either afferent stimulation, glutamate application, or specific mGluR agonist treatment. Further investigation revealed that SK channel downregulation was downstream of mGluR activation (Sourdet *et al.*, 2003). Paradoxically, voltage clamp analysis of dissociated cortical neurons showed that long-term application of an mGluR1 agonist reduced Na^{+} current amplitudes and AP frequency in a PKC-dependent manner, potentially acting as a homeostatic measure to reduce firing during periods of sustained glutamate release (Carlier *et al.*, 2006). Hippocampal CA1 pyramidal neurons also exhibited decreased AHP and increased AP firing rates in response to mGluR1 stimulation, but do not rely on PKC as an intracellular mediator (Cohen *et al.*, 1999; Ireland & Abraham, 2002).

Intrinsic plasticity can be induced by inhibitory input as well. The original demonstration of inhibition driving long-term excitability changes was in the spontaneously active neurons of the vestibular nucleus (Nelson *et al.*, 2003). The authors applied intermittent 80 Hz pulse trains to GABAergic afferents over 5 minutes and observed an upregulation of spontaneous firing that lasted more than 40 minutes. Plasticity could also be induced by both direct and sustained hyperpolarization as well as brief exposure to Ca^{2+}-free extracellular media. The mechanism relied on a suppression of BK channel activity and neurons post-induction had a decreased sensitivity to the specific blocker iberiotoxin. This study demonstrated that not just depolarizing stimuli could induce intrinsic plasticity but hyperpolarizing input as well. Furthermore, inhibitory interneurons themselves are also subject to plasticity of excitability. High-frequency stimulation of the Schaffer collateral induced an mGluR-dependent upregulation of firing frequency in PV-expressing basket cells of the CA1 region that resulted from a downregulation of Kv1 channels and decreased AP threshold (Campanac *et al.*, 2013). Another example of intrinsic plasticity in interneurons is the rapid reduction of intrinsic excitability of layer II/III PV-expressing interneurons in mouse somatosensory cortex following brief sensory deprivation (Gainey *et al.*, 2018). This depended on an upregulation of DTX-insensitive K^+ current through non-Kv1 channels that increased AP threshold and decreased spike frequency. Clearly, many neurons throughout the brain have mechanisms of long-term intrinsic plasticity that are mediated by myriad signaling cascades. The final section will take a closer look at intrinsic plasticity in cerebellar neurons.

4.2.1 Intrinsic plasticity in the cerebellum

Cerebellar neurons were some of the first in the brain to have rapidly-induced, activity-dependent, long-term intrinsic plasticity showcased. Aizenmann & Linden showed that high

frequency stimulation of mossy fiber afferents to neurons in the deep cerebellar nuclei (DCN) caused a persistent increase in their step-evoked AP frequency (Aizenman & Linden, 2000). Ca^{2+} flux through NMDA receptors was required for this potentiation as it could be inhibited by application of D-APV or Cd^{2+}. Direct membrane depolarization could also be used as the induction stimulus, although the amount of potentiation was to a lesser degree. Interestingly, both EPSP and IPSP bursts could cause this plasticity as well, and both could be inhibited by chelating intracellular Ca^{2+} with high concentrations of BAPTA (Zhang *et al.*, 2004). A similar mechanism was found at around the same time in granule cells which exhibited an increase in step-evoked AP frequency following theta-burst stimulation of their mossy fiber inputs (Armano *et al.*, 2000). These authors found that an increase in their excitability accompanied the more traditional synaptic LTP at the mossy fiber-granule cell synapse, and also depended on NMDA receptor activation. Purkinje cells also possess this kind of partnered synaptic and intrinsic LTP mechanism at their PF synapses. Tetanic stimulation of these afferents could induce a substantial increase in step-evoked firing both *in vitro* and *in vivo* lasting for >40 min (Belmeguenai *et al.*, 2010). This mechanism depended on a downregulation of SK channel activity and could be inhibited by application of both the SK blocker apamin as well as high intracellular BAPTA. Both PKA and CK2 were ultimately responsible for effecting this modulation of SK activity, and inhibiting either of these protein kinases could eliminate firing potentiation. Curiously, the authors found that this intrinsic plasticity does not affect spike output in the DCN, the immediate downstream contact of Purkinje cell efferents, but rather reduces the influence of subsequent PF input. This study provided a synaptic and molecular explanation to observations made by the lab of Daniel Alkon, the same group who first showed persistent changes in membrane excitability in the

hippocampus following behavioural task acquisition (Disterhoft *et al.*, 1986). Schreurs and colleagues found that the K^+ channel-mediated AHP in rabbit Purkinje dendrites was smaller in animals that had undergone a tone-shock classical conditioning paradigm (Schreurs *et al.*, 1998).

The lab of Christian Hansel has investigated other novel roles of SK channels related to intrinsic plasticity in Purkinje cells. Tetanic PF stimulation or strong somatic depolarization each induced a potentiation of CF-mediated EPSP amplitude, as well as an increased spikelet count recorded from the soma (Ohtsuki *et al.*, 2012). Dendritic plasticity depended on SK channel downregulation: both effects were occluded in the presence of extracellular apamin and in slices taken from $SK2^{-/-}$ mice. This plasticity was also quite localized, and imaging experiments revealed that potentiated CF-mediated Ca^{2+} transients observed in one dendritic branch were not observed in sections >30 µm away. Another study demonstrated that post-complex spike pauses could be shortened following tetanic somatic depolarization (5 Hz for 3 s) (Grasselli *et al.*, 2016). Plasticity was eliminated in $SK2^{-/-}$ mice as well as in the presence of external apamin. This work together illustrates the multifaceted contribution of a single ion channel family in regulating multiple kinds of membrane excitability in a single neuron.

To add further complexity to the regulation of long-term information storage in Purkinje cells, PF-Purkinje synaptic input can also lead to an LTD of intrinsic plasticity. Tetanic stimulation of PFs followed by a delayed single stimulation of CF afferents for five minutes leads to a reduction in PF-EPSCs recorded from Purkinje cells that is accompanied by an LTD of membrane excitability (Shim *et al.*, 2017). Although sharing some induction components with LTP of intrinsic excitability described in the previous paragraph such as dependence on Ca^{2+} and protein kinase

signaling, this LTD mechanism does not affect SK channels. Another study from the same year reported a conflicting finding of increased Purkinje AP firing that occurred simultaneously with PF-LTD induction (Yang & Santamaria, 2016). This pathway was induced by 3 minutes of concomitant PF stimulation and somatic depolarization at 1 Hz and caused by a downregulation of HCN-mediated I_h. The discrepancy may be explained by the difference in induction stimuli (somatic depolarization versus CF stimulation) since Ca^{2+} entry and subsequent intracellular dynamics between the two protocols are likely quite different. A type of intrinsic plasticity based in I_h modulation is also observed after activity-deprivation in organotypic cerebellar slice culture. After two days of TTX incubation Purkinje cells exhibited reduced step-evoked AP firing that could be prevented by inclusion of an mGluR1 inverse agonist in the culture media (Shim *et al.*, 2016). I_h current was potentiated after activity-deprivation and applying the specific HCN blocker ZD 7288 during recording equalized AP firing in both control and deprived Purkinje cells.

The last example of cerebellar intrinsic plasticity I will overview occurs in the GABAergic interneurons of the granule layer, the Golgi cells. Hull and colleagues identified a long-lasting increase in spontaneous firing frequency in these neurons following transient (~3 min) activation of mGluR2 receptors using the specific activator 2R,4R-4-aminopyrrolidine-2,4-dicarboxylate (APDC) (Hull *et al.*, 2013). Analysis of individual spontaneous APs post-APDC application revealed a reduction in AHP without an effect on spike width. Since mGluR2 stimulation resulted in global AP silencing in Golgi cells during the treatment, the authors found that direct somatic hyperpolarization for at least 20 seconds could also serve as an induction stimulus to increase spontaneous rates. Blockade of both CaMKII activity as well as BK channels eliminated long-term plasticity. These findings demonstrate that even inhibitory interneurons of the cerebellar cortex

are subject to persistent and activity-dependent intrinsic plasticity. However, it remains to be investigated if the other inhibitory cells in this region, the MLIs, possess such mechanisms.

5 RATIONALE AND OBJECTIVES

The goal of my thesis research is to gain deeper insight into the molecular mechanisms controlling intrinsic membrane excitability in cerebellar MLIs. Although studied extensively in terms of synaptic regulation and tonic firing ability, unanswered details remain. In the age of genetically targeted reporters and actuators, we have been given unprecedented access to probing the specific roles of these neurons in the awake, behaving animal (Astorga *et al.*, 2017; Gaffield & Christie, 2017; Rowan *et al.*, 2018). Although a picture of the *in vivo* function of MLIs is emerging, it is important to understand the underlying molecular components governing their activity. Over the course of my research I have characterized a seemingly inconvenient effect of electrophysiological recording, but through this unconventional induction regime I was able to investigate a novel form of long-term plasticity of excitability in these neurons. Although previously demonstrated in a variety of cerebellar neurons (Aizenman & Linden, 2000; Armano *et al.*, 2000; Hull *et al.*, 2013; Shim *et al.*, 2017), intrinsic plasticity in MLIs has been overlooked which is surprising given their direct and critical influence on Purkinje cell output (Mittmann *et al.*, 2005; Wulff *et al.*, 2009; Coddington *et al.*, 2013).

For the two results chapters that follow, a common approach was taken to investigate the dynamics of MLI excitability. Electrophysiological recordings, both whole-cell and cell-attached, were performed on MLIs in acute slices of cerebellar vermis tissue. Slice recordings were chosen to maintain the native circuit environment as much as possible, while also being able to accurately control external perfusion of channel blockers and modulators. SCs were chosen over BCs in order to reduce the variability between recordings in terms of neuronal

capacitance and input resistance, which have been shown to differ between these two classes of MLIs (Llano & Gerschenfeld, 1993b; Southan & Robertson, 1998). A main strength of this work is linking the changes in measured SC AP output in current clamp and modifications of pharmacologically-isolated voltage-dependent conductances in voltage clamp. To accomplish this, several strategies were employed to overcome issues associated with incomplete space-clamp in intact, ramified neuronal structures. First, nucleated patches were excised to examine gating properties in more well-controlled electronic compartments. Second, voltage command protocols were used that could compensate for voltage clamp errors present in intact neurons. Collaborative efforts with the McGill Department of Physiology (Anmar Khadra) allowed for the introduction of computational modeling to assess and verify the relevant changes that underlie MLI excitability. It was through this confluence of experimental approaches that allowed us to gain a unique understanding of MLI excitability dynamics.

Chapter 1:

Ion channel basis of changes in neuronal excitability induced by patch clamp

The first part of my thesis consists of the initial discovery and characterization of the excitability increase that occurs during patch clamp recording of cerebellar SCs. Although hinted at in earlier work in the same cell type (Alcami *et al.*, 2012), the specific changes that constitute this phenomenon in whole-cell configuration were previously undescribed. The objectives of this work were to first, define the hallmark features of AP firing modulation in current clamp, and second, to uncover the ion channel basis of these changes. The second objective was achieved using a combination of Hodgkin-Huxley modeling of neuronal AP firing and voltage clamp analysis

of pharmacologically-isolated voltage-dependent currents. Using these methods, we were able to demonstrate that the increase in SC excitability was driven primarily by shifts in Nav channel biophysical properties, while helped in some part by concurrent gating shifts in A-type Kv channels.

Chapter 2:

Patch clamp hijacks intrinsic plasticity in cerebellar stellate cells

The main criticism of the first results chapter is the lack of physiological context. Although the effect is striking and extremely reliable, the fact that these changes occur as a result of patch clamp investigation generates doubt about its relevance in the minds of most neurophysiologists. The aim of the second chapter was ultimately to legitimize my work by illustrating the molecular machinery behind the changes in voltage-gated channel activity described in Chapter 1, and moreover to discover a physiologically plausible induction scheme for its presumed deployment in the native tissue. To that end, further patch clamp recordings were performed in the presence of pharmacological agents to chelate cytosolic Ca^{2+} and inhibit various intracellular protein kinases. Both are important and interrelated parts of signaling cascades that have previously been shown to modulate voltage-gated channel activity in activity-dependent and -independent ways (Maurice *et al.*, 2001; Schrader *et al.*, 2002; Carr *et al.*, 2003; Chen *et al.*, 2008; Scheuer, 2011; Ben-Johny *et al.*, 2014). Using these approaches, we were able to show that intrinsic plasticity in SCs relies on increases in cytosolic Ca^{2+} and activation of CaMKII in a Nav-dependent manner. Finally, by providing a stable basal activity level in cell-attached mode, we could induce firing rate potentiation by stimulating NMDA receptors. Since the long-term elevation of spontaneous firing rate relied on the same intracellular signals as that of patch clamp-induced

plasticity, we concluded that they were utilizing the same signaling cascade. This type of NMDA receptor-/Nav channel-dependent intrinsic plasticity is rare in the nervous system, but has been observed in other cell types (Xu *et al.*, 2005). MLI intrinsic plasticity is another mechanism by which cerebellar neurons change their firing rates over long time scales.

PART II

EXPERIMENTAL SECTION

CHAPTER 1

Ion channel basis of changes in neuronal excitability induced by patch clamp

FOREWORD TO CHAPTER 1

I began work in the lab in November 2013 and a former PhD student had recently submitted his first paper to *Nature Communications*. The submission would ultimately be successful and the article was published in January the following year (Accardi *et al.*, 2014). This first study represented a growing interest in the lab, linking reactive oxygen species (ROS) to synaptic strengthening and changes to neuronal activity in general. The same student had some earlier data suggesting that elevating ROS also caused a reduction in the intrinsic excitability in cerebellar SCs (Accardi & Bowie, unpublished observation). Another observation he made was that SCs exhibit a time-dependent increase in their step-evoked AP firing throughout a standard electrophysiological recording without any manipulation. Derek and I were intrigued and together decided to pursue the underlying mechanism driving these changes, with the hopes that it would reveal some unique aspect of neurophysiology. What followed was a five year-long hunt for the molecular players behind this phenomenon, learning as I went about how to properly study neuronal excitability and voltage-gated channels.

The two chapters of this thesis were essentially constructed simultaneously, since many of the discoveries central to the following chapter were made early in my PhD. However, as the initial characterization dataset grew, we began to realize that there was too much for one paper. Once we began the collaboration with the Khadra lab, the story took on a new angle. We ultimately decided to split the paper into four main parts: characterizing the excitability phenomenon in current clamp, predicting changes in channel activity using computational modeling, measuring those isolated currents in voltage clamp to verify the predictions, and finally revising the model using experimentally-derived biophysical data to further validate our

understanding of the firing dynamics. This proved palatable to reviewers and the study was published in *eNeuro* in April 2019. Although the work was met with some initial criticism regarding its lack of physiological relevance and was rejected from *Journal of Neuroscience* and *Journal of Physiology*, we believed that the narrative was appropriate and decided to go to a different journal instead of radically reworking the paper. I think the results that comprise the following chapter provide a unique picture into lesser discussed phenomena associated with electrophysiological recording, but also give interesting and comprehensive insights into the complex nature of SC firing behaviour.

Article title:

Cerebellar stellate cell excitability is coordinated by shifts in the gating behavior of voltage-gated Na^+ and A-type K^+ channels

ABSTRACT

Neuronal excitability in the vertebrate brain is governed by the coordinated activity of both ligand- and voltage-gated ion channels. In the cerebellum, spontaneous action potential (AP) firing of inhibitory stellate cells (SCs) is variable, typically operating within the 5-30 Hz frequency range. AP frequency is shaped by the activity of somatodendritic A-type K^+ channels and the inhibitory effect of GABAergic transmission. An added complication, however, is that whole-cell recording from SCs induces a time-dependent and sustained increase in membrane excitability making it difficult to define the full range of firing rates. Here, we show that whole-cell recording in cerebellar SCs of both male and female mice augments firing rates by reducing the membrane potential at which APs are initiated. AP threshold is lowered due to a hyperpolarizing shift in the gating behavior of voltage-gated Na^+ channels. Whole-cell recording also elicits a hyperpolarizing shift in the gating behavior of A-type K^+ channels which contributes to increased firing rates. Hodgkin-Huxley modeling and pharmacological experiments reveal that gating shifts in A-type K^+ channel activity do not impact AP threshold, but rather promote channel inactivation which removes restraint on the upper limit of firing rates. Taken together, our work reveals an unappreciated impact of voltage-gated Na^+ channels that work in coordination with A-type K^+ channels to regulate the firing frequency of cerebellar SCs.

INTRODUCTION

Cerebellar stellate cells (SCs) are GABAergic interneurons that exert inhibitory tone onto both Purkinje cells (PCs) and SCs to shape motor function in awake, behaving animals (Astorga *et al.*, 2017; Gaffield & Christie, 2017). Investigations into the physiological activity of SCs both *in vitro* and *in vivo* have estimated their action potential (AP) firing rates to be in the range of 5 – 30 Hz (Armstrong & Rawson, 1979; Midtgaard, 1992; Hausser & Clark, 1997; Carter & Regehr, 2002), with some studies reporting even lower spontaneous rates (Jorntell & Ekerot, 2003; Liu *et al.*, 2014). SCs are also highly sensitive to minimal amounts of synaptic input (Carter & Regehr, 2002; Jorntell & Ekerot, 2003), suggesting that the excitability of SCs is finely tuned to ensure that their target cells receive robust and reliable feedforward inhibition.

Several molecular mechanisms have been shown to modulate the excitability of SCs. For example, elevations in cytosolic Ca^{2+} mediated by T-type voltage gated Ca^{2+} channels (VGCCs) have been shown to dynamically regulate the firing rates of SCs by modulation of somatodendritic A-type K^+ channels (Molineux *et al.*, 2005; Anderson *et al.*, 2013). Firing rates are further controlled by neurochemical transmission. The inhibitory tone of $GABA_A$ receptors constrains AP firing (Hausser & Clark, 1997) whereas the prolonged depolarization by NMDA-type ionotropic glutamate receptors (Liu *et al.*, 2014) activates axonal VGCCs (Christie & Jahr, 2008) and promotes GABA release (Glitsch & Marty, 1999; Duguid & Smart, 2004; Liu & Lachamp, 2006). To complicate matters, the firing rates of SCs are also affected by patch clamp recording conditions. The intrinsic excitability of SCs increases in a time-dependent manner in cell-attached recordings (Alcami *et al.*, 2012). The molecular events that give rise to this increase in excitability are still not fully understood, although observations in other cell types have demonstrated that

patch breakthrough during whole-cell recording can cause unintended changes to ion channel gating and activity, including an effect on voltage-gated Na^+ channels (Fenwick *et al.*, 1982b; Dani *et al.*, 1983; Fernandez *et al.*, 1984; Vandenberg & Horn, 1984; Townsend *et al.*, 1997). Whether a similar mechanism accounts for increased firing in SCs in whole-cell recordings has yet to be investigated.

Here, we have elucidated the molecular events responsible for the increase in excitability of SCs in whole-cell recording conditions. Using a combination of brain slice patch clamp electrophysiology and Hodgkin-Huxley modeling, we show that shifts in the gating properties of voltage-gated Na^+ channels cause an increase in SC excitability by promoting AP firing at more hyperpolarized potentials. These events occur concurrently with a hyperpolarizing shift in A-type K^+ channel gating which reduces the number of channels available for activation, and thus contributes to increased AP firing. Taken together, our data identify an unappreciated role of voltage-gated Na^+ channels that work in coordination with somatodendritic A-type K^+ channels to upregulate SC excitability upon whole-cell recording.

METHODS

Ethical approval

All experiments have been approved by the Animal Care Committee of McGill University and were performed in accordance with the guidelines of the Canadian Council on Animal Care.

Animals

Wild-type mice with a C57BL/6J background (RRID:IMSR_JAX:000664) were obtained from Jackson Laboratories (Bar Harbor, USA) and maintained as a breeding colony at McGill University. Both male and female wild-type mice were used for experiments and ranged from postnatal days 18 to 30.

Slice preparation

Mice were anesthetized with isoflurane and immediately decapitated. A block of cerebellar vermis was rapidly dissected from the mouse head and submerged in ice-cold cutting solution perfused with carbogen gas (95% O_2, 5% CO_2). Cutting solution contains (in mM): 235 sucrose, 2.5 KCl, 1.25 NaH_2PO_4, 28 $NaHCO_3$, 0.5 $CaCl_2$, 7 $MgCl_2$, 28 D-glucose, 1 ascorbic acid, 3 sodium pyruvate (pH 7.4; 305–315 mOsmol/L). The block of vermis is then fastened to a platform, transferred to the slicing chamber and again submerged in ice-cold cutting solution, bubbled with carbogen throughout the remainder of the procedure. Thin slices of cerebellar vermis (300 µm) were obtained with a vibrating tissue sectioner (Leica VT1200; Leica Instruments, Nussloch, Germany). The slices were transferred to oxygenated artificial cerebrospinal fluid (ACSF) and held at room temperature (21°C-23°C) for at least 1 h before recordings were performed. ACSF

contained the following (in mM): 125 NaCl, 2.5 KCl, 1.25 NaH_2PO_4, 26 $NaHCO_3$, 2 $CaCl_2$, 1 $MgCl_2$, 25 D-glucose (pH of 7.4; 305–315 mOsmol/L).

Electrophysiology

Slice experiments were performed on an Olympus BX51 upright microscope (Olympus, Southall, UK) equipped with differential interference contrast/infrared optics. Whole-cell patch clamp recordings were made from visually-identified stellate, granule or Purkinje cells in acute sagittal slices of cerebellar vermis. Stellate cells (SCs) were distinguished from misplaced or migrating granule, glial or basket cells by their small soma diameter (8–9 µm), location in the outer two-thirds of the molecular layer and whole-cell capacitance measurement (4-12 pF). Granule cells were identified based on location in the granule layer (immediately less superficial to the Purkinje layer), small soma size and whole-cell capacitance measurement (1-3 pF). Purkinje cells were identified based on large relative size, location in the Purkinje monolayer and whole-cell capacitance measurement (25-35 pF). Patch pipettes were prepared from thick-walled borosilicate glass (GC150F-10, OD 1.5 mm, ID 0.86 mm; Harvard Apparatus Ltd, Kent, UK) and had open tip resistances of 4–7 MΩ when filled with an intracellular recording solution. Recordings were performed using a Multiclamp 700A amplifier (Molecular Devices, Sunnyvale, CA, USA) at a holding potential of -70 mV (stellate and Purkinje) or -80 mV (granule). Series resistance and whole-cell capacitance were estimated by cancelling the fast transients evoked at the onset and offset of brief (10 ms) 5 mV voltage-command steps. Access resistance during whole-cell recording (7–25 MΩ) was compensated between 60 and 80% and checked for stability throughout the experiments (~15% tolerance). Recordings where pipette offset changed by more than 3 mV were excluded. Liquid junction potential was not corrected for. The bath was

continuously perfused at room temperature (21–23 °C) with ACSF at a rate of 1–2 mL/min. Currents were filtered at 5 kHz with an eight-pole low-pass Bessel filter (Frequency Devices, Haverhill, MA, USA) and digitized at either 25 or 100 kHz with a Digidata 1322A data acquisition board and Clampex 10.1 (pClamp, RRID:SCR_011323) software. For voltage clamp recordings, the online P/N leak-subtraction suite in Clampex 10.1 was used to assess voltage-gated responses.

For recording voltage-dependence of activation of A-type K^+ current (I_A) a protocol was applied consisting of 500 ms steps evoked from a holding potential of -100 mV, ranging from -100 mV to +20 mV in 10 mV increments. An inactivation protocol was applied consisting of 500 ms prepulse steps ranging from -120 mV to -30 mV in 5 mV increments, followed by a probe step to -20 mV to assess channel availability. For recording voltage-dependence of activation of delayed rectifier K^+ current (I_K), a protocol was applied consisting of 1 s steps evoked from a holding potential of -50 mV, ranging from -50 mV to +40 mV in 5 mV increments. The holding potential of -50 mV was chosen in order to selectively inactivate I_A, because of its relatively hyperpolarized $V_{1/2}$ inactivation, and study a more isolated I_K. For recording voltage-dependence of activation of Na^+ current (I_{Na}), a protocol designed to circumvent space-clamp errors in neurons was used (Milescu *et al.*, 2010) consisting of a 5 ms suprathreshold step from -80 mV to -35 mV in order to evoke an action current, followed by a ~1 ms step to -60 mV, followed by 100 ms steps ranging from -80 mV to +30 mV in 5 mV increments. To measure steady-state channel availability, an inactivation protocol consisting of 100 ms steps ranging from -110 mV to -20 mV in 5 mV increments, followed by a probe step to -20 mV.

Recording solutions

All chemicals were obtained from Sigma Aldrich (St. Louis, MO, USA) unless otherwise indicated. Internal pipette solution for most current clamp experiments as well as voltage clamp experiments, both whole-cell and nucleated patch, examining I_K in SCs contained (in mM): 126 K-gluconate, 5 HEPES, 4 NaCl, 15 D-glucose, 0.05 $CaCl_2$, 1 $MgSO_4$, 0.15 K_4-BAPTA, 2 Mg-ATP, 0.1 Na-GTP (adjusted to pH 7.4 with KOH, 300-310 mOsmol/L). I_K experiments had external ACSF supplemented with 100 nM tetrodotoxin (TTX) to block AP firing, as well as 5 mM 4-aminopyridine (4-AP) to limit the activity of I_A-mediating channels. In one set of experiments, all K-gluconate in this internal solution was substituted by K-methanesulfonate to examine the effect of different anions on intrinsic membrane properties. Pipette solution for voltage clamp experiments, both whole-cell and nucleated patch, examining I_A contained (in mM): 140 KCl, 10 HEPES, 2.5 $MgCl_2$, 0.15 K_4-BAPTA (adjusted to pH 7.4 with KOH, 300-310 mOsmol/L). For these experiments, the external ACSF was supplemented with 5 mM TEA-Cl and 2 mM CsCl to block non-I_A-mediating K^+ channels, and 100 nM TTX to block AP firing. Pipette solution for voltage clamp experiments examining I_{Na} contained (in mM): 110 Cs-methanesulfonate, 5 HEPES, 4 NaCl, 15 D-glucose, 0.05 $CaCl_2$, 0.15 Cs_4-BAPTA, 4 Mg-ATP, 0.1 Na-GTP, 10 TEA-Cl, 10 4-AP (adjusted to pH 7.4 with CsOH, 300-310 mOsmol/L). Pipette solution for voltage clamp experiments examining I_{Na} in excised membrane patches contained (in mM): 140 CsCl, 10 HEPES, 10 EGTA, 2 $MgCl_2$, 2 Na_2-ATP (adjusted to pH 7.4 with CsOH, 300-310 mOsmol/L). Free Ca^{2+} concentration for all current clamp internal solutions was calculated to be ~100 nM using MaxChelator freeware (Bers *et al.*, 2010). For all experiments investigating I_{Na}, the external ACSF was supplemented with 100 µM $CdCl_2$ and 1 µM Mibefradil dihydrochloride (Tocris Bioscience, Ellisville, MO, USA) to block

voltage-gated calcium channels. Additional current clamp experiments were performed in the presence of hyperpolarization-activated cyclic nucleotide-gated channel (HCN) blocker ZD 7288 in the ACSF (20 µM; Tocris Bioscience). Except where indicated, all experiments were performed in the presence of fast excitatory and inhibitory synaptic blockers: NMDA receptor antagonist D-(-)-2-Amino-5 phosphonopentanoic acid (D-APV; 10 µM), AMPA/kainate receptor antagonist 2,3-Dioxo-6-nitro-1,2,3,4-tetrahydrobenzo[f]quinoxaline-7-sulfonamide (NBQX; 10 µM), and $GABA_A$ receptor antagonist bicuculline (BIC; 10 µM), all of which were purchased from Abcam (Cambridge, UK).

Mathematical model

A modified Hodgkin-Huxley type model was adopted from Molineux *et al*. (2005) and Anderson *et al*. (2010). The model consists of 5 ionic currents, including I_{Na}, I_K, I_A, T-type Ca^{2+} current (I_T) and nonspecific leak current (I_L). The A-type K^+ and T-type Ca^{2+} current were added in Molineux *et al*. (2005) to capture biphasic first spike latency profile. The resulting voltage equation associated with this model is expressed as

$$C_m \frac{dV}{dt} = -[I_{Na} + I_K + I_A + I_T + I_L] + I_{app},$$

where C_m is the membrane capacitance per unit area and I_{app} is the applied current. The kinetics of the various ionic currents included in the model are as described below (Molineux *et al.*, 2005; Anderson *et al.*, 2010a):

(1) Fast activating Na^+ current:

$$I_{Na} = \bar{g}_{Na} m_\infty^3 h(V - V_{Na}),$$

with maximum conductance $\bar{g}_{Na}$ and Nernst potential for Na^+ V_{Na}. Its gating is governed by both the steady state activation function

$$m_\infty = \left(1 + e^{-(V-v_m)/s_m}\right)^{-1}$$

and the inactivation variable h satisfying the dynamic equation

$$\frac{dh}{dt} = \frac{h_\infty(V) - h}{\tau_h(V)},$$

where $h_\infty(V)$ is the steady state inactivation function given by

$$h_\infty = \left(1 + e^{(V-v_h)/s_h}\right)^{-1}$$

and $\tau_h(V)$ is its time constant described by the Lorentzian function

$$\tau_h(V) = y_0 + \frac{2Aw}{4\pi(V - V_c)^2 + w^2}.$$

(2) Delayed rectifier K^+ current:

$$I_K = \bar{g}_K n^4 (V - V_K),$$

with maximum conductance $\bar{g}_K$ and Nernst potential for K^+ V_K. The gating of this current is governed by the activation variable n only, which satisfies the dynamic equation

$$\frac{dn}{dt} = \frac{n_\infty(V) - n}{\tau_n(V)},$$

where $n_\infty(V)$ is the steady state activation function given by

$$n_\infty = \left(1 + e^{-(V-v_n)/s_n}\right)^{-1}$$

and $\tau_n(V)$ is its time constant defined by

$$\tau_n(V) = \frac{6}{1 + e^{(V+23)/15}}.$$

(3) A-type K^+ current:

$$I_A = \bar{g}_A n_A h_A (V - V_K)$$

with maximum conductance $\bar{g}_A$ and Nernst potential V_K. Its activation/inactivation kinetics are governed by the gating variables n_A and h_A, respectively, each satisfying the dynamic equations

$$\frac{dn_A}{dt} = \frac{n_{A,\infty}(V) - n_A}{\tau_{n_A}}$$

and

$$\frac{dh_A}{dt} = \frac{h_{A,\infty}(V) - h_A}{\tau_{h_A}}$$

where $n_{A,\infty}$ and $h_{A,\infty}$ are, respectively, the steady state activation and inactivation functions given by

$$n_{A,\infty} = \left(1 + e^{-\left(V - v_{n_A}\right)/s_{n_A}}\right)^{-1} \quad \text{and} \quad h_{A,\infty} = \left(1 + e^{\left(V - v_{h_A}\right)/s_{h_A}}\right)^{-1}, \tag{1}$$

and τ_{n_A} and τ_{h_A} are their corresponding time constants that are independent of membrane voltage V.

(4) Fast activating T-type Ca^{2+} current:

$$I_T = \bar{g}_T m_{T,\infty} h_T (V - V_{Ca}),$$

with maximum conductance $\overline{g}_T$ and Nernst potential for Ca^{2+} V_{Ca}. Its gating is governed by the steady state activation function

$$m_{T,\infty} = \left(1 + e^{-(V - v_{m_T})/s_{m_T}}\right)^{-1}$$

and the inactivation variable h_T satisfying the dynamic equation

$$\frac{dh_T}{dt} = \frac{h_{T,\infty}(V) - h_T}{\tau_{h_T}},$$

where $h_\infty(V)$ is the steady state inactivation function given by

$$h_{T,\infty} = \left(1 + e^{(V - v_{h_T})/s_{h_T}}\right)^{-1}$$

and τ_{h_T} is its voltage-independent time constant.

(5) Non-specific leak current:

$$I_A = \overline{g}_L(V - V_L)$$

with constant maximum conductance $\overline{g}_L$ and Nernst potential V_L.

The model is thus described by a six-dimensional system representing the time-dependent membrane voltage V and the five time-dependent gating variables m, n, n_A, h_A and h_T.

Model parameter values

Simulations of the model using parameter values listed in Molineux *et al*. (2005) and Anderson *et al*. (2010) produced cycles of action potentials in the $(V, dV/dt)$ −plane that did not match the activities at either baseline (0 min) or the activities after the increase in excitability

(data not shown). To capture the dynamics of the increase in excitability, we first fitted the expressions of $n_{A,\infty}$ and $h_{A,\infty}$ to the steady state activation/inactivation kinetic data of I_A prior to and after the shift (see Figure 1.7), then used the full model to manually fit its numerical simulations to baseline data prior to the increase in excitability. This was done in two sequential steps: (i) by first capturing all features of the AP cycles in the $(V, dV/dt)$ −plane at baseline, followed by (ii) matching the firing frequency obtained from the temporal profiles of membrane voltage. We will refer to this model associated with baseline data as the "baseline" model. To capture all features of the AP cycle after the increase in excitability (i.e, after 25 min), we identified the list of all parameters that need to be adjusted to produce these features in the $(V, dV/dt)$ −plane and the higher firing frequency. Because our analysis revealed that the T-type Ca^{2+} current played a minor role in inducing the increase in excitability within the model, we left the kinetic parameters of activation/inactivation of I_T listed in Molineux *et al*. (2005) and Anderson *et al*. (2010) unchanged for both prior to and after the increase in excitability. The reversal potentials of Na^{+}, K^{+} and Ca^{2+} were also left unchanged. As for the remaining parameters, they were estimated based on fitting and parsimony. The resulting model that produced the increase in excitability will be referred to hereafter as "revised" model. The list of all parameter values for the baseline and revised models are provided in Table 1. Simulations were run in Mathematica 11.2 (Wolfram Mathematica, RRID:SCR_014448).

Table 1.1 Parameter values for Hodgkin-Huxley model

Parameter	Value/ Units	Parameter	Value/ units	Parameter	Value/ units	Parameter	Value/ units
C_M	1.50148 µF/cm^2	V_{Ca}	22 mV	w	46 mV	v_{m_T}	-50 mV
$\bar{g}_{Na}$	3.4 µS/cm^2	V_L	-38 mV	V_c	-74 mV	s_{m_T}	3 mV
$\bar{g}_K$	9.0556 µS/cm^2	v_m	-37 (-44) mV	v_n	-23 mV	v_{h_T}	-68 mV
$\bar{g}_A$	15.0159 µS/cm^2	s_M	3 mV	s_n	5 mV	s_{h_T}	3.75 mV
$\bar{g}_T$	0.45045 µS/cm^2	v_h	-40 (-48.5) mV	v_{n_A}	-27 (-41) mV	τ_{n_A}	5 ms
$\bar{g}_L$	0.07407 µS/cm^2	s_h	4 mV	s_{n_A}	13.2 mV	τ_{h_A}	10 ms
V_{Na}	55 mV	y_0	0.1 ms	v_{h_A}	-80 (-96) mV	τ_{h_T}	15 ms
V_K	-80 mV	A	322 ms·mV	s_{h_A}	6.5 (9.2) mV		

Parameter values of ionic currents included in the baseline and revised models whenever two values are provided for a given parameter, the first corresponds to the baseline model (before the increase in excitability at baseline) while the second shown between parentheses corresponds to the revised model (after the increase in excitability at 25 min).

Experimental design and statistical analysis

Paired t-tests were used to compare electrophysiological data recorded at baseline and after 25 minutes (step-evoked AP frequency, AP threshold, AP cycle parameters, $V_{1/2}$ values for I_{Na}). In the cases of I_A and I_K gating properties, a two-way mixed design ANOVA was used with Tukey's *post hoc* test to compare patch configuration data (nucleated and whole-cell) between groups while comparing data over time (baseline and 25 minutes) within each group. For each experimental group, recordings from a minimum of 5 cells from a minimum of 3 animals were collected. Analysis was not blinded.

Voltage-dependence of activation for all current types was analyzed by first calculating conductance (G) values from the peak currents elicited by each respective activation protocol using the formula:

$$G_x = \frac{I_x}{V_m - V_{rev_x}}$$

where I_x is the peak current of current type x (ie. I_A, I_K, I_{Na}) evoked at membrane potential V_m, and V_{rev_x} is the reversal potential of current type x. Conductance-voltage relationships for each current type were then fit to a Boltzmann function using the formula:

$$G_x = \frac{G_{max}}{1 + \exp((V_{1/2} - V_m)/k)}$$

where G_x is the conductance at membrane potential V_m for current type x, G_{max} is the maximum conductance for current type x, $V_{1/2}$ is the membrane potential where G_x is 50% of G_{max}, and k is the slope factor. Boltzmann fits were performed for each time point in each cell in order to calculate normalized conductance values. Summary conductance-voltage relationships for each current type were calculated by averaging the normalized conductance values across all cells in the dataset. $V_{1/2}$ values reported in the Results section for each current type were calculated by fitting the normalized conductance averages.

Data are reported as mean +/- SEM. Significance was denoted with * $p < 0.05$, ** $p < 0.01$ and *** $p < 0.001$. All fitting was performed with Origin 7.0 (Microcal Origin, RRID:SCR_002815). Statistical analyses were performed using SPSS 17.0 (SPSS, RRID:SCR_002865).

RESULTS

Action potential firing in cerebellar stellate and granule cells, but not Purkinje cells, increases during whole-cell recording

To examine time-dependent changes in membrane excitability, whole-cell patch clamp recordings were obtained from 3 types of visually-identified cerebellar neurons, namely stellate, granule and Purkinje cells (Figure 1.1A-C). After obtaining the whole-cell current clamp configuration, negative current was injected into each neuron to maintain the membrane potential at -70 or -80 mV (see Methods). To assess membrane excitability following breakthrough, incremental depolarizing current steps were applied within the first minute (termed *baseline*), and then once every 5 minutes during a typical 25 minute recording (Figure 1.1A-F).

Under these conditions, both stellate and granule cells fired many more action potentials (APs) at the 25 minute time point (Figure 1.1D,E). For example, in stellate cells (SCs), AP frequency evoked by a 16 pA current step at baseline was 9.8 ± 2.9 Hz versus 30.0 ± 5.6 Hz after 25 minutes ($t = 4.73$, $p < 0.001$; n = 11 cells) (Figure 1.1A,D). In contrast, firing rates in Purkinje cells remained stable throughout the recording (Figure 1.1C,F) but required larger step depolarizations to elicit APs. For example, AP frequency evoked by a 400 pA step at baseline was 59.1 ± 6.1 Hz versus 56.9 ± 4.2 Hz after 25 minutes ($t = -0.88$, $p = 0.41$; n = 7 cells). The increase in AP frequency in SCs was not accompanied by a change in input resistance (1011 ± 148 MΩ at baseline vs. 967 ± 137 MΩ at 25 min; $t = -1.21$, $p = 0.26$; n = 11 cells) or resting membrane potential (-50.6 ± 1.3 mV at baseline vs. -52.2 ± 1.6 mV at 25 min; $t = -1.33$, $p = 0.23$; n = 7 cells) suggesting that the increase in membrane excitability was primarily due to changes in the activity of active membrane

conductances (i.e. ion channels). In contrast, the increase in step-evoked AP frequency in granule cells (Figure 1.1B,E; 16 pA step: 1.2 ± 1.2 Hz at baseline vs. 25.2 ± 6.7 Hz at 25 min; t = 4.07, p = 0.015; n = 5 cells) was accompanied by a concurrent increase in membrane input resistance (44.5 ± 13.4% increase, n = 3 cells). Given this, we focused the rest of our study on SCs to pinpoint the molecular events that give rise to the increase in membrane excitability.

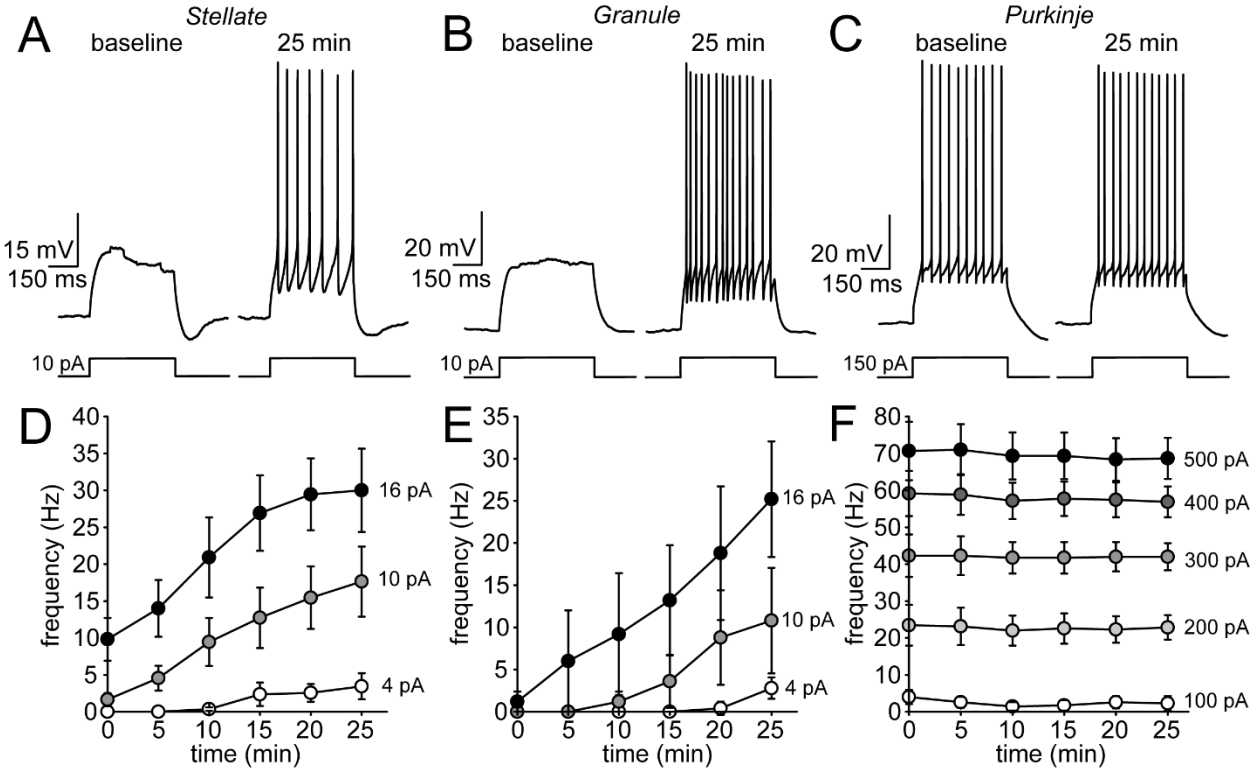

Figure 1.1 Stellate and granule cells, but not Purkinje cells, exhibit excitability increases during whole-cell recording (A) Example SC current clamp recording applying a 10 pA step protocol shortly following breakthrough and after 25 minutes. **(B,C)** Same for granule cell and Purkinje cell examples using 10 pA and 150 pA current steps, respectively. **(D)** Summary SC action potential frequency over 25 minute recording for multiple step amplitudes (n = 11 cells). **(E,F)** Same for granule (n = 6 cells) and Purkinje cells (n = 6 cells).

A closer examination of SC recordings revealed a decrease in spike latency in response to current injection (Figure 1.2A) at all current step amplitudes tested (Figure 1.2B). For example, the latency to first spike in response to a 16 pA current step at baseline was 89.9 ± 14.4 ms versus

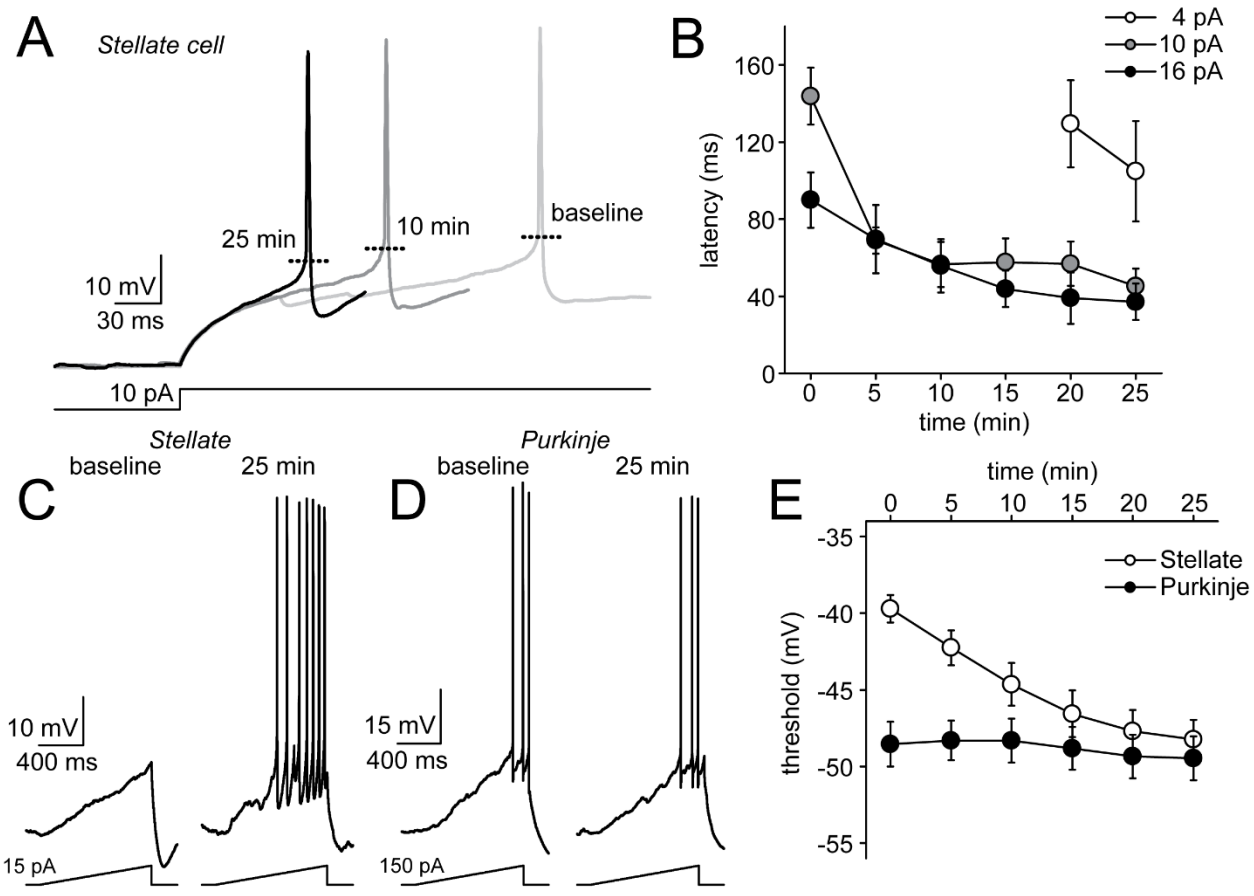

Figure 1.2 Excitability increase is underpinned by decrease in spike latency and hyperpolarization of AP threshold **(A)** First APs fired by a SC in response to 10 pA current step at 3 different time points: 1 min, 10 min, and 25 min after breakthrough. The spike latency in response to the step decreases substantially over the course of the recording. **(B)** Summary plot of spike latencies for multiple step amplitudes over the course of a 25 minute recording (n = 11 cells). **(C)** Example current clamp responses evoked by ramp protocol at baseline (left) and after 25 minutes (right) in a SC (patch # 150129p2). **(D)** Same for an example Purkinje cell (patch # 141010p5). **(E)** Summary plot depicting change in AP threshold over time in stellate (n = 11 cells) and Purkinje cells (n = 6 cells).

37.1 ± 9.5 ms at 25 min (t = -6.68, p < 0.001; n = 11 cells). To measure the shift precisely, we used a 1 s current ramp protocol to monitor the membrane potential at the initiation of the AP upstroke. To ensure that the ramp protocol had no direct effect on spike threshold, the protocol began with a 5 pA ramp that increased 5 times in increments of 5 pA. The threshold for each cell was then calculated by averaging the value obtained at each ramp amplitude. For comparison, we also repeated these experiments on both granule (not shown) and Purkinje cells (Figure

1.2D,E). As anticipated, SCs exhibited a shift in AP threshold starting at -39.7 ± 0.9 mV following breakthrough and hyperpolarizing to -48.2 ± 1.3 mV at 25 min (Figure 1.2C,E; t = -15.74, p < 0.001; n = 12 cells). Granule cells exhibited an even more substantial hyperpolarizing shift in AP threshold (-35.9 ± 0.6 mV at baseline vs. -52.5 ± 2.1 mV at 25 min; t = -7.31, p < 0.001; n = 6 cells) whereas the threshold in Purkinje cells remained constant (-48.5 ± 1.5 mV at baseline vs. -49.5 ± 1.4 mV at 25 min; t = -.073, p = 0.51; n = 5 cells) (Figure 1.2E).

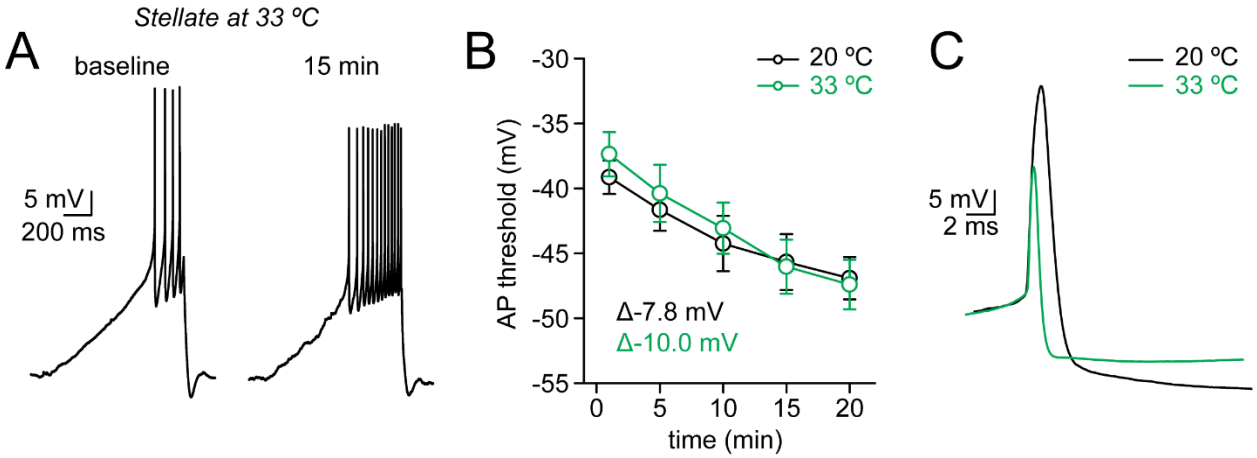

Figure 1.3 Threshold hyperpolarization in stellate cells is present at near-physiological temperature
(A) Example stellate cell AP firing in response to a 20 pA ramp stimulus soon after patch breakthrough and after 15 minutes of recording. **(B)** Summary time course data of stellate cells recorded at room temperature (black; n = 11 cells) and at near-physiological temperature (green; n = 5 cells). **(C)** Single AP overlay from stellate cells at room and elevated temperatures.

To ensure that the excitability increase in SCs was present in physiologically relevant conditions, the temperature of the ACSF perfusion was raised to near-physiological level (33-34 °C) and current clamp experiments were repeated. SCs at elevated ambient temperatures still exhibited hyperpolarizing AP thresholds that closely resembled those at room temperature (Figure 1.3B; -37.4 ± 1.7 mV at baseline vs. -47.4 ± 1.9 mV at 20 min; t = 10.04, p < 0.001; n = 5 cells). Lastly, since others have noted that internal anions can affect intrinsic membrane properties of neurons during whole-cell recording (Kaczorowski *et al.*, 2007), we repeated

current clamp experiments in SCs using a K-methanesulfonate-based intracellular solution in place of the initial K-gluconate version. Although slightly hyperpolarized at baseline compared to gluconate, the presence of methanesulfonate did not prevent the decrease of AP threshold over the duration of patch clamp recording (-42.8 ± 1.1 mV at baseline vs. -51.0 ± 1.8 mV at recording endpoint; $t = 6.14$, $p < 0.001$; n = 7 cells).

Modified Hodgkin-Huxley model predicts a dominant role for voltage-gated Na^+ channels

To better understand the change in excitability of SCs, we used a modified Hodgkin-Huxley model to examine the potential impact of ion channels that are likely to be involved. The model was based on a previous study that included a voltage-gated Na^+ current (I_{Na}), a delayed rectifier K^+ current (I_K), an A-type K^+ current (I_A), a T-type Ca^{2+} current (I_T) and a leak current (I_L) (Molineux *et al.*, 2005). The A-type K^+ and T-type Ca^{2+} currents were specifically included in the model as they have been shown to play key roles in determining first spike latencies (Molineux *et al.*, 2005; Anderson *et al.*, 2010a; Anderson *et al.*, 2013). The model parameters were then adjusted to match observations of spontaneous AP firing at the beginning of SC recordings (see Methods).

To provide an accurate experimental baseline to use as a template for modeling spontaneous AP firing, gap-free recordings from multiple SCs were made in the absence of injected current (Figure 1.4 and 1.5A). In line with the previous current step and ramp experiments, spontaneous AP firing in all SCs increased significantly over 25 minutes (Figure 1.4A and 1.5A; 12.5 ± 3.2 Hz at baseline vs. 17.9 ± Hz at 25 min; $t = 2.60$, $p = 0.041$; n = 7 cells). The AP

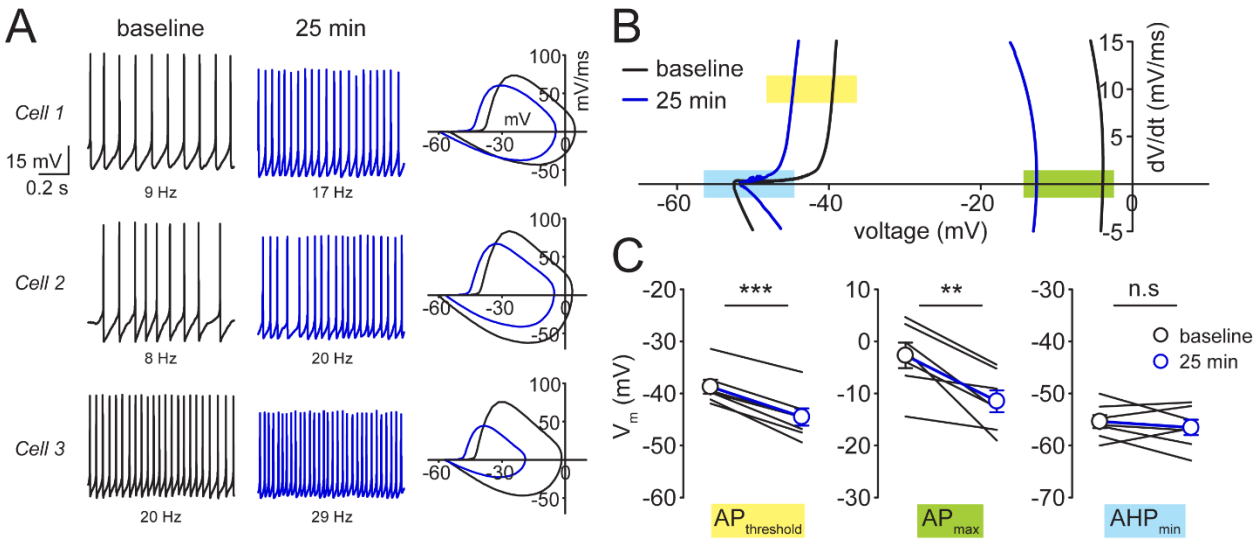

Figure 1.4 Defining the hallmark membrane features of stellate cell excitability increase
(A) (left panels) Spontaneous AP firing traces from 3 example SCs at baseline (black) and after 25 minutes (blue) (patch #s 150129p2, 181111p6, 181109p3). (right panels) AP cycles for each cell calculated from voltage-time data at baseline (black) and 25 minutes (blue). **(B)** AP cycle plot of an example SC with y-axis expanded. Colored rectangles designate quantities of interest (yellow - AP threshold; green – AP maximum; light blue – AHP minimum). **(C)** Summary comparison of these 3 features measured from individual AP cycles (n = 7 cells).

cycle, which was obtained from these data by taking the derivative of the measured voltage plotted against membrane potential (Figures 1.4A and 1.5B), revealed two defining characteristics of time-dependent changes in AP shape: (i) a negative shift in AP upstroke, indicating the hyperpolarization of spike threshold (Figure 1.4B, yellow box; defined as dV/dt = 10 mV/ms); (ii) a reduction in the peak of the AP cycle where it intersects with the voltage-axis (Figure 1.4B, green box). These measurements were compared over multiple SCs, demonstrating significant differences in AP threshold (Figure 1.4C; -38.7 ± 1.3 mV at baseline vs. -44.5 ± 1.7 at 25 min; t = -11.25, $p < 0.001$; n = 7 cells) as well as AP maximum (Figure 1.4C; -2.7 ± 2.4 mV at baseline vs. -11.5 ± 2.1 mV at 25 min; t = -4.41, p = 0.0045; n = 7 cells). The change in after-hyperpolarization (AHP) minimum (Figure 1.4B, light blue box) was variable across cells (3 examples in Figure 1.4A), but this was not significant (Figure 1.4C; -55.4 ± 1.3 mV at baseline vs. -56.5 ± 1.5 mV at 25 min; t = -0.88, p = 0.41; n = 7 cells). Together, these findings identify three

cardinal features that are observed during whole-cell recording from SCs: (i) an increase in spontaneous AP frequency, (ii) a hyperpolarizing shift of AP threshold and (iii) a hyperpolarizing shift in the AP maximum.

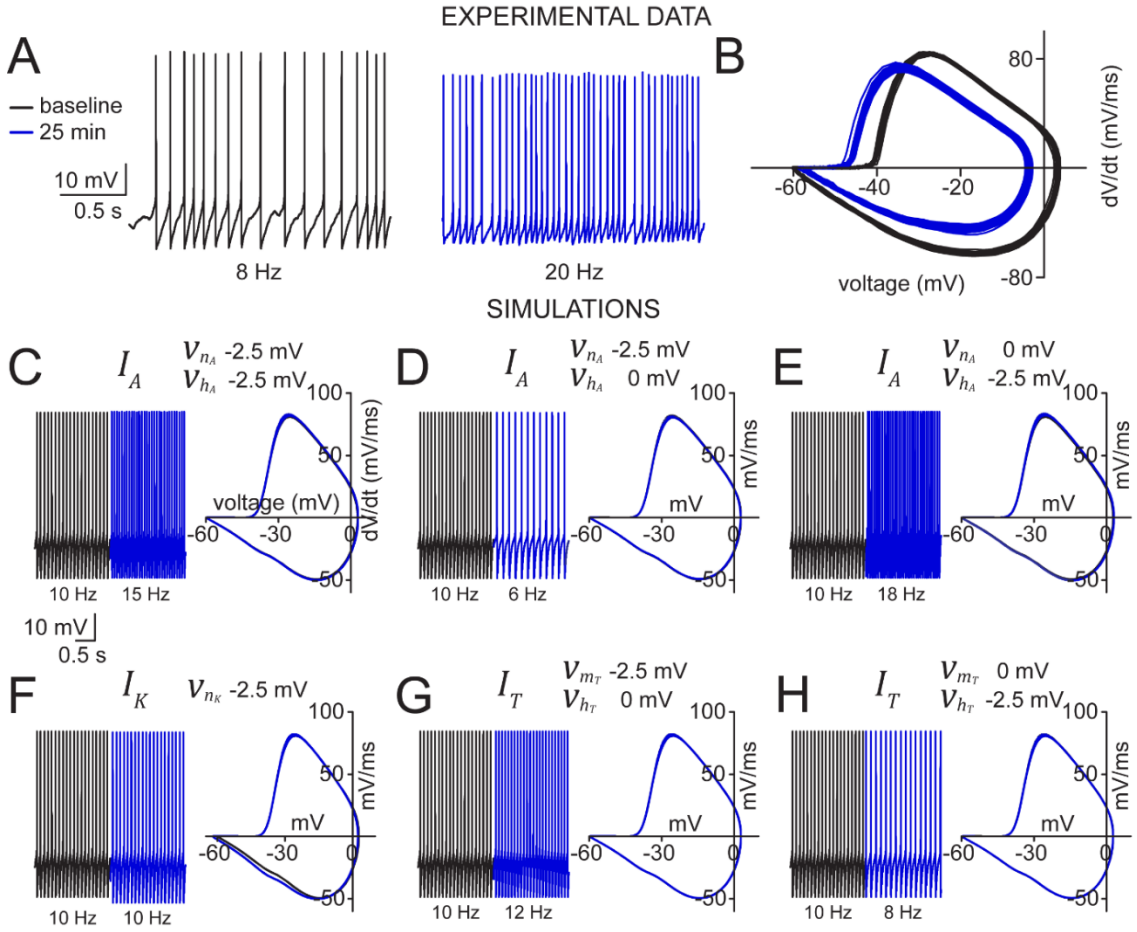

Figure 1.5 Simulating I_A, I_K and I_T shifts predicts little contribution to excitability increase
(A) Example SC current clamp recording depicting spontaneous AP firing at baseline (black) and after 25 minutes (blue) (patch # 181111p5). **(B)** AP cycle calculated from current clamp data from (A) at baseline (black) and 25 minutes (blue). **(C,D,E)** Simulated spontaneous firing and AP cycle from baseline model (black) and after making symmetric and asymmetric shifts in v_{n_A} and v_{h_A} (blue). **(F)** Same for I_K after shifting v_{n_K} (blue). **(G,H)** Same for I_T after shifting either v_{m_T} or v_{h_T}.

To examine the potential impact of each ionic current, we systematically modified their activation and inactivation kinetic parameters in the baseline model and compared the resulting AP cycle with experimental data. For example, a symmetrical negative shift of both activation ($n_{A,\infty}$) and inactivation ($h_{A,\infty}$) functions of I_A, obtained by decreasing both v_{n_A} and v_{h_A} by -2.5

mV, yielded a ~50% increase in AP firing frequency but no change in the shape of the AP cycle (Figure 1.5C). Likewise, shifts in either activation (Figure 1.5D) or inactivation (Figure 1.5E) functions of I_A separately showed substantial shifts in firing frequency without altering the AP cycle shape or threshold. A negative shift in the activation function (n_∞) of I_K, obtained by decreasing v_n by -2.5 mV, resulted in no change in AP firing frequency but produced a leftward extension of the AHP in the AP cycle (Figure 1.5F). Shifting either the activation function $m_{T,\infty}$ (Figure 1.5G) or inactivation function $h_{T,\infty}$ (Figure 1.5H) of I_T, obtained by decreasing each v_{m_T} and v_{h_T} separately by -2.5 mV, had little effect on AP firing frequency (where only an ~20% increase in the former and a ~20% decrease in the latter were observed) and no effect on the AP cycle. Given this, we concluded that T-type Ca^{2+} channels are unlikely to contribute to the temporal increase in excitability of SCs. Although the A-type K^+ channel may contribute to the increase in AP firing rates, other ion channels must be responsible for the hyperpolarizing shift in AP threshold.

Modification of the model parameters defining I_{Na} had a substantial impact on AP firing and the AP cycle profile (Figure 1.6). Identical negative shifts in both activation and inactivation parameters resulted in a concomitant shift in the AP cycle upstroke as well as an increase in AP firing frequency, although a reduction in the AP maximum was absent (Figure 1.6A). Likewise, a differential left-shift in favor of the activation function (given by -5 mV for activation and -2.5 mV for inactivation) produced a ~80% increase in AP firing frequency, but was unable to generate a reduction in AP maximum (Figure 1.6B). In contrast, a differential left-shift in favor of inactivation resulted in a ~100% increase in AP firing as well as reproducing the profile of the AP cycle similar to that observed experimentally (Figure 1.6C). Taken together, the model suggests that

hyperpolarizing shifts in the gating properties of I_{Na} alone can account for the increase in firing rate as well as the characteristic AP cycle changes exhibited by SCs during patch clamp recording.

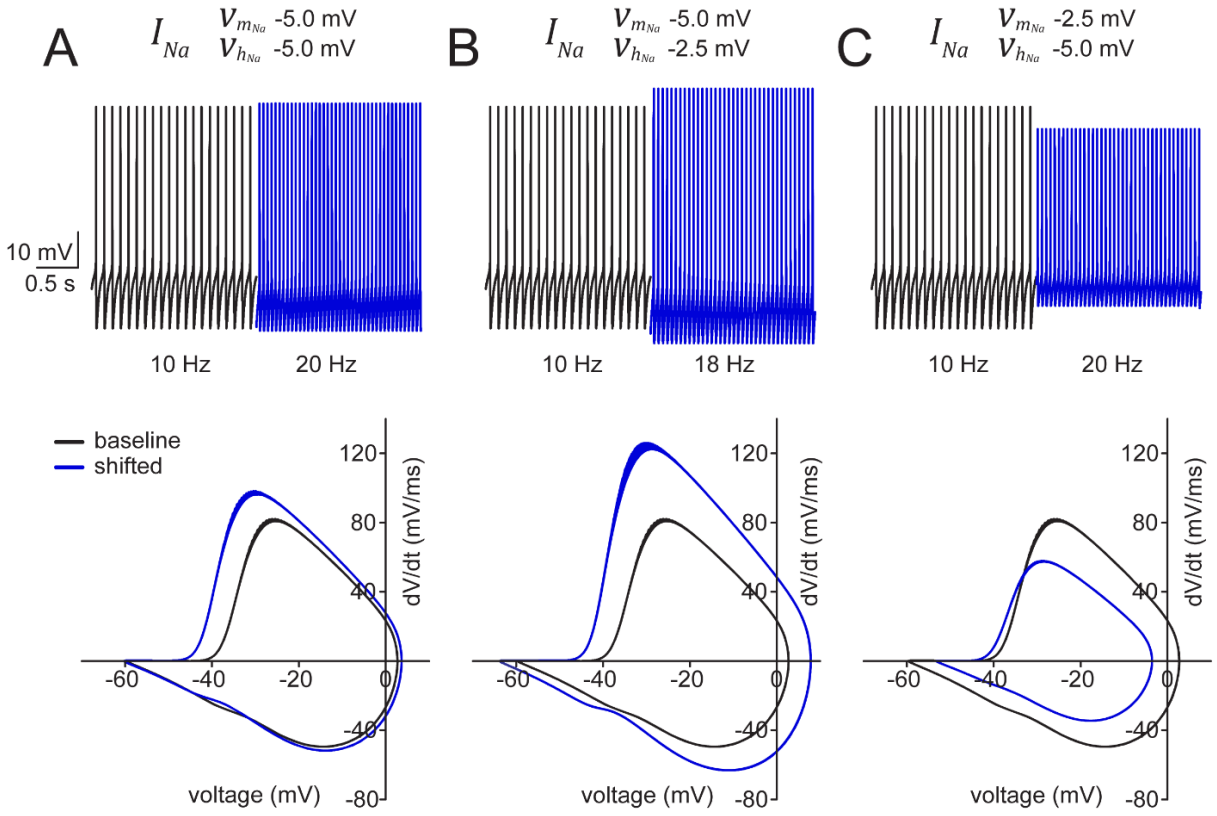

Figure 1.6 Simulated I_{Na} shifts suggest primary role for sodium channel in excitability increase
Simulated spontaneous firing (upper panels) and AP cycles (lower panels) from baseline model (black) and after either symmetric **(A)** or asymmetric **(B,C)** shifts in $v_{m_{Na}}$ and $v_{h_{Na}}$.

Stellate cell excitability is accompanied by gating shifts in I_A, but not I_K

To directly test the prediction of the model, we used customized activation and inactivation voltage clamp protocols to isolate two subtypes of K^+ current, I_A and I_K (Figures 1.7 and 1.8, see Methods). Since it can be problematic to accurately measure voltage-gated ion channel activity in highly ramified structures such as neurons, we repeated experiments in nucleated patches where a more faithful voltage clamp control can be achieved. In whole-cell recordings, we observed a significant time-dependent shift in the voltage-dependence of both activation and inactivation of I_A (Figure 1.7B,D). From Boltzmann fits of conductance-voltage rela-

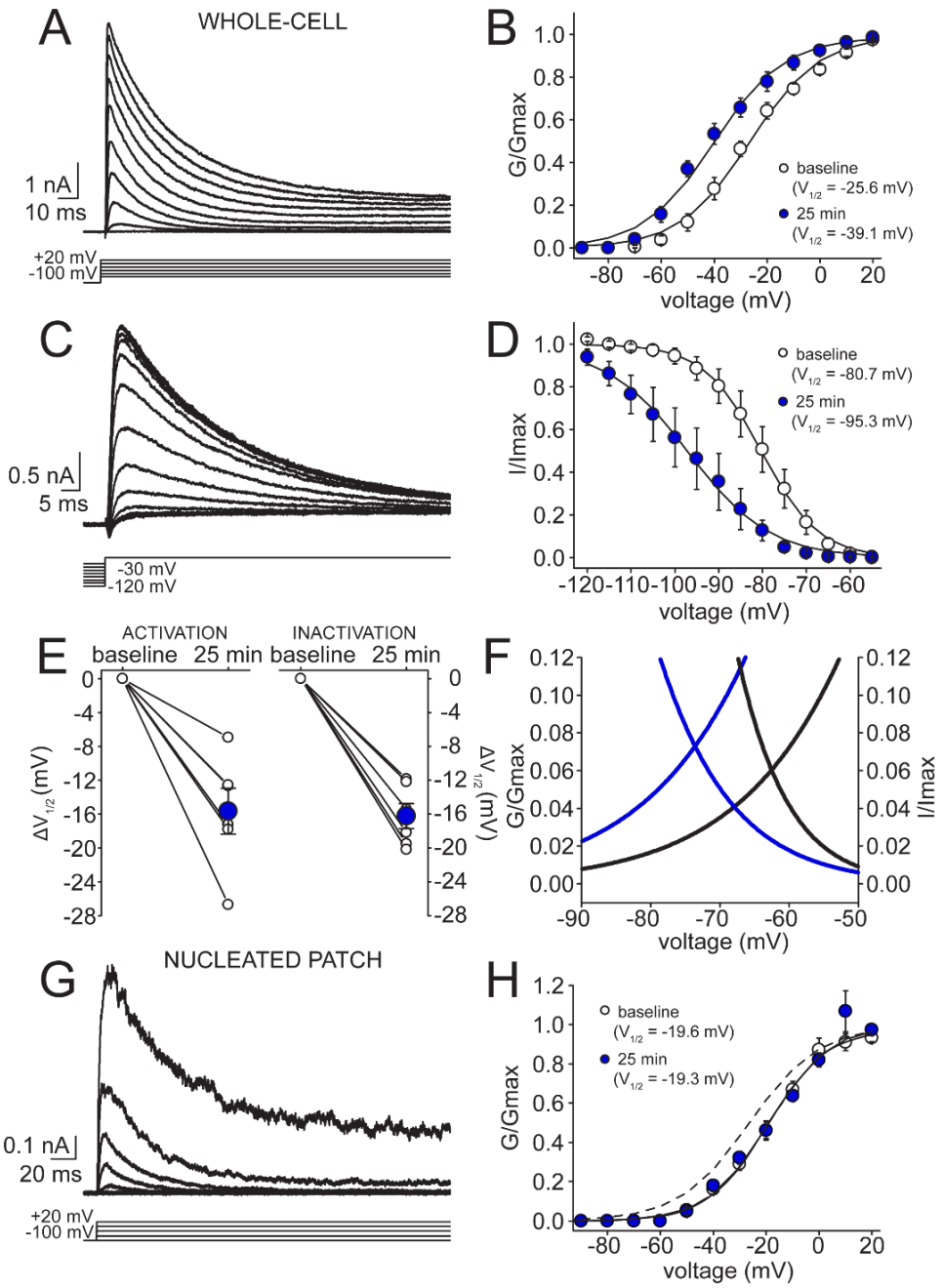

Figure 1.7 I_A exhibits shifts in both activation and inactivation during 25 minute recording
(A) Example voltage clamp traces of I_A currents at baseline during activation protocol. **(B)** Summary plot of voltage dependence of activation of I_A at baseline (white circles) and after 25 minutes of recording (blue circles; n = 7 cells). **(C)** Example voltage clamp traces of I_A currents evoked during inactivation protocol. **(D)** Summary plot of voltage dependence of inactivation of I_A at baseline (white circles) and after 25 minutes of recording (blue circles; n = 7 cells, same as in B). **(E)** Normalized $V_{1/2}$ activation (left) and inactivation (right) compared to delta shift after 25 minute recording for each cell (white circles), along with summary mean delta for each measure (blue circles). **(F)** Zoom-in of Boltzmann fits for both voltage-dependence of activation and inactivation at baseline (black lines) and at 25 minutes (blue lines) from B and D, respectively, depicting symmetrical translocation of I_A window current. **(G)** Example voltage clamp traces of I_A currents during activation protocol observed in a SC nucleated patch. **(H)** Summary plot of voltage-dependence of activation of I_A at baseline (white circles) and 25 minutes (blue circles; n = 6 patches). Dashed line depicts baseline activation curve measured in whole-cell configuration from (B).

tionships, $V_{1/2}$ activation of I_A shifted from -25.8 ± 2.4 mV at baseline to -39.1 ± 2.6 mV after 25 minutes (F = 7.07, p < 0.001, Tukey's *post-hoc* test; n = 7 cells), while $V_{1/2}$ inactivation changed from -80.7 ± 2.8 mV at baseline to -95.3 ± 4.6 mV at 25 minutes (t = -11.91, p < 0.001; n = 7 cells). Plotting the normalized changes in $V_{1/2}$ measurements between baseline and after 25 minutes for individual cells yielded a comparable result (Figure 1.7E; $\Delta V_{1/2}$ activation: -15.7 ± 2.7 mV; $\Delta V_{1/2}$ inactivation: -16.2 ± 1.5 mV). Since the changes in $V_{1/2}$ activation and $V_{1/2}$ inactivation are very similar, this produced a hyperpolarizing shift in the window current of about -11 mV with the midpoint moving from -62.5 mV to -73.5 mV (Figure 1.7F). Interestingly, the shift in the voltage-dependence of activation of I_A was completely lost in nucleated patches suggesting that the time-dependent change in the gating properties of I_A is probably mediated by a cytoplasmic signaling pathway, such as phosphorylation (Figure 1.7G,H). The $V_{1/2}$ activation was -19.6 mV at baseline and -19.3 mV after 25 minutes of recording (F = 0.07, p = 0.96, Tukey's *post-hoc* test; n = 6 patches), which was slightly more depolarized than measurements in whole-cell recordings (Figure 1.7H; F = 3.31, p = 0.038, Tukey's *post-hoc* test), possibly reflecting the improvement in voltage clamp control.

In contrast to I_A, there was no significant time-dependent change in the voltage dependence of I_K activation in whole-cell recording, nor in nucleated patches (Figure 1.8A-D; F = 3.88, p = 0.081, 2-way mixed design ANOVA). In whole-cell configuration, $V_{1/2}$ activation at baseline was -17.7 mV compared to -17.5 mV at 25 minutes (n = 8 cells), while the voltage-dependence of activation in excised patches (n = 6) was -3.6 mV at baseline compared to +2.6 mV at 25 minutes. There was, however, a significant difference in $V_{1/2}$ values between measurements made in whole-cell and nucleated patches (F = 23.42, p < 0.001, 2-way mixed

design ANOVA), suggesting that the recording configuration (whole-cell vs. patch) affects I_K gating.

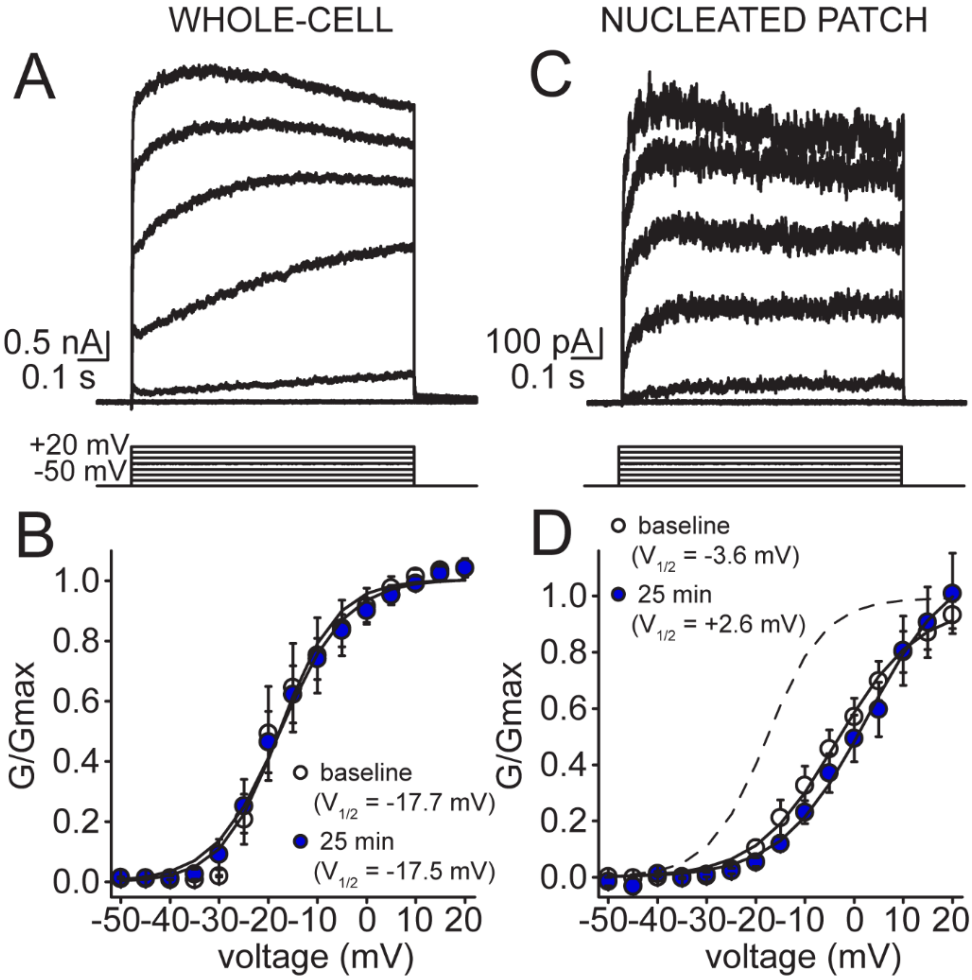

Figure 1.8 I_K voltage-dependence of activation remains stable over patch clamp recording in both whole-cell and nucleated patch configurations (A) Example whole-cell voltage clamp traces of delayed rectifier K^+ current at baseline during activation protocol evoked from -50 mV holding potential (5 mV increments, up to +20 mV; patch # 180521p2). **(B)** Summary plot of voltage dependence of activation of delayed rectifier K^+ current at baseline (white circles) and after 25 minutes of recording (blue circles; n = 8 cells). **(C)** Example voltage clamp traces after excising a nucleated patch of delayed rectifier K^+ current at baseline during activation protocol evoked from -50 mV holding potential (5 mV increments, up to +20 mV; patch # 180510p3). **(D)** Summary plot of voltage dependence of activation of delayed rectifier K^+ current at baseline (white circles) and after 25 minutes of recording (blue circles; n = 6 cells). Dashed line depicts baseline activation curve measured in whole-cell configuration from (B).

I_{Na} exhibits hyperpolarizing shifts in both activation and inactivation

Due to space clamp issues, it is not possible to record the fast gating of I_{Na} in SCs with conventional voltage clamp protocols. The main problem is the inability to accurately record Na^+

channel activity in distant processes such as axons. To circumvent this, we adapted a protocol using a depolarizing prepulse step to inactivate Na^+ channels distant from the recording electrode which was followed shortly afterwards with a second test step to record Na^+ channels close to the cell soma (Milescu *et al.*, 2010). Using this approach, we reliably resolved well-clamped, albeit smaller, I_{Na} responses in SCs to profile their activation and inactivation properties (Figure 1.9A-D). Performing this protocol over a 25 minute period revealed that SC Na^+ channels undergo a hyperpolarizing shift of -7.8 mV in their activation (Figure 1.9A,B; -32.4 ± 1.5 mV at baseline vs. -40.2 ± 1.6 mV at 25 min; t = -9.10, p < 0.001; n = 11 cells) and a similar hyperpolarizing shift in steady-state inactivation (Figure 1.9C,D; -49.3 ± 0.7 mV at baseline to -57.4 ± 1.0 mV at 25 min; t = -8.95, p < 0.001; n = 11 cells). This finding is in agreement with the hyperpolarizing shift in Na^+ channel gating predicted by the modified Hodgkin-Huxley model applied to stellate AP firing (Figure 1.6).

Interestingly, we also observed a reduction in peak I_{Na} current density that developed over the duration of the experiment (Figure 1.9E; -75.5 ± 8.4 pA/pF at baseline vs. -45.1 ± 6.7 pA/pF at 25 min; t = 6.64, p < 0.001; n = 11 cells). To test whether this was due to a reduction in I_{Na} current density or a consequence of the hyperpolarizing shift in inactivation, we compared peak currents from the first step of the inactivation protocol (Figure 1.9F; -110 mV to -20 mV probe). At this voltage, all SC Na^+ channels are available for activation both at baseline and after a 25 minute recording. According to this measure, there is no difference between Na^+ current density before and after 25 minutes and this reduction reflects the shift in steady-state inactivation alone (Figure 1.9F,G; peak current: -2012.3 ± 149.1 pA at baseline vs. -1984.5 ± 162.8 pA at 25 min; t = 0.43, p = 0.68; n = 11 cells).

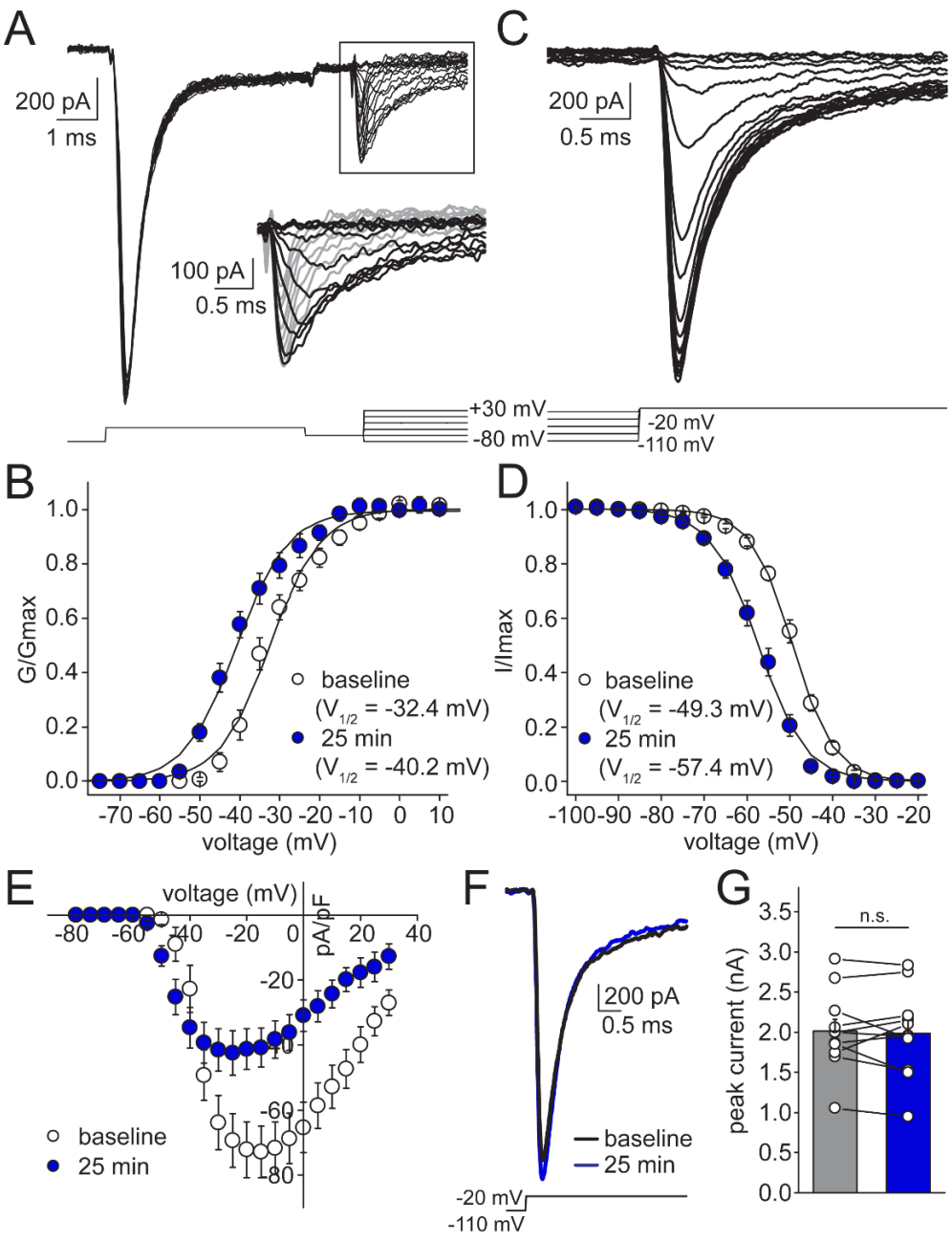

Figure 1.9 Stellate cell I_{Na} exhibits shift in both activation and inactivation properties, but not current density
(A) Example voltage clamp traces of Na^+ currents evoked with a prepulse protocol. (inset) Zoom-in of portion of traces depicting strong voltage clamp of Na^+ currents evoked after prepulse. **(B)** Summary plot of voltage-dependence of activation of Na^+ current at baseline (white circles) and at 25 minutes (blue circles; n = 11 cells). **(C)** Example traces from a Na^+ inactivation protocol. **(D)** Summary plot of voltage-dependence of inactivation at baseline (white circles) and at 25 minutes (blue circles; n = 11 cells). **(E)** Summary current density-voltage plot (data used to construct conductance-voltage plots in B and D) of sodium responses at baseline (white circles) and at 25 minutes (blue circles). **(F)** Example peak sodium current traces evoked by a -110 mV to -20 mV probe at baseline (black) and at 25 minutes (blue). **(G)** Summary graph of peak sodium currents evoked from a holding potential of -110 mV at baseline (grey) and at 25 minutes (blue).

Pharmacological block of K^+, Ca^{2+} or HCN channels has no effect on AP threshold

To test the hypothesis that the shift in Na^+ channel gating is primarily responsible for the increase in SC excitability, we examined whether pharmacological block of I_A with 4-aminopyridine (4-AP) attenuates the hyperpolarizing shift in AP threshold. As expected, block of I_A with bath application of 2 mM 4-AP resulted in a more depolarized inter-spike membrane potential at baseline compared to control cells (Figure 1.10B). 4-AP, however, did not attenuate the shift in AP threshold (Figure 1.10A) which hyperpolarized from -40.7 ± 0.9 mV at baseline to -48.6 ± 0.9 mV after 25 min (t = -9.37, p < 0.001; n = 5 cells). Interestingly, 2 mM 4-AP also attenuated the after-hyperpolarization (AHP) of the AP (Figure 1.10B) which may reflect pharmacological block of delayed rectifier K^+ channels. In keeping with this, block of I_K with 2 mM external tetraethylammonium (TEA) had the expected effect on AP shape at baseline but did not attenuate the shift in AP threshold (Figure 1.10C,D). AP threshold observed in 2 mM TEA hyperpolarized from -37.2 ± 0.4 mV at baseline to -47.5 ± 1.4 mV after 25 min of recording (t = -8.99, p < 0.001; n = 5 cells) (Figure 1.10C,D). Since hyperpolarization-activated cyclic nucleotide-gated (HCN) channels (which mediate the mixed cation current I_h) and voltage-gated Ca^{2+} channels (VGCCs) have also been shown to affect excitability of molecular layer interneurons (Molineux *et al.*, 2005; Anderson *et al.*, 2010a; Anderson *et al.*, 2013), we tested the effect of the selective I_h blocker, ZD 7288 (20 µM) and nonselective VGCC blocker $CdCl_2$ (200 – 300 µM) on AP threshold (Figure 1.10E-H). In each case, the hyperpolarizing shift in AP threshold was unaffected by either ZD 7288 or $CdCl_2$. The AP threshold with 20 µM ZD 7288 was -38.2 ± 1.3 mV at baseline and hyperpolarized to -46.8 ± 1.3 mV at 25 min (t = -10.13, p < 0.001; n = 6 cells). Likewise, the threshold shifted from -38.1 ± 0.8 mV at baseline with $CdCl_2$ to -47.7 ± 1.3 mV after 25 min of

recording (t =-7.69, p = 0.0015; n = 5 cells). Taken together, these data demonstrate that I_A, I_K, I_h and VGCCs do not contribute to the hyperpolarization of AP threshold of SCs, consistent with our hypothesis that the primary mechanism for the shift is mediated by Na^+ channels.

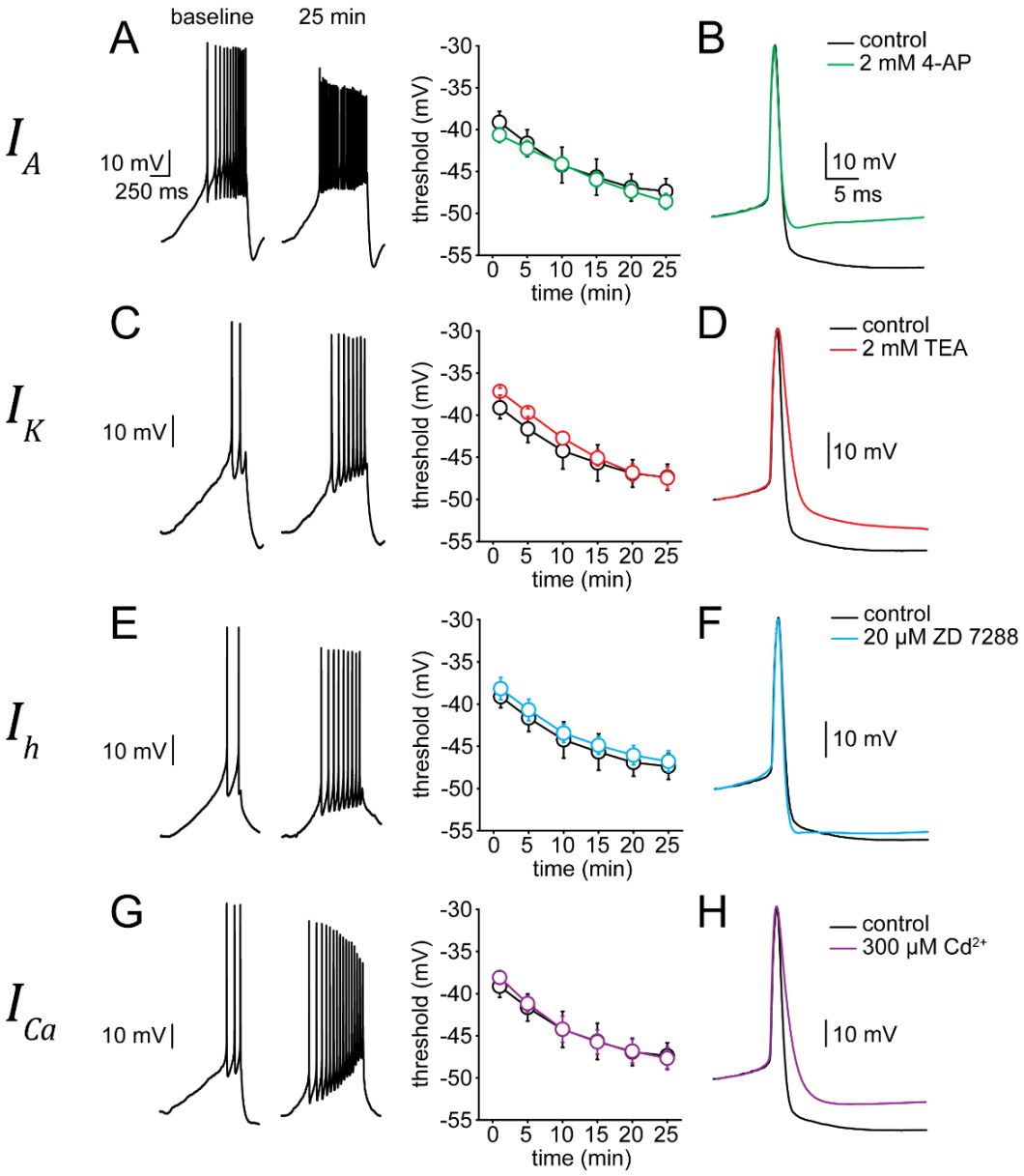

Figure 1.10 AP threshold hyperpolarization persists with pharmacological blockade of I_K, I_A, I_{Ca} and I_h
(A) (left panel) Example traces recorded at baseline and after 25 minutes of action potentials evoked by a current ramp protocol (25 pA over 1 s) in a SC. (right panel) Summary AP threshold data for control conditions (black open circles; n = 6 cells) and in the presence of 2 mM TEA in the ACSF (red open circles; n = 5 cells). **(B)** Superimposed first APs evoked by ramp protocol in control (black) and external TEA (red) conditions. TEA scaled to control. **(C,D)** Same as A and B, but in the presence of 2 mM 4-AP (green lines; n = 5 cells). **(E,F)** Same as A and B, but in the presence of 20 µM ZD 7288 (blue lines; n = 6 cells). **(G,H)** Same as in A and B, but in the presence of 200 - 300 µM $CdCl_2$ (purple lines; n = 5 cells).

Revised Hodgkin-Huxley model recapitulates the increase in stellate cell excitability

Based on the voltage clamp data, we revised the Hodgkin-Huxley model to match the observed changes in I_{Na} and I_A (see Methods section). To do this, we targeted only their activation/inactivation properties without altering their conductances. Specifically, $v_{m_{Na}}$ was shifted by -7 mV and $v_{h_{Na}}$ by -8.5 mV, while v_{n_A} was shifted by -14 mV and v_{h_A} by -16 mV (Table 1.1), which reproduced well the observed increase in excitability of SCs (Figure 11.1A-D). With respect to the changes in the AP cycle described earlier (Figure 1.4), the revised model captures all the cardinal features seen in the experimental recordings (Figure 11.1A,B). Specifically, the AP threshold of the revised model hyperpolarized by -5.8 mV from -38.7 mV to -44.5 mV, which agrees well with the -6.0 mV hyperpolarization observed experimentally. The simulated AP maximum hyperpolarized by -8.4 mV from 3.9 mV to -4.5 mV, which is comparable to the hyperpolarization of -8.8 mV measured experimentally. Finally, the AHP minimum observed in the revised model depolarized by +1.8 mV from -60.1 mV to -58.3 mV, which is within the margin of error of the experimental results (Figure 1.4C). The fact that these specific adjustments are able to closely capture the dynamics observed experimentally further supports the dominance of I_{Na} in driving the increase in SC excitability, with an additional role for I_A in further modulating AP firing.

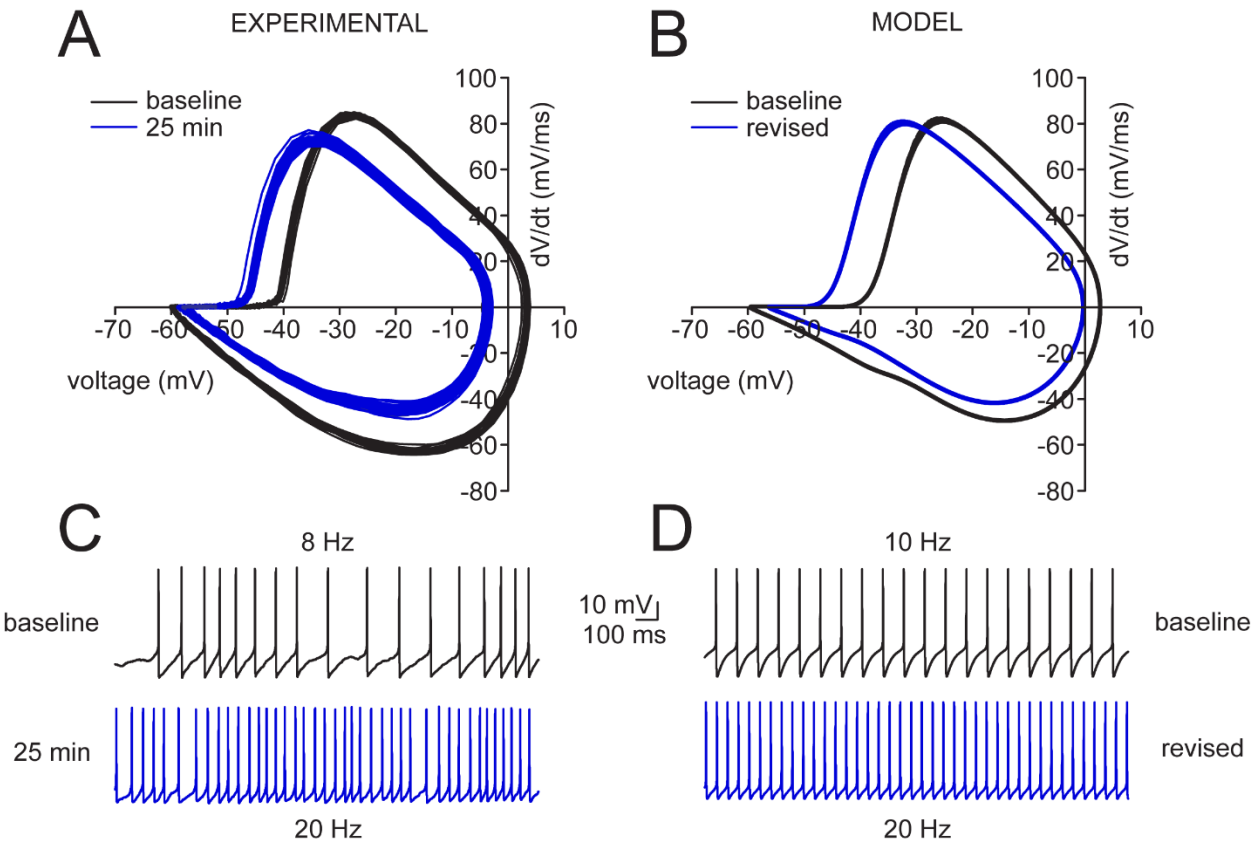

Figure 1.11 Voltage clamp-informed model recapitulates the dynamics of current clamp experimental data
(A) AP cycle calculated from experimental SC current clamp recording at baseline (black) and 25 minutes (blue). **(C)** Same current clamp recording data as above, presented as voltage vs. time at baseline (black) and 25 minutes (blue). **(B)** Simulated AP cycle of baseline (black) and revised (blue) models after modifying all gating parameters based on values measured experimentally in voltage clamp in SCs. **(D)** Simulated firing properties of baseline (black) and revised (blue) models.

DISCUSSION

The present study advances our understanding of the neurophysiology of cerebellar SCs in two important ways. First, we identify a predominant role of voltage-gated Na^+ channels in upregulating the excitability of cerebellar SCs following membrane patch breakthrough. Under these conditions, the threshold for AP initiation is shifted to more hyperpolarized membrane potentials due to changes in the activation and inactivation properties of Na^+ channels. Since similar shifts in gating behavior are observed in other central neurons by physiological stimuli, such as NMDAR activation (e.g. (Xu *et al.*, 2005)), it is possible that Na^+ channels are targeted in a comparable manner in SCs to upregulate AP firing. Second, we report hyperpolarizing shifts in both the activation and inactivation properties of A-type K^+ channels that contribute to the time-dependent increase in firing rates observed in SCs but do not participate in the hyperpolarizing shift in AP threshold. Previous work has established that *depolarizing* shifts in A-type K^+ channel inactivation are triggered by elevations in cytosolic Ca^{2+} due to T-type Ca^{2+} channel activity in SCs (Molineux *et al.*, 2005; Anderson *et al.*, 2010a; Anderson *et al.*, 2013). Given this distinction with the present study, it is likely that different signaling events are at play to regulate the gating behavior of A-type K^+ channels in cerebellar SCs.

Increased membrane excitability following whole-cell recording is not unique to stellate cells

SCs are not the only neuronal cell type that undergo functional changes after the establishment of the whole-cell patch clamp configuration. In fact, early patch clamp studies of voltage-gated ion channels noted time-dependent changes in both activation and inactivation properties including changes to voltage-gated Na^+ channels (Fenwick *et al.*, 1982b; Fernandez *et al.*, 1984; Vandenberg & Horn, 1984; Marty & Neher, 1985). The mechanism(s) underlying these

changes has remained largely unexplored and thus ignored - as has been the case for cerebellar SCs. In the cerebellum, the increased firing rate we have observed in granule cells (GCs) (cf. Figure 1.1) may be attributed to the cell's buffering capacity for cytosolic Ca^{2+} which is further compromised when GCs lack the calcium binding protein, calretinin (Gall *et al.*, 2003). Similarly, Alcami and colleagues also linked a rise in intracellular Ca^{2+} to an increase in firing rates of SCs (Alcami *et al.*, 2012) suggesting that there may be overlapping signaling pathways at play in both cell types (see below). A distinction with SCs, however, is that we have observed an increase in the input resistance of GCs following patch breakthrough. Whether the change in membrane leak is due to the activity of other ion channels, such as TASK-1 (Millar *et al.*, 2000) or HCN channels (Zuniga *et al.*, 2016), in GCs remains to be studied. Why the excitability of SCs and GCs increases after patch breakthrough whereas Purkinje cells remain stable is not clear. It is tempting to speculate that the smaller soma of SCs makes their subcellular Ca^{2+} stores more susceptible to perturbation during whole-cell recording compared to Purkinje cells. It is also possible that SCs are mechanosensitive which is in keeping with the observation that SC excitability increases during cell-attached recordings, particularly in recordings with a tight seal (Alcami *et al.*, 2012). As discussed below, the events that are initiated by membrane patch breakthrough suggest that voltage-gated Na^+ channels may be impacted by several endogenous signaling pathways in SCs.

Expression and regulation of Na^+ channels in cerebellar stellate cells

Cerebellar molecular layer interneurons (MLIs) are thought to express several Na^+ channel pore-forming subunits that include $Na_v1.1$, $Na_v1.2$ and $Na_v1.6$ (Schaller & Caldwell, 2003), however, more recent data suggest that the $Na_v1.2$ protein is expressed only on presynaptic terminals of granule cells (Jarnot & Corbett, 2006; Martinez-Hernandez *et al.*, 2013). This latter

finding agrees with our experiments using the $Na_v1.2$-selective inhibitor, Phrixotoxin-III, which has negligible pharmacological effect on SC excitability (Alexander & Bowie, unpublished observation). Based on antibody staining, both $Na_v1.1$ and 1.6 subunits are expressed in MLIs (Kalume *et al.*, 2007), however, their subcellular distribution is distinct (Lorincz & Nusser, 2008). The Nav1.6 subunit is almost exclusively expressed at the axon initial segment (AIS), a region of the axon close to the cell body where action potentials are initiated. In contrast, Nav1.1 is expressed throughout the axon, though it is also found in the proximal AIS (Lorincz & Nusser, 2008). Given this arrangement, both Nav1.1 and Nav1.6 subunits may contribute to the Na^+ channel currents we have recorded from SCs. Whether these subunits are also expressed in the dendrites has not be formally investigated, although SC dendrites are apparently devoid of Na^+ channels (Myoga *et al.*, 2009). It is curious that the expression pattern of the delayed rectifier K^+ channel subunits, Kv1.1 and 1.2, overlap with Nav1.6 subunits, but yet, are not subject to modulation following patch breakthrough (see Figure 1.8). This observation suggests that the signaling pathway(s) that promotes gating shifts in Na^+ channels is tightly compartmentalized from other ion channels, such as Kv1.1 and 1.2, even within the AIS.

Gating shifts in Na^+ channel activation and inactivation, as observed in the present study (see Figure 1.9) may, in principle, be mediated by a number of mechanisms that include direct binding by cytosolic Ca^{2+}, binding of the Ca^{2+}-calmodulin complex and/or changes in the phosphorylation state of the Na^+ channel (Cantrell & Catterall, 2001; Van Petegem *et al.*, 2012). Regulation of recombinant Nav1.6 channels has primarily focused on the effect of channel phosphorylation where protein kinase A (PKA) stimulation (Chen *et al.*, 2008) and p38 mitogen-activated protein kinase (Wittmack *et al.*, 2005) both cause a reduction in peak Na^+ channel

current. In the latter case, the reduction in current density did not affect channel gating (Wittmack *et al.*, 2005), unlike the present study (cf. Fig 8) but was due to the internalization of Nav1.6 channels (Gasser *et al.*, 2010). In contrast, inhibition of glycogen-synthase kinase 3β (GSK3β) causes a decrease in recombinant Nav1.6 responses (Scala *et al.*, 2018) suggesting that phosphorylation sustains channel activity in HEK 293 cells. Likewise, in medium spiny neurons of the nucleus accumbens, regulation of GSK3β activity impacts firing rates in a Nav1.6-dependent manner (Scala *et al.*, 2018) suggesting that phosphorylation and dephosphorylation events may be critical in fine-tuning neuronal output. Much less is known about the regulation of Nav1.1 channels, although, earlier recombinant studies and more recent proteomic work has identified putative phosphorylation sites which often overlap with sites identified for Nav1.2 channels (Smith & Goldin, 1998; Berendt *et al.*, 2010). Interestingly, forskolin activation of PKA causes a hyperpolarizing shift in both the activation and inactivation curves for recombinant Nav1.1 (Liu & Zheng, 2013) as observed in the present study on cerebellar SCs. An identical gating shift is observed in hippocampal CA1 pyramidal cells, probably mediated by Nav1.2 channels, that is triggered by NMDA receptor activation and the activity of CaMKII (Xu *et al.*, 2005). Given the similarity in how Nav1.1 and Nav1.2 channels are regulated by phosphorylation, it would be interesting to test if a NMDA receptor-mediated signaling pathway could induce a similar shift in the gating behavior of Na^+ channels in cerebellar SCs. Likewise, experiments using dynamic clamp to test the effect of a Nav channel gating model on SC excitability would be interesting to test in future studies.

Multiple families of voltage-gated ion channels control stellate cell excitability

Although SCs express a variety of voltage-gated ion channels, somatodendritic A-type K^+ channels are an important regulator of their firing rates (Molineux *et al.*, 2005; Anderson *et al.*, 2010a; Anderson *et al.*, 2013). Specifically, AP firing rates are regulated by Kv4.2/4.3 subunits whose basal activity is fine-tuned by elevations in cytosolic Ca^{2+} mediated by the Ca^{2+} channel subunits, Cav3.2 and 3.3 (Anderson *et al.*, 2010a). Both ion channel families form a signaling complex through the modulatory protein, KChIP3, which contains an EF hand domain and thus is able to act as a Ca^{2+} sensor that couples the activity of Ca^{2+} channels to the regulation of K^+ channels (Pongs & Schwarz, 2010). Elevations in intracellular Ca^{2+} selectively promote depolarizing shifts in steady-state inactivation of A-type K^+ channels and, in doing so, attenuate membrane depolarization and AP firing (Anderson *et al.*, 2010a; Anderson *et al.*, 2013). In contrast, our data establish that A-type K^+ channels contribute to an *increase* in AP firing of SCs via a hyperpolarizing shift in channel activation and inactivation (see Figure 1.7). Although the formation of the whole-cell recording is likely to elevate cytosolic Ca^{2+} in SCs, as discussed above, the shifts A-type K^+ channel gating observed in this study are probably not reliant on KChIP3 modulation. Finally, although other voltage-gated ion channels may be involved in controlling SC excitability, pharmacological block of many of these channels (Figure 1.10) reveals that they do not impact AP threshold. Consequently, our work identifies a predominant role of voltage-gated Na^+ channels in upregulating the firing rates of cerebellar SCs.

AUTHOR CONTRIBUTIONS

R.P.D.A., A.K. and D.B. designed research; R.P.D.A., J.M. and V.S. performed research and analyzed data; R.P.D.A., A.K. and D.B. wrote the paper.

ACKNOWLEDGEMENTS

This research was supported by Canadian Institutes of Health Research Operating Grants MOP 142431 to D. Bowie. and a National Natural Sciences and Engineering Research Council of Canada (NSERC) Discovery Grant to A. Khadra. R.P.D. Alexander was funded by a NSERC CGS-D doctoral fellowship. We thank members of the Bowie laboratory for comments on the manuscript and Z. Nusser for discussions on sodium channel expression patterns.

CHAPTER 2

Patch clamp hijacks intrinsic plasticity in cerebellar stellate cells

FOREWORD TO CHAPTER 2

As stated in the foreword to Chapter 1, significant portions of the data included in Chapter 2 were collected during the same period as the first chapter. The main criticism from colleagues was that the effect was simply not relevant or realistic to an intact physiological system, so of course my main goal was to show some evidence to the contrary. Other groups had previously shown the importance of free cytosolic Ca^{2+} in regulating cerebellar neuronal excitability (Gall *et al.*, 2003), so that was an obvious link to make. Moreover, the fact that blockade of intracellular kinase activity could stabilize SC AP firing was a major early clue that patch clamp was overriding a signaling mechanism normally invoked by a physiological stimulus. Later we showed that Ca^{2+} and CaMKII also could influence Nav channel gating behaviour. Induction of intrinsic plasticity via NMDA receptor stimulation had previously been demonstrated in multiple cerebellar neurons (Aizenman & Linden, 2000; Armano *et al.*, 2000), and the fact that Ca^{2+} and CaMKII were also involved provided good support for this receptor being a suitable trigger for this mechanism.

Article title:

NMDA receptor signaling to voltage-gated Na^+ channels mediates intrinsic plasticity in cerebellar stellate cells

Reproduced with permission from Ryan P.D. Alexander and Derek Bowie.
NMDA receptor signaling to voltage-gated Na^+ channels mediates intrinsic plasticity in cerebellar stellate cells. 2019.
To be submitted to **Journal of Neuroscience**.

ABSTRACT

Intrinsic plasticity is one of the strategies used by neurons to encode stimulus information across time. Activity-dependent changes in voltage-gated ion channel activity either locally or globally fine-tunes the likelihood of postsynaptic action potential (AP) firing in response to subsequent input. Although demonstrated in other types of cerebellar neurons, whether intrinsic plasticity mechanisms are present in molecular layer interneurons (MLIs) remains unknown. Here we show that NMDA receptor signaling, already involved in other kinds of synaptic plasticity in these cells, also mediates a long-lasting increase in AP firing in cerebellar stellate cells (SCs). As described in our previous study, whole-cell recording in SCs initiates a gradual hyperpolarization of AP threshold over time that depends on shifts in voltage-gated Na^+ channel (Nav) gating properties. Perforated patch and calcium chelation experiments reveal that AP threshold hyperpolarization is independent of whole-cell dialysis. We find that the SC threshold decrease depends on intracellular calcium as well as the activity of protein kinases. We then demonstrate that CaMKII activity ultimately results in a negative shift in voltage-gated Na^+ channel (Nav) gating properties, but not A-type K^+ channels. Cell-attached electrophysiological recordings demonstrate that NMDA receptor stimulation causes an upregulation of spontaneous firing in a Ca^{2+}- and CaMKII-dependent manner. These findings uncover a previously uncharacterized mode of Nav-dependent intrinsic plasticity in cerebellar MLIs and provides an unconventional mechanism for fine-tuning motor behavior.

INTRODUCTION

Plasticity of intrinsic excitability, or intrinsic plasticity, has been proposed as a regulatory tool employed by neurons that functions together with more localized synapse modulation to preserve information in the brain over long timescales (Daoudal & Debanne, 2003; Zhang & Linden, 2003). Long-term changes in voltage-gated ion channel activity have been observed in many systems and scenarios: in neuronal cultures after a period of activity-deprivation (Turrigiano *et al.*, 1994; Desai *et al.*, 1999), in neocortical pyramidal neurons (Sourdet *et al.*, 2003), hippocampal pyramidal neurons (Brager & Johnston, 2007), as well as basket cells (Campanac *et al.*, 2013) in response to afferent stimulation, and as a direct result of memory consolidation in the hippocampus (Moyer *et al.*, 1996; Thompson *et al.*, 1996). Other studies have observed a persistent upregulation of action potential (AP) firing in various cerebellar neurons such as granule cells (Armano *et al.*, 2000), Purkinje cells (Belmeguenai *et al.*, 2010), Golgi cells (Hull *et al.*, 2013), and in the deep cerebellar nuclei (Aizenman & Linden, 2000). However, relatively little is known about intrinsic plasticity in the molecular layer interneurons (MLIs).

Basket and stellate cells (SCs), known collectively as MLIs, are GABAergic interneurons that provide hyperpolarizing input to Purkinje cells and feedforward inhibition to other MLIs. These neurons have properties, specifically, short membrane time-constant and rapid spike initiation (Clark & Cull-Candy, 2002; Jorntell & Ekerot, 2003), that make them optimal for providing fast and precise spike output to their downstream partners. Activity in these neurons has been associated with vestibulo-oculomotor reflex gain (Wulff *et al.*, 2009), oromotor rhythm tuning (Astorga *et al.*, 2017; Gaffield & Christie, 2017), and shaping cutaneous receptive fields *in vivo* (Jorntell & Ekerot, 2003). More recently it has been shown that activity in these neurons

directly controls the plasticity valence of parallel fiber EPSPs on Purkinje cells, which has a direct impact on motor learning (Rowan *et al.*, 2018). Many types of input shape the firing rates of MLIs, but relatively little is known about long-term, activity-dependent regulatory processes that control their global membrane excitability, especially with respect to voltage-gated Na^+ channels.

Intrinsic plasticity via Na^+ channel modulation is relatively rare in the central nervous system but has been observed in pyramidal neurons in the prefrontal cortex (Maurice *et al.*, 2001; Carr *et al.*, 2002; Carr *et al.*, 2003) and hippocampal CA1 (Xu *et al.*, 2005). Our previous study identified and characterized an upregulation of cerebellar SC excitability that is underpinned by a hyperpolarizing AP threshold caused by a left-shift in biophysical properties of voltage-gated Na^+ channels (Alexander *et al.*, 2019). Although this phenomenon was apparently induced by patch clamp recording itself, we wanted to investigate the underlying cellular signaling that was responsible for this effect and ask whether it could be invoked using more physiologically-relevant stimuli. To that end, we demonstrate here that the hyperpolarization of AP threshold observed in SCs during patch clamp recording is dialysis-independent, relies upon intracellular Ca^{2+}, and is ultimately effected by CaMKII activation. Furthermore, by providing a stable baseline excitability via loose-seal cell-attached electrophysiology, we find that long-term intrinsic plasticity can be induced by NMDA receptor stimulation in a Ca^{2+} and CaMKII-dependent manner. These results demonstrate a previously undescribed, NMDA receptor-mediated form of intrinsic plasticity in cerebellar MLIs.

METHODS

Ethical approval

All experiments were performed in accordance with the guidelines of the Canadian Council on Animal Care and were approved by the Animal Care Committee of McGill University.

Animals

Wild-type mice with a C57BL/6J background were obtained from Charles River Laboratories (Wilmington, MA, USA) and maintained as a breeding colony at McGill University. Both male and female wild-type mice used for experiments ranged from postnatal days 18 to 30.

Slice preparation

Mice were anesthetized with isoflurane and immediately decapitated. A block of cerebellar vermis was rapidly dissected from the mouse head and submerged in ice-cold cutting solution perfused with carbogen gas (95% O_2, 5% CO_2). Cutting solution contains (in mM): 235 sucrose, 2.5 KCl, 1.25 NaH_2PO_4, 28 $NaHCO_3$, 0.5 $CaCl_2$, 7 $MgCl_2$, 28 D-glucose, 1 ascorbic acid, 3 sodium pyruvate (pH 7.4; 305–315 mOsmol/L). The block of vermis is then fastened to a platform, transferred to the slicing chamber and again submerged in ice-cold cutting solution, bubbled with carbogen throughout the remainder of the procedure. Thin slices of cerebellar vermis (300 µm) were obtained with a vibrating tissue sectioner (Leica VT1200; Leica Instruments, Nussloch, Germany). The slices were transferred to oxygenated artificial cerebrospinal fluid (ACSF) and held at room temperature (21°C-23°C) for at least 1 h before recordings were performed. ACSF contained the following (in mM): 125 NaCl, 2.5 KCl, 1.25 NaH_2PO_4, 26 $NaHCO_3$, 2 $CaCl_2$, 1 $MgCl_2$, 25 D-glucose (pH of 7.4; 305–315 mOsmol/L).

Electrophysiology

Slice experiments were performed on an Olympus BX51 upright microscope (Olympus, Southall, UK) equipped with differential interference contrast/infrared optics. Whole-cell patch clamp recordings were made from either visually-identified stellate, granule or Purkinje cells in acute sagittal slices of cerebellar vermis. Stellate cells which were distinguished from misplaced or migrating granule, glial or basket cells by their small soma diameter (8–9 µm), location in the outer two-thirds of the molecular layer and whole-cell capacitance measurement (4-12 pF). Patch pipettes were prepared from thick-walled borosilicate glass (GC150F-10, OD 1.5 mm, ID 0.86 mm; Harvard Apparatus Ltd, Kent, UK) and had open tip resistances of 4–7 MΩ when filled with an intracellular recording solution. Recordings were made with a Multiclamp 700A amplifier (Molecular Devices, Sunnyvale, CA, USA) at a holding potential of -70 mV. Series resistance and whole-cell capacitance were estimated by cancelling the fast transients evoked at the onset and offset of brief (10 ms) 5 mV voltage-command steps. Access resistance during whole-cell recording (7–25 MΩ) was compensated between 60 and 80% and checked for stability throughout the experiments (~15% tolerance). The bath was continuously perfused at room temperature (21–23 °C) with ACSF at a rate of 1–2 mL/min. Currents were filtered at 5 kHz with an eight-pole low-pass Bessel filter (Frequency Devices, Haverhill, MA, USA) and digitized at either 25 or 100 kHz with a Digidata 1322A data acquisition board and Clampex 10.1 (Molecular Devices) software. For voltage clamp recordings, the online P/N leak-subtraction suite in Clampex 10.1 was used to assess voltage-gated responses, and raw current traces were collected simultaneously.

Perforated-patch recordings were obtained in the same external ACSF described above. Amphotericin B powder was dissolved in DMSO the day of the experiment at a concentration of 60 mg/mL. This stock solution was added to an aliquot of internal pipette solution at a concentration of 300 μg/mL. Borosilicate patch electrodes (4–6 MΩ) were first dipped in an antibiotic-free internal solution for a few seconds, followed by back-filling with the amphotericin B-containing internal solution.

For recording voltage-dependence of activation of I_A, a protocol was applied consisting of 500 ms steps evoked from a holding potential of -100 mV, ranging from -100 mV to +20 mV in 10 mV increments. An inactivation protocol was applied consisting of 500 ms prepulse steps ranging from -120 mV to -30 mV in 5 mV increments, followed by a probe step to -20 mV to assess channel availability. For recording voltage-dependence of activation of I_{Na}, a 'pre-pulse' protocol (Milescu *et al.*, 2010) consisting of a suprathreshold step from -80 mV to -35 mV in order to evoke an action current, followed by a ~1 ms step to -60 mV, followed by steps ranging from -80 mV to +30 mV in 5 mV increments. To measure steady-state channel availability, an inactivation protocol consisting of 100 ms steps ranging from -110 mV to -20 mV in 5 mV increments, followed by a probe step to -20 mV.

Recording solutions

All chemicals were obtained from Sigma Aldrich (St. Louis, MO, USA) unless otherwise indicated. Internal pipette solution for most current clamp experiments contained (in mM): 126 K-gluconate, 5 HEPES, 4 NaCl, 15 D-glucose, 0.05 $CaCl_2$, 1 $MgSO_4$, 0.15 K_4-BAPTA, 3 Mg-ATP, 0.1 Na-GTP (adjusted to pH 7.4 with KOH, 300-310 mOsmol/L). For current clamp experiments with

high internal BAPTA, K_4-BAPTA was increased to 10 mM and K-gluconate reduced to 110 mM. For current clamp recordings obtained using perforated-patch, internal pipette solution was supplemented with 1 mM Lucifer Yellow to verify integrity of the plasma membrane post-recording. Pipette solution for voltage clamp experiments examining A-type K^+ current (I_A) contained (in mM): 140 KCl, 10 HEPES, 2.5 $MgCl_2$, 0.15 K_4-BAPTA (adjusted to pH 7.4 with KOH, 300-310 mOsmol/L). For these experiments the external ACSF was supplemented with 5 mM TEA-Cl and 2 mM CsCl to block non-I_A-mediating K^+ channels, and 100 nM TTX to block firing. Pipette solution for voltage clamp experiments examining transient Na^+ current (I_{Na}) contained (in mM): 110 Cs-methanosulfate, 5 HEPES, 4 NaCl, 15 D-glucose, 0.05 $CaCl_2$, 0.15 Cs_4-BAPTA, 4 Mg-ATP, 0.1 Na-GTP, 10 TEA-Cl, 10 4-AP (adjusted to pH 7.4 with CsOH, 300-310 mOsmol/L). For the experiments isolating I_{Na}, the external ACSF was supplemented with 100 µM $CdCl_2$ and 1 µM Mibefradil dihydrochloride (Tocris Bioscience, Ellisville, MO, USA) to block voltage-gated calcium channels. BAPTA-AM (Abcam, Cambridge, UK) was used to incubate slices in a membrane-permeable Ca^{2+} chelator. For cell-attached experiments, internal solution contained (in mM): 125 NaCl, 10 HEPES, 40 D-Glucose, 2.5 $MgCl_2$ (adjusted to pH 7.4 with NaOH, 300-310 mOsmol/L). Except where indicated, all experiments were performed in the presence of fast excitatory and inhibitory synaptic blockers: NMDA receptor antagonist D-(-)-2-Amino-5 phosphonopentanoic acid (D-APV; 10 µM), AMPA/kainate receptor antagonist 2,3-Dioxo-6-nitro-1,2,3,4-tetrahydrobenzo[f]quinoxaline-7-sulfonamide (NBQX; 10 µM), and GABA-A receptor antagonist bicuculline (BIC; 10 µM) were purchased from Abcam (Cambridge, UK).

Data analysis and statistics

Voltage-dependence of activation for all current types was analyzed by first calculating conductance (G) values from the peak currents elicited by each respective activation protocol using the formula:

$$G_x = \frac{I_x}{V_m - V_{rev_x}}$$

where I_x is the peak current of current type x (ie. I_A, I_K, I_{Na}) evoked at membrane potential V_m, and V_{rev_x} is the reversal potential of current type x. Conductance-voltage relationships for each current type were then fit to a Boltzmann function using the formula:

$$G_x = \frac{G_{max}}{(1 + (\exp(V_{1/2} - V_m)/k))}$$

where G_x is the conductance at membrane potential V_m for current type x, G_{max} is the maximum conductance for current type x, $V_{1/2}$ is the membrane potential where G_x is 50% of G_{max}, and k is the slope factor. Boltzmann fits were performed for each time point in each cell in order to calculate normalized conductance values. Summary conductance-voltage relationships for each current type were calculated by averaging the normalized conductance values across all cells in the dataset. $V_{1/2}$ values reported in the Results section for each current type were calculated by fitting the normalized conductance averages.

Data are reported as mean +/- SEM. Significance was denoted with * $p < 0.05$, ** $p < 0.01$, and *** $p < 0.001$. All fitting was performed with Origin 7.0. Statistical analyses were performed using SPSS 17.0.

RESULTS

Cerebellar neurons exhibit differential patch-induced excitability changes

As characterized in our previous study, cerebellar SCs exhibit a time-dependent increase in firing behavior over tens of minutes of whole-cell patch clamp recording (Alexander *et al.*, 2019). For example, AP frequency evoked by a 16 pA step significantly increased in SCs over a 25 minute recording (Figure 2.1A,B; 9.8 ± 2.9 Hz at baseline vs. 30.0 ± 5.6 Hz at 25 min; $t = 4.73$, $p < 0.001$; n = 11 cells), whereas AP frequency in response to a 100 pA step remained stable in Purkinje cells (4.0 ± 1.9 Hz at baseline vs. 2.3 ± 2.0 Hz at 25 min; $t = 0.69$, $p = 0.52$; n = 7 cells). Likewise, where SC AP threshold hyperpolarized significantly over 25 minutes (Figure 2.1C,D; -39.7 ± 1.0 mV at baseline vs. 48.1 ± 1.4 mV at 25 min; $t = 15.74$, $p < 0.001$; n = 12 cells), Purkinje cell AP threshold remained stable (-48.6 ± 1.5 mV at baseline vs. -49.5 ± 1.4 mV at 25 min; $t = 0.73$, $p < 0.51$; n = 5 cells). We next wanted to investigate the signaling events that are necessary for AP threshold hyperpolarization in SCs.

Perforated patch recordings demonstrate dialysis-independent threshold hyperpolarization

To confirm that internal solution dialysis was not responsible for the change in AP threshold, we aimed to investigate cerebellar SC firing with minimal disruption to the intracellular compartment. To that end, we performed perforated patch recordings to avoid cytoplasm washout artifacts observed in other whole-cell recording paradigms (Kato *et al.*, 1993). Lucifer Yellow (1 mM) was added to the internal solution in order to verify that the membrane patch did not rupture during recording (Figure 2.2B; see also (Kass & Mintz, 2006)).

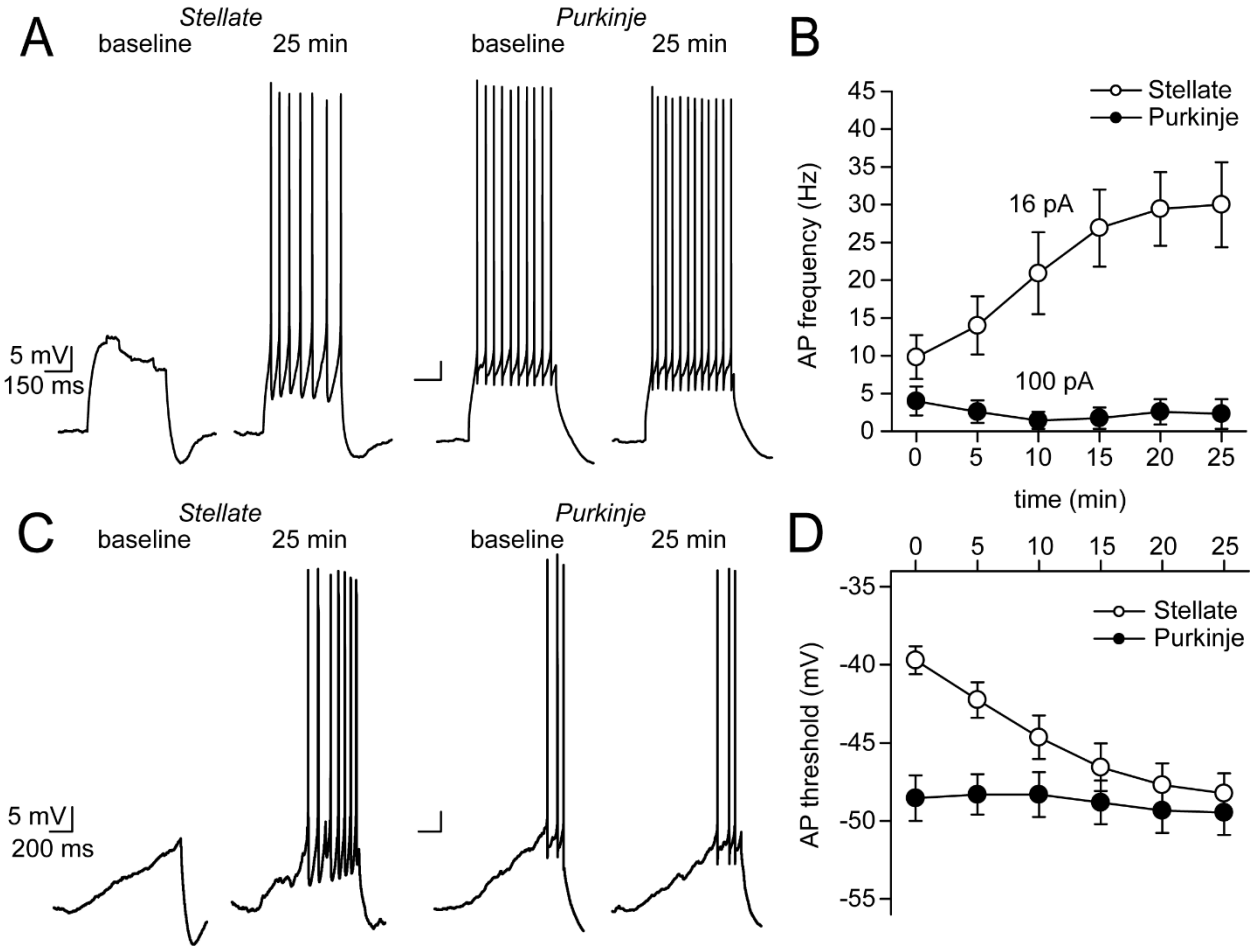

Figure 2.1 Cerebellar stellate cells, and not Purkinje cells, exhibit excitability increases during patch clamp recording (A) Step-evoked AP firing in example stellate and Purkinje cells at baseline and after 25 minutes of whole-cell patch clamp recording. Scale bars indicate 5 mV and 150 ms. **(B)** Time course plot of averaged AP frequency evoked by one example step amplitude for stellate (16 pA) and Purkinje cells (100 pA). **(C)** Example current clamp responses evoked by ramp protocol at baseline (left) and after 25 minutes (right) in a stellate and Purkinje cell. Scale bars indicate 5 mV and 200 ms. **(D)** Summary plot depicting change in AP threshold over time in stellate and Purkinje cells. Data taken from Figures 1.1 and 1.2.

Using this approach, SC excitability initially appeared to remain stable over the duration of the recording. For example, the number of APs evoked by a 16 pA step current did not significantly change over a 25 minute recording duration (Figure 2.2A; 10.2 ± 4.2 at baseline vs. 10.6 ± 3.9 at 25 min; t = 0.43, p = 0.69; n = 5 cells). In agreement with this, although the AP threshold did hyperpolarize over time (Figure 2.2C; -49.4 ± 1.8 at baseline vs. -52.2 ± 1.9 mV at 25 min; t = 4.10, p = 0.015; n = 5 cells), the extent of the time-dependent decrease was

significantly reduced compared to control (Figure 2.2C; Δ-2.8 ± 0.7 mV for perforated patch vs. Δ-8.3 ± 0.6 mV for control; $t = 6.00$, $p < 0.001$; perforated patch: n = 5 cells, control: n = 11 cells). However, comparing the mean AP threshold for each recording condition shows that the baseline threshold measurements in perforated patch were significantly hyperpolarized compared to control whole-cell configuration (Figure 2.2C; -49.4 ± 1.8 mV for perforated patch vs. -39.5 ± 1.0 mV for control; $t = 5.16$, $p < 0.001$; perforated patch: n = 5 cells, control: n = 11 cells). When considering the nature of the experimental approach, the term 'baseline' is more variable in the perforated patch condition than in the control whole-cell group. During whole-cell recording, from seal formation to patch breakthrough to capacitance compensation to first protocol initiation, a baseline measurement can be obtained after roughly 1 minute. Once the seal is achieved at the start of a perforated patch recording, the antibiotic works on the timescale of 5 – 15 minutes, creating small pores in the neuronal membrane through which electrical access to the intracellular compartment is obtained (Linley, 2013). Because of the necessary delay to optimize access resistance, the duration of time between initial seal formation and baseline AP threshold measurement was variable. To that end, we tested the degree of correlation between these two variables across all configuration modes, including the unintentionally ruptured patches (see Figure 2.2B). We found a significant negative relationship between time delay post-seal and baseline threshold (Figure 2.2D; Pearson's $r = -0.70$, $p = 0.002$; n = 17 cells), demonstrating that threshold hyperpolarization proceeds regardless of configuration.

This is important because it suggests further that there is a pre-whole-cell trigger, independent of solution dialysis, that causes a gradual decrease in AP threshold in SCs.

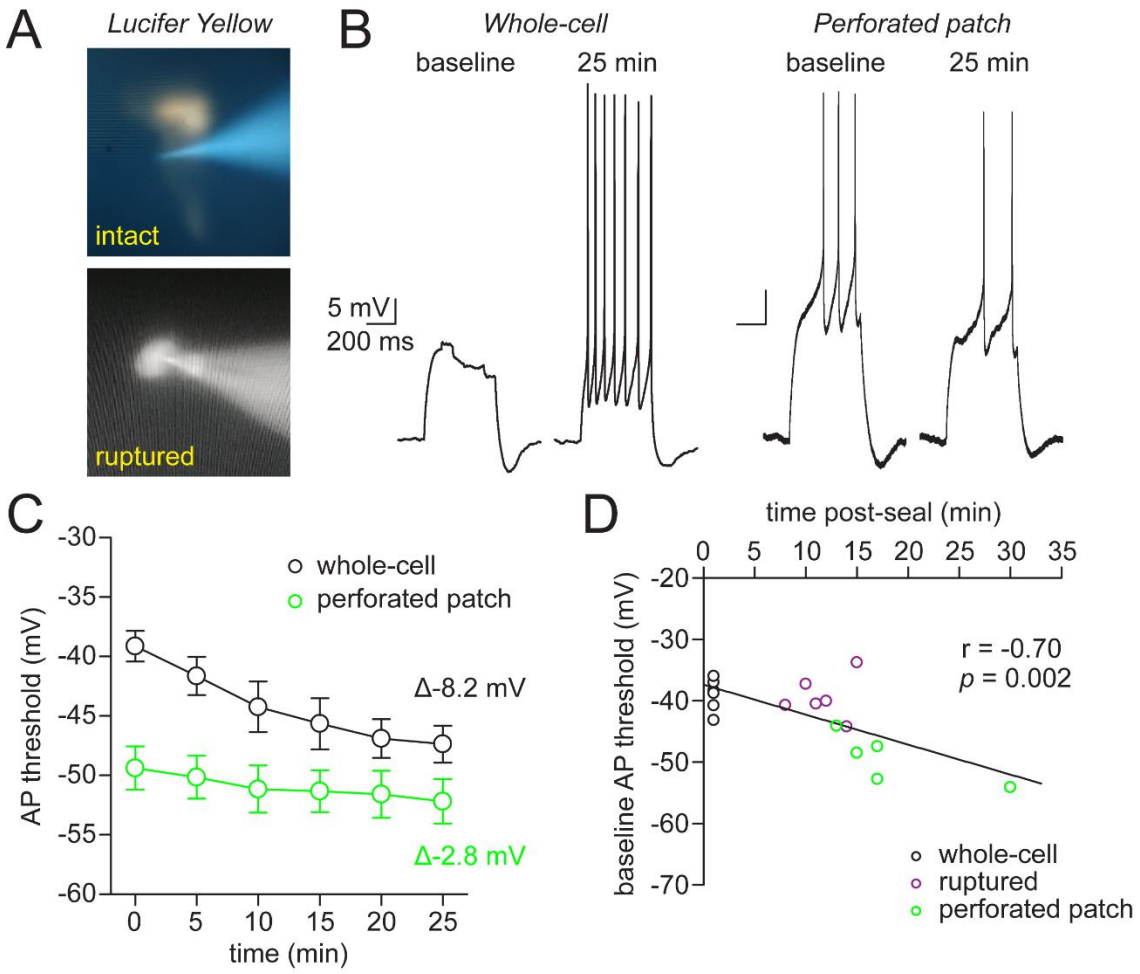

Figure 2.2 Perforated patch recordings demonstrate dialysis-independent AP threshold decrease
(A) Example current clamp traces from a stellate cell recorded in perforated patch configuration depicting APs evoked by step and ramp protocols, respectively, over a 25 minute duration. **(B)** Example images of ruptured or 'spontaneous whole-cell' and perforated patch configuration of neurons in slice, visualized using Lucifer Yellow dye. **(C)** Summary plot of AP threshold over time comparing whole-cell to perforated patch data. **(D)** Regression analysis demonstrates a significant relationship between time post-seal and AP threshold measured at baseline, regardless of configuration.

AP threshold hyperpolarization in stellate cells depends on intracellular Ca^{2+}

To understand the sequence of events that give rise to this experimentally-induced phenomenon, we sought to identify the intracellular signals necessary for its induction. Other studies have noted increases in cytosolic Ca^{2+} as a result of plasma membrane distension, either through changes in bath osmotic pressure or via patch electrode (Chavas *et al.*, 2004; Alcami *et*

al., 2012). To address this possibility, we included a saturating concentration (10 mM) of the Ca^{2+} chelator BAPTA in the patch pipette and performed current clamp experiments to measure AP threshold over time.

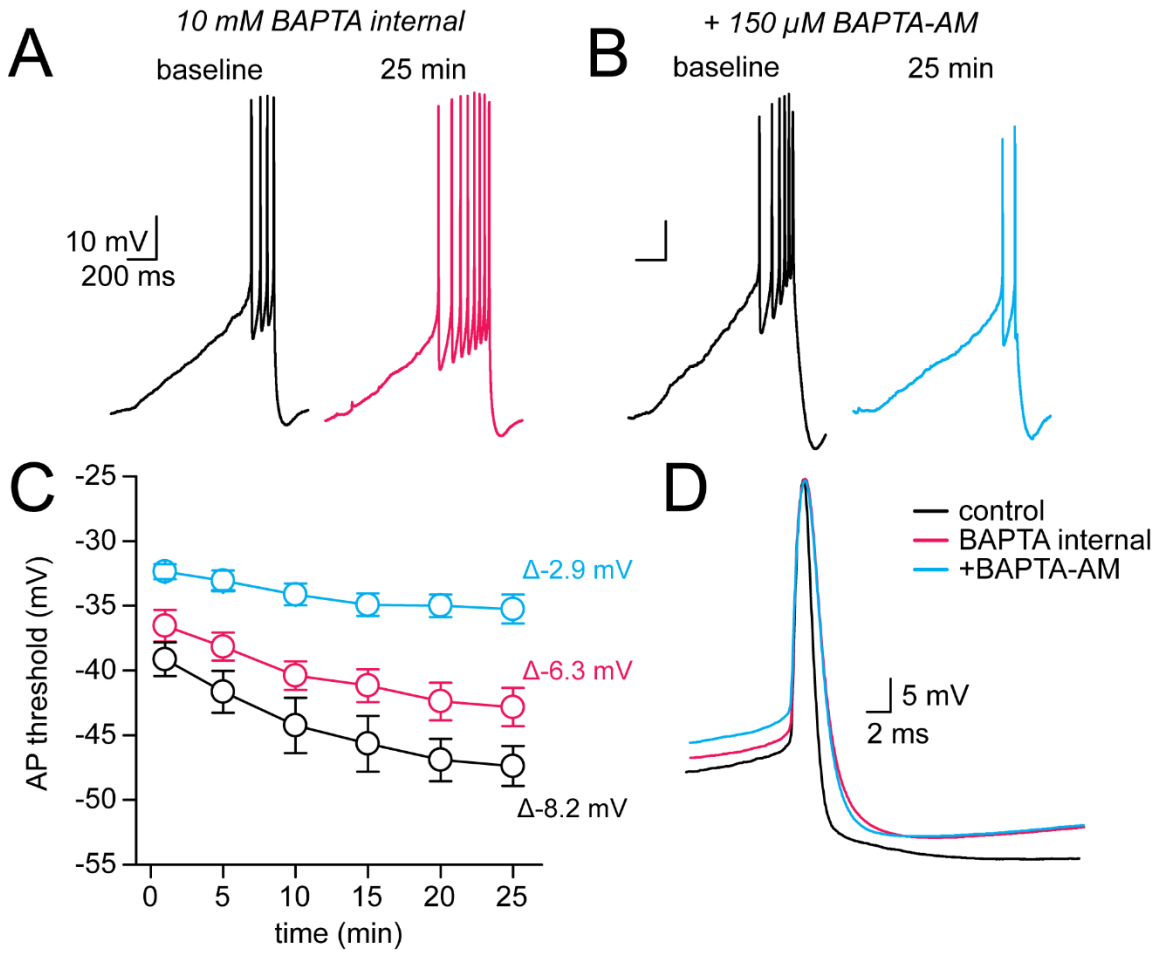

Figure 2.3: Timing of cytosolic Ca^{2+} chelation has graded effects on AP threshold hyperpolarization
(A,B) Example stellate cell traces recorded in the presence of saturating BAPTA (10 mM) either without incubation in 150 µM BAPTA-AM (A) or with incubation (B) at the start and end of a 25 minute recording. Scale bars indicate 10 mV and 200 ms. **(C)** Summary time course AP threshold data of both high internal BAPTA and BAPTA-AM conditions compared to control. **(D)** Early vs. pre-emptive Ca^{2+} chelation has graded effects on basal AP properties.

AP threshold hyperpolarized significantly over a 25 minute recording duration (Figure 2.3A,C; -36.6 ± 1.2 mV at baseline vs. -42.8 ± 1.5 mV at 25 min; t = 6.12, p = 0.0036; n = 5 cells), but to a lesser degree than in control cells (Figure 2.3C; Δ-8.3 ± 0.6 mV for control vs. Δ-6.3 ± 1.0 mV for 10 mM BAPTA internal; t = 2.11, p = 0.052; control: n = 11 cells, BAPTA internal: n = 5

cells). Although there seemed to be an attenuation on amount of threshold hyperpolarization compared to control, we wanted to test the possibility that a cytosolic Ca^{2+} increase is evoked prior to patch breakthrough. To accomplish this, cerebellar slices were incubated in ACSF containing the membrane-permeable chelator BAPTA-AM (150 µM) for at least 1 hour before recordings were attempted. This would pre-buffer cytosolic free Ca^{2+}, and potentially make the neuron less susceptible to long-term downstream effects of unintentional Ca^{2+} increases. Current clamp recordings on stellate cells after incubation in BAPTA-AM yielded a stronger attenuation of the time-dependent AP threshold decrease compared to control cells (Figure 2.3B,C; Δ-2.9 ± 0.9 mV for BAPTA-AM vs. Δ-8.3 ± 0.6 mV for control; $t = 5.83$, $p < 0.001$; BAPTA-AM: n = 7 cells, control: n = 11 cells). These observations both suggest that intracellular Ca^{2+} plays an important role in AP threshold hyperpolarization, but that the effects of Ca^{2+} chelation are graded and depend on timing. 'Early' (pre-whole-cell) chelation has a stronger attenuation on threshold than 'late' (post-whole-cell), arguing for a pre-breakthrough Ca^{2+} rise. Furthermore, the level of free cytosolic Ca^{2+} also influences AP threshold at baseline; the more complete the Ca^{2+} chelation treatment, the more depolarized the initial AP threshold (Figure 2.3C,D; $F = 16.79$, $p < 0.001$; one-way ANOVA).

Together these findings demonstrate the importance of intracellular Ca^{2+} in mediating the AP threshold hyperpolarization in SCs. They also suggest pre-dialysis, Ca^{2+}-mediated effects induced by patch clamp, in line with observations by previous groups (Chavas *et al.*, 2004; Alcami *et al.*, 2012). Since this ultimately is effected by regulation of voltage-gated channels, mainly Na^{+} channels (Alexander *et al.*, 2019), we wanted to probe the signaling pathway that targets these channels downstream of this patch-induced Ca^{2+} increase.

Protein kinases influence AP threshold hyperpolarization

Since protein phosphorylation has been demonstrated to be an important regulator of voltage-gated ion channel gating behavior (Levitan, 1994), we decided to probe the role of kinase activity in AP threshold hyperpolarization in SCs. When the broad-spectrum kinase inhibitor staurosporine (2 μM) was included in the internal solution and perfusing ACSF, SC AP threshold still significantly decreased over a 25 minute recording (Figure 2.4A-B, left; -39.0 ± 1.0 mV at baseline vs. -42.7 ± 1.3 mV at 25 min; t = 5.34, p = 0.0018; n = 7 cells), but the extent of hyperpolarization was significantly attenuated compared to control (Δ-3.7 ± 0.7 mV for staurosporine vs. Δ-8.3 ± 0.6 mV for control; t = 5.40, p < 0.001; staurosporine: n = 7 cells, control: n = 11 cells). This finding implicated protein kinase activity in general in the threshold decrease, but we next wanted to identify the specific kinases involved.

We blocked cAMP-dependent kinase (PKA) activity by first incubating the slice for at least 1 hour in the membrane-permeable inhibitor fragment PKI 14-22 amide (0.5 μM) while also including PKI 6-22 amide (5 μM) in the internal solution. Using these PKA inhibitors, we did not observe a hyperpolarizing AP threshold over time (Figure 2.4A-B, middle left; -36.8 ± 1.2 mV at baseline vs. -40.2 ± 2.2 mV at 25 min; t = 2.37, p = 0.077; n = 5 cells), which was significantly different from control SCs (Δ-3.4 ± 1.4 mV for PKI 6-22 vs. Δ-8.3 ± 0.6 mV for control; t = 4.15, p < 0.001; PKI 6-22: n = 5 cells, control: n = 11 cells). Blocking protein kinase C (PKC) function with Gö 6983 (1 μM) yielded little difference relative to control cells (Figure 2.4A-B, middle right; Δ-8.6 ± 1.5 mV for Gö 6983 vs. Δ-8.3 ± 0.6 mV for control; t = 0.05, p = 0.96; Gö 6983: n = 5 cells, control: n = 11 cells). Lastly, we used KN93 (5 μM) to selectively block CaMKII and although we observed a decrease in AP threshold (Figure 2.4A-B, right; -36.5 ± 0.2 mV at baseline vs. -39.5 ±

0.5 mV at 25 min; $t = 7.41$, $p < 0.001$; n = 6 cells), this was significantly attenuated compared to control (Δ-3.0 ± 0.4 mV for KN93 vs. Δ-8.3 ± 0.6 mV for control; $t = 6.70$, $p < 0.001$; KN93: n = 6 cells, control: n = 11 cells). Taken together, these data implicated the activity of certain protein kinases, namely PKA and CaMKII, in the AP threshold hyperpolarization seen in SCs during patch clamp recording. These observations in current clamp identified these kinases as the next step in the signaling pathway beginning with cytosolic Ca^{2+} rise and ending with VGIC modulation. We then wanted to use these same reagents in voltage clamp to verify that the pharmacological conditions uncovered in the previous experiments (ie. Ca^{2+} chelation and kinase inhibition) also prevent the shifts in gating properties of VGICs already shown to be present in SCs (Alexander *et al.*, 2019).

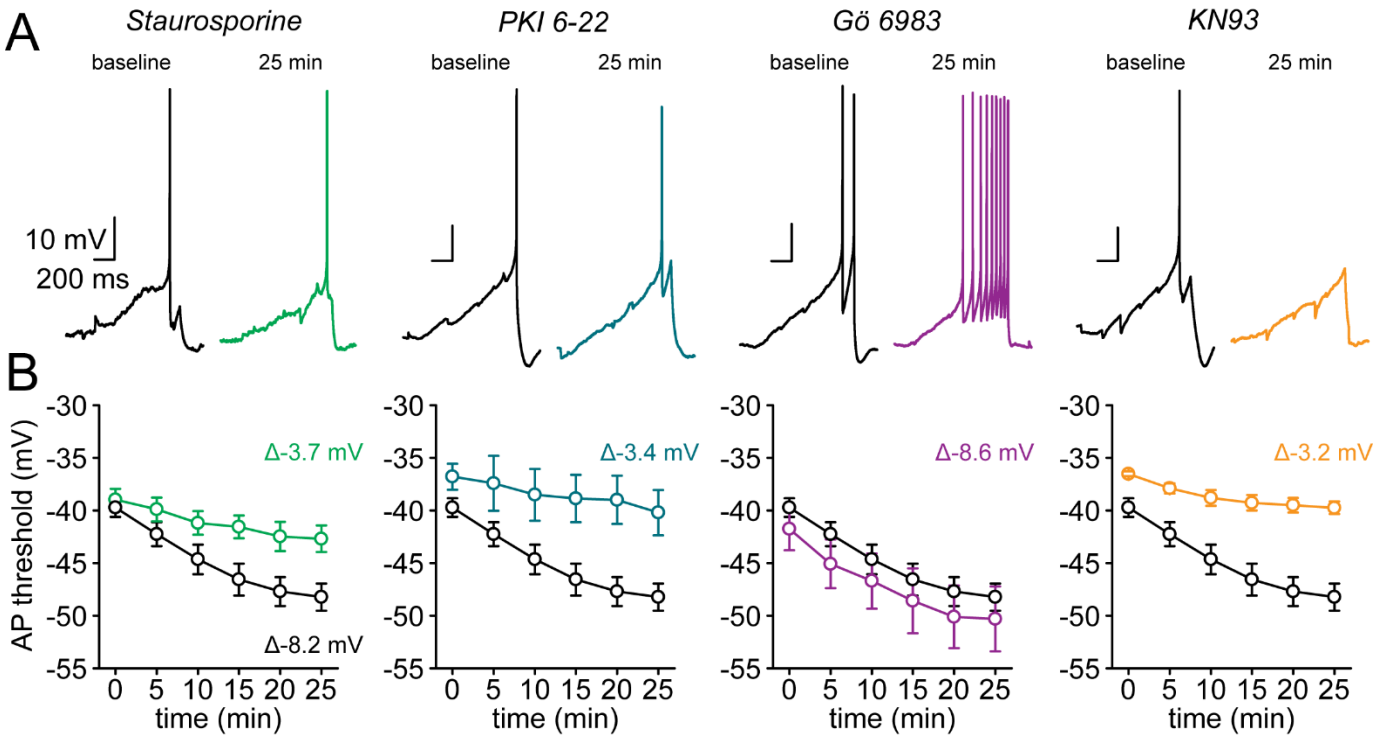

Figure 2.4: Downstream protein kinases influence AP threshold hyperpolarization
(A) Current clamp traces from example stellate cells in the presence of various protein kinase inhibitors. In each case the left trace is soon after patch breakthrough and the right trace is 25 minutes later. Staurosporine: non-specific kinase inhibitor; PKI 6-22: PKA inhibitor; Gö 6983: PKC inhibitor; KN93: CaMKII inhibitor. **(B)** Summary time course plots depicting AP threshold change in the presence of each kinase inhibitor compared to control.

Gating shifts in I_{Na} are regulated by Ca^{2+} and CaMKII

In our previous study, we showed that the excitability increase in cerebellar SCs (Figure 2.1) is primarily driven by a hyperpolarizing shift in the gating behaviour of voltage-gated Na^+ channels, but is further shaped by changing A-type K^+ channel properties (Alexander *et al.*, 2019). Although we provided multiple lines of evidence that the threshold decrease that underlies the excitability upregulation relies on Na^+ and not A-type K^+ channels, we wanted to test whether the specific kinases implicated above have a role in the K^+ channel shifts. To that end, we performed voltage clamp experiments isolating for the I_A in the presence of either PKI 6-22 or KN93. For PKI 6-22, there was not a significant attenuation of shift in voltage-dependence of activation (Figure 2.5B middle; Δ-11.4 ± 1.1 mV for PKI 6-22 vs. Δ-13.3 ± 3.3 mV for control; t = 0.52, p = 0.62; PKI 6-22: n = 6 cells, control: n = 7 cells) or inactivation (Δ-14.1 ± 0.9 mV for PKI 6-22 vs. Δ-15.8 ± 1.3 mV for control; t = 0.97, p = 0.36; PKI 6-22: n = 5 cells, control: n = 7 cells) compared to control. Likewise, KN93 did not significantly affect these shifts (Figure 2.5B right; activation: Δ-11.8 ± 1.9 mV for KN93 vs. Δ-13.3 ± 3.3 mV for control; t = 0.35, p = 0.73; inactivation: Δ-15.3 ± 1.8 mV for KN93 vs. Δ-15.8 ± 1.3 mV for control; t = 0.22, p = 0.83; KN93: n = 5 cells, control: n = 7 cells) compared to control. These findings suggest that the attenuation of AP threshold decrease in the presence of kinase inhibitors (Figure 2.4) was not a result of effects on the A-type K^+ current.

As described above, the threshold hyperpolarization in SCs is driven by negative shifts in Nav gating. If this is true, we should be able to prevent the changes in Nav biophysical properties seen in the control condition by chelating Ca^{2+} and blocking protein kinase activity. To investigate this, we performed voltage clamp experiments isolating for Na^+ current using the prepulse

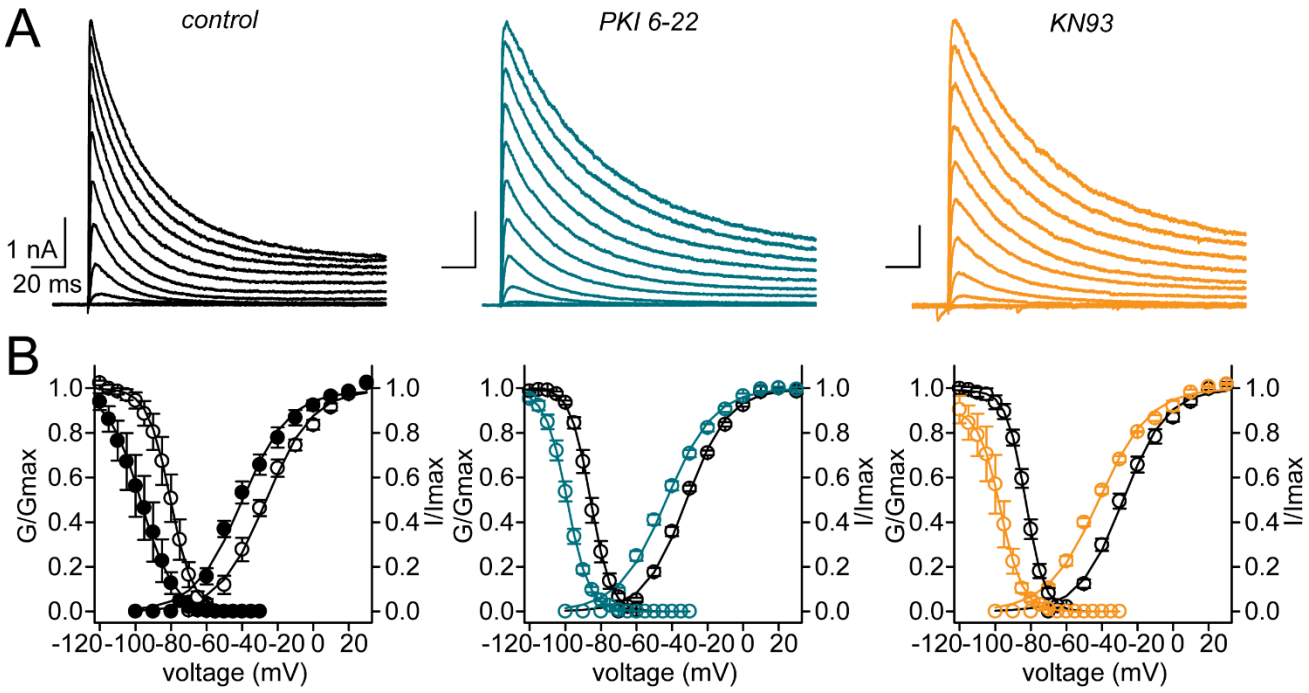

Figure 2.5 Kinase activity has no effect on gating shifts in I_A
(A) Voltage clamp traces of A-type K^+ current evoked during activation protocols. Left: control; center: PKI 6-22; right: KN93. **(B)** Superimposed voltage-dependence of activation and steady-state inactivation curves of in each pharmacological condition at baseline (open circles) and after 25 minutes (filled circles or coloured lines).

activation protocol adapted from Milescu *et al*. (2010) and used in our previous study (Alexander *et al.*, 2019). High concentration of BAPTA (10 mM) in the internal pipette solution yielded a shift of voltage-dependence of activation with a trend toward significance (Figure 2.6A left, B; -31.9 ± 0.7 mV at baseline vs. -36.7 ± 1.9 mV at 25 min; t = 2.64, p = 0.057; n = 5 cells) and a substantial shift in steady-state inactivation (-46.1 ± 1.3 mV at baseline vs. -52.9 ± 2.1 mV at 25 min; t = 7.22, p < 0.001; n = 6 cells) during patch clamp recording. There was a modest attenuation of $V_{1/2}$ activation shift compared to control (Figure 2.6C; Δ-4.8 ± 1.8 mV for BAPTA internal vs. Δ-7.7 ± 0.9 mV for control; Fisher's LSD, p = 0.082; BAPTA internal: n = 5 cells, control: n = 11 cells), but not with respect to inactivation (Figure 2.6D; Δ-6.8 ± 0.9 mV for BAPTA internal vs. Δ-8.1 ± 0.9 mV for control; Fisher's LSD, p = 0.28). Supplementing this high BAPTA internal by first incubating

slices in BAPTA-AM (150 µM) for at least 1 hour also produced a modest attenuation of $V_{1/2}$ activation compared to control (Figure 2.6A middle left, B middle left, C; Δ-5.5 ± 0.9 mV for BAPTA-AM vs. Δ-7.7 ± 0.9 mV for control; Fisher's LSD, p = 0.18; BAPTA-AM: n = 5 cells, control: n = 11 cells) but again not for steady-state inactivation (Figure 2.6D; Δ-6.8 ± 0.4 mV for BAPTA-AM vs. Δ-8.1 ± 0.9 mV for control; Fisher's LSD, p = 0.28). These findings suggest a small role for cytosolic Ca^{2+} on the shift of Nav activation, but the shift in inactivation is relatively Ca^{2+} independent. Inhibiting PKA had no effect on the shifts in both activation (Figure 2.6A middle right, B middle right, C; Δ-9.2 ± 1.6 mV for PKI 6-22 vs. Δ-7.7 ± 0.9 mV for control; Fisher's LSD, p = 0.34; PKI 6-22: n = 6 cells, control: n = 11 cells) and inactivation properties (Figure 2.6D; Δ-8.0 ± 1.1 mV for PKI 6-22 vs. Δ-8.1 ± 0.9 mV for control; Fisher's LSD, p = 0.90) with respect to control. The presence of external and internal KN93 to block the activity of CaMKII had a significant attenuating effect on the shifts of both voltage-dependence of activation (Figure 2.6A right, B right, C; Δ-4.3 ± 0.6 mV for KN93 vs. Δ-7.7 ± 0.9 mV for control; Fisher's LSD, p = 0.043; KN93: n = 5 cells, control: n = 11 cells) as well as inactivation (Figure 2.6D; Δ-4.2 ± 0.9 mV for KN93 vs. Δ-8.1 ± 0.9 mV for control; Fisher's LSD, p = 0.006) compared to control. These data demonstrate that CaMKII, but not PKA, is responsible for hyperpolarizing shifts in Nav gating behavior observed during patch clamp investigation.

Adding further complexity to the situation of Nav regulation in SCs, an analysis of the baseline absolute $V_{1/2}$ measurements in each pharmacological condition yields important qualifying information. First, there is no difference in baseline $V_{1/2}$ activation properties due to pharmacological manipulation (Figure 2.6C right; one-way ANOVA, $F_{4, 31}$ = 0.27, p = 0.90), suggesting that neither Ca^{2+} nor kinase activity has constitutive regulation of Nav activation in

SCs. There was, however, a significant group difference between conditions with respect to baseline $V_{1/2}$ inactivation (Figure 2.6D right; one-way ANOVA, $F_{4, 33} = 14.81$, $p < 0.001$). Specifically, $V_{1/2}$ activation was significantly depolarized at baseline for both high BAPTA internal (-46.1 ± 1.3 mV for BAPTA internal vs. -49.3 ± 0.7 mV for control; Fisher's LSD, $p = 0.019$) as well as BAPTA-AM (-43.9 ± 1.3 mV for BAPTA-AM vs. -49.3 ± 0.7 mV for control; Fisher's LSD, $p < 0.001$) conditions compared to control. Conversely, baseline $V_{1/2}$ inactivation was significantly hyperpolarized compared to control in the presence of KN93 (-54.4 ± 1.0 mV for KN93 vs. -49.3 ± 0.7 mV for control; Fisher's LSD, $p < 0.001$). These data suggest that there is constitutive regulation of Nav steady-state inactivation characteristics at rest in SCs, which complicates the interpretation of this experiment.

Regardless, these findings overall demonstrate that both Ca^{2+} and CaMKII have some influence of the shift of Nav gating behavior. We next sought to ask whether this kinase-mediated Nav-driven AP threshold hyperpolarization that can be induced by patch clamp in SCs could be overriding intracellular signaling components that are in fact triggered by another, more physiologically-relevant stimulus *in vivo*. To address this, we needed to first provide a stable baseline for measuring SC firing rates upon which a candidate induction stimulus could be applied.

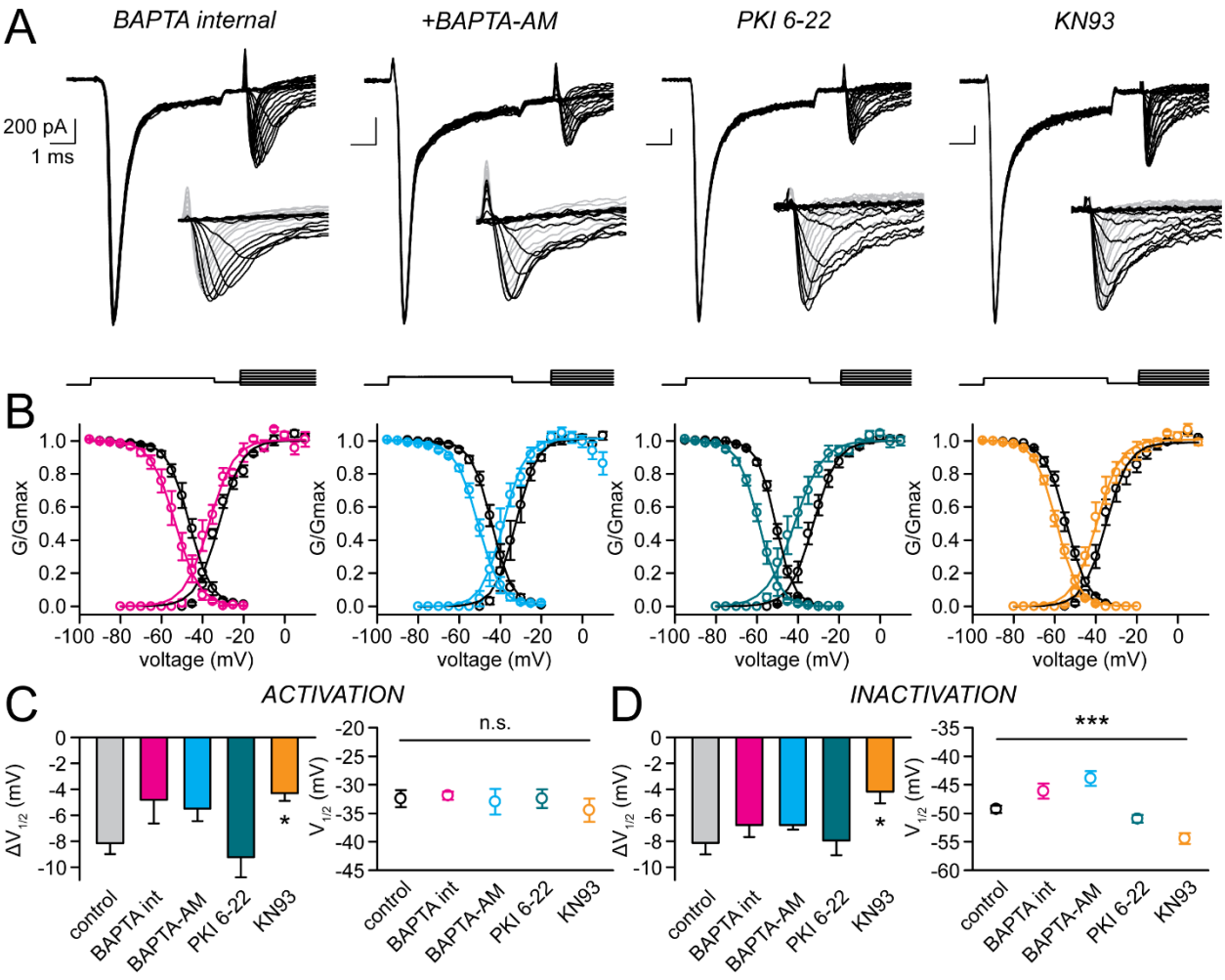

Figure 2.6 Cytosolic Ca^{2+} and CaMKII control shifts in Nav gating properties
(A) Voltage clamp traces from example stellate cells in response to pre-pulse activation protocol from each labeled condition. Insets are zoom-ins of I_{Na} peaks used for calculation of each conductance-voltage relationship. **(B)** Summary voltage-dependence of conductance and steady-state inactivation functions for each condition at baseline (black lines) and after 25 minutes (coloured lines). **(C)** (left) Change in $V_{1/2}$ activation over 25 minute recording in each condition. Statistical notation refers to comparison with control condition. (right) Absolute $V_{1/2}$ activation at baseline across all conditions. **(D)** Same as in (C) but for steady-state inactivation.

NMDA receptor stimulation potentiates basal AP firing in a Ca^{2+} and CaMKII-dependent manner

To eliminate the possibility of a mechanically-induced Ca^{2+} rise, we performed loose-seal cell-attached recordings on stellate cells, an approach previously demonstrated to limit the changes in firing rates in this cell type (Alcami *et al.*, 2012). Using this strategy, SC firing remained stable over a duration of 15 minutes (Figure 2.7A,C; 5.2 ± 1.9 Hz at 1 min vs. 5.1 ± 2.1 Hz at 15min;

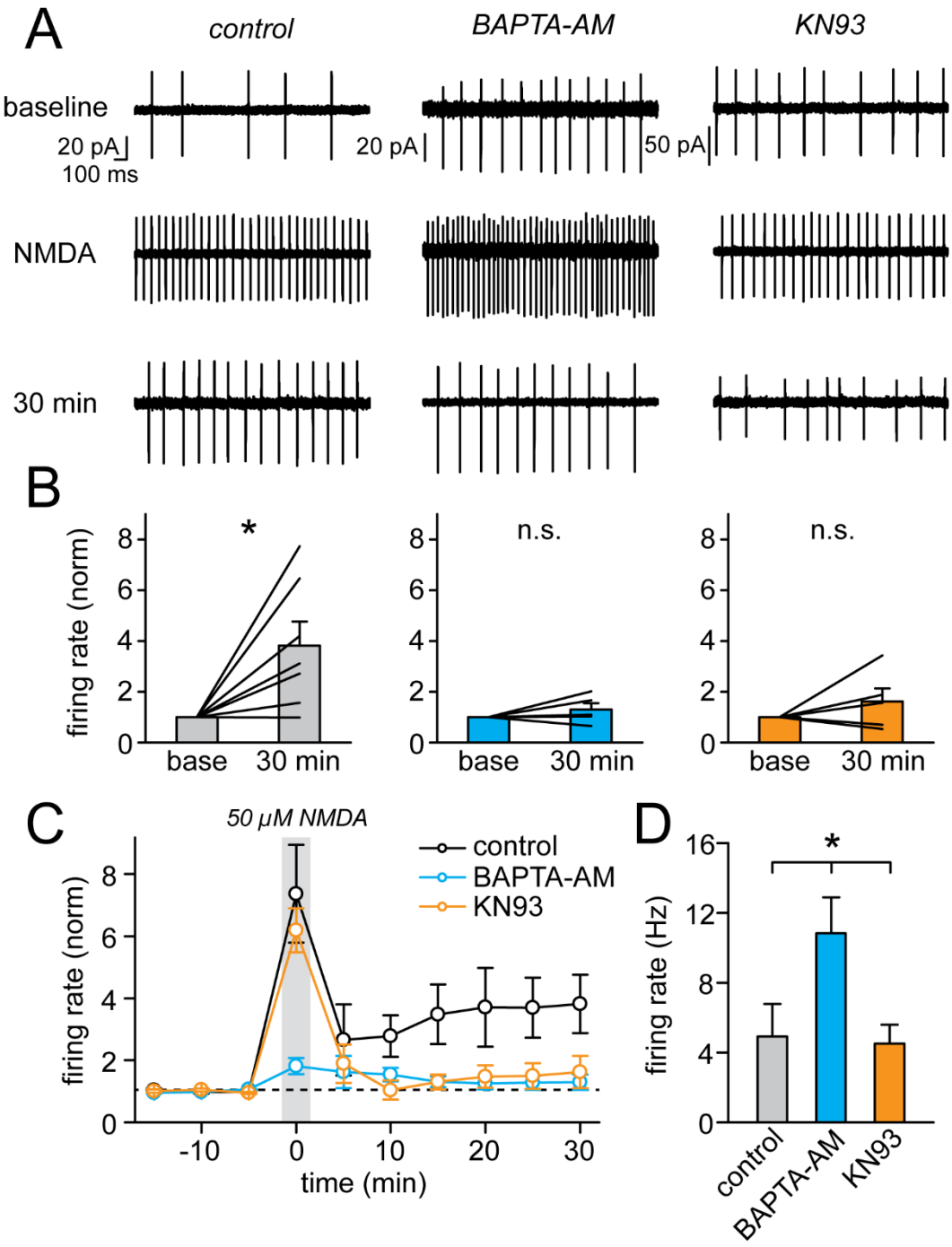

Figure 2.7 NMDA receptor stimulation induces excitability increase in a Ca^{2+}- and CaMKII-dependent manner
(A) Example loose-seal (<50 MΩ) cell-attached recordings from a stellate cell during baseline, bath application of 50 µM NMDA, and 30 minutes after NMDA application in normal ACSF (left), following >1 hour incubation in 150 µM BAPTA-AM (centre), and in the presence of 1 µM KN93 (right). **(B)** Plots depicting normalized firing rate at baseline and 30 minutes after NMDA exposure of individual cells (lines) and summary averages (bars). A significant increase in normalized stellate cell firing was induced by NMDA application in the control condition (gray) that could be occluded by pre-incubation in BAPTA-AM (blue) or external KN93 (orange) (paired t-tests). **(C)** Time course plot of summary normalized firing data over multiple cells in each condition. **(D)** Absolute firing rate summary data for each pharmacological condition show that cells incubated in BAPTA-AM had significantly increased excitability at baseline (one-way ANOVA). Graphs depict mean ± SEM. * denotes $p < 0.05$.

t = 0.21, p = 0.84; n = 7 cells). Since NMDA receptor stimulation is canonically associated with Ca^{2+}-mediated CaMKII activation (Malenka & Nicoll, 1999) and SCs receive NMDA receptor-mediated excitatory input (Carter & Regehr, 2000; Clark & Cull-Candy, 2002; Szapiro & Barbour, 2007), we decided to test whether NMDA receptors could serve as the induction trigger for the excitability increase pathway described above.

To that end, after a stable 15 minute baseline was achieved, 50 µM NMDA was applied through the ACSF perfusion which resulted in a transient increase in firing rates (Figure 2.7A,C; 4.92 ± 1.9 Hz at baseline vs. 21.4 ± 3.7 Hz during NMDA application; t = 4.15, p = 0.006; n = 7 cells) which subsided after ~5 minutes (Figure 2.7C). This probably reflects direct membrane depolarization from cation flux across activated channels since the highly elevated firing rates subsided substantially once NMDA was no longer present. Interestingly, 30 minutes after NMDA application SC AP firing was significantly increased compared to baseline rates (Figure 2.7B,C; 3.8 ± 0.9 fold change at 30 min; t = 3.00, p = 0.024; n = 7 cells). This effect could be completely occluded by first incubating slices in 150 µM BAPTA-AM (Figure 2.7B,C; 1.3 ± 0.2 fold change at 30 min; t = 1.23, p = 0.29; n = 5 cells), or in the presence of 5 µM KN93 (Figure 2.7B,C; 1.6 ± 0.5 fold change at 30 min; t = 1.20, p = 0.30; n = 5 cells), suggesting that the excitability increase is both Ca^{2+} and CaMKII-dependent. Notably, absolute firing rates at baseline after incubation in BAPTA-AM were significantly increased compared to control (Figure 2.7D; one-way ANOVA, $F_{2, 16}$ = 3.61, p = 0.054; Fisher's LSD, p = 0.032), which could reflect the role of Ca^{2+}-activated K^+ channels in regulating basal firing. However, the fact that basal AP firing was unchanged in the presence of KN93 provides compelling evidence that this NMDA receptor-mediated effect harnesses the same pathway as that triggered by patch clamp (Figures 2.4 and 2.6). Taken

together, these data demonstrate that SCs contain a Nav-dependent pathway to dynamically and persistently upregulate their excitability in response to NMDA receptor stimulation that is unintentionally perturbed by patch clamp investigation.

DISCUSSION

The present work advances our understanding of excitability regulation in SCs in several key ways. First, we demonstrate that the patch-induced excitability increase described in our previous study (Alexander *et al.*, 2019) is dialysis-independent and that AP threshold hyperpolarization depends on cytosolic Ca^{2+} concentration as well as the activity of specific protein kinases. Second, the finding that negative shifts of Na^{+} channel gating properties were shown to be controlled by Ca^{2+} and CaMKII further demonstrates that this is the major process underlying threshold decrease in SCs. Finally, since firing rate increases can be observed upon NMDA receptor stimulation in a Ca^{2+} and CaMKII-dependent manner, we argue that this is the signaling cascade that patch clamp recording overrides to induce AP threshold hyperpolarization in SCs. Taken together, we have shown a form of NMDA receptor-dependent intrinsic plasticity previously undescribed in MLIs, and that apparent recording artifacts can give insight into important neurophysiological regulation.

Phosphorylation has a variety of effects on Nav gating

Voltage-gated gated sodium channels are well-characterized targets of various intracellular protein kinases. Previous studies have demonstrated phosphorylation sites on virtually the entire length of the channel (Scheuer, 2011), but there appears to be a preferential hub for kinase activity on the cytoplasmic DI-DII linker region (Rossie *et al.*, 1987; Cantrell *et al.*, 2002). For example, PKA acts on multiple serine residues in Nav1.2 to reduce current density in mammalian neurons (Li *et al.*, 1992). PKC also acts on several DI-DII residues as well as a conserved consensus site in the inactivation gate (S1506 in rat Nav1.2) to reduce current and slow inactivation (Numann *et al.*, 1991; Cantrell *et al.*, 2002). With respect to CaMKII, most of the

work has been focused on the dominant cardiac isoform Nav1.5 (Scheuer, 2011), where there have been dozens of potential phosphorylation sites identified. The main effect of CaMKII on Nav1.5 has been demonstrated to be a hyperpolarization of channel availability (Wagner *et al.*, 2006), although there is some conflicting evidence (Aiba *et al.*, 2010). There is less known about the effects of CaMKII on neuronal sodium channels, but one study has demonstrated its role in setting channel availability of Nav1.2 (Thompson *et al.*, 2017), which is important to note for the current work since applying the CaMKII inhibitor KN93 shifted baseline steady-state inactivation of SC I_{Na} (see Figure 2.6). Although Nav1.2 is not a likely contributor to AP firing in these neurons (Alexander & Bowie, unpublished observation), others have demonstrated that CaMKII can have regulatory effects on Nav1.1 (Li *et al.*, 2018), which is expressed at the axon initial segment in SCs (Lorincz & Nusser, 2008).

Another question that arises is does the action of CaMKII even need to be direct phosphorylation of the Na^+ channel alpha subunit itself? Although there is a litany of candidate serines and threonines as targets for CaMKII action (Scheuer, 2011), there are other possibilities. Pore-forming Nav proteins, including neuronal isoforms, have many accessory subunits and binding partners that serve to traffic, accumulate, anchor, and modify gating (Ahern *et al.*, 2016). Fibroblast growth factors (FGFs), ankyrins, spectrins, and β subunits have all been shown to bind to neuronal sodium channels, with many having a role in channel gating. For example, FGF14 acts as a regulator for Nav1.1 and Nav1.6 channel trafficking in cerebellar Purkinje cells, with knockout animals exhibiting reduced I_{Na} and dysregulated AP firing (Xiao *et al.*, 2013; Bosch *et al.*, 2015). In the cardiac context, CaMKII requires the presence of a βIV-spectrin complex in order to confer

its regulatory properties (Hund *et al.*, 2010). Whether the same is true in SCs remains to be investigated.

Ca^{2+}, calmodulin, and CaMKII: independent and interdependent effects on Nav function

Our data support the role of free cytosolic Ca^{2+} in AP threshold hyperpolarization, and, in light of our previous study (Alexander *et al.*, 2019), this effect should be entirely driven by shifts in Nav gating behaviour. In the experiments presented here, we observed an incomplete stabilization of Nav gating properties, especially inactivation, in voltage clamp during Ca^{2+} chelation protocols. Our previous work demonstrates that the shift in $V_{1/2}$ activation is ultimately responsible for the threshold decrease, while the shift in availability contributes to the reduction in AP height as well as a slight supplement to the frequency increase (Alexander *et al.*, 2019). This agrees with the more substantial attenuating effect of BAPTA and BAPTA-AM on activation $V_{1/2}$, and gives good coherence to the current clamp Ca^{2+} chelation experiments (see Figure 2.3). Why doesn't Ca^{2+} chelation attenuate the shift in channel availability?

There may be some confounding effect of the different internal solutions between voltage clamp and current clamp recordings based on the constituent anion used (Dani *et al.*, 1983; Kaczorowski *et al.*, 2007; Alexander *et al.*, 2019). The methanesulfonate used in the internal solutions for voltage clamp recordings could induce an additional shift in Nav gating properties not present when using gluconate. The other finding of variable baseline channel availability $V_{1/2}$ is also a factor. More depolarized inactivation $V_{1/2}$ with increasing chelation of Ca^{2+}, and more hyperpolarized inactivation $V_{1/2}$ with KN93 suggests a constitutive regulation of this property by these signaling molecules. Interestingly, it also suggests uncoupling of activation and inactivation

in SC Nav in the context of free Ca^{2+}: the fact that Ca^{2+} buffering affects the shift of activation but not baseline levels, and that baseline availability is Ca^{2+} dependent but its shift over time is not, is interesting but complex. Previous studies have described the regulatory role of free Ca^{2+} on Nav channel availability, with some finding that free Ca^{2+} itself binding to EF hand domains as responsible (Wingo *et al.*, 2004), but others argue that calmodulin regulates this property via the conserved IQ domain on the Nav C-terminus (Tan *et al.*, 2002; Ben-Johny *et al.*, 2014). There is also evidence showing constitutive CaMKII regulation of Nav biophysical properties (Wagner *et al.*, 2006), which is itself Ca^{2+}- and calmodulin-dependent, demonstrating the complex interplay of signaling involved (Van Petegem *et al.*, 2012). Of course, many of these studies are focused on either Nav1.4 or Nav1.5, or both, so it is unclear if these modulatory processes have any impact on neuronal Nav. It has been argued that the Nav1.2 EF hands do not bind Ca^{2+}, but rather Ca^{2+}-bound calmodulin interacts with the C-terminus IQ domain (Miloushev *et al.*, 2009; Wang *et al.*, 2014). Furthermore, previous work has demonstrated that Nav1.6 in dorsal root ganglion neurons can be regulated by Ca^{2+} in a calmodulin- and IQ domain-dependent manner (Herzog *et al.*, 2003). The work presented in this study provides good indication that there is constitutive Ca^{2+} and CaMKII regulation on the Nav present in SCs, likely Nav1.1 and Nav1.6.

A-type K^+ channels exhibit kinase-independent shifts in gating behaviour

Although we focus mostly on AP threshold hyperpolarization as the defining feature of SC excitability, A-type K^+ channel shifts contribute to the overall increase in AP firing seen during patch clamp recording, as described in our previous study. The fact that neither of the kinase inhibitors that have clear effects in current clamp yield any significant attenuation of A-type K^+ shifts measured in voltage clamp demonstrate that there are other patch-induced signaling

pathways that mediate these changes. Other groups have characterized dynamic modulation of I_A steady state inactivation by Ca^{2+} influx through T-type Ca^{2+} channels binding to auxiliary KChIP sensors (Molineux *et al.*, 2005; Anderson *et al.*, 2010a; Anderson *et al.*, 2013). First, this regulation only affects inactivation and has no effect on voltage-dependence of activation, which distinguishes it from the process discussed here. Secondly, the shifts in A-type gating are persistent and do not depend on local Ca^{2+} influx. More experiments are needed to investigate the effect of general cytosolic Ca^{2+} concentration on these shifts, but their gradual and long-term nature seem to suggest another kind of regulation, like a different protein kinase not tested for in the present study. A more recent paper suggests that Kv4 channels (which mediate I_A) are regulated in an activity-dependent manner by extracellular signal-regulated protein kinase (ERK) in cerebellar granule cells (Rizwan *et al.*, 2016). Whether unintentional ERK activation is responsible for the shifts in A-type K^+ channel gating during patch recording remains to be tested.

AUTHOR CONTRIBUTIONS

R.P.D.A. and D.B. designed research; R.P.D.A. performed research and analyzed data; R.P.D.A. and D.B. wrote the paper.

ACKNOWLEDGEMENTS

This research was supported by Canadian Institutes of Health Research Operating Grants MOP 142431 to D. Bowie. R.P.D. Alexander was funded by a NSERC CGS-D doctoral fellowship. We thank members of the Bowie laboratory for comments on the manuscript.

PART III

GENERAL DISCUSSION

1 GENERAL THOUGHTS

Over the course of this thesis I have presented two manuscript-based chapters that are essentially two halves of the same overarching project. The first reports and characterizes an excitability phenomenon in cerebellar SCs that occurs as a result of patch clamp investigation and assigns Nav channels as its primary driver. The second unravels the molecular events that give rise to the excitability increase and provides a reasonable physiological context for its use by SCs. These studies together provide significant insight into the dynamic nature of firing rate control in these neurons and suggests an unconventional Nav-dependent mode of intrinsic plasticity that could be found elsewhere in the brain.

MLIs' electrical compactness promotes unique characteristics like somatic APs propagating passively into dendrites (Myoga *et al.*, 2009), distant subthreshold signals invading axonal boutons (Christie *et al.*, 2011), and strong firing regulation by individual quanta (Carter & Regehr, 2002). These characteristics make them a very interesting subject of comprehensive neurophysiological investigation. Regulation of MLI activity has been a topic well-studied by the broader cerebellar physiology community, but the ionic mechanisms underlying long-term firing rate modulation have received less attention. Since MLIs are significant players in controlling cerebellar output and behaviour (Wulff *et al.*, 2009; Astorga *et al.*, 2017; Gaffield & Christie, 2017; Rowan *et al.*, 2018), these processes are worthwhile to understand.

In the following section, I will discuss more deeply some of the implications of the results presented in this thesis and propose future experiments to further the investigation into SC excitability control.

2 ACTIVITY-DEPENDENT NAV CHANNEL MODULATION IN STELLATE CELLS

Although Experimental Section, Chapter 2 attempts to specifically address the context of AP threshold hyperpolarization in SCs, the induction stimuli were far from physiological. Over the course of two chapters, the limitations of my experimental approach and apparent delicacy of SCs only allowed for the initiation of plasticity using either patch clamp itself or bath application of NMDA. Although the molecular signaling uncovered in Chapter 2 suggests strongly that SCs could use this machinery to regulate excitability in this way, I never give direct evidence for true synaptic induction. How might this mechanism be engaged in a synaptically-driven, activity-dependent manner and/or in the awake, behaving animal?

As outlined in the Literature Review (Section 1.2.1), SCs express extrasynaptic NMDA receptors that are activated almost exclusively via glutamate spillover. This can occur as a result of high frequency PF activity or through CF-mediated volume release of glutamate in the molecular layer (Carter & Regehr, 2000; Clark & Cull-Candy, 2002; Szapiro & Barbour, 2007; Coddington *et al.*, 2013). *In vivo* recordings of granule cells show that they elicit bursts of APs at ~80 Hz during sensory stimulation (Chadderton *et al.*, 2004), which would provide sufficient transmitter release to promote glutamate spillover at PF-MLI synapses. Furthermore, single MLIs have been shown to receive appreciable input from multiple CFs (Szapiro & Barbour, 2007), so it is conceivable that upon strong activation of a neighbouring group of these afferents glutamate concentration would reach levels sufficient to elicit strong NMDA receptor activation in nearby MLIs. Since MLIs are tonically firing at rest, basal Mg^{2+} block of NMDA receptors would be relatively weak, allowing substantial ion flux and Ca^{2+} entry. Figure 2.7 of the Experimental Section demonstrates this scenario, albeit without CF stimulation itself. Bath application of

NMDA immediately caused an increase in tonic firing frequency in SCs that is dramatically higher than levels at either baseline or following plasticity 25 minutes later. This increase can be reasonably attributed to simple depolarization of membrane potential due to sustained cation inward flux through NMDA receptors unfettered by intracellular Mg^{2+} block. Since both fast excitatory and inhibitory neurotransmission were pharmacologically eliminated in this experiment, firing rate was not affected by the spontaneous synaptic input from PFs and partnered MLIs. Therefore, the transient effect of NMDA on firing must be restricted to the recorded SC and not due to some upstream circuit perturbation. This demonstrates that SCs at rest are susceptible to NMDA receptor-mediated inward currents, including Ca^{2+} permeation, as the BAPTA-AM condition in Figure 2.7 demonstrates directly. Physiologically-relevant afferent stimulation has previously been demonstrated to induce long-lasting, NMDA receptor-mediated, Ca^{2+}-dependent plasticity in SCs. High frequency PF-stimulation can induce both an AMPA receptor subunit switch at postsynaptic sites as well as an increase of release probability at presynaptic GABAergic terminals (Liu & Lachamp, 2006; Liu *et al.*, 2008). This demonstrates the potential of NMDA receptors to cause long-lasting changes to membrane excitability in SCs. A key future experiment to establish intrinsic plasticity as an activity-dependent process would be to activate SC NMDA receptors via afferent stimulation.

An outstanding question from the results of this thesis is the specific cellular geography of the signaling cascade; namely, how might dendritic NMDA receptor activation lead to CaMKII-mediated phosphorylation of Nav channel subunits, presumably located in the AIS? Since CaMKII is well-known to be associated in close proximity to NMDA receptor subunits themselves and its translocation tightly regulated (Leonard *et al.*, 1999; Bayer *et al.*, 2001), initially it seems

implausible for activated molecules to travel to the 'distant' spike initiation zone and exert effects on Nav subunits located there. However, SC NMDA receptors appear to be relatively unrestricted in their localization. Aside from their aforementioned extrasynaptic sites near dendritic PF synapses (Carter & Regehr, 2000; Clark & Cull-Candy, 2002), they are also found in axonal varicosities (Liu & Lachamp, 2006), as well as directly on the soma (Dubois *et al.*, 2016). This means that upon sufficiently strong release of glutamate from either PF or CF afferents, NMDA receptors located relatively nearby to spike initiating-Nav channels would be activated and subsequent CaMKII-mediated phosphorylation of those channels could occur. Conversely, dendritic signals in SCs have been previously demonstrated to cause axonal Ca^{2+} transients through passive electrotonic propagation. CaMKII in SCs could possibly be located next to Nav channels in the AIS and be activated upon Ca^{2+} entry through VGCCs. CaMKII has been shown to directly interact with L-type Cav channels (Hudmon *et al.*, 2005), so the classical NMDA receptor-CaMKII complex does not need to explain the situation in SCs. A useful experiment to tease apart the potential role of VGCCs in SC intrinsic plasticity would be to apply NMDA during cell-attached recording in the presence of external Cd^{2+}, which would eliminate flux through axonal Cav channels.

Regardless of the precise location of SC CaMKII, there is precedence in central neurons for this type of NMDA receptor-/Nav channel-dependent intrinsic plasticity. As mentioned in the Chapter 1 Discussion, Xu and colleagues demonstrate a remarkably similar mechanism accompanying synaptic LTP in hippocampal CA1 pyramidal neurons (Xu *et al.*, 2005). Correlated stimulation of Schaffer collateral afferents with depolarizing current injection of pyramidal neurons caused a selective decrease in AP threshold lasting more than 6 hours with no change in

input resistance or RMP. Voltage clamp recordings revealed that this correlated stimulation protocol induced symmetric shifts of both voltage-dependence of activation and availability of pyramidal Nav currents, thus causing the AP threshold decrease. Current injection alone could not induce plasticity, demonstrating that Ca^{2+} flux through dendritic NMDA receptors was necessary. Consistent with this, the presence of external APV or intracellular BAPTA completely occluded plasticity, along with the CaMKII inhibitor KN62 (Xu *et al.*, 2005). The parallels between signaling cascades present in pyramidal neurons and SCs are striking and demonstrate that seemingly distant input can mediate long-range effects across neuronal compartments.

3 EFFECT ON THE CIRCUIT

If physiologically-relevant afferent stimulation can provide the necessary induction stimulus for intrinsic plasticity in MLIs, what would the consequences be for their downstream partners? A long-lasting increase in spontaneous AP firing would exert effects in two main ways: first, increased AP-dependent GABA release onto both connected Purkinje cells and other MLIs, and second, increased depolarizing influence onto electrically coupled MLIs. SCs and BCs are both chemically and electrically connected to one another (Rieubland *et al.*, 2014), although the degree as well as strength of these connections may differ between these two cell types. Paired recordings have shown that BCs are electrically coupled with ~4 of their BC neighbours, while SCs have only ~1 electrical partner on average (Alcami & Marty, 2013). Furthermore, the strength of potential spread across gap junctions has been estimated to be 1.7% in BCs, and significantly weaker in SCs at 0.2% (Alcami & Marty, 2013). Postsynaptic voltage spikelets are observed in coupled MLIs upon presynaptic AP firing, but a quantitative increase in postsynaptic spontaneous spiking is unclear. Since spontaneous MLI-MLI IPSCs are relatively large and frequent (Nusser *et*

al., 1997; Accardi *et al.*, 2014), the increased inhibitory drive from an MLI that has undergone Nav-dependent intrinsic plasticity may override the depolarizing effect of increased spiking spreading through electrical synapses. This increase in spontaneous inhibition throughout the circuit would likely manifest in a similar way after considering PF input. Once an MLI has undergone intrinsic plasticity, the same PF-EPSP would more easily elicit spiking in that neuron, which would provide a greater degree of feedforward inhibition on its MLI neighbours. What would be the ultimate consequence on Purkinje cell activity?

PF stimulation yields a biphasic postsynaptic response in Purkinje cells, a rapid monosynaptic EPSP, followed by a delayed disynaptic IPSP that sharpens the initial depolarization and briefly silences membrane excitability (Mittmann *et al.*, 2005). These IPSPs are disynaptic, deriving from PF-evoked MLI firing causing delayed GABA release recorded in the Purkinje cell. Feedforward inhibition from MLIs promotes temporal precision of PF-induced Purkinje cell spiking and suppresses the response to subsequent excitation (Mittmann *et al.*, 2005). Furthermore, PF-evoked MLI-MLI feedforward inhibition is significantly weaker than MLI-Purkinje cell. It is unclear whether this is related to differences in GABA receptor composition or simply the number of recruited upstream inhibitory partners from PF activity (Mittmann *et al.*, 2005). A similar result arises via CF-mediated feedforward inhibition. Electrical stimulation of single CFs causes excitation of nearby MLIs through glutamate spillover within the molecular layer (Coddington *et al.*, 2013). The effect on Purkinje cells is a strong suppression of AP probability for almost 100 ms following CF stimulation in a manner dependent on GABA release. Interestingly, more distant neighbouring Purkinje cells from the activated CF input experience significant disinhibition due to silencing of their nearest MLI partners (Coddington *et al.*, 2013),

demonstrating the functional modularity of distinct microzones in the cerebellar cortex. Following induction of intrinsic plasticity, MLI-derived feedforward inhibition would be enhanced through both PF and CF channels, causing stronger inhibition of Purkinje cells near to the excited afferents but enhanced disinhibition of those cells more distant to them. MLI intrinsic plasticity could serve as a further layer of long-term gain control of feedforward inhibition in the molecular layer.

MLI-mediated inhibition is associated with spike irregularity in downstream Purkinje cells. Blocking GABA receptors transforms irregular tonic spiking into highly regular spike patterns in Purkinje cells (Hausser & Clark, 1997). In agreement with this result, mutant mice where GABA receptors are selectively eliminated from Purkinje cells exhibit a high degree of spike regularity compared to wild-type mice (Wulff *et al.*, 2009). Following MLI intrinsic plasticity, the degree of spontaneous spike output onto Purkinje cells would result in a greater degree of post-AP pausing behaviour and stronger spike irregularity. Recent evidence has shown that MLI activity can also directly suppress CF-mediated Ca^{2+} signals in Purkinje cell dendrites (Rowan *et al.*, 2018). Furthermore, depending on the level of activity in MLIs, the valence of PF-EPSP plasticity exhibited by Purkinje cells strongly affected. Following intrinsic plasticity, MLI firing rates would be elevated at baseline, creating a circuit environment that favours EPSP potentiation following conjunctive PF-CF stimulation instead of depression. Increased MLI activity would override the ability of CF-mediated error signals to influence Purkinje cell activity, as has been demonstrated in the context of the vestibulo-ocular reflex gain control (Rowan *et al.*, 2018). In this way, intrinsic plasticity in MLIs could function as a long-term regulatory mechanism for gating the strength of CF-mediated instructive signaling onto Purkinje cells.

4 NEURONAL SUBTYPE DETERMINANTS OF INTRINSIC PLASTICITY

An outstanding question of significant concern following the results of this thesis is how widespread is this mode of excitability regulation in the CNS? As mentioned earlier, pyramidal neurons in hippocampal CA1 have been demonstrated to have a mechanism of Nav-dependent intrinsic plasticity that depends on NMDA receptor-mediated activation of CaMKII that resembles the situation in cerebellar MLIs quite closely (Xu *et al.*, 2005). At first this is surprising given the many differences between the two cell types. CA1 pyramidal neurons, like pyramidal neurons in other parts of cortex, express Nav1.2 and Nav1.6 at different locations at the AIS (Westenbroek *et al.*, 1989; Garrido *et al.*, 2003; Lorincz & Nusser, 2008; Hu *et al.*, 2009), with Nav1.6 playing a more significant role in AP generation (Royeck *et al.*, 2008; Hu *et al.*, 2009; Katz *et al.*, 2018). Cerebellar MLIs express Nav1.1 and Nav1.6 at distinct sections of AIS (Lorincz & Nusser, 2008), with a notable absence of Nav1.2 (Martinez-Hernandez *et al.*, 2013). Apart from the differences in Nav1.1 and Nav1.2 expression between these cell types, the common presence and importance for spike initiation of Nav1.6 might be a tempting candidate for signifying intrinsic plasticity. However, Nav1.6 is common throughout the brain as the AP-driving Na^+ channel (Lorincz & Nusser, 2008), so why is this plasticity mechanism so rare?

Purkinje cells, for example, express a high density of Nav1.6 at the AIS (Lorincz & Nusser, 2008) and its function is critical for normal firing behaviour (Raman *et al.*, 1997). As shown in the results of Chapter 1, Purkinje cells are not susceptible to changes in excitability during patch clamp recording (Figures 1.1 and 1.2). However, although induction by patch clamp and induction by NMDA receptor stimulation activate the same signaling pathway that converges upon Nav channels, SCs may be especially sensitive to this method compared to other cell types. The fact

that Purkinje cells do not experience excitability changes does not mean that any cell that expresses Nav1.6 but is unaffected by electrophysiological recording cannot possess Nav-dependent intrinsic plasticity. For example, Purkinje cells express a multitude of endogenous Ca^{2+} binding proteins including calbindin-D28k, calmodulin, parvalbumin, and calretinin, whereas MLIs are enriched with only parvalbumin and calmodulin (Schwaller *et al.*, 2002; Bastianelli, 2003). Purkinje cells express high quantities of calbindin-D28k which is more effective and faster at binding Ca^{2+} than parvalbumin (Lee *et al.*, 2000), and in fact Purkinje cells have been demonstrated to have incredibly high buffering capacity compared to other neurons (Fierro & Llano, 1996). Since patch clamp-induced intrinsic plasticity in SCs depends on a cytosolic Ca^{2+} rise upon pipette sealing (Figures 2.2 and 2.3), this signal could be buffered in Purkinje cells before the subsequent signaling cascade can be activated. CA1 pyramidal neurons also express calbindin-D28k (Klapstein *et al.*, 1998), which could serve as evidence as to why patch-induced excitability changes have not been reported in these neurons. However, distinctions between endogenous Ca^{2+} buffers cannot explain why both pyramidal neurons and SCs possess NMDA receptor-induced intrinsic plasticity.

Presence of CaMKII also falls short as a determinant of Nav-dependent intrinsic plasticity. CaMKII can be found as 28 similar isoforms that are expressed from four genes, α, β, γ, and δ (Lisman *et al.*, 2002). The α and β versions are predominant in the brain and both are involved in NMDA receptor-mediated LTP in hippocampal CA1 (Fukunaga *et al.*, 1995). If we can assume one of these isoforms also mediates Nav-dependent intrinsic plasticity in CA1 pyramidal neurons, these forms of CaMKII should also be found in MLIs. However, MLIs express neither CaMKIIα nor β, while Purkinje cells express high levels of CaMKIIα (Wang *et al.*, 2013). Although there is no

direct evidence other than this thesis that demonstrates any presence of or function for CaMKII in MLIs, *in situ* hybridization data from the Allen Institute suggest that MLIs express high levels of mRNA for CaMKIIδ (Lein *et al.*, 2007). Since there is no isoform-selectivity for Nav-dependent intrinsic plasticity and CaMKII is expressed by many neuronal subtypes throughout the brain, this again cannot be a predictive factor for plasticity. What else could confer susceptibility of CaMKII regulation on Nav channels?

As described in the Literature Review (Section 3.1.3), cardiac Nav1.5 requires the presence of βIV spectrin in order for phosphorylation by CaMKII to have an effect on channel function (Hund *et al.*, 2010). Similarly, there could be a specific macromolecular complex in MLIs consisting of auxiliary β subunits or FGF proteins that provide conformational conditions that are favourable for CaMKII modulation, as is the case for some Kv subunits (Schrader *et al.*, 2002). Unfortunately, little is known about the precise molecular architecture of the MLI AIS, including the binding partners of Nav channels located there, so these hypotheses are only speculative absent further experiments.

5 RELEVANCE OF TECHNIQUE-INDUCED PHENOMENA

In the last section of the Discussion, I would like to address the origin of this project and argue for the merit of studying apparent artifacts of measurement. The observation of changes induced by patch clamp recording itself was striking on its own, but the greatest challenge has been convincing reviewers and colleagues of its value to the broader neuroscience community that it merits physiological relevance. Studies involving patch clamp electrophysiology, especially those investigating phenomena that occur over longer time scales, generally demonstrate a stable basal activity or channel property in the absence of manipulation. Then, upon application

of some activating stimulus like electrical stimulation or pharmacological agent, changes observed subsequent are believed to be physiological since the stimuli are substitutes of those present in the native tissue. Patch clamp itself, however, does not have a counterpart like axonal APs or neurotransmitter binding that would reasonably exist in that system before the measurement was attempted. It was our philosophy, however, that patch clamp was perturbing or activating some interesting aspect of the biology of the neuron that provoked a change in activity. The fact that the effect was so substantial led us to believe that it was worthy of further investigation. Although it was our strategy to build upon this observation by eventually legitimizing it after many experiments, many others have reported experimentally-induced changes to neuronal activity and channel properties.

Early in the history of patch clamp, Erwin Neher's group noticed changes to ion channel behaviour during periods of prolonged recording in bovine chromaffin cells. Although reversal potentials for smaller ions like Na^+ stabilized within 30 seconds following patch breakthrough (Fenwick *et al.*, 1982a), endogenous Ca^{2+} currents exhibit rundown over the next 10 – 20 minutes (Fenwick *et al.*, 1982b). Interestingly, this was not due to changes in voltage dependency of activation or inactivation, and no effect on Na^+ currents was observed. The authors describe this as washout of an "intracellular substance" that endogenous Cav channels require for proper activation (Fenwick *et al.*, 1982b). This work is bolstered by observations made in rabbit atrial myocytes where spontaneous drift in Na^+ channel kinetics could be prevented by preserving membrane integrity at the pipette interface using perforated patch (Wendt *et al.*, 1992). However, previous work had shown that even in cell-attached configuration Na^+ channels exhibited hyperpolarized availability and speeding of inactivation kinetics over tens of minutes

after sealing (Kimitsuki *et al.*, 1990). This finding demonstrated that, at least in certain preparations, Na^+ channels were susceptible to significant biophysical modulation purely through mechanical perturbation. A more recent study that highlights this result and put it in a neuronal context is from Kole and colleagues (Kole *et al.*, 2008). The authors showed that cell-attached recordings of Na^+ currents in cortical pyramidal neurons show no difference in Nav channel density between dendrites, soma, and AIS, even though immunohistochemical analysis finds a concentration of Nav at the AIS. This discrepancy was due to an effect of patch clamp itself, where Nav channel anchoring to the cytoskeleton prevented them from being drawn into the pipette tip during sealing. Forcing the depolymerization of actin using pharmacological agents yielded a substantial increase in the measured Na^+ current density at the AIS selectively (Kole *et al.*, 2008). Although Nav channels were known to associate with cytoskeletal anchoring proteins like ankyrin G and βIV spectrin (Zhou *et al.*, 1998; Komada & Soriano, 2002), the tight physical coupling was unexpected and apparently unique to Nav, as this property is not found for Kv channels at the AIS (Kole *et al.*, 2007). Kole and colleagues chose to investigate this apparent recording artifact and advanced the understanding of Nav-AIS physiology in neurons.

An interesting result from Chapter 1 related to this topic is the time-dependent shift in gating properties in A-type K^+ current observed during whole-cell recording being completely absent in nucleated patch configuration (Figure 1.7). Voltage-dependence of activation values are relatively similar at baseline between the two configurations, so it is not as though the shift is already saturated upon pulling the patch. In the Chapter 1 text I suggest that a cytoplasmic modulatory factor may be lost when isolating the nucleated membrane from other neuronal compartments. However, the nucleated patch configuration has previously been shown to

preserve certain signaling machinery responsible for the modulation of voltage-gated K^+ channels in hippocampal interneurons (Lien *et al.*, 2002). The mechanism of the time-dependent shift of A-type K^+ current in stellate cells remains mysterious.

Returning to Nav channels, additional work demonstrated that Na^+ currents in frog skeletal muscle were sensitive to the anion species present in the intracellular solution (Dani *et al.*, 1983). Thiocyanate (SCN^-) shifted voltage dependence of activation and availability more than 10 mV more hyperpolarized compared to Cl^-, showing that the composition of the experimental solution has a profound effect on the measured channel properties. Furthermore, internal solution containing K-methanesulfonate as the constituent anion caused time-dependent changes in input resistance and fast afterdepolarizations in CA1 pyramidal neurons, an effect not observed when K-Gluconate was used (Kaczorowski *et al.*, 2007). These findings remind me of experiments I performed late in my PhD concerning anion modulation of native AMPA receptors that built upon the work of my former labmate Brent Dawe (Dawe *et al.*, 2019). He found that external anion switches not only caused changes in rates into and out of desensitization of recombinant AMPA receptors, but that anion switches could induce structural compression of receptors in the absence of agonist. Although the concentrations of external anions were completely unphysiological (ie. 150 mM NaF, NaI and NaBr), they were used to gain insight into the gating and physiology of these receptors (Dawe *et al.*, 2019). Furthermore, findings from my supervisor during his postdoctoral fellowship demonstrate the power of investigating apparent recording artifacts. He showed that the rundown in AMPA and kainate receptor currents in HEK 293 cells was due to washout of endogenous polyamines during prolonged whole-cell recording, and channel block could be reintroduced with the inclusion of relatively low concentrations of

spermine in the pipette solution (Bowie & Mayer, 1995; Bahring *et al.*, 1997; Bowie *et al.*, 1998). This phenomenon had apparently been observed for years by others in the field, although it had been largely disregarded as an uninteresting artifact of electrophysiological recording (Derek Bowie, personal communication). Channel block by intracellular polyamines is now seen as a fundamental property of glutamate receptors that has a large impact on neuronal function (Bowie, 2018). I see my work as extension of this philosophy, that interesting and important discoveries about ion channel and neuronal biology can arise from appreciating the relevance of phenomena induced by recording technique.

6 CONCLUSION

In **Part I** of this thesis I have provided an overview of cerebellar anatomy and physiology focusing on MLIs, ionic components of neuronal AP firing in cerebellum and elsewhere, the layers of regulation that dictate voltage-gated ion channel behaviour in their physiological context, and finally, modes of intrinsic plasticity that affect the ability of neurons to change their responsiveness to incoming stimuli. **Part II** is composed of two chapters that contain my experimental results. Chapter 1 characterizes an excitability increase in cerebellar SCs that occurs during patch clamp recording. I use electrophysiology and Hodgkin-Huxley modeling to argue that this phenomenon is driven primarily by changes in the biophysical properties of Nav channels, while being further modulated by shifts in A-type Kv gating. Chapter 2 aims to define the physiological importance of this observation, and I demonstrate the molecular signaling events that underlie this Nav-dependent plasticity while providing a synaptic receptor-based induction scheme. Finally, **Part III** of this thesis discusses the specifics of how intrinsic plasticity might be evoked in an activity-dependent manner as well as its impact on the cerebellar microcircuit. Furthermore, I argue for the importance of understanding apparent artifacts of electrophysiological recording and their potential for yielding novel insights into ion channel biology and neurophysiological systems. Overall, my work has revealed a novel form of intrinsic plasticity in cerebellar MLIs through unconventional means, and further work is necessary to define its role in higher order cerebellar functions.

7 REFERENCES

Abbott GW & Goldstein SA. (2002). Disease-associated mutations in KCNE potassium channel subunits (MiRPs) reveal promiscuous disruption of multiple currents and conservation of mechanism. *FASEB J* **16,** 390-400.

Accardi MV, Daniels BA, Brown PM, Fritschy JM, Tyagarajan SK & Bowie D. (2014). Mitochondrial reactive oxygen species regulate the strength of inhibitory GABA-mediated synaptic transmission. *Nat Commun* **5,** 3168.

Accili EA, Kiehn J, Wible BA & Brown AM. (1997). Interactions among inactivating and noninactivating Kvbeta subunits, and Kvalpha1.2, produce potassium currents with intermediate inactivation. *J Biol Chem* **272,** 28232-28236.

Afshari FS, Ptak K, Khaliq ZM, Grieco TM, Slater NT, McCrimmon DR & Raman IM. (2004). Resurgent Na currents in four classes of neurons of the cerebellum. *J Neurophysiol* **92,** 2831-2843.

Ahern CA, Payandeh J, Bosmans F & Chanda B. (2016). The hitchhiker's guide to the voltage-gated sodium channel galaxy. *J Gen Physiol* **147,** 1-24.

Ahn M, Beacham D, Westenbroek RE, Scheuer T & Catterall WA. (2007). Regulation of Na(v)1.2 channels by brain-derived neurotrophic factor, TrkB, and associated Fyn kinase. *J Neurosci* **27,** 11533-11542.

Aiba T, Hesketh GG, Liu T, Carlisle R, Villa-Abrille MC, O'Rourke B, Akar FG & Tomaselli GF. (2010). Na+ channel regulation by Ca2+/calmodulin and Ca2+/calmodulin-dependent protein kinase II in guinea-pig ventricular myocytes. *Cardiovasc Res* **85,** 454-463.

Aizenman CD & Linden DJ. (2000). Rapid, synaptically driven increases in the intrinsic excitability of cerebellar deep nuclear neurons. *Nat Neurosci* **3,** 109-111.

Akemann W & Knopfel T. (2006). Interaction of Kv3 potassium channels and resurgent sodium current influences the rate of spontaneous firing of Purkinje neurons. *J Neurosci* **26,** 4602-4612.

Albus JS. (1971). A theory of cerebellar function. *Mathematical Biosciences* **10,** 25-61.

Alcami P, Franconville R, Llano I & Marty A. (2012). Measuring the firing rate of high-resistance neurons with cell-attached recording. *J Neurosci* **32,** 3118-3130.

Alcami P & Marty A. (2013). Estimating functional connectivity in an electrically coupled interneuron network. *Proc Natl Acad Sci U S A* **110,** E4798-4807.

Alder R & Barbas H. (1995). Complementary distribution of the phosphoproteins DARPP-32 and I-1 in the cerebellar system. *Neuroreport* **6,** 2368-2372.

Alexander RPD, Mitry J, Sareen V, Khadra A & Bowie D. (2019). Cerebellar stellate cell excitability is coordinated by shifts in the gating behavior of voltage-gated Na(+) and A-type K(+) channels. *eNeuro* **6**.

Alzheimer C, Schwindt PC & Crill WE. (1993). Modal gating of Na+ channels as a mechanism of persistent Na+ current in pyramidal neurons from rat and cat sensorimotor cortex. *J Neurosci* **13,** 660-673.

Aman TK, Grieco-Calub TM, Chen C, Rusconi R, Slat EA, Isom LL & Raman IM. (2009). Regulation of persistent Na current by interactions between beta subunits of voltage-gated Na channels. *J Neurosci* **29,** 2027-2042.

Amarillo Y, De Santiago-Castillo JA, Dougherty K, Maffie J, Kwon E, Covarrubias M & Rudy B. (2008). Ternary Kv4.2 channels recapitulate voltage-dependent inactivation kinetics of A-type K+ channels in cerebellar granule neurons. *J Physiol* **586,** 2093-2106.

Amat SB, Rowan MJM, Gaffield MA, Bonnan A, Kikuchi C, Taniguchi H & Christie JM. (2017). Using c-kit to genetically target cerebellar molecular layer interneurons in adult mice. *PLoS One* **12,** e0179347.

An WF, Bowlby MR, Betty M, Cao J, Ling HP, Mendoza G, Hinson JW, Mattsson KI, Strassle BW, Trimmer JS & Rhodes KJ. (2000). Modulation of A-type potassium channels by a family of calcium sensors. *Nature* **403,** 553-556.

Anderson D, Engbers JD, Heath NC, Bartoletti TM, Mehaffey WH, Zamponi GW & Turner RW. (2013). The Cav3-Kv4 complex acts as a calcium sensor to maintain inhibitory charge transfer during extracellular calcium fluctuations. *J Neurosci* **33,** 7811-7824.

Anderson D, Mehaffey WH, Iftinca M, Rehak R, Engbers JD, Hameed S, Zamponi GW & Turner RW. (2010a). Regulation of neuronal activity by Cav3-Kv4 channel signaling complexes. *Nat Neurosci* **13,** 333-337.

Anderson D, Rehak R, Hameed S, Mehaffey WH, Zamponi GW & Turner RW. (2010b). Regulation of the KV4.2 complex by CaV3.1 calcium channels. *Channels (Austin)* **4,** 163-167.

Andre P, Pompeiano O & White SR. (1993). Activation of muscarinic receptors induces a long-lasting enhancement of Purkinje cell responses to glutamate. *Brain Res* **617,** 28-36.

Armano S, Rossi P, Taglietti V & D'Angelo E. (2000). Long-term potentiation of intrinsic excitability at the mossy fiber-granule cell synapse of rat cerebellum. *J Neurosci* **20,** 5208-5216.

Armstrong DM & Rawson JA. (1979). Activity patterns of cerebellar cortical neurones and climbing fibre afferents in the awake cat. *J Physiol* **289,** 425-448.

Astorga G, Li D, Therreau L, Kassa M, Marty A & Llano I. (2017). Concerted Interneuron Activity in the Cerebellar Molecular Layer During Rhythmic Oromotor Behaviors. *J Neurosci* **37,** 11455-11468.

Attwell PJ, Cooke SF & Yeo CH. (2002). Cerebellar function in consolidation of a motor memory. *Neuron* **34,** 1011-1020.

Bahring R, Bowie D, Benveniste M & Mayer ML. (1997). Permeation and block of rat GluR6 glutamate receptor channels by internal and external polyamines. *J Physiol* **502 (Pt 3),** 575-589.

Barhanin J, Lesage F, Guillemare E, Fink M, Lazdunski M & Romey G. (1996). K(V)LQT1 and lsK (minK) proteins associate to form the I(Ks) cardiac potassium current. *Nature* **384,** 78-80.

Barro-Soria R, Perez ME & Larsson HP. (2015). KCNE3 acts by promoting voltage sensor activation in KCNQ1. *Proc Natl Acad Sci U S A* **112,** E7286-7292.

Bastianelli E. (2003). Distribution of calcium-binding proteins in the cerebellum. *Cerebellum* **2,** 242-262.

Bayer KU, De Koninck P, Leonard AS, Hell JW & Schulman H. (2001). Interaction with the NMDA receptor locks CaMKII in an active conformation. *Nature* **411,** 801-805.

Beacham D, Ahn M, Catterall WA & Scheuer T. (2007). Sites and molecular mechanisms of modulation of Na(v)1.2 channels by Fyn tyrosine kinase. *J Neurosci* **27,** 11543-11551.

Bean BP. (2007). The action potential in mammalian central neurons. *Nat Rev Neurosci* **8,** 451-465.

Begum R, Bakiri Y, Volynski KE & Kullmann DM. (2016). Action potential broadening in a presynaptic channelopathy. *Nat Commun* **7,** 12102.

Beierlein M & Regehr WG. (2006). Local interneurons regulate synaptic strength by retrograde release of endocannabinoids. *J Neurosci* **26,** 9935-9943.

Belmeguenai A, Hosy E, Bengtsson F, Pedroarena CM, Piochon C, Teuling E, He Q, Ohtsuki G, De Jeu MT, Elgersma Y, De Zeeuw CI, Jorntell H & Hansel C. (2010). Intrinsic plasticity complements long-term potentiation in parallel fiber input gain control in cerebellar Purkinje cells. *J Neurosci* **30,** 13630-13643.

Ben-Johny M, Yang PS, Niu J, Yang W, Joshi-Mukherjee R & Yue DT. (2014). Conservation of Ca2+/calmodulin regulation across Na and Ca2+ channels. *Cell* **157,** 1657-1670.

Berendt FJ, Park KS & Trimmer JS. (2010). Multisite phosphorylation of voltage-gated sodium channel alpha subunits from rat brain. *J Proteome Res* **9,** 1976-1984.

Berkefeld H, Fakler B & Schulte U. (2010). Ca2+-activated K+ channels: from protein complexes to function. *Physiol Rev* **90,** 1437-1459.

Berkefeld H, Sailer CA, Bildl W, Rohde V, Thumfart JO, Eble S, Klugbauer N, Reisinger E, Bischofberger J, Oliver D, Knaus HG, Schulte U & Fakler B. (2006). BKCa-Cav channel complexes mediate rapid and localized Ca2+-activated K+ signaling. *Science* **314,** 615-620.

Bers DM, Patton CW & Nuccitelli R. (2010). A practical guide to the preparation of Ca(2+) buffers. *Methods Cell Biol* **99,** 1-26.

Blot A & Barbour B. (2014). Ultra-rapid axon-axon ephaptic inhibition of cerebellar Purkinje cells by the pinceau. *Nat Neurosci* **17,** 289-295.

Bosch MK, Carrasquillo Y, Ransdell JL, Kanakamedala A, Ornitz DM & Nerbonne JM. (2015). Intracellular FGF14 (iFGF14) Is Required for Spontaneous and Evoked Firing in Cerebellar Purkinje Neurons and for Motor Coordination and Balance. *J Neurosci* **35,** 6752-6769.

Bowie D. (2018). Polyamine-mediated channel block of ionotropic glutamate receptors and its regulation by auxiliary proteins. *J Biol Chem* **293,** 18789-18802.

Bowie D, Lange GD & Mayer ML. (1998). Activity-dependent modulation of glutamate receptors by polyamines. *J Neurosci* **18,** 8175-8185.

Bowie D & Mayer ML. (1995). Inward rectification of both AMPA and kainate subtype glutamate receptors generated by polyamine-mediated ion channel block. *Neuron* **15,** 453-462.

Brager DH & Johnston D. (2007). Plasticity of intrinsic excitability during long-term depression is mediated through mGluR-dependent changes in I(h) in hippocampal CA1 pyramidal neurons. *J Neurosci* **27,** 13926-13937.

Brette R. (2013). Sharpness of spike initiation in neurons explained by compartmentalization. *PLoS Comput Biol* **9,** e1003338.

Brickley SG, Revilla V, Cull-Candy SG, Wisden W & Farrant M. (2001). Adaptive regulation of neuronal excitability by a voltage-independent potassium conductance. *Nature* **409,** 88-92.

Brown DA & Adams PR. (1980). Muscarinic suppression of a novel voltage-sensitive K+ current in a vertebrate neurone. *Nature* **283,** 673-676.

Cai X, Liang CW, Muralidharan S, Kao JP, Tang CM & Thompson SM. (2004). Unique roles of SK and Kv4.2 potassium channels in dendritic integration. *Neuron* **44,** 351-364.

Caillard O, Moreno H, Schwaller B, Llano I, Celio MR & Marty A. (2000). Role of the calcium-binding protein parvalbumin in short-term synaptic plasticity. *Proc Natl Acad Sci U S A* **97,** 13372-13377.

Cain SM & Snutch TP. (2010). Contributions of T-type calcium channel isoforms to neuronal firing. *Channels (Austin)* **4,** 475-482.

Callsen B, Isbrandt D, Sauter K, Hartmann LS, Pongs O & Bahring R. (2005). Contribution of N- and C-terminal Kv4.2 channel domains to KChIP interaction [corrected]. *J Physiol* **568,** 397-412.

Campanac E, Gasselin C, Baude A, Rama S, Ankri N & Debanne D. (2013). Enhanced intrinsic excitability in basket cells maintains excitatory-inhibitory balance in hippocampal circuits. *Neuron* **77,** 712-722.

Cantrell AR & Catterall WA. (2001). Neuromodulation of Na+ channels: an unexpected form of cellular plasticity. *Nat Rev Neurosci* **2,** 397-407.

Cantrell AR, Tibbs VC, Yu FH, Murphy BJ, Sharp EM, Qu Y, Catterall WA & Scheuer T. (2002). Molecular mechanism of convergent regulation of brain Na(+) channels by protein kinase C and protein kinase A anchored to AKAP-15. *Mol Cell Neurosci* **21,** 63-80.

Carlier E, Sourdet V, Boudkkazi S, Deglise P, Ankri N, Fronzaroli-Molinieres L & Debanne D. (2006). Metabotropic glutamate receptor subtype 1 regulates sodium currents in rat neocortical pyramidal neurons. *J Physiol* **577,** 141-154.

Carr DB, Cooper DC, Ulrich SL, Spruston N & Surmeier DJ. (2002). Serotonin receptor activation inhibits sodium current and dendritic excitability in prefrontal cortex via a protein kinase C-dependent mechanism. *J Neurosci* **22,** 6846-6855.

Carr DB, Day M, Cantrell AR, Held J, Scheuer T, Catterall WA & Surmeier DJ. (2003). Transmitter modulation of slow, activity-dependent alterations in sodium channel availability endows neurons with a novel form of cellular plasticity. *Neuron* **39,** 793-806.

Carter AG & Regehr WG. (2000). Prolonged synaptic currents and glutamate spillover at the parallel fiber to stellate cell synapse. *J Neurosci* **20,** 4423-4434.

Carter AG & Regehr WG. (2002). Quantal events shape cerebellar interneuron firing. *Nat Neurosci* **5,** 1309-1318.

Catterall WA. (2000). From ionic currents to molecular mechanisms: the structure and function of voltage-gated sodium channels. *Neuron* **26,** 13-25.

Catterall WA. (2011). Voltage-gated calcium channels. *Cold Spring Harb Perspect Biol* **3,** a003947.

Catterall WA. (2017). Forty Years of Sodium Channels: Structure, Function, Pharmacology, and Epilepsy. *Neurochem Res* **42,** 2495-2504.

Chadderton P, Margrie TW & Hausser M. (2004). Integration of quanta in cerebellar granule cells during sensory processing. *Nature* **428,** 856-860.

Chan CS, Guzman JN, Ilijic E, Mercer JN, Rick C, Tkatch T, Meredith GE & Surmeier DJ. (2007). 'Rejuvenation' protects neurons in mouse models of Parkinson's disease. *Nature* **447,** 1081-1086.

Chavas J, Forero ME, Collin T, Llano I & Marty A. (2004). Osmotic tension as a possible link between GABA(A) receptor activation and intracellular calcium elevation. *Neuron* **44,** 701-713.

Chen Y, Yu FH, Sharp EM, Beacham D, Scheuer T & Catterall WA. (2008). Functional properties and differential neuromodulation of Na(v)1.6 channels. *Mol Cell Neurosci* **38,** 607-615.

Chen Y, Yu FH, Surmeier DJ, Scheuer T & Catterall WA. (2006). Neuromodulation of Na+ channel slow inactivation via cAMP-dependent protein kinase and protein kinase C. *Neuron* **49,** 409-420.

Cheron G, Sausbier M, Sausbier U, Neuhuber W, Ruth P, Dan B & Servais L. (2009). BK channels control cerebellar Purkinje and Golgi cell rhythmicity in vivo. *PLoS One* **4,** e7991.

Chevalier M, Lory P, Mironneau C, Macrez N & Quignard JF. (2006). T-type CaV3.3 calcium channels produce spontaneous low-threshold action potentials and intracellular calcium oscillations. *Eur J Neurosci* **23,** 2321-2329.

Christie JM, Chiu DN & Jahr CE. (2011). Ca(2+)-dependent enhancement of release by subthreshold somatic depolarization. *Nat Neurosci* **14,** 62-68.

Christie JM & Jahr CE. (2008). Dendritic NMDA receptors activate axonal calcium channels. *Neuron* **60,** 298-307.

Clark BA & Cull-Candy SG. (2002). Activity-dependent recruitment of extrasynaptic NMDA receptor activation at an AMPA receptor-only synapse. *J Neurosci* **22,** 4428-4436.

Clark BA, Monsivais P, Branco T, London M & Hausser M. (2005). The site of action potential initiation in cerebellar Purkinje neurons. *Nat Neurosci* **8,** 137-139.

Clarkson YL, Perkins EM, Cairncross CJ, Lyndon AR, Skehel PA & Jackson M. (2014). beta-III spectrin underpins ankyrin R function in Purkinje cell dendritic trees: protein complex critical for sodium channel activity is impaired by SCA5-associated mutations. *Hum Mol Genet* **23,** 3875-3882.

Coddington LT, Rudolph S, Vande Lune P, Overstreet-Wadiche L & Wadiche JI. (2013). Spillover-mediated feedforward inhibition functionally segregates interneuron activity. *Neuron* **78,** 1050-1062.

Coetzee WA, Amarillo Y, Chiu J, Chow A, Lau D, McCormack T, Moreno H, Nadal MS, Ozaita A, Pountney D, Saganich M, Vega-Saenz de Miera E & Rudy B. (1999). Molecular diversity of K+ channels. *Ann N Y Acad Sci* **868,** 233-285.

Cohen AS, Coussens CM, Raymond CR & Abraham WC. (1999). Long-lasting increase in cellular excitability associated with the priming of LTP induction in rat hippocampus. *J Neurophysiol* **82,** 3139-3148.

Connor JA & Stevens CF. (1971). Prediction of repetitive firing behaviour from voltage clamp data on an isolated neurone soma. *J Physiol* **213,** 31-53.

Connor JX, McCormack K, Pletsch A, Gaeta S, Ganetzky B, Chiu SY & Messing A. (2005). Genetic modifiers of the Kv beta2-null phenotype in mice. *Genes Brain Behav* **4,** 77-88.

Cooke SF, Attwell PJ & Yeo CH. (2004). Temporal properties of cerebellar-dependent memory consolidation. *J Neurosci* **24,** 2934-2941.

Coombs JS, Eccles JC & Fatt P. (1955). The electrical properties of the motoneurone membrane. *J Physiol* **130,** 291-325.

Coulter DA, Lo Turco JJ, Kubota M, Disterhoft JF, Moore JW & Alkon DL. (1989). Classical conditioning reduces amplitude and duration of calcium-dependent afterhyperpolarization in rabbit hippocampal pyramidal cells. *J Neurophysiol* **61,** 971-981.

Covarrubias M, Wei A, Salkoff L & Vyas TB. (1994). Elimination of rapid potassium channel inactivation by phosphorylation of the inactivation gate. *Neuron* **13,** 1403-1412.

Crill WE. (1996). Persistent sodium current in mammalian central neurons. *Annu Rev Physiol* **58,** 349-362.

Critz SD, Wible BA, Lopez HS & Brown AM. (1993). Stable expression and regulation of a rat brain K+ channel. *J Neurochem* **60,** 1175-1178.

Crowley JJ, Fioravante D & Regehr WG. (2009). Dynamics of fast and slow inhibition from cerebellar golgi cells allow flexible control of synaptic integration. *Neuron* **63,** 843-853.

Cudmore RH, Fronzaroli-Molinieres L, Giraud P & Debanne D. (2010). Spike-time precision and network synchrony are controlled by the homeostatic regulation of the D-type potassium current. *J Neurosci* **30,** 12885-12895.

Cudmore RH & Turrigiano GG. (2004). Long-term potentiation of intrinsic excitability in LV visual cortical neurons. *J Neurophysiol* **92,** 341-348.

Cui J, Cox DH & Aldrich RW. (1997). Intrinsic voltage dependence and Ca2+ regulation of mslo large conductance Ca-activated K+ channels. *J Gen Physiol* **109,** 647-673.

D'Angelo E, Solinas S, Mapelli J, Gandolfi D, Mapelli L & Prestori F. (2013). The cerebellar Golgi cell and spatiotemporal organization of granular layer activity. *Front Neural Circuits* **7,** 93.

Dani JA, Sanchez JA & Hille B. (1983). Lyotropic anions. Na channel gating and Ca electrode response. *J Gen Physiol* **81,** 255-281.

Daoudal G & Debanne D. (2003). Long-term plasticity of intrinsic excitability: learning rules and mechanisms. *Learn Mem* **10,** 456-465.

Dawe GB, Kadir MF, Venskutonyte R, Perozzo AM, Yan Y, Alexander RPD, Navarrete C, Santander EA, Arsenault M, Fuentes C, Aurousseau MRP, Frydenvang K, Barrera NP, Kastrup JS, Edwardson JM & Bowie D. (2019). Nanoscale Mobility of the Apo State and TARP Stoichiometry Dictate the Gating Behavior of Alternatively Spliced AMPA Receptors. *Neuron* **102,** 976-992 e975.

de Jonge MC, Black J, Deyo RA & Disterhoft JF. (1990). Learning-induced afterhyperpolarization reductions in hippocampus are specific for cell type and potassium conductance. *Exp Brain Res* **80,** 456-462.

de San Martin JZ, Jalil A & Trigo FF. (2015). Impact of single-site axonal GABAergic synaptic events on cerebellar interneuron activity. *J Gen Physiol* **146,** 477-493.

Debanne D, Inglebert Y & Russier M. (2019). Plasticity of intrinsic neuronal excitability. *Curr Opin Neurobiol* **54,** 73-82.

Desai NS, Rutherford LC & Turrigiano GG. (1999). Plasticity in the intrinsic excitability of cortical pyramidal neurons. *Nat Neurosci* **2,** 515-520.

Diana MA & Marty A. (2003). Characterization of depolarization-induced suppression of inhibition using paired interneuron--Purkinje cell recordings. *J Neurosci* **23,** 5906-5918.

Diana MA & Marty A. (2004). Endocannabinoid-mediated short-term synaptic plasticity: depolarization-induced suppression of inhibition (DSI) and depolarization-induced suppression of excitation (DSE). *Br J Pharmacol* **142,** 9-19.

Diana MA, Otsu Y, Maton G, Collin T, Chat M & Dieudonne S. (2007). T-type and L-type Ca2+ conductances define and encode the bimodal firing pattern of vestibulocerebellar unipolar brush cells. *J Neurosci* **27,** 3823-3838.

Dieudonne S & Dumoulin A. (2000). Serotonin-driven long-range inhibitory connections in the cerebellar cortex. *J Neurosci* **20,** 1837-1848.

Dino MR, Perachio AA & Mugnaini E. (2001). Cerebellar unipolar brush cells are targets of primary vestibular afferents: an experimental study in the gerbil. *Exp Brain Res* **140,** 162-170.

Disterhoft JF, Coulter DA & Alkon DL. (1986). Conditioning-specific membrane changes of rabbit hippocampal neurons measured in vitro. *Proc Natl Acad Sci U S A* **83,** 2733-2737.

Drain P, Dubin AE & Aldrich RW. (1994). Regulation of Shaker K+ channel inactivation gating by the cAMP-dependent protein kinase. *Neuron* **12,** 1097-1109.

Dubois CJ, Lachamp PM, Sun L, Mishina M & Liu SJ. (2016). Presynaptic GluN2D receptors detect glutamate spillover and regulate cerebellar GABA release. *J Neurophysiol* **115,** 271-285.

Dubois CJ, Ramamoorthy P, Whim MD & Liu SJ. (2012). Activation of NPY type 5 receptors induces a long-lasting increase in spontaneous GABA release from cerebellar inhibitory interneurons. *J Neurophysiol* **107,** 1655-1665.

Duguid I, Branco T, London M, Chadderton P & Hausser M. (2012). Tonic inhibition enhances fidelity of sensory information transmission in the cerebellar cortex. *J Neurosci* **32,** 11132-11143.

Duguid IC & Smart TG. (2004). Retrograde activation of presynaptic NMDA receptors enhances GABA release at cerebellar interneuron-Purkinje cell synapses. *Nat Neurosci* **7,** 525-533.

Eccles JC. (1967). *The cerebellum as a neuronal machine*. Springer Science & Business Media.

Edgerton JR & Reinhart PH. (2003). Distinct contributions of small and large conductance Ca2+-activated K+ channels to rat Purkinje neuron function. *J Physiol* **548,** 53-69.

Egorov AV, Hamam BN, Fransen E, Hasselmo ME & Alonso AA. (2002). Graded persistent activity in entorhinal cortex neurons. *Nature* **420,** 173-178.

Ekerot CF & Jorntell H. (2001). Parallel fibre receptive fields of Purkinje cells and interneurons are climbing fibre-specific. *Eur J Neurosci* **13,** 1303-1310.

Erisir A, Lau D, Rudy B & Leonard CS. (1999). Function of specific K(+) channels in sustained high-frequency firing of fast-spiking neocortical interneurons. *J Neurophysiol* **82,** 2476-2489.

Farrant M & Nusser Z. (2005). Variations on an inhibitory theme: phasic and tonic activation of GABA(A) receptors. *Nat Rev Neurosci* **6,** 215-229.

Fenwick EM, Marty A & Neher E. (1982a). A patch-clamp study of bovine chromaffin cells and of their sensitivity to acetylcholine. *J Physiol* **331,** 577-597.

Fenwick EM, Marty A & Neher E. (1982b). Sodium and calcium channels in bovine chromaffin cells. *J Physiol* **331,** 599-635.

Fernandez FR, Mehaffey WH, Molineux ML & Turner RW. (2005). High-threshold K+ current increases gain by offsetting a frequency-dependent increase in low-threshold K+ current. *J Neurosci* **25,** 363-371.

Fernandez JM, Fox AP & Krasne S. (1984). Membrane patches and whole-cell membranes: a comparison of electrical properties in rat clonal pituitary (GH3) cells. *J Physiol* **356,** 565-585.

Fierro L & Llano I. (1996). High endogenous calcium buffering in Purkinje cells from rat cerebellar slices. *J Physiol* **496 (Pt 3),** 617-625.

Fiszman ML, Barberis A, Lu C, Fu Z, Erdelyi F, Szabo G & Vicini S. (2005). NMDA receptors increase the size of GABAergic terminals and enhance GABA release. *J Neurosci* **25,** 2024-2031.

Fiszman ML, Erdelyi F, Szabo G & Vicini S. (2007). Presynaptic AMPA and kainate receptors increase the size of GABAergic terminals and enhance GABA release. *Neuropharmacology* **52,** 1631-1640.

Fleidervish IA, Friedman A & Gutnick MJ. (1996). Slow inactivation of Na+ current and slow cumulative spike adaptation in mouse and guinea-pig neocortical neurones in slices. *J Physiol* **493 (Pt 1),** 83-97.

Forti L, Cesana E, Mapelli J & D'Angelo E. (2006). Ionic mechanisms of autorhythmic firing in rat cerebellar Golgi cells. *J Physiol* **574,** 711-729.

Forti L, Pouzat C & Llano I. (2000). Action potential-evoked Ca2+ signals and calcium channels in axons of developing rat cerebellar interneurones. *J Physiol* **527 Pt 1,** 33-48.

Fukunaga K, Muller D & Miyamoto E. (1995). Increased phosphorylation of Ca2+/calmodulin-dependent protein kinase II and its endogenous substrates in the induction of long-term potentiation. *J Biol Chem* **270,** 6119-6124.

Gaffield MA & Christie JM. (2017). Movement Rate Is Encoded and Influenced by Widespread, Coherent Activity of Cerebellar Molecular Layer Interneurons. *J Neurosci* **37,** 4751-4765.

Gaffield MA, Rowan MJM, Amat SB, Hirai H & Christie JM. (2018). Inhibition gates supralinear Ca(2+) signaling in Purkinje cell dendrites during practiced movements. *Elife* **7**.

Gainey MA, Aman JW & Feldman DE. (2018). Rapid Disinhibition by Adjustment of PV Intrinsic Excitability during Whisker Map Plasticity in Mouse S1. *J Neurosci* **38,** 4749-4761.

Galante M & Diana MA. (2004). Group I metabotropic glutamate receptors inhibit GABA release at interneuron-Purkinje cell synapses through endocannabinoid production. *J Neurosci* **24,** 4865-4874.

Gall D, Roussel C, Susa I, D'Angelo E, Rossi P, Bearzatto B, Galas MC, Blum D, Schurmans S & Schiffmann SN. (2003). Altered neuronal excitability in cerebellar granule cells of mice lacking calretinin. *J Neurosci* **23,** 9320-9327.

Garrido JJ, Giraud P, Carlier E, Fernandes F, Moussif A, Fache MP, Debanne D & Dargent B. (2003). A targeting motif involved in sodium channel clustering at the axonal initial segment. *Science* **300,** 2091-2094.

Gasparini S & DiFrancesco D. (1997). Action of the hyperpolarization-activated current (Ih) blocker ZD 7288 in hippocampal CA1 neurons. *Pflugers Arch* **435,** 99-106.

Gasser A, Cheng X, Gilmore ES, Tyrrell L, Waxman SG & Dib-Hajj SD. (2010). Two Nedd4-binding motifs underlie modulation of sodium channel Nav1.6 by p38 MAPK. *J Biol Chem* **285,** 26149-26161.

Gershon E, Weigl L, Lotan I, Schreibmayer W & Dascal N. (1992). Protein kinase A reduces voltage-dependent Na+ current in Xenopus oocytes. *J Neurosci* **12,** 3743-3752.

Giese KP, Storm JF, Reuter D, Fedorov NB, Shao LR, Leicher T, Pongs O & Silva AJ. (1998). Reduced K+ channel inactivation, spike broadening, and after-hyperpolarization in Kvbeta1.1-deficient mice with impaired learning. *Learn Mem* **5,** 257-273.

Glitsch M, Llano I & Marty A. (1996). Glutamate as a candidate retrograde messenger at interneurone-Purkinje cell synapses of rat cerebellum. *J Physiol* **497 (Pt 2),** 531-537.

Glitsch M & Marty A. (1999). Presynaptic effects of NMDA in cerebellar Purkinje cells and interneurons. *J Neurosci* **19,** 511-519.

Goldberg JA & Wilson CJ. (2005). Control of spontaneous firing patterns by the selective coupling of calcium currents to calcium-activated potassium currents in striatal cholinergic interneurons. *J Neurosci* **25,** 10230-10238.

Grasselli G, He Q, Wan V, Adelman JP, Ohtsuki G & Hansel C. (2016). Activity-Dependent Plasticity of Spike Pauses in Cerebellar Purkinje Cells. *Cell Rep* **14,** 2546-2553.

Grieco TM, Malhotra JD, Chen C, Isom LL & Raman IM. (2005). Open-channel block by the cytoplasmic tail of sodium channel beta4 as a mechanism for resurgent sodium current. *Neuron* **45,** 233-244.

Gu C, Zhou W, Puthenveedu MA, Xu M, Jan YN & Jan LY. (2006). The microtubule plus-end tracking protein EB1 is required for Kv1 voltage-gated K+ channel axonal targeting. *Neuron* **52,** 803-816.

Gulbis JM, Mann S & MacKinnon R. (1999). Structure of a voltage-dependent K+ channel beta subunit. *Cell* **97,** 943-952.

Gutman GA, Chandy KG, Grissmer S, Lazdunski M, McKinnon D, Pardo LA, Robertson GA, Rudy B, Sanguinetti MC, Stuhmer W & Wang X. (2005). International Union of Pharmacology. LIII. Nomenclature and molecular relationships of voltage-gated potassium channels. *Pharmacol Rev* **57,** 473-508.

Hammond RS, Bond CT, Strassmaier T, Ngo-Anh TJ, Adelman JP, Maylie J & Stackman RW. (2006). Small-conductance Ca2+-activated K+ channel type 2 (SK2) modulates hippocampal learning, memory, and synaptic plasticity. *J Neurosci* **26,** 1844-1853.

Hausser M & Clark BA. (1997). Tonic synaptic inhibition modulates neuronal output pattern and spatiotemporal synaptic integration. *Neuron* **19,** 665-678.

Heath NC, Rizwan AP, Engbers JD, Anderson D, Zamponi GW & Turner RW. (2014). The expression pattern of a Cav3-Kv4 complex differentially regulates spike output in cerebellar granule cells. *J Neurosci* **34,** 8800-8812.

Heinemann S, Rettig J, Scott V, Parcej DN, Lorra C, Dolly J & Pongs O. (1994). The inactivation behaviour of voltage-gated K-channels may be determined by association of alpha- and beta-subunits. *J Physiol Paris* **88,** 173-180.

Heinemann SH, Rettig J, Graack HR & Pongs O. (1996). Functional characterization of Kv channel beta-subunits from rat brain. *J Physiol* **493 (Pt 3),** 625-633.

Heinemann SH, Rettig J, Wunder F & Pongs O. (1995). Molecular and functional characterization of a rat brain Kv beta 3 potassium channel subunit. *FEBS Lett* **377,** 383-389.

Herzog RI, Liu C, Waxman SG & Cummins TR. (2003). Calmodulin binds to the C terminus of sodium channels Nav1.4 and Nav1.6 and differentially modulates their functional properties. *J Neurosci* **23,** 8261-8270.

Hirono M & Obata K. (2006). Alpha-adrenoceptive dual modulation of inhibitory GABAergic inputs to Purkinje cells in the mouse cerebellum. *J Neurophysiol* **95,** 700-708.

Hodgkin AL & Huxley AF. (1952). A quantitative description of membrane current and its application to conduction and excitation in nerve. *J Physiol* **117,** 500-544.

Hoffman DA & Johnston D. (1998). Downregulation of transient K+ channels in dendrites of hippocampal CA1 pyramidal neurons by activation of PKA and PKC. *J Neurosci* **18,** 3521-3528.

Hoffman DA & Johnston D. (1999). Neuromodulation of dendritic action potentials. *J Neurophysiol* **81,** 408-411.

Hoffman DA, Magee JC, Colbert CM & Johnston D. (1997). K+ channel regulation of signal propagation in dendrites of hippocampal pyramidal neurons. *Nature* **387,** 869-875.

Hotson JR, Prince DA & Schwartzkroin PA. (1979). Anomalous inward rectification in hippocampal neurons. *J Neurophysiol* **42,** 889-895.

Hsu WC, Scala F, Nenov MN, Wildburger NC, Elferink H, Singh AK, Chesson CB, Buzhdygan T, Sohail M, Shavkunov AS, Panova NI, Nilsson CL, Rudra JS, Lichti CF & Laezza F. (2016). CK2 activity is required for the interaction of FGF14 with voltage-gated sodium channels and neuronal excitability. *FASEB J* **30,** 2171-2186.

Hu H & Jonas P. (2014). A supercritical density of Na(+) channels ensures fast signaling in GABAergic interneuron axons. *Nat Neurosci* **17,** 686-693.

Hu H, Roth FC, Vandael D & Jonas P. (2018). Complementary Tuning of Na(+) and K(+) Channel Gating Underlies Fast and Energy-Efficient Action Potentials in GABAergic Interneuron Axons. *Neuron* **98,** 156-165 e156.

Hu W & Bean BP. (2018). Differential Control of Axonal and Somatic Resting Potential by Voltage-Dependent Conductances in Cortical Layer 5 Pyramidal Neurons. *Neuron* **99,** 1355.

Hu W, Tian C, Li T, Yang M, Hou H & Shu Y. (2009). Distinct contributions of Na(v)1.6 and Na(v)1.2 in action potential initiation and backpropagation. *Nat Neurosci* **12,** 996-1002.

Huang CY & Rasband MN. (2018). Axon initial segments: structure, function, and disease. *Ann N Y Acad Sci* **1420,** 46-61.

Huang XY, Morielli AD & Peralta EG. (1993). Tyrosine kinase-dependent suppression of a potassium channel by the G protein-coupled m1 muscarinic acetylcholine receptor. *Cell* **75,** 1145-1156.

Huang XY, Morielli AD & Peralta EG. (1994). Molecular basis of cardiac potassium channel stimulation by protein kinase A. *Proc Natl Acad Sci U S A* **91,** 624-628.

Hudmon A, Schulman H, Kim J, Maltez JM, Tsien RW & Pitt GS. (2005). CaMKII tethers to L-type Ca2+ channels, establishing a local and dedicated integrator of Ca2+ signals for facilitation. *J Cell Biol* **171,** 537-547.

Hull CA, Chu Y, Thanawala M & Regehr WG. (2013). Hyperpolarization induces a long-term increase in the spontaneous firing rate of cerebellar Golgi cells. *J Neurosci* **33,** 5895-5902.

Hund TJ, Koval OM, Li J, Wright PJ, Qian L, Snyder JS, Gudmundsson H, Kline CF, Davidson NP, Cardona N, Rasband MN, Anderson ME & Mohler PJ. (2010). A beta(IV)-spectrin/CaMKII signaling complex is essential for membrane excitability in mice. *J Clin Invest* **120,** 3508-3519.

Ireland DR & Abraham WC. (2002). Group I mGluRs increase excitability of hippocampal CA1 pyramidal neurons by a PLC-independent mechanism. *J Neurophysiol* **88,** 107-116.

Isom LL, Ragsdale DS, De Jongh KS, Westenbroek RE, Reber BF, Scheuer T & Catterall WA. (1995). Structure and function of the beta 2 subunit of brain sodium channels, a transmembrane glycoprotein with a CAM motif. *Cell* **83,** 433-442.

Ito M & Itō M. (1984). *The cerebellum and neural control*. Raven press.

Ito M & Kano M. (1982). Long-lasting depression of parallel fiber-Purkinje cell transmission induced by conjunctive stimulation of parallel fibers and climbing fibers in the cerebellar cortex. *Neurosci Lett* **33,** 253-258.

Jaarsma D, Ruigrok TJ, Caffe R, Cozzari C, Levey AI, Mugnaini E & Voogd J. (1997). Cholinergic innervation and receptors in the cerebellum. *Prog Brain Res* **114,** 67-96.

Jarnot M & Corbett AM. (2006). Immunolocalization of NaV1.2 channel subtypes in rat and cat brain and spinal cord with high affinity antibodies. *Brain Res* **1107,** 1-12.

Jelitai M, Puggioni P, Ishikawa T, Rinaldi A & Duguid I. (2016). Dendritic excitation-inhibition balance shapes cerebellar output during motor behaviour. *Nat Commun* **7,** 13722.

Jentsch TJ. (2000). Neuronal KCNQ potassium channels: physiology and role in disease. *Nat Rev Neurosci* **1,** 21-30.

Jerng HH, Kunjilwar K & Pfaffinger PJ. (2005). Multiprotein assembly of Kv4.2, KChIP3 and DPP10 produces ternary channel complexes with ISA-like properties. *J Physiol* **568,** 767-788.

Jerng HH, Lauver AD & Pfaffinger PJ. (2007). DPP10 splice variants are localized in distinct neuronal populations and act to differentially regulate the inactivation properties of Kv4-based ion channels. *Mol Cell Neurosci* **35,** 604-624.

Jerng HH & Pfaffinger PJ. (2008). Multiple Kv channel-interacting proteins contain an N-terminal transmembrane domain that regulates Kv4 channel trafficking and gating. *J Biol Chem* **283,** 36046-36059.

Jorntell H, Bengtsson F, Schonewille M & De Zeeuw CI. (2010). Cerebellar molecular layer interneurons - computational properties and roles in learning. *Trends Neurosci* **33,** 524-532.

Jorntell H & Ekerot CF. (2002). Reciprocal bidirectional plasticity of parallel fiber receptive fields in cerebellar Purkinje cells and their afferent interneurons. *Neuron* **34,** 797-806.

Jorntell H & Ekerot CF. (2003). Receptive field plasticity profoundly alters the cutaneous parallel fiber synaptic input to cerebellar interneurons in vivo. *J Neurosci* **23,** 9620-9631.

Kaczorowski CC, Disterhoft J & Spruston N. (2007). Stability and plasticity of intrinsic membrane properties in hippocampal CA1 pyramidal neurons: effects of internal anions. *J Physiol* **578,** 799-818.

Kalume F, Yu FH, Westenbroek RE, Scheuer T & Catterall WA. (2007). Reduced sodium current in Purkinje neurons from Nav1.1 mutant mice: implications for ataxia in severe myoclonic epilepsy in infancy. *J Neurosci* **27,** 11065-11074.

Kanda VA, Lewis A, Xu X & Abbott GW. (2011a). KCNE1 and KCNE2 inhibit forward trafficking of homomeric N-type voltage-gated potassium channels. *Biophys J* **101,** 1354-1363.

Kanda VA, Lewis A, Xu X & Abbott GW. (2011b). KCNE1 and KCNE2 provide a checkpoint governing voltage-gated potassium channel alpha-subunit composition. *Biophys J* **101,** 1364-1375.

Kang C, Tian C, Sonnichsen FD, Smith JA, Meiler J, George AL, Jr., Vanoye CG, Kim HJ & Sanders CR. (2008). Structure of KCNE1 and implications for how it modulates the KCNQ1 potassium channel. *Biochemistry* **47,** 7999-8006.

Karmarkar UR & Buonomano DV. (2006). Different forms of homeostatic plasticity are engaged with distinct temporal profiles. *Eur J Neurosci* **23,** 1575-1584.

Kass JI & Mintz IM. (2006). Silent plateau potentials, rhythmic bursts, and pacemaker firing: three patterns of activity that coexist in quadristable subthalamic neurons. *Proc Natl Acad Sci U S A* **103,** 183-188.

Kato K, Clifford DB & Zorumski CF. (1993). Long-term potentiation during whole-cell recording in rat hippocampal slices. *Neuroscience* **53,** 39-47.

Katz E, Stoler O, Scheller A, Khrapunsky Y, Goebbels S, Kirchhoff F, Gutnick MJ, Wolf F & Fleidervish IA. (2018). Role of sodium channel subtype in action potential generation by neocortical pyramidal neurons. *Proc Natl Acad Sci U S A* **115,** E7184-E7192.

Kerr CWH & Bishop GA. (1991). Topographical Organization in the Origin of Serotoninergic Projections to Different Regions of the Cat Cerebellar Cortex. *J Comp Neurol* **304,** 502-515.

Khaliq ZM, Gouwens NW & Raman IM. (2003). The contribution of resurgent sodium current to high-frequency firing in Purkinje neurons: an experimental and modeling study. *J Neurosci* **23,** 4899-4912.

Khaliq ZM & Raman IM. (2006). Relative contributions of axonal and somatic Na channels to action potential initiation in cerebellar Purkinje neurons. *J Neurosci* **26,** 1935-1944.

Kim J, Lee S, Tsuda S, Zhang X, Asrican B, Gloss B, Feng G & Augustine GJ. (2014). Optogenetic mapping of cerebellar inhibitory circuitry reveals spatially biased coordination of interneurons via electrical synapses. *Cell Rep* **7,** 1601-1613.

Kim J, Wei DS & Hoffman DA. (2005). Kv4 potassium channel subunits control action potential repolarization and frequency-dependent broadening in rat hippocampal CA1 pyramidal neurones. *J Physiol* **569,** 41-57.

Kim LA, Furst J, Gutierrez D, Butler MH, Xu S, Goldstein SA & Grigorieff N. (2004). Three-dimensional structure of I(to); Kv4.2-KChIP2 ion channels by electron microscopy at 21 Angstrom resolution. *Neuron* **41,** 513-519.

Kimitsuki T, Mitsuiye T & Noma A. (1990). Negative shift of cardiac Na+ channel kinetics in cell-attached patch recordings. *Am J Physiol* **258,** H247-254.

Kitazawa M, Kubo Y & Nakajo K. (2015). Kv4.2 and accessory dipeptidyl peptidase-like protein 10 (DPP10) subunit preferentially form a 4:2 (Kv4.2:DPP10) channel complex. *J Biol Chem* **290,** 22724-22733.

Klapstein GJ, Vietla S, Lieberman DN, Gray PA, Airaksinen MS, Thoenen H, Meyer M & Mody I. (1998). Calbindin-D28k fails to protect hippocampal neurons against ischemia in spite of its cytoplasmic calcium buffering properties: evidence from calbindin-D28k knockout mice. *Neuroscience* **85,** 361-373.

Kole MH & Brette R. (2018). The electrical significance of axon location diversity. *Curr Opin Neurobiol* **51,** 52-59.

Kole MH, Ilschner SU, Kampa BM, Williams SR, Ruben PC & Stuart GJ. (2008). Action potential generation requires a high sodium channel density in the axon initial segment. *Nat Neurosci* **11,** 178-186.

Kole MH, Letzkus JJ & Stuart GJ. (2007). Axon initial segment Kv1 channels control axonal action potential waveform and synaptic efficacy. *Neuron* **55,** 633-647.

Kole MJ, Qian J, Waase MP, Klassen TL, Chen TT, Augustine GJ & Noebels JL. (2015). Selective Loss of Presynaptic Potassium Channel Clusters at the Cerebellar Basket Cell Terminal Pinceau in Adam11 Mutants Reveals Their Role in Ephaptic Control of Purkinje Cell Firing. *J Neurosci* **35,** 11433-11444.

Komada M & Soriano P. (2002). [Beta]IV-spectrin regulates sodium channel clustering through ankyrin-G at axon initial segments and nodes of Ranvier. *J Cell Biol* **156,** 337-348.

Kondo S & Marty A. (1997). Protein kinase A-mediated enhancement of miniature IPSC frequency by noradrenaline in rat cerebellar stellate cells. *J Physiol-London* **498,** 165-176.

Kondo S & Marty A. (1998). Differential effects of noradrenaline on evoked, spontaneous and miniature IPSCs in rat cerebellar stellate cells. *J Physiol-London* **509,** 233-243.

Konnerth A, Dreessen J & Augustine GJ. (1992). Brief dendritic calcium signals initiate long-lasting synaptic depression in cerebellar Purkinje cells. *Proc Natl Acad Sci U S A* **89,** 7051-7055.

Kreitzer AC & Regehr WG. (2001). Cerebellar depolarization-induced suppression of inhibition is mediated by endogenous cannabinoids. *J Neurosci* **21,** RC174.

Kress GJ, Dowling MJ, Eisenman LN & Mennerick S. (2010). Axonal sodium channel distribution shapes the depolarized action potential threshold of dentate granule neurons. *Hippocampus* **20,** 558-571.

Kuba H. (2012). Structural tuning and plasticity of the axon initial segment in auditory neurons. *J Physiol* **590,** 5571-5579.

Lachamp PM, Liu Y & Liu SJ. (2009). Glutamatergic modulation of cerebellar interneuron activity is mediated by an enhancement of GABA release and requires protein kinase A/RIM1alpha signaling. *J Neurosci* **29,** 381-392.

Laezza F, Lampert A, Kozel MA, Gerber BR, Rush AM, Nerbonne JM, Waxman SG, Dib-Hajj SD & Ornitz DM. (2009). FGF14 N-terminal splice variants differentially modulate Nav1.2 and Nav1.6-encoded sodium channels. *Mol Cell Neurosci* **42,** 90-101.

Laine J & Axelrad H. (1998). Lugaro cells target basket and stellate cells in the cerebellar cortex. *Neuroreport* **9,** 2399-2403.

Lancaster B & Nicoll RA. (1987). Properties of two calcium-activated hyperpolarizations in rat hippocampal neurones. *J Physiol* **389,** 187-203.

Larkum ME, Zhu JJ & Sakmann B. (2001). Dendritic mechanisms underlying the coupling of the dendritic with the axonal action potential initiation zone of adult rat layer 5 pyramidal neurons. *J Physiol* **533,** 447-466.

Latham A & Paul DH. (1971). Spontaneous activity of cerebellar Purkinje cells and their responses to impulses in climbing fibres. *J Physiol* **213,** 135-156.

Lawrence JJ, Saraga F, Churchill JF, Statland JM, Travis KE, Skinner FK & McBain CJ. (2006). Somatodendritic Kv7/KCNQ/M channels control interspike interval in hippocampal interneurons. *J Neurosci* **26,** 12325-12338.

Lee SH, Schwaller B & Neher E. (2000). Kinetics of Ca2+ binding to parvalbumin in bovine chromaffin cells: implications for [Ca2+] transients of neuronal dendrites. *J Physiol* **525 Pt 2,** 419-432.

Lein ES, Hawrylycz MJ, Ao N, Ayres M, Bensinger A, Bernard A, Boe AF, Boguski MS, Brockway KS, Byrnes EJ, Chen L, Chen L, Chen TM, Chin MC, Chong J, Crook BE, Czaplinska A, Dang CN, Datta S, Dee NR, Desaki AL, Desta T, Diep E, Dolbeare TA, Donelan MJ, Dong HW, Dougherty JG, Duncan BJ, Ebbert AJ, Eichele G, Estin LK, Faber C, Facer BA, Fields R, Fischer SR, Fliss TP, Frensley C, Gates SN, Glattfelder KJ, Halverson KR, Hart MR, Hohmann JG, Howell MP, Jeung DP, Johnson RA, Karr PT, Kawal R, Kidney JM, Knapik RH, Kuan CL, Lake JH, Laramee AR, Larsen KD, Lau C, Lemon TA, Liang AJ, Liu Y, Luong LT, Michaels J, Morgan JJ, Morgan RJ, Mortrud MT, Mosqueda NF, Ng LL, Ng R, Orta GJ, Overly CC, Pak TH, Parry SE, Pathak SD, Pearson OC, Puchalski RB, Riley ZL, Rockett HR, Rowland SA, Royall JJ, Ruiz MJ, Sarno NR, Schaffnit K, Shapovalova NV, Sivisay T, Slaughterbeck CR, Smith SC, Smith KA, Smith BI, Sodt AJ, Stewart NN, Stumpf KR, Sunkin SM, Sutram M, Tam A, Teemer CD, Thaller C, Thompson CL, Varnam LR, Visel A, Whitlock RM, Wohnoutka PE, Wolkey CK, Wong VY, Wood M, Yaylaoglu MB, Young RC, Youngstrom BL, Yuan XF, Zhang B, Zwingman TA & Jones AR. (2007). Genome-wide atlas of gene expression in the adult mouse brain. *Nature* **445,** 168-176.

Leonard AS, Lim IA, Hemsworth DE, Horne MC & Hell JW. (1999). Calcium/calmodulin-dependent protein kinase II is associated with the N-methyl-D-aspartate receptor. *Proc Natl Acad Sci U S A* **96,** 3239-3244.

Levin G, Keren T, Peretz T, Chikvashvili D, Thornhill WB & Lotan I. (1995). Regulation of RCK1 currents with a cAMP analog via enhanced protein synthesis and direct channel phosphorylation. *J Biol Chem* **270,** 14611-14618.

Levitan IB. (1994). Modulation of ion channels by protein phosphorylation and dephosphorylation. *Annu Rev Physiol* **56,** 193-212.

Lewis A, McCrossan ZA & Abbott GW. (2004). MinK, MiRP1, and MiRP2 diversify Kv3.1 and Kv3.2 potassium channel gating. *J Biol Chem* **279,** 7884-7892.

Lewis AH & Raman IM. (2014). Resurgent current of voltage-gated Na(+) channels. *J Physiol* **592,** 4825-4838.

Li J, Yu Z, Xu J, Feng R, Gao Q, Boczek T, Liu J, Li Z, Wang Q, Lei M, Gong J, Hu H, Minobe E, Ji HL, Kameyama M & Guo F. (2018). The Effect of Ca(2+), Lobe-Specificity, and CaMKII on CaM Binding to NaV1.1. *Int J Mol Sci* **19**.

Li M, West JW, Lai Y, Scheuer T & Catterall WA. (1992). Functional modulation of brain sodium channels by cAMP-dependent phosphorylation. *Neuron* **8,** 1151-1159.

Li M, West JW, Numann R, Murphy BJ, Scheuer T & Catterall WA. (1993). Convergent regulation of sodium channels by protein kinase C and cAMP-dependent protein kinase. *Science* **261,** 1439-1442.

Lien CC, Martina M, Schultz JH, Ehmke H & Jonas P. (2002). Gating, modulation and subunit composition of voltage-gated K(+) channels in dendritic inhibitory interneurones of rat hippocampus. *J Physiol* **538,** 405-419.

Linley JE. (2013). Perforated whole-cell patch-clamp recording. *Methods Mol Biol* **998,** 149-157.

Lisman J, Schulman H & Cline H. (2002). The molecular basis of CaMKII function in synaptic and behavioural memory. *Nat Rev Neurosci* **3,** 175-190.

Liu H, Zhao SN, Zhao GY, Sun L, Chu CP & Qiu DL. (2014). N-methyl-d-aspartate inhibits cerebellar Purkinje cell activity via the excitation of molecular layer interneurons under in vivo conditions in mice. *Brain Res* **1560,** 1-9.

Liu S & Zheng P. (2013). Altered PKA modulation in the Na(v)1.1 epilepsy variant I1656M. *J Neurophysiol* **110,** 2090-2098.

Liu SJ. (2007). Biphasic modulation of GABA release from stellate cells by glutamatergic receptor subtypes. *J Neurophysiol* **98,** 550-556.

Liu SJ & Lachamp P. (2006). The activation of excitatory glutamate receptors evokes a long-lasting increase in the release of GABA from cerebellar stellate cells. *J Neurosci* **26,** 9332-9339.

Liu SJ, Lachamp P, Liu Y, Savtchouk I & Sun L. (2008). Long-term synaptic plasticity in cerebellar stellate cells. *Cerebellum* **7,** 559-562.

Liu Y, Formisano L, Savtchouk I, Takayasu Y, Szabo G, Zukin RS & Liu SJ. (2010). A single fear-inducing stimulus induces a transcription-dependent switch in synaptic AMPAR phenotype. *Nat Neurosci* **13,** 223-231.

Liu Y, Savtchouk I, Acharjee S & Liu SJ. (2011). Inhibition of Ca2+-activated large-conductance K+ channel activity alters synaptic AMPA receptor phenotype in mouse cerebellar stellate cells. *J Neurophysiol* **106,** 144-152.

Llano I & Gerschenfeld HM. (1993a). Beta-Adrenergic Enhancement of Inhibitory Synaptic Activity in Rat Cerebellar Stellate and Purkinje-Cells. *J Physiol-London* **468,** 201-224.

Llano I & Gerschenfeld HM. (1993b). Inhibitory synaptic currents in stellate cells of rat cerebellar slices. *J Physiol* **468,** 177-200.

Llano I, Leresche N & Marty A. (1991). Calcium entry increases the sensitivity of cerebellar Purkinje cells to applied GABA and decreases inhibitory synaptic currents. *Neuron* **6,** 565-574.

Llano I & Marty A. (1995). Presynaptic metabotropic glutamatergic regulation of inhibitory synapses in rat cerebellar slices. *J Physiol* **486 (Pt 1),** 163-176.

Llano I, Tan YP & Caputo C. (1997). Spatial heterogeneity of intracellular Ca2+ signals in axons of basket cells from rat cerebellar slices. *J Physiol* **502 (Pt 3),** 509-519.

Llinas R & Sugimori M. (1980). Electrophysiological properties of in vitro Purkinje cell somata in mammalian cerebellar slices. *J Physiol* **305,** 171-195.

Llinas RR. (1988). The intrinsic electrophysiological properties of mammalian neurons: insights into central nervous system function. *Science* **242,** 1654-1664.

Long SB, Campbell EB & Mackinnon R. (2005a). Crystal structure of a mammalian voltage-dependent Shaker family K+ channel. *Science* **309,** 897-903.

Long SB, Campbell EB & Mackinnon R. (2005b). Voltage sensor of Kv1.2: structural basis of electromechanical coupling. *Science* **309,** 903-908.

Lorincz A & Nusser Z. (2008). Cell-type-dependent molecular composition of the axon initial segment. *J Neurosci* **28,** 14329-14340.

Lou JY, Laezza F, Gerber BR, Xiao M, Yamada KA, Hartmann H, Craig AM, Nerbonne JM & Ornitz DM. (2005). Fibroblast growth factor 14 is an intracellular modulator of voltage-gated sodium channels. *J Physiol* **569,** 179-193.

Ma Z, Lou XJ & Horrigan FT. (2006). Role of charged residues in the S1-S4 voltage sensor of BK channels. *J Gen Physiol* **127,** 309-328.

Maccaferri G, Mangoni M, Lazzari A & DiFrancesco D. (1993). Properties of the hyperpolarization-activated current in rat hippocampal CA1 pyramidal cells. *J Neurophysiol* **69,** 2129-2136.

Maccaferri G & McBain CJ. (1996). The hyperpolarization-activated current (Ih) and its contribution to pacemaker activity in rat CA1 hippocampal stratum oriens-alveus interneurones. *J Physiol* **497 (Pt 1),** 119-130.

Maffei A & Turrigiano GG. (2008). Multiple modes of network homeostasis in visual cortical layer 2/3. *J Neurosci* **28,** 4377-4384.

Magee JC. (1998). Dendritic hyperpolarization-activated currents modify the integrative properties of hippocampal CA1 pyramidal neurons. *J Neurosci* **18,** 7613-7624.

Magee JC. (1999). Dendritic Ih normalizes temporal summation in hippocampal CA1 neurons. *Nat Neurosci* **2,** 848.

Malenka RC & Nicoll RA. (1999). Long-term potentiation--a decade of progress? *Science* **285,** 1870-1874.

Mann-Metzer P & Yarom Y. (1999). Electrotonic coupling interacts with intrinsic properties to generate synchronized activity in cerebellar networks of inhibitory interneurons. *J Neurosci* **19,** 3298-3306.

Mann-Metzer P & Yarom Y. (2002a). Jittery trains induced by synaptic-like currents in cerebellar inhibitory interneurons. *J Neurophysiol* **87,** 149-156.

Mann-Metzer P & Yarom Y. (2002b). Pre- and postsynaptic inhibition mediated by GABA(B) receptors in cerebellar inhibitory interneurons. *J Neurophysiol* **87,** 183-190.

Marr D. (1969). A theory of cerebellar cortex. *J Physiol* **202,** 437-470.

Marrion NV & Tavalin SJ. (1998). Selective activation of Ca2+-activated K+ channels by co-localized Ca2+ channels in hippocampal neurons. *Nature* **395,** 900-905.

Martina M & Jonas P. (1997). Functional differences in Na+ channel gating between fast-spiking interneurones and principal neurones of rat hippocampus. *J Physiol* **505 (Pt 3),** 593-603.

Martinez-Hernandez J, Ballesteros-Merino C, Fernandez-Alacid L, Nicolau JC, Aguado C & Lujan R. (2013). Polarised localisation of the voltage-gated sodium channel Na(v)1.2 in cerebellar granule cells. *Cerebellum* **12,** 16-26.

Marty A & Neher E. (1985). Potassium channels in cultured bovine adrenal chromaffin cells. *J Physiol* **367,** 117-141.

Mathews PJ, Lee KH, Peng Z, Houser CR & Otis TS. (2012). Effects of climbing fiber driven inhibition on Purkinje neuron spiking. *J Neurosci* **32,** 17988-17997.

Maurice N, Mercer J, Chan CS, Hernandez-Lopez S, Held J, Tkatch T & Surmeier DJ. (2004). D2 dopamine receptor-mediated modulation of voltage-dependent Na+ channels reduces autonomous activity in striatal cholinergic interneurons. *J Neurosci* **24,** 10289-10301.

Maurice N, Tkatch T, Meisler M, Sprunger LK & Surmeier DJ. (2001). D1/D5 dopamine receptor activation differentially modulates rapidly inactivating and persistent sodium currents in prefrontal cortex pyramidal neurons. *J Neurosci* **21,** 2268-2277.

McCormick DA & Huguenard JR. (1992). A model of the electrophysiological properties of thalamocortical relay neurons. *J Neurophysiol* **68,** 1384-1400.

McCrossan ZA & Abbott GW. (2004). The MinK-related peptides. *Neuropharmacology* **47,** 787-821.

McKay BE & Turner RW. (2004). Kv3 K+ channels enable burst output in rat cerebellar Purkinje cells. *Eur J Neurosci* **20,** 729-739.

Meadows LS, Malhotra J, Loukas A, Thyagarajan V, Kazen-Gillespie KA, Koopman MC, Kriegler S, Isom LL & Ragsdale DS. (2002). Functional and biochemical analysis of a sodium channel beta1 subunit mutation responsible for generalized epilepsy with febrile seizures plus type 1. *J Neurosci* **22,** 10699-10709.

Meeks JP & Mennerick S. (2007). Action potential initiation and propagation in CA3 pyramidal axons. *J Neurophysiol* **97,** 3460-3472.

Mejia-Gervacio S & Marty A. (2006). Control of interneurone firing pattern by axonal autoreceptors in the juvenile rat cerebellum. *J Physiol* **571,** 43-55.

Melchitzky DS & Lewis DA. (2000). Tyrosine hydroxylase- and dopamine transporter-immunoreactive axons in the primate cerebellum. Evidence for a lobular- and laminar-specific dopamine innervation. *Neuropsychopharmacology* **22,** 466-472.

Meza RC, Lopez-Jury L, Canavier CC & Henny P. (2018). Role of the Axon Initial Segment in the Control of Spontaneous Frequency of Nigral Dopaminergic Neurons In Vivo. *J Neurosci* **38,** 733-744.

Midtgaard J. (1992). Membrane properties and synaptic responses of Golgi cells and stellate cells in the turtle cerebellum in vitro. *J Physiol* **457,** 329-354.

Milescu LS, Bean BP & Smith JC. (2010). Isolation of somatic Na+ currents by selective inactivation of axonal channels with a voltage prepulse. *J Neurosci* **30,** 7740-7748.

Millar JA, Barratt L, Southan AP, Page KM, Fyffe RE, Robertson B & Mathie A. (2000). A functional role for the two-pore domain potassium channel TASK-1 in cerebellar granule neurons. *Proc Natl Acad Sci U S A* **97,** 3614-3618.

Miloushev VZ, Levine JA, Arbing MA, Hunt JF, Pitt GS & Palmer AG, 3rd. (2009). Solution structure of the NaV1.2 C-terminal EF-hand domain. *J Biol Chem* **284,** 6446-6454.

Milshtein-Parush H, Frere S, Regev L, Lahav C, Benbenishty A, Ben-Eliyahu S, Goshen I & Slutsky I. (2017). Sensory Deprivation Triggers Synaptic and Intrinsic Plasticity in the Hippocampus. *Cereb Cortex* **27,** 3457-3470.

Misonou H, Mohapatra DP, Park EW, Leung V, Zhen D, Misonou K, Anderson AE & Trimmer JS. (2004). Regulation of ion channel localization and phosphorylation by neuronal activity. *Nat Neurosci* **7,** 711-718.

Mitoma H & Konishi S. (1999). Monoaminergic long-term facilitation of GABA-mediated inhibitory transmission at cerebellar synapses. *Neuroscience* **88,** 871-883.

Mittmann W, Koch U & Hausser M. (2005). Feed-forward inhibition shapes the spike output of cerebellar Purkinje cells. *J Physiol* **563,** 369-378.

Molineux ML, Fernandez FR, Mehaffey WH & Turner RW. (2005). A-type and T-type currents interact to produce a novel spike latency-voltage relationship in cerebellar stellate cells. *J Neurosci* **25,** 10863-10873.

Moosmang S, Biel M, Hofmann F & Ludwig A. (1999). Differential distribution of four hyperpolarization-activated cation channels in mouse brain. *Biol Chem* **380,** 975-980.

Morin TJ & Kobertz WR. (2008). Counting membrane-embedded KCNE beta-subunits in functioning K+ channel complexes. *Proc Natl Acad Sci U S A* **105,** 1478-1482.

Moubarak E, Engel D, Dufour MA, Tapia M, Tell F & Goaillard JM. (2019). Robustness to Axon Initial Segment Variation Is Explained by Somatodendritic Excitability in Rat Substantia Nigra Dopaminergic Neurons. *J Neurosci* **39,** 5044-5063.

Moyer JR, Jr., Thompson LT & Disterhoft JF. (1996). Trace eyeblink conditioning increases CA1 excitability in a transient and learning-specific manner. *J Neurosci* **16,** 5536-5546.

Mugnaini E, Sekerkova G & Martina M. (2011). The unipolar brush cell: a remarkable neuron finally receiving deserved attention. *Brain Res Rev* **66,** 220-245.

Mukamel EA, Nimmerjahn A & Schnitzer MJ. (2009). Automated analysis of cellular signals from large-scale calcium imaging data. *Neuron* **63,** 747-760.

Myoga MH, Beierlein M & Regehr WG. (2009). Somatic spikes regulate dendritic signaling in small neurons in the absence of backpropagating action potentials. *J Neurosci* **29,** 7803-7814.

Nadal MS, Ozaita A, Amarillo Y, Vega-Saenz de Miera E, Ma Y, Mo W, Goldberg EM, Misumi Y, Ikehara Y, Neubert TA & Rudy B. (2003). The CD26-related dipeptidyl aminopeptidase-like protein DPPX is a critical component of neuronal A-type K+ channels. *Neuron* **37,** 449-461.

Nedergaard S, Flatman JA & Engberg I. (1993). Nifedipine- and omega-conotoxin-sensitive Ca2+ conductances in guinea-pig substantia nigra pars compacta neurones. *J Physiol* **466,** 727-747.

Nelson AB, Krispel CM, Sekirnjak C & du Lac S. (2003). Long-lasting increases in intrinsic excitability triggered by inhibition. *Neuron* **40,** 609-620.

Nolan MF, Malleret G, Lee KH, Gibbs E, Dudman JT, Santoro B, Yin D, Thompson RF, Siegelbaum SA, Kandel ER & Morozov A. (2003). The hyperpolarization-activated HCN1 channel is important for motor learning and neuronal integration by cerebellar Purkinje cells. *Cell* **115,** 551-564.

Numann R, Catterall WA & Scheuer T. (1991). Functional modulation of brain sodium channels by protein kinase C phosphorylation. *Science* **254,** 115-118.

Nunzi MG, Birnstiel S, Bhattacharyya BJ, Slater NT & Mugnaini E. (2001). Unipolar brush cells form a glutamatergic projection system within the mouse cerebellar cortex. *J Comp Neurol* **434,** 329-341.

Nusser Z, Cull-Candy S & Farrant M. (1997). Differences in synaptic GABA(A) receptor number underlie variation in GABA mini amplitude. *Neuron* **19,** 697-709.

O'Donoghue DL, King JS & Bishop GA. (1989). Physiological and anatomical studies of the interactions between Purkinje cells and basket cells in the cat's cerebellar cortex: evidence for a unitary relationship. *J Neurosci* **9,** 2141-2150.

O'Malley HA & Isom LL. (2015). Sodium channel beta subunits: emerging targets in channelopathies. *Annu Rev Physiol* **77,** 481-504.

Ogawa Y, Horresh I, Trimmer JS, Bredt DS, Peles E & Rasband MN. (2008). Postsynaptic density-93 clusters Kv1 channels at axon initial segments independently of Caspr2. *J Neurosci* **28,** 5731-5739.

Ohtsuki G, Piochon C, Adelman JP & Hansel C. (2012). SK2 channel modulation contributes to compartment-specific dendritic plasticity in cerebellar Purkinje cells. *Neuron* **75,** 108-120.

Oliver D, Lien CC, Soom M, Baukrowitz T, Jonas P & Fakler B. (2004). Functional conversion between A-type and delayed rectifier K+ channels by membrane lipids. *Science* **304,** 265-270.

Otsu Y, Marcaggi P, Feltz A, Isope P, Kollo M, Nusser Z, Mathieu B, Kano M, Tsujita M, Sakimura K & Dieudonne S. (2014). Activity-dependent gating of calcium spikes by A-type K+ channels controls climbing fiber signaling in Purkinje cell dendrites. *Neuron* **84,** 137-151.

Ozden I, Dombeck DA, Hoogland TM, Tank DW & Wang SS. (2012). Widespread state-dependent shifts in cerebellar activity in locomoting mice. *PLoS One* **7,** e42650.

Pablo JL, Wang C, Presby MM & Pitt GS. (2016). Polarized localization of voltage-gated Na+ channels is regulated by concerted FGF13 and FGF14 action. *Proc Natl Acad Sci U S A* **113,** E2665-2674.

Palay SL & Chan-Palay V. (1974). *Cerebellar cortex: cytology and organization*. Springer, Berlin, Heidelberg, New York,.

Palmer LM & Stuart GJ. (2006). Site of action potential initiation in layer 5 pyramidal neurons. *J Neurosci* **26,** 1854-1863.

Pan Z, Kao T, Horvath Z, Lemos J, Sul JY, Cranstoun SD, Bennett V, Scherer SS & Cooper EC. (2006). A common ankyrin-G-based mechanism retains KCNQ and NaV channels at electrically active domains of the axon. *J Neurosci* **26,** 2599-2613.

Pape HC. (1996). Queer current and pacemaker: the hyperpolarization-activated cation current in neurons. *Annu Rev Physiol* **58,** 299-327.

Park KS, Mohapatra DP, Misonou H & Trimmer JS. (2006). Graded regulation of the Kv2.1 potassium channel by variable phosphorylation. *Science* **313,** 976-979.

Park KS, Yang JW, Seikel E & Trimmer JS. (2008). Potassium channel phosphorylation in excitable cells: providing dynamic functional variability to a diverse family of ion channels. *Physiology (Bethesda)* **23,** 49-57.

Patel SP, Campbell DL & Strauss HC. (2002). Elucidating KChIP effects on Kv4.3 inactivation and recovery kinetics with a minimal KChIP2 isoform. *J Physiol* **545,** 5-11.

Pedarzani P, Mosbacher J, Rivard A, Cingolani LA, Oliver D, Stocker M, Adelman JP & Fakler B. (2001). Control of electrical activity in central neurons by modulating the gating of small conductance Ca2+-activated K+ channels. *J Biol Chem* **276,** 9762-9769.

Perkins EM, Clarkson YL, Sabatier N, Longhurst DM, Millward CP, Jack J, Toraiwa J, Watanabe M, Rothstein JD, Lyndon AR, Wyllie DJ, Dutia MB & Jackson M. (2010). Loss of beta-III spectrin leads to Purkinje cell dysfunction recapitulating the behavior and neuropathology of spinocerebellar ataxia type 5 in humans. *J Neurosci* **30,** 4857-4867.

Pongs O & Schwarz JR. (2010). Ancillary subunits associated with voltage-dependent K+ channels. *Physiol Rev* **90,** 755-796.

Pouzat C & Marty A. (1998). Autaptic inhibitory currents recorded from interneurones in rat cerebellar slices. *J Physiol* **509 (Pt 3),** 777-783.

Pouzat C & Marty A. (1999). Somatic recording of GABAergic autoreceptor current in cerebellar stellate and basket cells. *J Neurosci* **19,** 1675-1690.

Pugh JR & Jahr CE. (2011). NMDA receptor agonists fail to alter release from cerebellar basket cells. *J Neurosci* **31,** 16550-16555.

Raman IM & Bean BP. (1997). Resurgent sodium current and action potential formation in dissociated cerebellar Purkinje neurons. *J Neurosci* **17,** 4517-4526.

Raman IM & Bean BP. (1999a). Ionic currents underlying spontaneous action potentials in isolated cerebellar Purkinje neurons. *J Neurosci* **19,** 1663-1674.

Raman IM & Bean BP. (1999b). Properties of sodium currents and action potential firing in isolated cerebellar Purkinje neurons. *Ann N Y Acad Sci* **868,** 93-96.

Raman IM & Bean BP. (2001). Inactivation and recovery of sodium currents in cerebellar Purkinje neurons: evidence for two mechanisms. *Biophys J* **80,** 729-737.

Raman IM, Sprunger LK, Meisler MH & Bean BP. (1997). Altered subthreshold sodium currents and disrupted firing patterns in Purkinje neurons of Scn8a mutant mice. *Neuron* **19,** 881-891.

Ramon y Cajal S. (1911). Histologie du système nerveux de l'homme et des vertébrés. *Maloine, Paris* **2,** 153-173.

Rancz EA & Hausser M. (2006). Dendritic calcium spikes are tunable triggers of cannabinoid release and short-term synaptic plasticity in cerebellar Purkinje neurons. *J Neurosci* **26,** 5428-5437.

Ransdell JL, Dranoff E, Lau B, Lo WL, Donermeyer DL, Allen PM & Nerbonne JM. (2017). Loss of Navbeta4-Mediated Regulation of Sodium Currents in Adult Purkinje Neurons Disrupts Firing and Impairs Motor Coordination and Balance. *Cell Rep* **20,** 1502.

Rettig J, Heinemann SH, Wunder F, Lorra C, Parcej DN, Dolly JO & Pongs O. (1994). Inactivation properties of voltage-gated K+ channels altered by presence of beta-subunit. *Nature* **369,** 289-294.

Rieubland S, Roth A & Hausser M. (2014). Structured connectivity in cerebellar inhibitory networks. *Neuron* **81,** 913-929.

Rizwan AP, Zhan X, Zamponi GW & Turner RW. (2016). Long-Term Potentiation at the Mossy Fiber-Granule Cell Relay Invokes Postsynaptic Second-Messenger Regulation of Kv4 Channels. *J Neurosci* **36,** 11196-11207.

Roeper J, Lorra C & Pongs O. (1997). Frequency-dependent inactivation of mammalian A-type K+ channel KV1.4 regulated by Ca2+/calmodulin-dependent protein kinase. *J Neurosci* **17,** 3379-3391.

Rossie S & Catterall WA. (1987). Cyclic-AMP-dependent phosphorylation of voltage-sensitive sodium channels in primary cultures of rat brain neurons. *J Biol Chem* **262,** 12735-12744.

Rossie S & Catterall WA. (1989). Phosphorylation of the alpha subunit of rat brain sodium channels by cAMP-dependent protein kinase at a new site containing Ser686 and Ser687. *J Biol Chem* **264,** 14220-14224.

Rossie S, Gordon D & Catterall WA. (1987). Identification of an intracellular domain of the sodium channel having multiple cAMP-dependent phosphorylation sites. *J Biol Chem* **262,** 17530-17535.

Rowan MJ, DelCanto G, Yu JJ, Kamasawa N & Christie JM. (2016). Synapse-Level Determination of Action Potential Duration by K(+) Channel Clustering in Axons. *Neuron* **91,** 370-383.

Rowan MJ, Tranquil E & Christie JM. (2014). Distinct Kv channel subtypes contribute to differences in spike signaling properties in the axon initial segment and presynaptic boutons of cerebellar interneurons. *J Neurosci* **34,** 6611-6623.

Rowan MJM, Bonnan A, Zhang K, Amat SB, Kikuchi C, Taniguchi H, Augustine GJ & Christie JM. (2018). Graded Control of Climbing-Fiber-Mediated Plasticity and Learning by Inhibition in the Cerebellum. *Neuron* **99,** 999-1015 e1016.

Rowan MJM & Christie JM. (2017). Rapid State-Dependent Alteration in Kv3 Channel Availability Drives Flexible Synaptic Signaling Dependent on Somatic Subthreshold Depolarization. *Cell Rep* **18,** 2018-2029.

Royeck M, Horstmann MT, Remy S, Reitze M, Yaari Y & Beck H. (2008). Role of axonal NaV1.6 sodium channels in action potential initiation of CA1 pyramidal neurons. *J Neurophysiol* **100,** 2361-2380.

Rudolph S, Hull C & Regehr WG. (2015). Active Dendrites and Differential Distribution of Calcium Channels Enable Functional Compartmentalization of Golgi Cells. *J Neurosci* **35,** 15492-15504.

Rudy B & McBain CJ. (2001). Kv3 channels: voltage-gated K+ channels designed for high-frequency repetitive firing. *Trends Neurosci* **24,** 517-526.

Rusakov DA, Saitow F, Lehre KP & Konishi S. (2005). Modulation of presynaptic Ca2+ entry by AMPA receptors at individual GABAergic synapses in the cerebellum. *J Neurosci* **25,** 4930-4940.

Russo MJ, Mugnaini E & Martina M. (2007). Intrinsic properties and mechanisms of spontaneous firing in mouse cerebellar unipolar brush cells. *J Physiol* **581,** 709-724.

Russo MJ, Yau HJ, Nunzi MG, Mugnaini E & Martina M. (2008). Dynamic metabotropic control of intrinsic firing in cerebellar unipolar brush cells. *J Neurophysiol* **100,** 3351-3360.

Saar D, Grossman Y & Barkai E. (1998). Reduced after-hyperpolarization in rat piriform cortex pyramidal neurons is associated with increased learning capability during operant conditioning. *Eur J Neurosci* **10,** 1518-1523.

Saar D, Grossman Y & Barkai E. (2001). Long-lasting cholinergic modulation underlies rule learning in rats. *J Neurosci* **21,** 1385-1392.

Sah P. (1996). Ca(2+)-activated K+ currents in neurones: types, physiological roles and modulation. *Trends Neurosci* **19,** 150-154.

Saitow F & Konishi S. (2000). Excitability increase induced by beta-adrenergic receptor-mediated activation of hyperpolarization-activated cation channels in rat cerebellar basket cells. *J Neurophysiol* **84,** 2026-2034.

Sanchez-Andres JV & Alkon DL. (1991). Voltage-clamp analysis of the effects of classical conditioning on the hippocampus. *J Neurophysiol* **65,** 796-807.

Sanguinetti MC, Curran ME, Zou A, Shen J, Spector PS, Atkinson DL & Keating MT. (1996). Coassembly of K(V)LQT1 and minK (IsK) proteins to form cardiac I(Ks) potassium channel. *Nature* **384,** 80-83.

Satake S, Saitow F, Yamada J & Konishi S. (2000). Synaptic activation of AMPA receptors inhibits GABA release from cerebellar interneurons. *Nat Neurosci* **3,** 551-558.

Scala F, Nenov MN, Crofton EJ, Singh AK, Folorunso O, Zhang Y, Chesson BC, Wildburger NC, James TF, Alshammari MA, Alshammari TK, Elfrink H, Grassi C, Kasper JM, Smith AE, Hommel JD, Lichti CF, Rudra JS, D'Ascenzo M, Green TA & Laezza F. (2018). Environmental Enrichment and Social Isolation Mediate Neuroplasticity of Medium Spiny Neurons through the GSK3 Pathway. *Cell Rep* **23,** 555-567.

Scelfo B, Sacchetti B & Strata P. (2008). Learning-related long-term potentiation of inhibitory synapses in the cerebellar cortex. *Proc Natl Acad Sci U S A* **105,** 769-774.

Schaller KL & Caldwell JH. (2003). Expression and distribution of voltage-gated sodium channels in the cerebellum. *Cerebellum* **2,** 2-9.

Scheuer T. (2011). Regulation of sodium channel activity by phosphorylation. *Semin Cell Dev Biol* **22,** 160-165.

Schiffmann SN, Lledo PM & Vincent JD. (1995). Dopamine D1 receptor modulates the voltage-gated sodium current in rat striatal neurones through a protein kinase A. *J Physiol* **483 (Pt 1),** 95-107.

Schrader LA, Anderson AE, Mayne A, Pfaffinger PJ & Sweatt JD. (2002). PKA modulation of Kv4.2-encoded A-type potassium channels requires formation of a supramolecular complex. *J Neurosci* **22,** 10123-10133.

Schreurs BG, Gusev PA, Tomsic D, Alkon DL & Shi T. (1998). Intracellular correlates of acquisition and long-term memory of classical conditioning in Purkinje cell dendrites in slices of rabbit cerebellar lobule HVI. *J Neurosci* **18,** 5498-5507.

Schroeder BC, Waldegger S, Fehr S, Bleich M, Warth R, Greger R & Jentsch TJ. (2000). A constitutively open potassium channel formed by KCNQ1 and KCNE3. *Nature* **403,** 196-199.

Schwaller B, Meyer M & Schiffmann S. (2002). 'New' functions for 'old' proteins: the role of the calcium-binding proteins calbindin D-28k, calretinin and parvalbumin, in cerebellar physiology. Studies with knockout mice. *Cerebellum* **1,** 241-258.

Schweighofer N, Doya K & Kuroda S. (2004). Cerebellar aminergic neuromodulation: towards a functional understanding. *Brain Res Brain Res Rev* **44,** 103-116.

Seroussi Y, Brosh I & Barkai E. (2002). Learning-induced reduction in post-burst after-hyperpolarization (AHP) is mediated by activation of PKC. *Eur J Neurosci* **16,** 965-969.

Shao LR, Halvorsrud R, Borg-Graham L & Storm JF. (1999). The role of BK-type Ca2+-dependent K+ channels in spike broadening during repetitive firing in rat hippocampal pyramidal cells. *J Physiol* **521 Pt 1,** 135-146.

Shavkunov AS, Wildburger NC, Nenov MN, James TF, Buzhdygan TP, Panova-Elektronova NI, Green TA, Veselenak RL, Bourne N & Laezza F. (2013). The fibroblast growth factor 14.voltage-gated sodium channel complex is a new target of glycogen synthase kinase 3 (GSK3). *J Biol Chem* **288,** 19370-19385.

Shim HG, Jang DC, Lee J, Chung G, Lee S, Kim YG, Jeon DE & Kim SJ. (2017). Long-Term Depression of Intrinsic Excitability Accompanied by Synaptic Depression in Cerebellar Purkinje Cells. *J Neurosci* **37,** 5659-5669.

Shim HG, Jang SS, Jang DC, Jin Y, Chang W, Park JM & Kim SJ. (2016). mGlu1 receptor mediates homeostatic control of intrinsic excitability through Ih in cerebellar Purkinje cells. *J Neurophysiol* **115,** 2446-2455.

Simpson JI, Hulscher HC, Sabel-Goedknegt E & Ruigrok TJ. (2005). Between in and out: linking morphology and physiology of cerebellar cortical interneurons. *Prog Brain Res* **148,** 329-340.

Smith RD & Goldin AL. (1998). Functional analysis of the rat I sodium channel in xenopus oocytes. *J Neurosci* **18,** 811-820.

Sokolova O, Kolmakova-Partensky L & Grigorieff N. (2001). Three-dimensional structure of a voltage-gated potassium channel at 2.5 nm resolution. *Structure* **9,** 215-220.

Somogyi P, Fritschy JM, Benke D, Roberts JD & Sieghart W. (1996). The gamma 2 subunit of the GABAA receptor is concentrated in synaptic junctions containing the alpha 1 and beta 2/3 subunits in hippocampus, cerebellum and globus pallidus. *Neuropharmacology* **35,** 1425-1444.

Sotelo C. (2011). Camillo Golgi and Santiago Ramon y Cajal: the anatomical organization of the cortex of the cerebellum. Can the neuron doctrine still support our actual knowledge on the cerebellar structural arrangement? *Brain Res Rev* **66,** 16-34.

Sourdet V, Russier M, Daoudal G, Ankri N & Debanne D. (2003). Long-term enhancement of neuronal excitability and temporal fidelity mediated by metabotropic glutamate receptor subtype 5. *J Neurosci* **23,** 10238-10248.

Southan AP, Morris NP, Stephens GJ & Robertson B. (2000). Hyperpolarization-activated currents in presynaptic terminals of mouse cerebellar basket cells. *J Physiol* **526 Pt 1,** 91-97.

Southan AP & Robertson B. (1998). Patch-clamp recordings from cerebellar basket cell bodies and their presynaptic terminals reveal an asymmetric distribution of voltage-gated potassium channels. *J Neurosci* **18,** 948-955.

Southan AP & Robertson B. (2000). Electrophysiological characterization of voltage-gated K(+) currents in cerebellar basket and purkinje cells: Kv1 and Kv3 channel subfamilies are present in basket cell nerve terminals. *J Neurosci* **20,** 114-122.

Stackman RW, Hammond RS, Linardatos E, Gerlach A, Maylie J, Adelman JP & Tzounopoulos T. (2002). Small conductance Ca2+-activated K+ channels modulate synaptic plasticity and memory encoding. *J Neurosci* **22,** 10163-10171.

Storm JF. (1987a). Action potential repolarization and a fast after-hyperpolarization in rat hippocampal pyramidal cells. *J Physiol* **385,** 733-759.

Storm JF. (1987b). Intracellular injection of a Ca2+ chelator inhibits spike repolarization in hippocampal neurons. *Brain Res* **435,** 387-392.

Stuart G, Schiller J & Sakmann B. (1997). Action potential initiation and propagation in rat neocortical pyramidal neurons. *J Physiol* **505 (Pt 3),** 617-632.

Stuart G & Spruston N. (1998). Determinants of voltage attenuation in neocortical pyramidal neuron dendrites. *J Neurosci* **18,** 3501-3510.

Stuart G, Spruston N & Häusser M. (2016). *Dendrites*. Oxford University Press, Oxford ;.

Surmeier DJ, Eberwine J, Wilson CJ, Cao Y, Stefani A & Kitai ST. (1992). Dopamine receptor subtypes colocalize in rat striatonigral neurons. *Proc Natl Acad Sci U S A* **89,** 10178-10182.

Swensen AM & Bean BP. (2003). Ionic mechanisms of burst firing in dissociated Purkinje neurons. *J Neurosci* **23,** 9650-9663.

Szabo B, Urbanski MJ, Bisogno T, Di Marzo V, Mendiguren A, Baer WU & Freiman I. (2006). Depolarization-induced retrograde synaptic inhibition in the mouse cerebellar cortex is mediated by 2-arachidonoylglycerol. *J Physiol* **577,** 263-280.

Szapiro G & Barbour B. (2007). Multiple climbing fibers signal to molecular layer interneurons exclusively via glutamate spillover. *Nat Neurosci* **10,** 735-742.

Tan HL, Kupershmidt S, Zhang R, Stepanovic S, Roden DM, Wilde AA, Anderson ME & Balser JR. (2002). A calcium sensor in the sodium channel modulates cardiac excitability. *Nature* **415,** 442-447.

Tan YP & Llano I. (1999). Modulation by K+ channels of action potential-evoked intracellular Ca2+ concentration rises in rat cerebellar basket cell axons. *J Physiol* **520 Pt 1,** 65-78.

ten Brinke MM, Boele HJ, Spanke JK, Potters JW, Kornysheva K, Wulff P, AC IJ, Koekkoek SK & De Zeeuw CI. (2015). Evolving Models of Pavlovian Conditioning: Cerebellar Cortical Dynamics in Awake Behaving Mice. *Cell Rep* **13,** 1977-1988.

Thompson CH, Hawkins NA, Kearney JA & George AL, Jr. (2017). CaMKII modulates sodium current in neurons from epileptic Scn2a mutant mice. *Proc Natl Acad Sci U S A* **114,** 1696-1701.

Thompson LT, Moyer JR, Jr. & Disterhoft JF. (1996). Transient changes in excitability of rabbit CA3 neurons with a time course appropriate to support memory consolidation. *J Neurophysiol* **76,** 1836-1849.

Townsend C, Hartmann HA & Horn R. (1997). Anomalous effect of permeant ion concentration on peak open probability of cardiac Na+ channels. *J Gen Physiol* **110,** 11-21.

Tran-Van-Minh A, Abrahamsson T, Cathala L & DiGregorio DA. (2016). Differential Dendritic Integration of Synaptic Potentials and Calcium in Cerebellar Interneurons. *Neuron* **91,** 837-850.

Tretter V, Ehya N, Fuchs K & Sieghart W. (1997). Stoichiometry and assembly of a recombinant GABAA receptor subtype. *J Neurosci* **17,** 2728-2737.

Turrigiano G, Abbott LF & Marder E. (1994). Activity-dependent changes in the intrinsic properties of cultured neurons. *Science* **264,** 974-977.

Van Petegem F, Lobo PA & Ahern CA. (2012). Seeing the forest through the trees: towards a unified view on physiological calcium regulation of voltage-gated sodium channels. *Biophys J* **103,** 2243-2251.

Vandenberg CA & Horn R. (1984). Inactivation viewed through single sodium channels. *J Gen Physiol* **84,** 535-564.

Vincent P, Armstrong CM & Marty A. (1992). Inhibitory synaptic currents in rat cerebellar Purkinje cells: modulation by postsynaptic depolarization. *J Physiol* **456,** 453-471.

Wagner S, Dybkova N, Rasenack EC, Jacobshagen C, Fabritz L, Kirchhof P, Maier SK, Zhang T, Hasenfuss G, Brown JH, Bers DM & Maier LS. (2006). Ca2+/calmodulin-dependent protein kinase II regulates cardiac Na+ channels. *J Clin Invest* **116,** 3127-3138.

Wang C, Chung BC, Yan H, Wang HG, Lee SY & Pitt GS. (2014). Structural analyses of Ca(2)(+)/CaM interaction with NaV channel C-termini reveal mechanisms of calcium-dependent regulation. *Nat Commun* **5,** 4896.

Wang H, Kunkel DD, Schwartzkroin PA & Tempel BL. (1994). Localization of Kv1.1 and Kv1.2, two K channel proteins, to synaptic terminals, somata, and dendrites in the mouse brain. *J Neurosci* **14,** 4588-4599.

Wang H, Yan Y, Liu Q, Huang Y, Shen Y, Chen L, Chen Y, Yang Q, Hao Q, Wang K & Chai J. (2007). Structural basis for modulation of Kv4 K+ channels by auxiliary KChIP subunits. *Nat Neurosci* **10,** 32-39.

Wang X, Zhang C, Szabo G & Sun QQ. (2013). Distribution of CaMKIIalpha expression in the brain in vivo, studied by CaMKIIalpha-GFP mice. *Brain Res* **1518,** 9-25.

Watanabe D, Inokawa H, Hashimoto K, Suzuki N, Kano M, Shigemoto R, Hirano T, Toyama K, Kaneko S, Yokoi M, Moriyoshi K, Suzuki M, Kobayashi K, Nagatsu T, Kreitman RJ, Pastan I & Nakanishi S. (1998). Ablation of cerebellar Golgi cells disrupts synaptic integration involving GABA inhibition and NMDA receptor activation in motor coordination. *Cell* **95,** 17-27.

Weiser M, Bueno E, Sekirnjak C, Martone ME, Baker H, Hillman D, Chen S, Thornhill W, Ellisman M & Rudy B. (1995). The potassium channel subunit KV3.1b is localized to somatic and axonal membranes of specific populations of CNS neurons. *J Neurosci* **15,** 4298-4314.

Wendt DJ, Starmer CF & Grant AO. (1992). Na channel kinetics remain stable during perforated-patch recordings. *Am J Physiol* **263,** C1234-1240.

West JW, Numann R, Murphy BJ, Scheuer T & Catterall WA. (1991). A phosphorylation site in the Na+ channel required for modulation by protein kinase C. *Science* **254,** 866-868.

Westenbroek RE, Merrick DK & Catterall WA. (1989). Differential subcellular localization of the RI and RII Na+ channel subtypes in central neurons. *Neuron* **3,** 695-704.

Wildburger NC, Ali SR, Hsu WC, Shavkunov AS, Nenov MN, Lichti CF, LeDuc RD, Mostovenko E, Panova-Elektronova NI, Emmett MR, Nilsson CL & Laezza F. (2015). Quantitative proteomics reveals protein-protein interactions with fibroblast growth factor 12 as a component of the voltage-gated sodium channel 1.2 (nav1.2) macromolecular complex in Mammalian brain. *Mol Cell Proteomics* **14,** 1288-1300.

Williams SR, Christensen SR, Stuart GJ & Hausser M. (2002). Membrane potential bistability is controlled by the hyperpolarization-activated current I(H) in rat cerebellar Purkinje neurons in vitro. *J Physiol* **539,** 469-483.

Williams SR & Stuart GJ. (1999). Mechanisms and consequences of action potential burst firing in rat neocortical pyramidal neurons. *J Physiol* **521 Pt 2,** 467-482.

Wingo TL, Shah VN, Anderson ME, Lybrand TP, Chazin WJ & Balser JR. (2004). An EF-hand in the sodium channel couples intracellular calcium to cardiac excitability. *Nat Struct Mol Biol* **11,** 219-225.

Wittmack EK, Rush AM, Hudmon A, Waxman SG & Dib-Hajj SD. (2005). Voltage-gated sodium channel Nav1.6 is modulated by p38 mitogen-activated protein kinase. *J Neurosci* **25,** 6621-6630.

Wolfart J, Neuhoff H, Franz O & Roeper J. (2001). Differential expression of the small-conductance, calcium-activated potassium channel SK3 is critical for pacemaker control in dopaminergic midbrain neurons. *J Neurosci* **21,** 3443-3456.

Womack M & Khodakhah K. (2002a). Active contribution of dendrites to the tonic and trimodal patterns of activity in cerebellar Purkinje neurons. *J Neurosci* **22,** 10603-10612.

Womack MD & Khodakhah K. (2002b). Characterization of large conductance Ca2+-activated K+ channels in cerebellar Purkinje neurons. *Eur J Neurosci* **16,** 1214-1222.

Womack MD & Khodakhah K. (2004). Dendritic control of spontaneous bursting in cerebellar Purkinje cells. *J Neurosci* **24,** 3511-3521.

Wulff P, Schonewille M, Renzi M, Viltono L, Sassoe-Pognetto M, Badura A, Gao Z, Hoebeek FE, van Dorp S, Wisden W, Farrant M & De Zeeuw CI. (2009). Synaptic inhibition of Purkinje

cells mediates consolidation of vestibulo-cerebellar motor learning. *Nat Neurosci* **12,** 1042-1049.

Xiao M, Bosch MK, Nerbonne JM & Ornitz DM. (2013). FGF14 localization and organization of the axon initial segment. *Mol Cell Neurosci* **56,** 393-403.

Xu J, Kang N, Jiang L, Nedergaard M & Kang J. (2005). Activity-dependent long-term potentiation of intrinsic excitability in hippocampal CA1 pyramidal neurons. *J Neurosci* **25,** 1750-1760.

Yan H, Pablo JL, Wang C & Pitt GS. (2014). FGF14 modulates resurgent sodium current in mouse cerebellar Purkinje neurons. *Elife* **3,** e04193.

Yang Z & Santamaria F. (2016). Purkinje cell intrinsic excitability increases after synaptic long term depression. *J Neurophysiol* **116,** 1208-1217.

Yoshida T, Hashimoto K, Zimmer A, Maejima T, Araishi K & Kano M. (2002). The cannabinoid CB1 receptor mediates retrograde signals for depolarization-induced suppression of inhibition in cerebellar Purkinje cells. *J Neurosci* **22,** 1690-1697.

Yuan LL, Adams JP, Swank M, Sweatt JD & Johnston D. (2002). Protein kinase modulation of dendritic K+ channels in hippocampus involves a mitogen-activated protein kinase pathway. *J Neurosci* **22,** 4860-4868.

Zamponi GW, Striessnig J, Koschak A & Dolphin AC. (2015). The Physiology, Pathology, and Pharmacology of Voltage-Gated Calcium Channels and Their Future Therapeutic Potential. *Pharmacol Rev* **67,** 821-870.

Zhang W & Linden DJ. (2003). The other side of the engram: experience-driven changes in neuronal intrinsic excitability. *Nat Rev Neurosci* **4,** 885-900.

Zhang W, Shin JH & Linden DJ. (2004). Persistent changes in the intrinsic excitability of rat deep cerebellar nuclear neurones induced by EPSP or IPSP bursts. *J Physiol* **561,** 703-719.

Zhou D, Lambert S, Malen PL, Carpenter S, Boland LM & Bennett V. (1998). AnkyrinG is required for clustering of voltage-gated Na channels at axon initial segments and for normal action potential firing. *J Cell Biol* **143,** 1295-1304.

Zuniga R, Gonzalez D, Valenzuela C, Brown N & Zuniga L. (2016). Expression and cellular localization of HCN channels in rat cerebellar granule neurons. *Biochem Biophys Res Commun* **478,** 1429-1435.

PART IV
APPENDICES

APPENDIX I:

Nanoscale Mobility of the Apo State and TARP Stoichiometry Dictate the Gating Behavior of Alternatively Spliced AMPA Receptors

FOREWORD TO APPENDIX I

I began 2019 with my first paper under review at *Journal of Neuroscience* and Derek approached me with a request. He mentioned an old experiment performed by a former PhD student regarding ion permeation of native glutamate receptors in the cerebellum. To move forward the result would need to be replicated, which would entail outfitting my slice electrophysiology rig with the piezo-driven fast perfusion system used primarily in our lab for study of recombinant receptors in HEK 293 cells. In need of a break from action potentials and looking for a new challenge, I accepted and began to optimize and troubleshoot the perfusion setup. In the meantime, the manuscript of another former PhD student, Brent Dawe, concerning anion regulation of recombinant AMPA receptors was under review at *Neuron*. As I began to collect my first useable patch data, the manuscript came back as rejected, but with reasonably positive comments. The feedback was focused on physiological relevance, with specific implication of translating Brent's observations in homomeric receptors to heteromeric subunit combinations that are thought to represent native stoichiometry more accurately. Derek thought we could do them one better, and proposed the idea of me exposing native AMPA receptor patches pulled from cerebellar neurons to Brent's anion solutions. Although this was distinct from the original objective, I was generating clean data at a decent clip, so I agreed.

Without explaining the findings of the paper too explicitly, I was able to confirm Brent's results in native AMPA receptors, thereby increasing the generalizability of his observations. Furthermore, with the help of MSc student Edward Yan, we were able to make an important additional contribution to the field of AMPA receptors. We found that receptor properties were regulated differently by anions depending on the number of TARP auxiliary proteins allowed to

interact with the channel. Comparing his findings in HEK cells to my patches from the cerebellum, we demonstrated that stellate and Purkinje cells plausibly contain AMPA receptors with distinct TARP stoichiometries, interacting with two and four subunits, respectively. This was a significant contribution to the field of auxiliary protein modulation of glutamate receptors, and was, to our knowledge, only the second time that TARP stoichiometry was assessed functionally in native receptors. We resubmitted to *Neuron* after about 6 weeks of experiments and it was accepted and published online in April 2019.

Article title:

Nanoscale Mobility of the Apo State and TARP Stoichiometry Dictate the Gating Behavior of Alternatively Spliced AMPA Receptors

Article

Neuron

Nanoscale Mobility of the Apo State and TARP Stoichiometry Dictate the Gating Behavior of Alternatively Spliced AMPA Receptors

Graphical Abstract

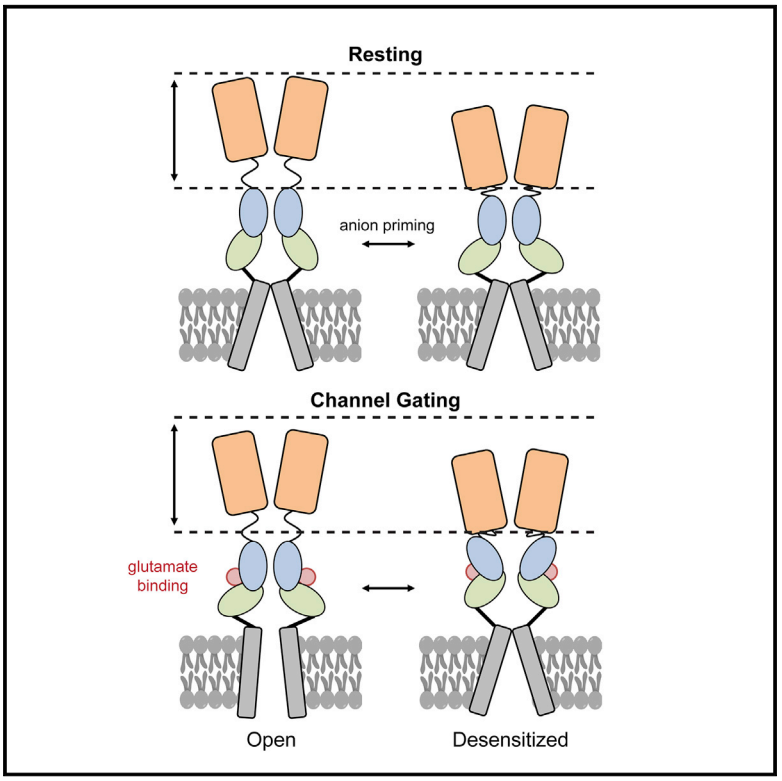

Authors

G. Brent Dawe, Md. Fahim Kadir, Raminta Venskutonytė, ..., Jette S. Kastrup, J. Michael Edwardson, Derek Bowie

Correspondence

derek.bowie@mcgill.ca

In Brief

Combining electrophysiology, atomic force microscopy, and X-ray crystallography, Dawe et al. reveal that nanoscale mobility of the apo state and TARP stoichiometry coordinate the responsiveness of alternatively spliced AMPA receptors to neurotransmitter, allosteric anions, and TARP auxiliary proteins.

Highlights

- Nanoscale mobility of the apo state predetermines gating of flip/flop AMPA receptors
- The flip/flop cassette exerts long-range control on the distant N-terminal domain
- TARP stoichiometry further dictates the functionality of flip/flop AMPA heteromers
- Neurons express two AMPA receptor classes that are either partially or fully TARPed

Dawe et al., 2019, Neuron *102*, 976–992
June 5, 2019
https://doi.org/10.1016/j.neuron.2019.03.046

CellPress

CellPress

Neuron
Article

Nanoscale Mobility of the Apo State and TARP Stoichiometry Dictate the Gating Behavior of Alternatively Spliced AMPA Receptors

G. Brent Dawe,[1,2,6] Md. Fahim Kadir,[3,6] Raminta Venskutonytė,[4,6] Amanda M. Perozzo,[1,2] Yuhao Yan,[1,2] Ryan P.D. Alexander,[1,2] Camilo Navarrete,[3,5] Eduardo A. Santander,[3] Marika Arsenault,[2] Christian Fuentes,[3,5] Mark R.P. Aurousseau,[2] Karla Frydenvang,[4] Nelson P. Barrera,[5] Jette S. Kastrup,[4,7] J. Michael Edwardson,[3,7] and Derek Bowie[2,7,8,*]

[1]Integrated Program in Neuroscience, McGill University, Montréal, QC H3A 2B4, Canada
[2]Department of Pharmacology and Therapeutics, McGill University, Montréal, QC H3G 1Y6, Canada
[3]Department of Pharmacology, University of Cambridge, Cambridge CB2 1PD, UK
[4]Department of Drug Design and Pharmacology, University of Copenhagen, 2100 Copenhagen, Denmark
[5]Department of Physiology, Pontificia Universidad Católica de Chile, 8331150 Santiago, Chile
[6]These authors contributed equally
[7]Senior Author
[8]Lead Contact
*Correspondence: derek.bowie@mcgill.ca
https://doi.org/10.1016/j.neuron.2019.03.046

SUMMARY

Neurotransmitter-gated ion channels are allosteric proteins that switch on and off in response to agonist binding. Most studies have focused on the agonist-bound, activated channel while assigning a lesser role to the apo or resting state. Here, we show that nanoscale mobility of resting α-amino-3-hydroxy-5-methyl-4-isoxazolepropionic acid (AMPA)-type ionotropic glutamate receptors (AMPA receptors) predetermines responsiveness to neurotransmitter, allosteric anions and TARP auxiliary subunits. Mobility at rest is regulated by alternative splicing of the flip/flop cassette of the ligand-binding domain, which controls motions in the distant AMPA receptor N-terminal domain (NTD). Flip variants promote moderate NTD movement, which establishes slower channel desensitization and robust regulation by anions and auxiliary subunits. In contrast, greater NTD mobility imparted by the flop cassette acts as a master switch to override allosteric regulation. In AMPA receptor heteromers, TARP stoichiometry further modifies these actions of the flip/flop cassette generating two functionally distinct classes of partially and fully TARPed receptors typical of cerebellar stellate and Purkinje cells.

INTRODUCTION

α-Amino-3-hydroxy-5-methyl-4-isoxazolepropionic acid (AMPA)-type ionotropic glutamate receptors (iGluRs) mediate most fast-excitatory neurotransmission in the mammalian brain (Dingledine et al., 1999; Traynelis et al., 2010). They form the hardwiring of glutamatergic circuits but also strengthen or weaken synaptic transmission during periods of sustained patterned activity or altered homeostasis (Herring and Nicoll, 2016; Turrigiano, 2017). AMPA receptors are also implicated in numerous CNS disorders and thus are targeted for the development of clinically relevant compounds (Bowie, 2008). Consequently, there has been a concerted effort to provide a full understanding of the structural and functional aspects of AMPA receptor signaling.

AMPA receptors assemble as tetramers in either a homomeric (Sobolevsky et al., 2009) or heteromeric (Herguedas et al., 2016, 2019) subunit arrangement that may additionally include accessory subunits such as the transmembrane AMPA receptor regulatory proteins (TARPs) and cornichon families (Greger et al., 2017; Jackson and Nicoll, 2011) (Figure 1A). The AMPA receptor subunit is composed of four functional domains that include (1) a cytoplasmic C-terminal domain (CTD; not shown in Figure 1A) that directs receptor trafficking and synaptic anchoring (Shepherd and Huganir, 2007); (2) a transmembrane domain (TMD), which forms a central ion channel pore that rapidly transports Na^+ and Ca^{2+} ions in response to binding of the neurotransmitter, L-glutamate (L-Glu) (Dingledine et al., 1999; Traynelis et al., 2010); (3) a clamshell-like ligand-binding domain (LBD; Figure 1B) (Mayer and Armstrong, 2004); and (4) an N-terminal domain (NTD), which directs subunit assembly and receptor clustering at synapses (García-Nafría et al., 2016).

In addition to these four distinct regions of the overall tetrameric structure, the LBD dimer interface has been shown to be critical in determining the time course of AMPA receptor gating (Dawe et al., 2015). Specifically, recent work from our lab has identified a novel cation-binding pocket that promotes channel activation by the formation of a network of electrostatic interactions at the apex of both the AMPA receptor (Dawe et al., 2016) and the kainate receptor (Dawe et al., 2013) LBD dimer interfaces. Interestingly, anions have also been shown to control

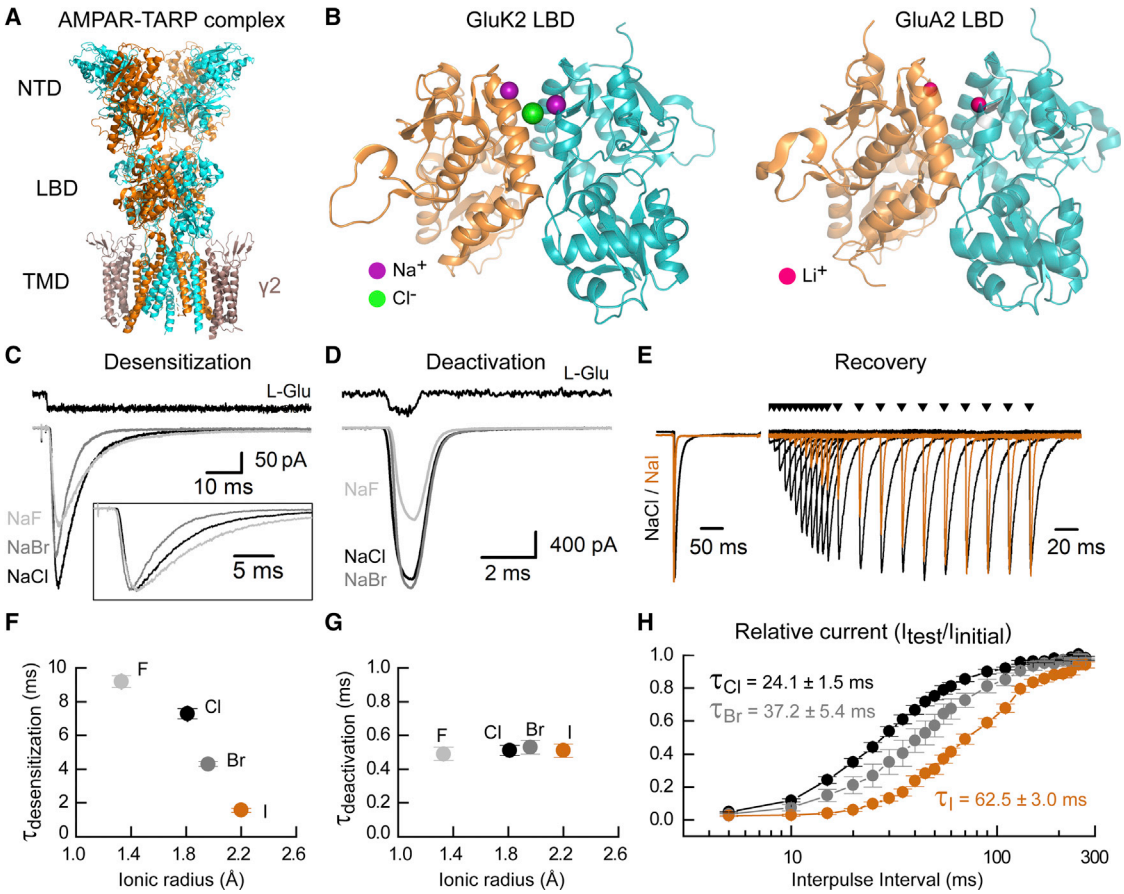

Figure 1. External Anions Selectively Modulate AMPA Receptor Desensitization

(A) Cryo-EM structure of the GluA2-TARP γ2 (pale pink) receptor complex (PDB: 5KBU) in an antagonist-bound form.

(B) Side view of the GluK2 (left, PDB: 3G3F) and GluA2 (right, PDB: 4IGT) LBD dimer, depicting the binding pockets for two Na^+ ions (purple) and one Cl^- ion (green) in GluK2 and two Li^+ ions (magenta) in GluA2.

(C and D) Typical current responses of $GluA2_i$ receptors to a 250 ms (C; patch 140228p6) or 1 ms (D; patch 150825p10) application of 10 mM L-Glu in external NaCl (black), NaBr (gray), and NaF (light gray). Inset: responses scaled to compare decay kinetics. The uppermost trace (black) shows the junction current recorded after the experiment to monitor the solution exchange rate.

(E) Recovery from desensitization for $GluA2_i$ receptors (patch 151201p9) in external NaCl (black) and NaI (orange).

(F and G) Mean time constants of current decay after 250 ms (F; $\tau_{desensitization}$) or 1 ms (G; $\tau_{deactivation}$) L-Glu applications plotted against ionic radius. Data represent mean ± SEM from 7 to 15 (F) or 5 to 12 (G) independent patch experiments.

(H) Recovery from desensitization experiments in different external anion solutions. Data represent mean ± SEM from 6 (NaI), 7 (NaBr), or 13 (NaCl) independent patch experiments. See also Table S1.

the time course of AMPA receptor gating (Bowie, 2002); however, the structural basis of this mechanism has yet to be understood. Another unresolved issue related to AMPA receptor gating is the possible role of the NTD in channel gating. Recent work has highlighted the dynamic motions in the NTD of both AMPA- and kainate-type iGluRs (Dürr et al., 2014; Dutta et al., 2015; Matsuda et al., 2016; Meyerson et al., 2014; Nakagawa et al., 2005) and interactions with auxiliary proteins (Cais et al., 2014; Möykkynen et al., 2014; Shaikh et al., 2016) that may facilitate transsynaptic contact formation (García-Nafría et al., 2016) and permit AMPA receptor trafficking during synapse strengthening (Díaz-Alonso et al., 2017; Watson et al., 2017). Since structural rearrangements of the NTD accompany receptor desensitization (Dürr et al., 2014; Meyerson et al., 2014; Nakagawa et al., 2005; Twomey et al., 2017a), it has been assumed that the underlying movement is triggered by agonist binding. However, it is also possible that the intrinsic thermodynamic mobility of the resting AMPA receptor determines NTD movement and its responsiveness to agonist.

Here, we have designed experiments to distinguish between these two possibilities. Our data identify a novel allosteric anion-binding pocket at the alternatively spliced flip/flop cassette that modifies NTD motions in the resting state prior to agonist binding and regulates channel gating in the presence and absence of auxiliary subunits. Ser775 of the GluA2flip isoform ($GluA2_i$) renders AMPA receptors sensitive to anion modulation, whereas Asn775 of the GluA2flop isoform ($GluA2_o$) almost eliminates the effects of anions on the NTD and channel

gating. Imaging by atomic force microscopy (AFM) reveals that the NTDs of GluA2$_o$ receptors are more mobile than those of GluA2$_i$ receptors, indicating differences in the intrinsic conformational flexibility of their resting states. This behavior is interchangeable via a single amino acid, the Ser775 residue, that operates as a molecular switch between flip and flop isoforms. TARP stoichiometry further modifies these actions of the flip/flop cassette on AMPA receptor heteromers, generating two distinct classes of partially and fully TARPed GluA1/A2 receptors that match the functional profile of native AMPA receptors expressed by cerebellar stellate and Purkinje cells, respectively.

RESULTS

Anions Modulate AMPA Receptor Desensitization

Although the structural and functional bases of anion and cation modulation of kainate receptors have been studied extensively (Bowie, 2002, 2010; Dawe et al., 2013; Wong et al., 2006), much less is known about the effect of external ions on AMPA receptors. Recent work identified the structural mechanism of cation regulation (Figure 1B) (Dawe et al., 2016); however, the nature of anion modulation of AMPA receptors (Bowie, 2002) remains unknown. The effect of external anions on AMPA receptor deactivation and desensitization was studied by recording agonist-evoked membrane currents in outside-out membrane patches excised from HEK293 cells expressing GluA2$_i$(Q) (Figures 1C–1H; see STAR Methods). As observed previously for GluA1$_i$ receptors (Bowie, 2002), the time course of entry into desensitization for GluA2$_i$ was sensitive to external halides, accelerating 1.7- and 4.6-fold in bromide (τ = 4.3 ± 0.2 ms; n = 7) and iodide (τ = 1.6 ± 0.1 ms; n = 7), respectively, compared to chloride (τ = 7.3 ± 0.3 ms; n = 15) (Figures 1C and 1F; Table S1). In contrast, deactivation rates were almost identical for all anions tested on GluA2$_i$ (Figures 1D and 1G; Table S1). In keeping with this, recovery rates out of desensitization were also anion dependent, with GluA2$_i$ recovering from desensitization ~3-fold more slowly in external iodide ($\tau_{recovery}$ = 62.5 ± 3.0 ms; n = 6) than in external chloride ($\tau_{recovery}$ = 24.1 ± 1.5 ms; n = 13) (Figures 1E and 1H; Table S1). Interestingly, rates into and out of desensitization have a predictive relationship with the ionic radius of the external anion (Figures 1F and 1H), with faster desensitization rates observed with anions of a larger radius. The relationship between ionic radius and channel desensitization is consistent with the existence of a specific anion-binding pocket. Previous work has located cation-binding pockets critical to AMPA and kainate receptor gating to the interface of LBD dimers (Dawe et al., 2013, 2016) (Figure 1B); consequently, we reasoned that anions might bind to this region too. Moreover, previous work has demonstrated the important role of the LBD dimer interface in regulating AMPA receptor gating, including desensitization (Dawe et al., 2015; Horning and Mayer, 2004; Sun et al., 2002).

To determine the location of the anion-binding pocket, two soluble constructs of the GluA2-LBD were crystallized in the presence of bromide ions (Figure 2). Since bromide ions give anomalous scattering, we used this property to identify the position of the bound bromide ions in the structure and to distinguish them from other ions and water molecules in the X-ray diffraction data (Figures 2A–2D), as also previously done for localization of the anion-binding site in kainate receptors (Plested and Mayer, 2007). Two X-ray structures were determined that correspond to the flop isoform (GluA2$_o$-LBD; PDB: 6GL4) and the flip-like mutant GluA2$_o$-LBD N775S (PDB: 6GIV). The structures are shown in Figures 2 and S1 along with statistics of data collection and refinement in Table S2. The anomalous scattering data clearly indicate the location of two bromide ions near the base of the D1-D1 dimer interface in both structures (Figures 2C, 2D, and S1A–S1C). More specifically, these anion-binding sites are in a hydrophobic space, surrounded by Pro515 and Leu772 from one subunit, Ile502, Leu504, and Pro515 from the partner subunit, and capped by Lys514 (Figures 2E, 2F, S1D, S1E, S2A, and S2B). There are also several water molecules surrounding each bromide, separating the ion from Ser775 (Figures 2C–2F). Interestingly, we also determined a structure of GluA2$_o$-LBD in the presence of a high concentration of chloride ions, and the electron density indicated that chloride ions bind to the same location as bromide in the LBD dimer interface (data not shown).

Ser775 is notable for interacting with positive modulators of AMPA receptors (Figure S1F) such as cyclothiazide (CTZ) (Partin et al., 1996), as well as being one of the residues that forms the alternatively spliced flip/flop cassette (Sommer et al., 1990). Given the high affinity for CTZ, we hypothesized that it would displace bromide ions from their bound positions. In agreement with this, electrophysiological responses observed in different external anions were non-decaying in each case (Figures S1G and S1H), consistent with the idea that CTZ outcompetes external anions for binding. Likewise, mutation of Leu504 to an Ala or Cys residue either reversed or eliminated anion regulation of GluA2$_i$ receptor decay kinetics, respectively (Figures S2C–S2F), further validating the location of the anion-binding pocket as being at the LBD dimer interface. Taken together, these results identify an anion-binding pocket, which, when occupied by halide ions, may be responsible for regulating the rates of entry into and exit from AMPA receptor desensitization.

The Ser/Asn Residue Regulates Anion Effects

To establish a causal relationship between the anion-binding pocket and the functional effects of external anions on GluA2, we focused on position 775, which, as mentioned previously, is modified by alternative splicing and is also involved in all regulatory effects of the flip/flop cassette (see below). The flip isoform of the AMPA receptor contains a Ser at position 775 whereas the flop isoform contains an Asn (Figures 3A and 3B) (Sommer et al., 1990), which we hypothesized may differentially affect anion modulation of AMPA receptors.

To test this, we first compared the effect of external anions on desensitization rates of GluA2$_i$ and GluA2$_o$ receptors, whose amino acid sequences differ at nine residues (Figure 3A) (Sommer et al., 1990). As anticipated, GluA2$_i$ and GluA2$_o$ receptors differed in their sensitivity to modulation by external ions (Figures 3C and 3D), though the trend of faster desensitization in the presence of larger anions persisted (Figure 3F). For example, in GluA2$_o$ receptors, iodide accelerated rates into desensitization

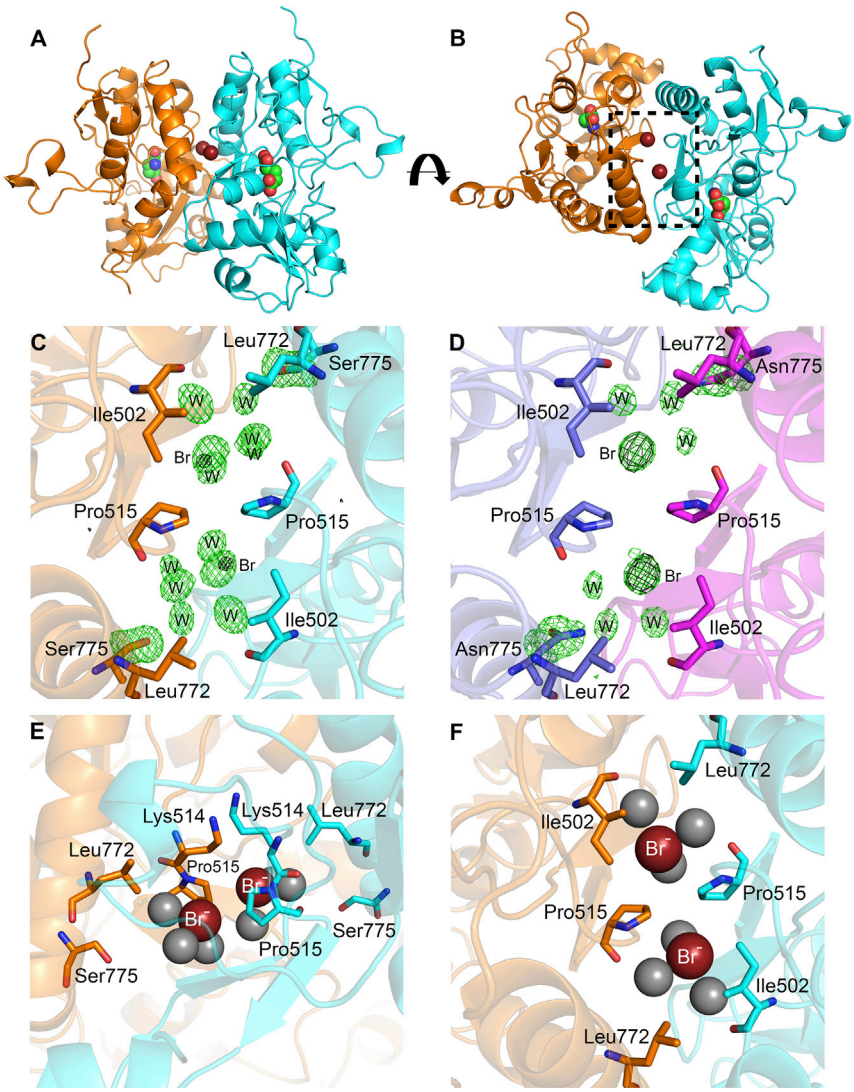

Figure 2. Detection of Bromide Ions in the GluA2-LBD Dimer Interface

(A and B) Side (A) and top (B) views of the $GluA2_o$-LBD N775S dimer. Bromide ions are shown in the dimer interface as brown spheres and glutamate with carbon atoms as green spheres. Nitrogen atoms are blue, and oxygen atoms are red.

(C and D) Anomalous difference electron density map (black; contoured at 7σ, before introduction of bromide ions in the structure) and Fo-Fc difference map (green; contoured at 3σ) from omitting Ser775/Asn775, bromide ions, and water molecules within 4 Å of bromide from $GluA2_o$-LBD N775S (C) and $GluA2_o$-LBD (chain A) (D).

(E and F) Magnified side (E) and top (F) views of the bromide-binding sites in the $GluA2_o$-LBD N775S dimer interface. Water molecules are shown as gray spheres, and amino acid residues surrounding the binding sites are shown as orange or cyan sticks based on their subunit of origin.

See also Figure S1 and Table S2.

~1.6-fold (τ = 0.8 ± 0.05 ms; n = 6) compared to chloride (τ = 1.3 ± 0.06 ms; n = 12), which was substantially less than the 4.6-fold difference observed on $GluA2_i$ receptors (Figures 3C, 3D, and 3F; Table S1). To examine whether this difference was due to residue 775, which is in close proximity to the bromide-binding site (Figure 2E), we repeated these experiments on the Ser775Asn $GluA2_i$ receptor (Figures 3E and 3F; Table S1). As anticipated, the $GluA2_i$ S775N receptor was much less sensitive to modulation by external anions. For example, iodide (τ = 3.6 ± 0.5 ms; n = 6) accelerated desensitization compared to chloride (τ = 5.2 ± 0.4 ms; n = 12) by only 1.4-fold (Figures 3E and 3F; Table S1). In contrast, mutation of the two more apical dimer interface residues that contribute to fast $GluA2_o$ desensitization (Figure 3B) (Quirk et al., 2004) produced a receptor (T765N/P766A) that still exhibited robust anion sensitivity (Figure S3). As a result, the near loss of anion modulation from flip- to flop-type GluA2 AMPA receptors can be primarily attributed to Asn775, consistent with our structural data placing bromide ions in the lower D1-D1 LBD dimer interface. Interestingly, anion modulation of recovery from desensitization was still present in $GluA2_i$ S775N receptors (Figures 3G and 3H), demonstrating that anion effects on rates into and out of desensitization have different mechanisms.

Anions Control Resting and Active AMPA Receptors

Anions may affect AMPA receptors by controlling the receptor's resting and/or activated state(s). To delineate between these possibilities, we investigated whether external halides elicited global, conformational changes in protein structure in the absence and/or presence of agonist. Specifically, we measured protein height as an indicator of conformation using AFM, since AMPA receptor activation and desensitization involve compression in the quaternary structure (Dürr et al., 2014; Herguedas et al., 2016; Meyerson et al., 2014; Twomey et al., 2017a, 2017b) as in NMDA-type iGluRs (Balasuriya et al., 2014; Suzuki et al., 2013). To image the receptor, we purified and reconstituted individual AMPA receptor complexes into lipid bilayers (Figures 4 and S4; see STAR Methods).

The addition of L-Glu to NaCl-based external solution prompted a 0.69 ± 0.11 nm (n = 11) reversible reduction in $GluA2_i$ receptor height (Figures 4A, 4C, and S5), which was prevented by the competitive antagonist, 6-cyano-7-nitroquinoxaline-2,3-dione (CNQX), and the positive allosteric modulator, CTZ (Table S3; Figure S5). AFM experiments were also repeated to determine if height changes could be induced by different anions (Figures 4B, 4D, and S5; Table S3). Unexpectedly, merely changing the main external anion species from NaCl to NaBr (0.74 ± 0.06 nm; n = 12) or NaI (0.87 ± 0.11 nm; n = 13) produced a substantial and reversible vertical compression of individual $GluA2_i$ receptors (Figures 4D and S5) comparable to L-Glu-evoked

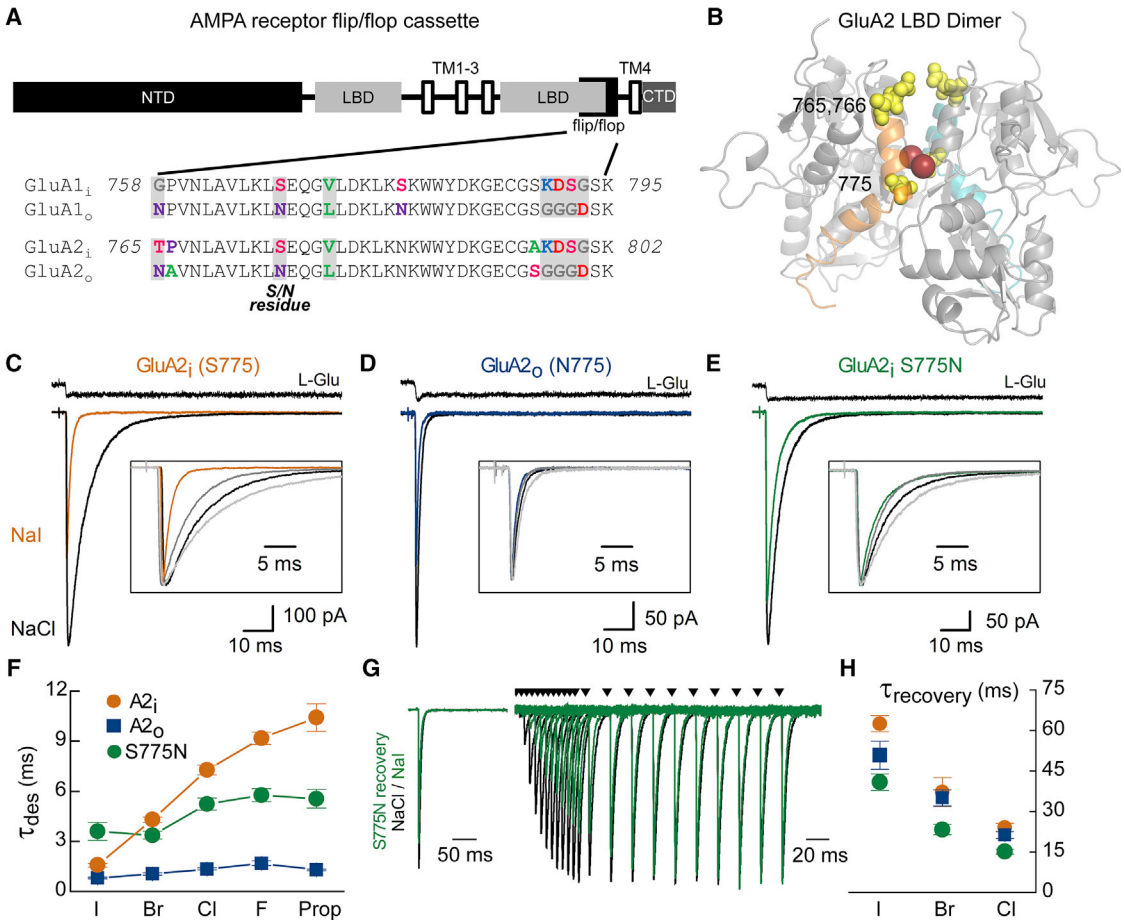

Figure 3. The Ser/Asn 775 Residue of the Flip/Flop Cassette Governs Anion Modulation of AMPA Receptors

(A) Sequence alignment of the GluA1 and GluA2 AMPA receptor flip/flop cassette, located toward the C-terminal end of the LBD. Positions that differ in both subunits are shaded gray, while residues are colored by chemical property (blue, positive charge; red, negative charge; pink, small polar; purple, large polar; green, hydrophobic).

(B) $GluA2_o$-LBD dimer with residues Asn765, Ala766, and Asn775 shown as yellow spheres and the two bromide ions as brown spheres. The flip/flop cassette is orange in one subunit and cyan in the other subunit.

(C–E) Typical current responses (250 ms, 10 mM L-Glu) of $GluA2_i$ (C; patch 151123p15), $GluA2_o$ (D; patch 160218p14), and $GluA2_i$ S775N (E; patch 160119p3) receptors in external NaCl (black) and NaI (colored trace). Inset: scaled responses in external NaI (colored trace), NaBr (gray), NaCl (black), and NaF (light gray). The uppermost trace (black) shows the junction current recorded after the experiment to monitor solution exchange rate.

(F) Desensitization time constants for data shown in (C)–(E), plotted against different halide ions. Data represent mean ± SEM from 6 to 15 independent patch experiments. Prop refers to propionate.

(G) Recovery from desensitization of $GluA2_i$ S775N receptors (patch 160401p15) in external NaCl (black) and NaI (green).

(H) Mean time constants of recovery from desensitization for $GluA2_i$ (orange), $GluA2_o$ (blue), and $GluA2_i$ S775N (green) in different external anions. Data represent mean ± SEM from 5 to 32 independent patch experiments.

See also Figures S2 and S3 and Table S1.

responses (Figure 4C). Interestingly, much less additional compression (~0.2 nm) was observed when L-Glu (10 mM) was added to NaBr or NaI solutions (Figure 4C), suggesting the principal role of anions is to prime the receptor. Since the action of L-Glu, however, was not entirely occluded, the structural rearrangements observed with anion substitution must differ from those elicited by agonist binding.

To establish a relationship between anion-induced height changes (Figure 4D) and their effect on desensitization (Figures 1C and 1F), we repeated AFM measurements on $GluA2_o$, whose gating properties are relatively anion insensitive. Remarkably, anion-induced height compression was almost completely absent from the $GluA2_o$ receptor when external solution containing NaCl was switched to either NaBr (0.03 ± 0.06 nm; n = 14) or NaI (0.08 ± 0.06 nm; n = 14) (Figure 4D; Table S3). Importantly, agonist binding continued to elicit reductions in the height of all anion species (Figure 4C), reaffirming that anion and agonist effects are different. In agreement with our electrophysiology data, iodide anions did not affect the AFM-reported height changes of $GluA2_i$ receptors containing the single S775N point mutation (Figure 4D; Table S3), establishing a critical role for the Ser/Asn residue and causal relationship between the effects

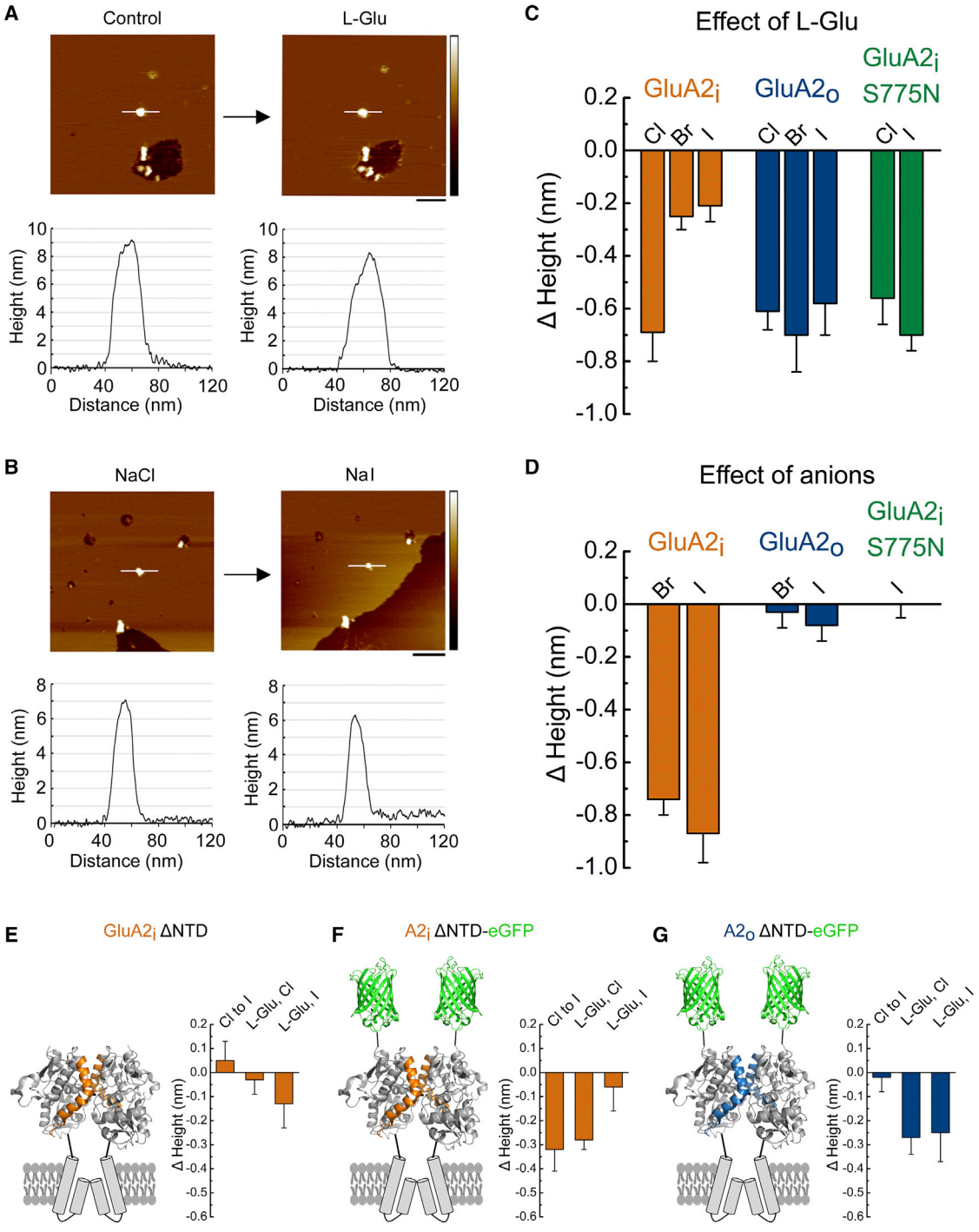

Figure 4. Anions Control the Resting and Active Quaternary Structure of the AMPA Receptor through the LBD

(A) Top: representative AFM images of a bilayer containing $GluA2_i$ receptors before (left) and after (right) application of L-Glu (10 mM). Scale bar, 100 nm; color-height scale, 0–10 nm. Bottom: sections through the receptor at the position indicated by the white line above.

(B) Top: representative AFM images of a bilayer containing $GluA2_i$ receptors before (left) and after (right) a switch from NaCl to NaI. Scale bar, 100 nm; color-height scale, 0–10 nm. Bottom: sections through the receptor at the position indicated by the white line above.

(C) Average height changes of $GluA2_i$, $GluA2_o$, and $GluA2_i$ S775N in response to L-Glu. Data represent mean ± SEM for 10–14 receptors.

(D) Average height changes of $GluA2_i$, $GluA2_o$ and $GluA2_i$ S775N in response to anion switches. Data represent mean ± SEM for 12–14 receptors.

(legend continued on next page)

of anions on channel gating and height changes. Finally, AFM-reported height changes elicited by switches in external anions were absent from the $GluA2_i$ L504A receptor, whereas L-Glu persisted in reducing height in all anion species tested (Figures S2G and S2H; Table S3).

Taken together, these data indicate two important points. First, external anions prime the receptor prior to activation. Whether priming then determines the rate of AMPA receptor desensitization prior to agonist binding is investigated below. Second, anion modulation reveals a coupling between the LBD dimer interface and the NTD. This latter possibility was examined in additional AFM experiments on GluA2 lacking the NTD (i.e., GluA2 ΔNTD).

The Flip/Flop Cassette Controls NTD Motions

Anion- and agonist-induced height changes were repeated using the truncated $GluA2_i$ ΔNTD receptor (Figures 4E–4G and S6). Contrary to wild-type behavior, virtually no height changes could be induced in the $GluA2_i$ ΔNTD receptor by replacing NaCl with NaI (−0.05 ± 0.08 nm; n = 15) or by agonist application (in NaCl, 0.03 ± 0.06 nm; n = 13) (Figure 4E; Table S3), demonstrating that receptor compression requires the NTD. To explore this further, we reengineered $GluA2_i$ and $GluA2_o$ receptors, replacing each NTD with an EGFP molecule (Figures 4F and 4G). Importantly, the expressed GluA2 ΔNTD-EGFP constructs exhibited similar functional behavior in terms of anion sensitivity and responsiveness to agonist (data not shown). We reasoned that although anions and agonists bind to the LBD, the energy of binding might induce a conformational change that is more prominently observed in distant regions of the protein, even if the NTD is replaced by EGFP. Consistent with this, compression induced by external anions (NaCl to NaI, 0.32 ± 0.09 nm; n = 18) and agonist application (in NaCl 0.28 ± 0.04 nm; n = 10) was restored in the $GluA2_i$ ΔNTD-EGFP construct, demonstrating that binding events in the LBD are transferred to the NTD. Since the $GluA2_i$ ΔNTD-EGFP construct retained the original linker sequences, we reasoned that the linkers might exert a similar downward pulling force on whatever is attached above. Since EGFP has a different size and likely does not form intersubunit dimers, these distinctions may explain why height changes were ~2-fold less with $GluA2_i$ ΔNTD-EGFP. Finally, agonist, but not anion, binding induced compression of the $GluA2_o$ ΔNTD-EGFP construct (Figure 4G), confirming that compression of the NTD is differentially controlled by the flip/flop cassette. Given this, we next tested if the intrinsic motions in resting GluA2 AMPA receptors may be a critical factor in determining its anion and agonist responsiveness.

AMPA Receptors Have Different Resting States

AFM visualization of the NTD movements of the GluA2 AMPA receptor (Figure 5) revealed that both isoforms exist as two distinct globular structures, which show mobility even in the resting state (Figure 5A; Videos S1 and S2). Unexpectedly, NTD movements at rest, expressed as cumulative squared displacement (CSD), were almost 3-fold greater for $GluA2_o$ (resting CSD, 15.53 ± 2.54 nm^2, n = 7) than for $GluA2_i$ (resting CSD, 5.58 ± 0.92 nm^2, n = 5) (Figures 5B and 5D; Table S4), revealing that NTD motions are controlled by the flip/flop cassette. Bath application of a saturating concentration of L-Glu (10 mM) increased the NTD mobility of the $GluA2_i$ AMPA receptor (CSD, 13.90 ± 2.11 nm^2, n = 9), but not that of $GluA2_o$ (CSD, 17.12 ± 0.59 nm^2, n = 5) (Figures 5C and 5D; Videos S3 and S4). As expected, the NTD mobility in the presence of L-Glu was reduced by CNQX for both $GluA2_i$ (5.33 ± 0.82 nm^2, n = 4) and $GluA2_o$ (9.50 ± 1.95 nm^2, n = 3) (Figure 5D; Table S4) demonstrating a direct relationship between NTD mobility and agonist binding. NTD movement of $GluA2_i$ was agonist-concentration dependent (Figure 5E; Table S4), whereas the mobility of $GluA2_o$ was not. Most importantly, the NTD mobility of the $GluA2_i$ S775N mutant (resting CSD, 14.00 ± 1.70, n = 9) was also greater than that of wild-type $GluA2_i$, but not $GluA2_o$ (Figure 5B; Table S4). This observation is important, as it establishes a causal link between the effects of anions on channel gating (Figures 1 and 3) and height changes (Figure 4) with the resting state of the AMPA receptor.

Given this, we reasoned that the lower conformational mobility of the $GluA2_i$ receptor at rest would favor more stable interactions in regions of the protein, such as the LBD dimer interface (Dawe et al., 2015, 2016). A more stable AMPA receptor structure would also favor anion binding to the LBD dimer interface and account for the greater effect of external halide ions on $GluA2_i$ receptors. Conversely, the higher mobility of the $GluA2_o$ receptor would disfavor anion binding (and its regulation) and destabilize the open state of the receptor, explaining its much more rapid desensitization kinetics and weaker anion sensitivity. Given this, we concluded that the flop cassette of the AMPA receptor acts as a master switch that overrides allosteric mechanisms, such as anion regulation that impacts the time AMPA receptors remain in the open state. We therefore hypothesized that $GluA2_o$ should also be similarly insensitive to regulation by auxiliary proteins, such as the prototypical TARP, stargazin (γ2).

To test this hypothesis, we compared the electrophysiological responses of $GluA2_i$, $GluA2_o$, and $GluA2_i$ S775N receptors expressed with γ2 (Figures 6A–6D). As noted previously (Dawe et al., 2016), co-assembly of $GluA2_i$ receptors with γ2 slowed desensitization rates (τ_{des}, ms) and reduced equilibrium desensitization ($I_{equilibrium}$, %) by ~4-fold and 22-fold, respectively (Figures 6A, 6C, and 6D; Table S1). Desensitization rates and equilibrium desensitization were also anion sensitive, exhibiting a rank order of potency similar to that described for $GluA2_i$ receptors alone (Figures 6B–6D; Table S1). In contrast, co-assembly of $GluA2_o$ receptors with γ2 almost eliminated the effect of the TARP on desensitization rates, equilibrium desensitization, and anion regulation (Figures 6A–6D; Table S1), in agreement with

(E–G) Mean height changes of $GluA2_i$ ΔNTD (E), $A2_i$ ΔNTD-EGFP (F), and $A2_o$ ΔNTD-EGFP (G) receptors in response to anion substitution as well as 10 mM L-Glu application in different external anions. Data represent mean ± SEM for 10–22 receptors. Cartoon uses GFP (PDB: 1GFL) and AMPA receptor LBD (PDB: 1FTJ) structures for illustrative purpose only.
See also Figures S4–S6 and Table S3.

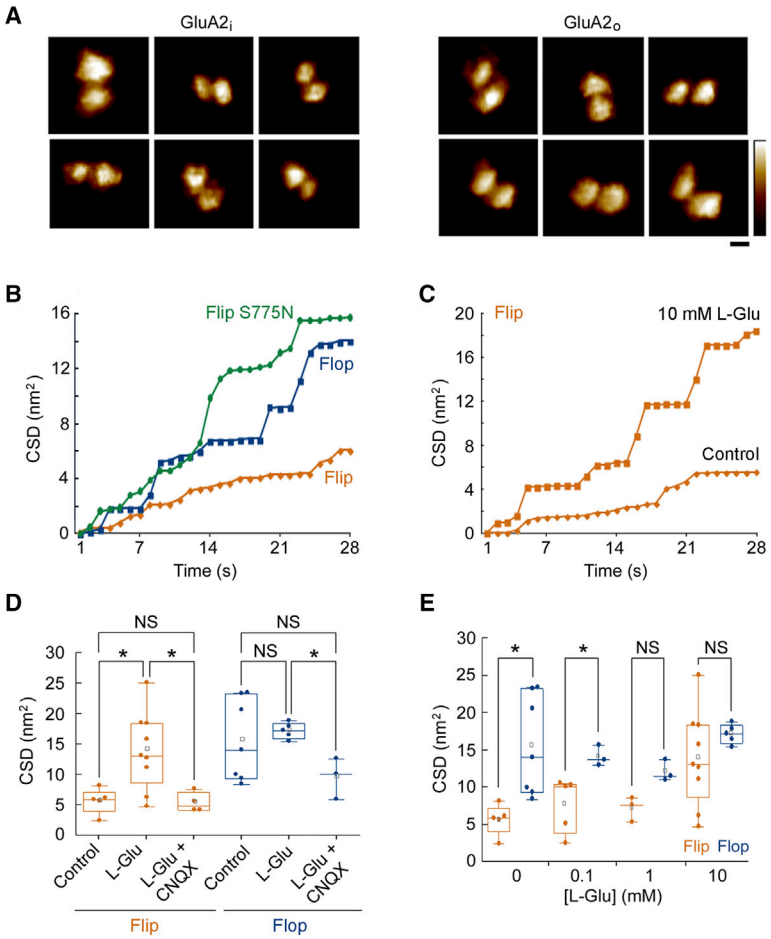

Figure 5. The Mobility of the Resting State of GluA2 AMPA Receptors Is Variable between Flip and Flop Isoforms

(A) Galleries of zoomed (120 × 120 nm) AFM images of individual flip (left) and flop (right) AMPA receptors. Scale bar, 20 nm; color-height scale, 0–8 nm.

(B) Representative cumulative second-by-second (up to 28 s) mobility data for individual flip, flop, and flip S775N AMPA receptors in the resting state.

(C) Representative cumulative second-by-second (up to 28 s) mobility data for individual flip AMPA receptors in the resting state and in the presence of L-Glu (10 mM).

(D) Combined mobility data (at 28 s) for flip and flop AMPA receptors in the resting state, in the presence of L-Glu and in the presence of L-Glu plus CNQX (0.5 mM). Asterisks indicate significant differences ($p < 0.05$) between groups (one-way ANOVA, Fisher's test). NS, not significant.

(E) Combined mobility data (at 28 s) for flip and flop AMPA receptors in the resting state and in the presence of different concentrations of L-Glu. Asterisks indicate significant differences ($p < 0.05$) between flip and flop receptors under equivalent conditions (Mann-Whitney *U* test). CSD, cumulative squared displacement.

See also Table S4 and Videos S1, S2, S3, and S4.

the hypothesis that the flop cassette overrides TARP regulation. Importantly, γ2 also had a greatly attenuated effect on GluA2$_i$ S775N receptors, further demonstrating the pivotal role of the 775 residue as a molecular switch (Figures 6A–6E; Table S1).

Native AMPA Receptors Are Also Sensitive to Anion Regulation

To examine how these actions of the flip/flop cassette impact native receptors, we studied the gating properties of AMPA receptors in outside-out and nucleated patches excised from cerebellar Purkinje and stellate cells, respectively (Figure 7; Table S5). Previous work has shown that AMPA receptors expressed by both cell types are regulated by γ2 but that their gating properties are distinct (Barbour et al., 1994; Bats et al., 2012; Yamazaki et al., 2015). In keeping with this, rapid application (250 ms) of 10 mM L-Glu to excised patches from Purkinje cells elicited AMPA receptor responses that decayed at a slower rate and to a lesser extent than responses from stellate cells (Figure 7A). There was a 6-fold difference in equilibrium desensitization between Purkinje and stellate cells corresponding to steady-state/peak values of 8.3% ± 0.6% (n = 21) and 1.4% ± 0.1% (n = 29), respectively (Figure 7B). Similarly, the decay kinetics of the responses from Purkinje cells were best fit with a weighted time constant of 7.5 ± 0.4 ms (n = 20) compared to 2.9 ± 0.1 ms (n = 30) for responses from stellate cells (Figure 7C). These distinctions in decay kinetics and the degree of equilibrium desensitization of Purkinje and stellate cells are reminiscent of the functional differences between GluA2$_i$/γ2 and GluA2$_o$/γ2 receptors, respectively (Figures 6A–6D). However, two subsequent observations suggested that a more complicated explanation was required to account for the properties of AMPA receptors expressed by Purkinje and stellate cells.

First, the positive allosteric modulator CTZ (100 μM) eliminated macroscopic desensitization of AMPA receptor-mediated responses of Purkinje and stellate cells (Figure 7A, insets), confirming that both cell types express flip-dominant AMPA receptors (Partin et al., 1994, 1995; Penn et al., 2012). Flop-dominant AMPA receptors continue to desensitize in the presence of CTZ, albeit at a reduced rate (Partin et al., 1994, 1995), which is distinct from the responses observed in patches from Purkinje and stellate cells. Second, although AMPA receptor responses exhibited by Purkinje and stellate cells were sensitive to external anion modulation (Figures 7D and 7E), their effects on decay kinetics were intermediate between GluA2$_i$/γ2 and GluA2$_o$/γ2 receptor responses (Figure 6D; Table S1). AMPA receptor decay kinetics in both cell types slowed by ~2- to 3-fold upon exchange of external Br^- (Purkinje, $\tau = 3.9 \pm 0.5$ ms, n = 5; stellate, $\tau = 2.0 \pm 0.2$ ms, n = 8) with F^- (Purkinje, $\tau = 10.6 \pm 0.9$ ms, n = 6; stellate, $\tau = 5.0 \pm 0.6$ ms, n = 5). These apparently inconsistent observations may be reconciled if Purkinje and/or stellate cells

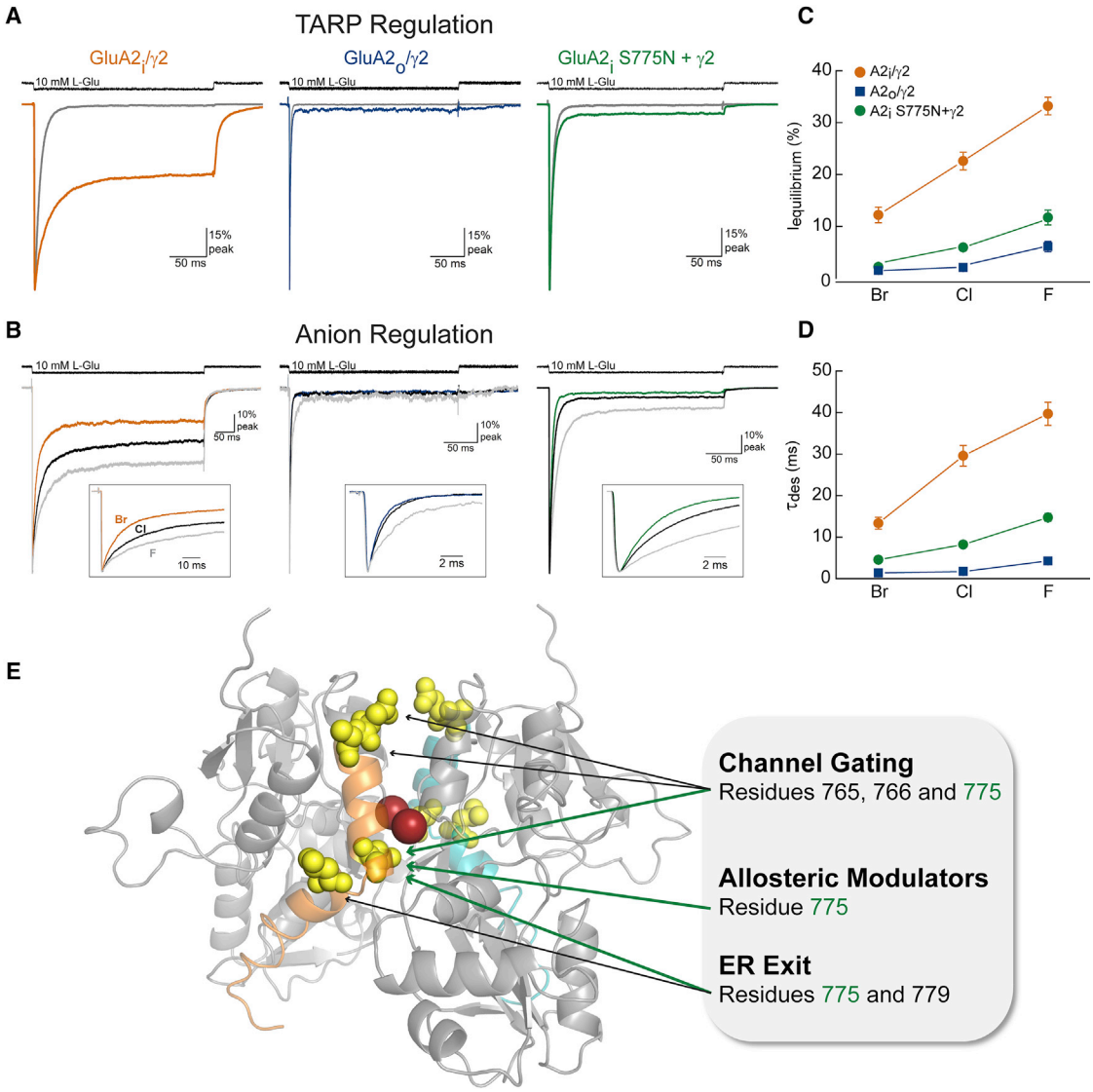

Figure 6. The Flop Cassette Acts as a Master Switch to Override Regulation of AMPA Receptors by TARP Auxiliary Subunits

(A) Typical current responses of $GluA2_i$ (patch 171120p1), $GluA2_o$ (patch 160324p7), and $GluA2_i$ S775N (patch 180813p9) receptors to a 250 ms application of 10 mM L-Glu when co-expressed with γ2 (colored trace). The AMPA receptor responses in the absence of γ2 were taken from patch numbers 180301p3 ($GluA2_i$), 160218p14 ($GluA2_o$), and 160119p3 ($GluA2_i$ S775N). The uppermost trace (black) shows the junction current recorded after the experiment to monitor solution exchange rate.

(B) Typical current responses in different external anions of wild-type and mutant $GluA2_i$ AMPA receptors co-assembled with γ2. ($GluA2_i$, patch 151214p3; $GluA2_o$, patch 160324p7; $GluA2_i$ S775N, patch 180813p9).

(C) Mean equilibrium current amplitude as a percentage of the peak response.

(D) Mean time constants of current decay in the continued presence of L-Glu.

(E) GluA2 LBD dimer highlighting the flip/flop cassette in orange (front) and cyan (back). Although different residues are responsible for the functional differences between flip and flop GluA2 isoforms in terms of channel gating (residues 765, 766, and 775), allosteric regulation by anions and CTZ (residue 775), and ER exit (residues 775 and 779), the 775 residue is implicated in all of these regulatory functions.

See also Table S1.

express AMPA receptor tetramers that contain both flip and flop variants. Consistent with this suggestion, previous work has shown that CTZ eliminates macroscopic desensitization of recombinant $GluA1_i/A2_o$ or $GluA1_o/A2_i$ heteromers (Partin et al., 1994), matching the responses from patches of Purkinje and stellate cells. Since the functional impact of the flip/flop cassette on GluA1/A2 heteromers has yet to be studied in terms of their modulation by TARP γ2 and sensitivity to external anions, we performed additional experiments to better understand this relationship.

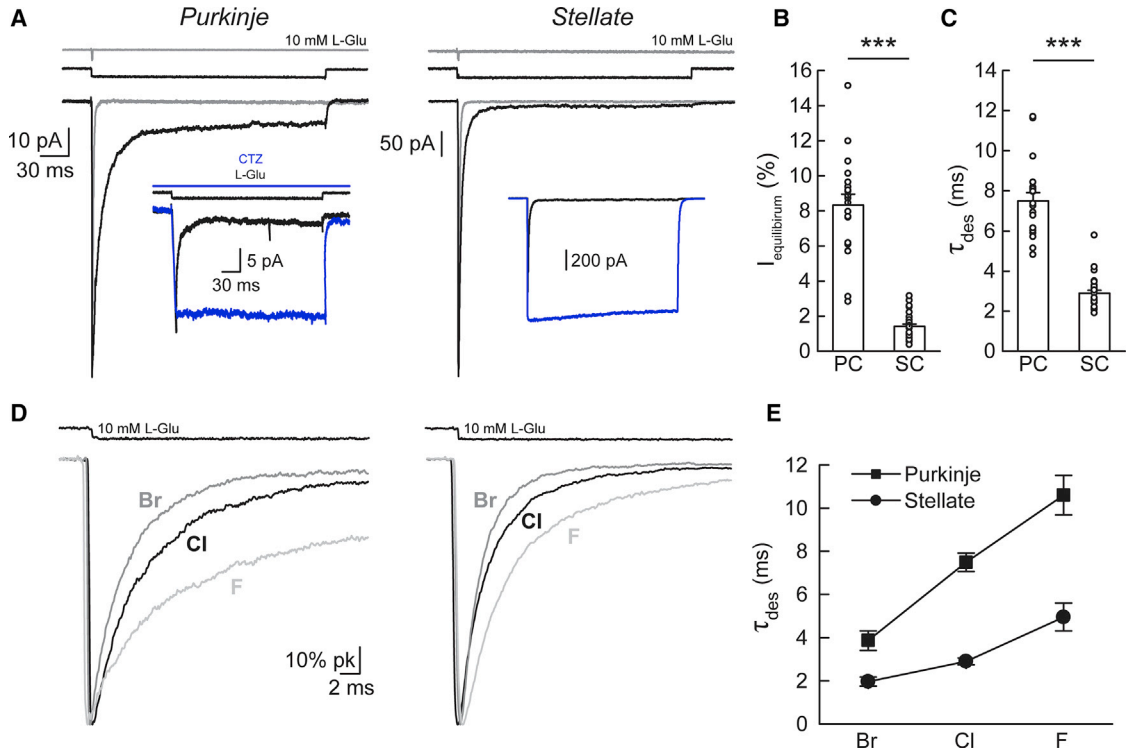

Figure 7. Native AMPA Receptors Are Modulated by External Anions

(A) Typical current responses of an excised Purkinje cell membrane patch (left, patch 190129p5) or stellate cell nucleated patch (right, patch 190205p4) to a 250 ms (black) or 1 ms (gray) application of 10 mM L-Glu. Insets show non-desensitizing responses in the presence of 100 μM CTZ (blue) (Purkinje, patch 190214p8; stellate, patch 190129p3).

(B) Mean equilibrium current amplitude as a percentage of peak response ($I_{equilibrium}$). ***$p < 0.0001$, unpaired t test.

(C) Mean weighted time constants of current decay following 250 ms L-Glu application (τ_{des}). ***$p < 0.0001$, Mann-Whitney *U* test.

(D) Normalized current responses to 250 ms application of L-Glu in NaCl (black), NaBr (dark gray), or NaF (light gray) in Purkinje (left, patch 190213p4) and stellate cell (right, patch 190205p4) patches.

(E) Mean weighted τ_{des} across anion conditions in Purkinje (black squares) and stellate cell (black circles) patches.

Data are presented as mean ± SEM. See also Table S5.

TARP Stoichiometry Shapes the Functional Behavior of AMPA Receptor Heteromers

To examine how alternative splicing impacts the function of GluA1/A2 heteromers, we initially focused on fully TARPed receptors by tethering the γ2 auxiliary subunit to flip/flop variants of GluA1(Q) and GluA2(R) subunits. GluA1/A2 heteromerization was confirmed in each recording by testing for the loss of cytoplasmic polyamine block (Figure S7; see STAR Methods), as described previously (Partin et al., 1995).

The flip/flop cassette had a profound and concomitant effect on the decay kinetics and equilibrium desensitization of fully TARPed GluA1/A2 heteromers (Figure 8A). Flip-only heteromers ($A1_i/\gamma2 + A2_i/\gamma2$) decayed at a slower rate ($\tau = 10.6 \pm 0.3$ ms, n = 6) and to a lesser extent (ss/peak = 18.5% ± 1.4%, n = 6) in response to agonist stimulation than flop-only receptors ($A1_o/\gamma2 + A2_o/\gamma2$), which had faster decay kinetics ($\tau = 3.0 \pm 0.2$ ms, n = 7) and more complete equilibrium desensitization (ss/peak = 3.5% ± 0.8%, n = 7) (Figures 8B–8D; Table S5). Although, GluA1/A2 heteromers containing both flip/flop variants had intermediate behavior, as might be expected, alternative splicing of GluA2 had the more dominant impact on channel gating. For example, $GluA1_i/A2_o$ receptors ($A1_i/\gamma2 + A2_o/\gamma2$) exhibited faster ($\tau = 3.3 \pm 0.3$ ms, n = 7) and more complete desensitization (ss/peak = 7.1% ± 0.7%, n = 7) than $GluA1_o/A2_i$ receptors ($A1_o/\gamma2 + A2_i/\gamma2$, $\tau = 8.9 \pm 0.5$ ms, n = 8; ss/peak = 14.3% ± 1.5%, n = 8) (Figures 8B–8D; Table S5). Analysis of anion effects on fully TARPed GluA1/A2 heteromers revealed a similar relationship, where flip-only heteromers were more sensitive to anion regulation than flop-only heteromers and alternative splicing of GluA2 had the more dominant effect (Figure 8E; Table S5). Interestingly, the decay kinetics and equilibrium desensitization of fully TARPed GluA1/A2 heteromers exhibited a linear relationship across all external anion conditions (Figure 8F). Given this, we reasoned that this relationship could be used to interrogate TARP γ2 stoichiometry of native AMPA receptors with the data already obtained from cerebellar Purkinje and stellate cells.

In keeping with this, anion modulation of native AMPA receptors of cerebellar Purkinje cells was well fit by a linear relationship that was statistically indistinguishable from fully TARPed recombinant GluA1/A2 heteromers (p = 0.10, ANOVA; Figure 8F, red). The data taken from stellate cells, however, did not match the

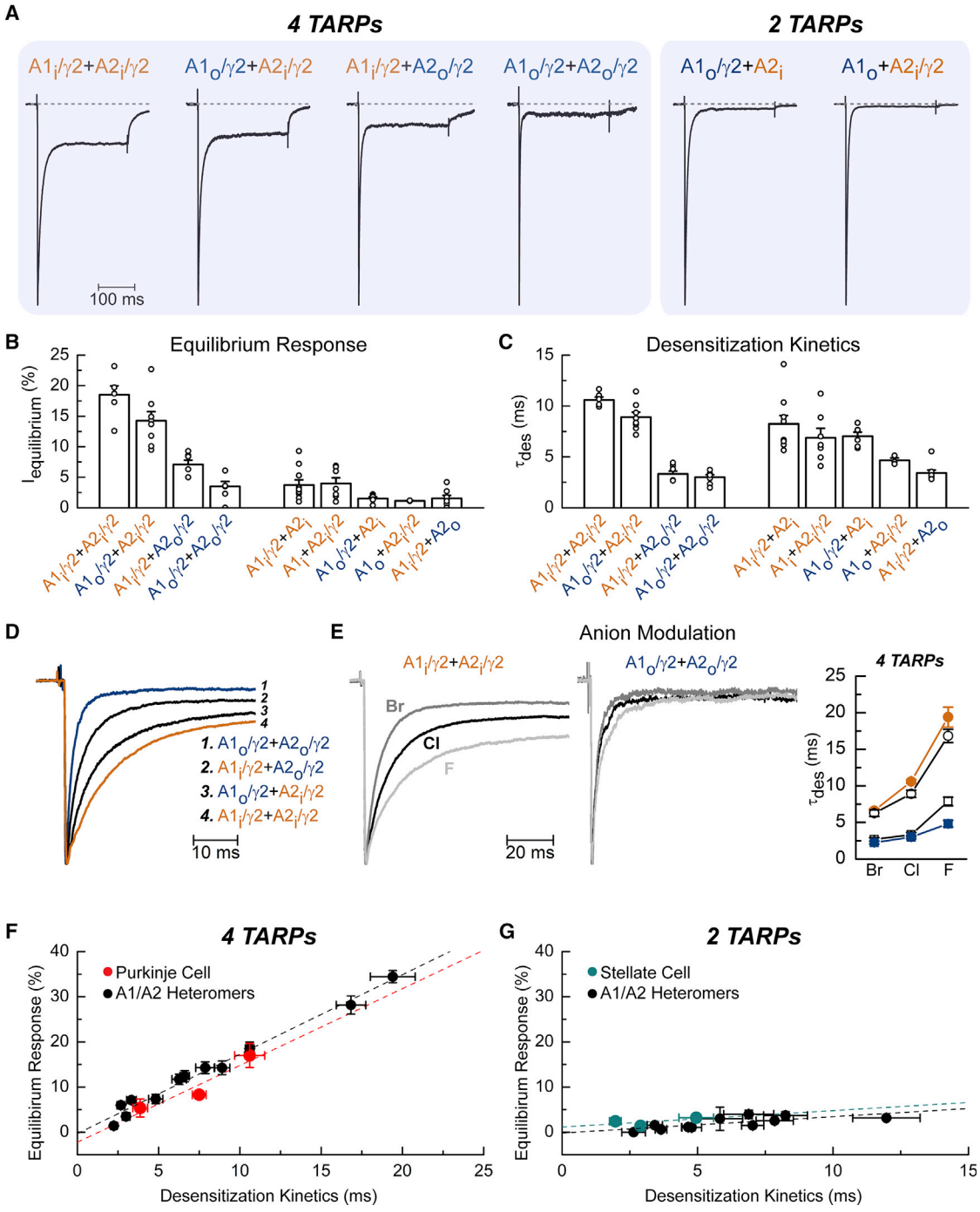

Figure 8. The Functional Behavior of AMPA Receptor Heteromers Is Shaped by TARP Stoichiometry

(A) Typical current responses of heteromeric AMPA receptors to a 250 ms application of 5 mM L-Glu in tandem with TARP γ2 when indicated. Example traces are in the following sequence from left to right: GluA1$_i$/γ2+GluA2$_i$/γ2 (patch 190215p2), GluA1$_o$/γ2+GluA2$_i$/γ2 (patch 190215p13), GluA1$_i$/γ2+GluA2$_o$/γ2 (patch 190228p2), GluA1$_o$/γ2+GluA2$_o$/γ2 (patch 190301p2), GluA1$_o$/γ2+GluA2$_i$ (patch 190213p3), and GluA1$_o$+GluA2$_i$/γ2 (patch 190204p11). All GluA2$_{i/o}$ plasmids are Q/R edited.

(B) Mean equilibrium current amplitude as a percentage of the peak response.

(C) Mean time constants of current decay in the continued presence of L-Glu. Data are presented as mean ± SEM with values of individual patches plotted as white circles.

(D) Overlay of current responses of heteromeric AMPA receptors co-expressed with 4 TARPs (A, left) on a shorter timescale.

(legend continued on next page)

relationship; even though the stellate cell data were well fit by linear regression, the relationship had a different slope (Figure 8G, cyan). Unlike fully TARPed receptors and AMPA receptors from Purkinje cells, equilibrium responses elicited by AMPA receptors from stellate cells were only weakly sensitive to anion modulation (Figure 7; Table S5). Given this, we reasoned that the response profile of AMPA receptors from stellate cells might be more consistent with a partially TARPed receptor.

To test this, we examined the functional behavior of flip/flop variants of GluA1/A2 heteromers in which γ2 was tethered to either the GluA1 or GluA2 subunit so that any GluA1/A2 tetramer combination would possess only two γ2 auxiliary subunits. As anticipated, the relationship between decay kinetics and equilibrium desensitization of partially TARPed GluA1/A2 receptors was different from that of fully TARPed heteromers (Figure 8G). For example, although flip-containing heteromers exhibited slower desensitization kinetics (e.g., $A1_i/\gamma2 + A2_i$, $\tau = 8.2 \pm 0.8$ ms, n = 10) than heteromers containing both flip and flop (e.g., $A1_i/\gamma2 + A2_o$, $\tau = 3.4 \pm 0.3$ ms, n = 8), the degree of equilibrium desensitization was similar in each case ($A1_i/\gamma2 + A2_i$, ss/peak = 3.7% ± 0.9%, n = 10 versus $A1_i/\gamma2 + A2_o$, ss/peak = 1.5% ± 0.5%, n = 8) (Figures 8B and 8C; Table S5). Although partially TARPed heteromers containing both flip/flop variants had intermediate behavior, alternative splicing of GluA2 had the more dominant impact on desensitization kinetics. For example, $GluA1_i/A2_o$ receptors exhibited faster desensitization kinetics ($A1_i/\gamma2 + A2_o$, $\tau = 3.4 \pm 0.3$ ms, n = 8) than $GluA1_o/A2_i$ receptors ($A1_o/\gamma2 + A2_i$, $\tau = 7.0 \pm 0.4$ ms, n = 6) (Figures 8B and 8C; Table S5). Thus, the decay kinetics of partially TARPed AMPA receptors varied according to subunit composition and the external anion type, whereas equilibrium desensitization was relatively unchanged (Figure 8G; Table S5), much like the behavior of AMPA receptors from stellate cells (Figure 7). In fact, linear regression plots of data from partially TARPed AMPA receptors and stellate cells were statistically indistinguishable (p = 0.20, ANOVA; Figure 8G), suggesting that stellate cells express partially TARPed AMPA receptors. Taken together, these data provide compelling evidence for the important role of TARP stoichiometry in dictating the functional behavior of recombinant and native AMPA receptor heteromers. Our results also provide a proof-of-principle approach for future enquiry interrogating the auxiliary subunit composition of native receptors.

DISCUSSION

The present study advances our understanding of a major neurotransmitter receptor in several important ways. First, it underlines the central importance of the apo state in priming the receptor prior to activation and dictating its responsiveness to channel activators, allosteric modulators, and auxiliary proteins. Second, it uncovers an unappreciated and new role of alternative splicing of the flip/flop cassette, which shapes AMPA receptor signaling by regulating the nature of the apo state. Third, it reveals the additional role of TARP stoichiometry in also dictating the functional behavior of AMPA receptor heteromers and its potential value in explaining the responsiveness of native AMPA receptors. Finally, it establishes that the LBD of AMPA receptors exerts a long-range allosteric control on motions in the NTD. As discussed below, differences in the nanoscale mobility of the NTD may affect the trafficking and/or synapse strengthening of different subtypes of native AMPA receptors at glutamatergic synapses.

The Dynamic Nature of the Apo or Resting State

For decades, it has been assumed that the work performed by signaling proteins, such as ion channels, is initiated by the binding energy derived from a plethora of soluble activators, such as neurotransmitters. As a result, the role of the apo or resting state has been largely overlooked. However, some observations, particularly on nicotinic acetylcholine receptors (nAChRs), have challenged this orthodoxy. For example, nAChRs expressed by skeletal muscle can access the open or activated state of the channel in the absence of receptor agonists (Jackson, 1984, 1986), suggesting an underlying dynamic nature to the apo state. The probability that wild-type, unbound nAChRs enter into the open state is small; however, many mutations throughout the protein can increase this probability almost as much as agonist binding (Jadey et al., 2011; Purohit and Auerbach, 2009). In keeping with this, some nAChR mutations associated with congenital myasthenic syndromes can be linked to selective changes in the apo state rather than the activated state (Engel et al., 2010; Jadey et al., 2011), highlighting the importance of the resting state in the context of human disease.

The *lurcher* mutation (A654T) of the delta2 (δ2) iGluR subunit gives rise to cerebellar ataxia (Zuo et al., 1997) and was also concluded to reflect changes in the apo state, since wild-type δ2 iGluRs are unresponsive to neurotransmitter (Hansen et al., 2009; Kohda et al., 2000; Taverna et al., 2000). The homologous mutation is also found in *de novo* missense mutations of GluA1 and GluA3 AMPA receptor subunits, where it is associated with severe neurodevelopmental delay and autism (Geisheker et al., 2017). It was initially proposed that the *lurcher* mutation in GluA1 channels also gives rise to constitutively active channels (Kohda et al., 2000; Schwarz et al., 2001; Taverna et al., 2000); however, a more recent assessment concluded that the mutation has little or no effect on the apo state but rather increases sensitivity to the neurotransmitter L-Glu (Klein and Howe, 2004). The

(E) Left: typical current responses of $GluA1_i/\gamma2$+$GluA2_i/\gamma2$ (patch 190215p2) and $GluA1_o/\gamma2$+$GluA2_o/\gamma2$ (patch 190301p1) in external NaCl (black), NaBr (dark gray), or NaF (light gray). Right: summary of τ_{des} of $GluA1_i/\gamma2$+$GluA2_i/\gamma2$ (orange circles), $GluA1_o/\gamma2$+$GluA2_i/\gamma2$ (white circles), $GluA1_i/\gamma2$+$GluA2_o/\gamma2$ (white squares), and $GluA1_o/\gamma2$+$GluA2_o/\gamma2$ (blue squares) in external NaCl, NaBr, and NaF.

(F and G) Mean equilibrium current percentage plotted against mean time constants of desensitization. (F) GluA1+GluA2 combinations in tandem with 4 TARPs (black circles) are included with pulled patches from cerebellar Purkinje cells (red circles). (G) GluA1+GluA2 combinations in tandem with 2 TARPs (black circles) are included with pulled patches from cerebellar stellate cells (cyan circles). Data were fit by linear regression: (F) black, $y = 1.76 - 0.30$, $r = 0.991$; red, $y = 1.70 - 2.23$, $r = 0.948$; $p = 0.10$, one-way ANOVA; (G) black, $y = 0.36 - 0.18$, $r = 0.738$; cyan, $y = 0.36 + 1.15$, $r = 0.614$; $p = 0.20$, one-way ANOVA.

See also Table S5.

present study uncovers the existence of functionally distinct apo states of the AMPA receptor that are regulated through alternative splicing of the LBD. Rather than facilitating entry into the main open state, the flip/flop cassette establishes the mobility of the apo state and, in doing so, fine-tunes the responsiveness of AMPA receptors to neurotransmitter, allosteric anions, and auxiliary proteins. As explained below, the complex expression pattern of flip and flop isoforms in the vertebrate brain suggests that the apo or resting state plays a critical role in neuronal signaling of developing and adult neuronal circuits.

A Unifying Role for the AMPA Receptor Flip/Flop Cassette

We identify an entirely new and unifying role for the AMPA receptor flip/flop cassette through its regulation of the apo or resting state of AMPA receptors. Previous studies have linked the flip/flop cassette to several important and apparently disparate properties of AMPA receptors that include determining the rates into AMPA receptor desensitization (Koike et al., 2000; Mosbacher et al., 1994; Quirk et al., 2004), regulation by positive allosteric modulators, such as CTZ, aniracetam, CX614, and PEPA (4-[2-(phenylsulfonylamino)ethylthio]-2,6-difluoro-phenoxyacetamide) (Jin et al., 2005; Partin et al., 1994, 1995; Sekiguchi et al., 1997; Sun et al., 2002), and controlling AMPA receptor secretion from the endoplasmic reticulum (ER) (Coleman et al., 2006; Penn et al., 2008) (Figure 6E).

Markov models describing the effect of alternative splicing on AMPA receptor channel gating and its regulation by allosteric modulators have assumed that the flip/flop cassette impacts AMPA receptors only *after* agonist binding (Koike et al., 2000; Partin et al., 1996). Our data provide an alternative explanation whereby the key events that shape channel gating and allosteric modulation occur *before* agonist binding predetermined by the intrinsic mobility of the apo state. In keeping with this, kinetic differences between flip/flop isoforms are controlled by three closely positioned residues in the flip/flop cassette (Figures 3B and 6E), including Ser775Asn (Quirk et al., 2004). As this same residue regulates the apo state, it establishes a causal link between the mobility of the apo state with channel gating and allosteric modulation.

The effect of alternative splicing on AMPA receptor secretion from the ER has also been associated with motions triggered by agonist-bound AMPA receptors, primarily through the Val/Leu779 residue in coordination with Ser/Asn775 (Coleman et al., 2006; Penn et al., 2012) (Figure 6E). Interestingly, mutating the Thr765 and Pro766 residues of the flip cassette to Asn and Ala in the flop isoform (Figures 3A and 3B) has no effect on AMPA receptor secretion from the ER (Penn et al., 2008) but yet with Ser775Asn, they fully account for the kinetic differences between flip and flop isoforms (Quirk et al., 2004). This distinction reveals that some of the amino acid residues of the flip/flop cassette that govern differences in channel gating and ER exit of AMPA receptors are separable. Importantly, the Ser/Asn775 residue is implicated in all of these known regulatory effects of alternative splicing, which is in keeping with its central structural position at the kink between helices J and K of the flip/flop cassette (Figure 6E) separating the 765/766 residues, which control channel gating, from the 779 residue, which controls ER exit. This structural arrangement has important ramifications for the developing and adult CNS, since the expression of the flip/flop cassette in neurons is developmentally regulated (Monyer et al., 1991), activity dependent (Penn et al., 2012), and cell-type specific (Sommer et al., 1990). Consequently, our work establishes for the first time that fine-tuning nanoscale movements of apo or resting AMPA receptors may be a critical factor governing glutamatergic signaling in the mammalian brain. Finally, whether the nearby arginine of the R/G site, which fits directly into the LBD dimer interface (Greger et al., 2006), could influence LBD stability as well as anion and TARP sensitivity awaits to be studied.

TARP Stoichiometry Dictates the Functional Behavior of Alternatively Spliced AMPA Receptors

Our study establishes that TARP stoichiometry modifies the actions of the flip/flop cassette on recombinant AMPA receptor heteromers, generating two functionally distinct classes that correspond to partially and fully TARPed AMPA receptors (Figures 8F and 8G). Biochemical analysis of AMPA receptors native to the cerebellum has suggested that TARP stoichiometry is fixed (Kim et al., 2010), although it was not possible to determine whether the number of TARPs per AMPA receptor tetramer corresponded to partial (i.e., 1, 2, or 3 TARPs) or full occupancy (i.e., 4 TARPs). Cryoelectron microscopy (cryo-EM) structures and single-molecule imaging studies of AMPA receptors have shown that the makeup of AMPA receptor-TARP complexes can be quite variable, with assemblies containing 1 or 2 (Hastie et al., 2013; Twomey et al., 2016) or 4 (Hastie et al., 2013; Twomey et al., 2017a; Zhao et al., 2016) TARP auxiliary subunits per AMPA receptor tetramer complex (Chen and Gouaux, 2019). Our data from AMPA receptors expressed by cerebellar Purkinje and stellate cells suggest that TARP stoichiometry is variable and, most likely, fixed in each neuronal class, in agreement with a previous study comparing TARP stoichiometry between hippocampal granule and CA1 pyramidal cells (Shi et al., 2009). These conclusions are reliant on the similarity between the data from cerebellar neurons and recombinant GluA1/A2 heteromers. Whether a similar relationship can be extended to GluA2/A3 heteromers, another abundant AMPA receptor composition in the CNS (Bowie, 2012; Henley and Wilkinson, 2016; Jacobi and von Engelhardt, 2017), remains to be determined. Since data from Purkinje and stellate cells are consistent with AMPA receptors being fully and partially occupied by TARPs, respectively, it is possible that CNS neurons may regulate AMPA receptor responsiveness by varying the number of auxiliary subunits per tetramer. Since differences in the duration and amplitude of AMPA receptor-mediated excitatory postsynaptic potentials determines whether postsynaptic neurons operate as integrators of synaptic activity or coincidence detectors (König et al., 1996; Shadlen and Newsome, 1994), it will be interesting in future studies to examine the role of TARP stoichiometry in shaping the complex behavior of neuronal circuits.

Long-Range Allosteric Control of the NTD by the Flip/Flop Cassette

Several studies have reported dynamic motions in the NTD of both AMPA- and kainate-type iGluRs (Dürr et al., 2014; Dutta et al., 2015; Matsuda et al., 2016; Meyerson et al., 2014;

Nakagawa et al., 2005), which have been assumed to be a consequence of agonist binding and receptor desensitization (Dürr et al., 2014; Meyerson et al., 2014; Nakagawa et al., 2005). Our data reveal unexpectedly that motions in the NTD occur in the apo state through long-range control exerted by the flip/flop cassette, which primes the receptor prior to agonist binding (Figure 4) and establishes its intrinsic mobility (Figure 5). This mechanism is distinct from the allosteric coupling described for NMDA-type iGluRs, where it is the NTD that dictates the behavior of the LBD of different GluN2-containing isoforms to determine agonist potency and channel kinetics (Gielen et al., 2009; Yuan et al., 2009). Flip variants promote moderate NTD movement and give rise to slower channel desensitization and robust regulation by anions and auxiliary subunits. The greater mobility imparted by the flop cassette overrides this allosteric regulation and acts as a master switch, presumably by rendering the LBD dimer interface less stable (Dawe et al., 2015). Removal of the NTD has only a modest slowing effect on AMPA receptor gating and allosteric regulation by anions (Table S1); consequently, it still unclear what role, if any, movements in the NTD may fulfill. An attractive possibility is that nanoscale mobility of the NTD controls transsynaptic contact formation at glutamatergic synapses (Elegheert et al., 2016; García-Nafría et al., 2016), permitting AMPA receptor trafficking during synapse strengthening (Díaz-Alonso et al., 2017; Watson et al., 2017), as recently proposed for GluA1 and GluA2 subunits. Given that most native AMPA receptors are either GluA1/A2 or GluA2/A3 heteromers (Bowie, 2012; Henley and Wilkinson, 2016; Jacobi and von Engelhardt, 2017), it will be interesting in future studies to determine how the flip/flop cassette contributes to receptor trafficking and synapse strengthening.

On a broader perspective, the unappreciated role of the apo or resting state may have far-reaching implications for our understanding of the inner workings of many types of signaling proteins, such as other ion channel families, G-protein-coupled receptors (GPCRs), transporters, and kinases. For example, alternative splicing also dramatically impacts the signaling properties of other iGluRs (Regan et al., 2018), as well as many other ligand- and voltage-gated ion channels (Catterall et al., 2005; Kadowaki, 2015; Latorre et al., 2017; Lipscombe and Andrade, 2015; Soreq, 2015). Whether it can also explain the multiplicity of drug action on signaling proteins, such as GPCR-biased agonism and modulation (Lane et al., 2017), also awaits future investigation.

STAR★METHODS

Detailed methods are provided in the online version of this paper and include the following:

SUPPLEMENTAL INFORMATION

Supplemental Information can be found online at https://doi.org/10.1016/j.neuron.2019.03.046.

ACKNOWLEDGMENTS

We would like to thank technician Heidi Peterson for contributing to expression and purification of protein for crystallization studies and MAX-lab (Lund, Sweden) for providing beamtime and help during data collections. We would also like to thank members of the Bowie lab for the critical reading and comments on the manuscript. This work was supported by operating grants from CIHR (D.B.), the Lundbeck Foundation, Danscatt, and Biostruct-X (J.K.), the Biotechnology and Biological Sciences Research Council (J.M.E.), and Newton-Picarte grant DPI-20140080 (N.B. and J.M.E.). A.P. and Y.Y. were supported by NSERC and FRQS masters fellowships, respectively, and G.D. and R.A. were supported by NSERC doctoral fellowships. M.F.K. was supported by a scholarship from the Islamic Development Bank. E.A.S. was supported by a CONICYT-Chile Cambridge Scholarship, and R.V. was supported by the Lundbeck Foundation.

AUTHOR CONTRIBUTIONS

In the Bowie lab, G.B.D., A.M.P., Y.Y., R.P.D.A., and M.A. carried out the electrophysiology experiments, made figures, and analyzed the data. G.B.D., A.M.P., Y.Y., and R.P.D.A. also contributed to the writing of the manuscript. M.R.P.A. generated the constructs for electrophysiology and AFM, made figures, and contributed to the discussions of the manuscript. D.B. conceived of the study, coordinated the experiments between the different labs, and wrote the manuscript. In the Edwardson and Barrera labs, M.F.K., C.N., C.F., and E.A.S. carried out the AFM experiments and analyzed data. N.P.B. designed the AFM experiments and analyzed data. J.M.E. designed the AFM experiments, analyzed data, and contributed to writing the manuscript. In the Kastrup lab, R.V. carried out crystallization of $GluA2_I$ and $GluA2_o$, collected diffraction data, refined structures, analyzed the structures, made figures, and contributed to writing of the manuscript. K.F. was involved in initial crystallization experiments, data collection, and refinements of $GluA2_o$. J.S.K. hypothesized the existence of an anion-binding site in AMPA receptors, participated in data collections, performed the final refinements of the structures, analyzed the structures, made figures, participated in writing of the manuscript, and generally supervised the work.

DECLARATION OF INTERESTS

The authors declare no competing interests.

Received: December 13, 2018
Revised: March 8, 2019
Accepted: March 28, 2019
Published: April 30, 2019

REFERENCES

Adams, P.D., Afonine, P.V., Bunkóczi, G., Chen, V.B., Davis, I.W., Echols, N., Headd, J.J., Hung, L.W., Kapral, G.J., Grosse-Kunstleve, R.W., et al. (2010). PHENIX: a comprehensive Python-based system for macromolecular structure solution. Acta Crystallogr. D Biol. Crystallogr. *66*, 213–221.

Balasuriya, D., Takahashi, H., Srivats, S., and Edwardson, J.M. (2014). Activation-induced structural change in the GluN1/GluN3A excitatory glycine receptor. Biochem. Biophys. Res. Commun. *450*, 1452–1457.

Barbour, B., Keller, B.U., Llano, I., and Marty, A. (1994). Prolonged presence of glutamate during excitatory synaptic transmission to cerebellar Purkinje cells. Neuron *12*, 1331–1343.

Bats, C., Soto, D., Studniarczyk, D., Farrant, M., and Cull-Candy, S.G. (2012). Channel properties reveal differential expression of TARPed and TARPless AMPARs in stargazer neurons. Nat. Neurosci. *15*, 853–861.

Bowie, D. (2002). External anions and cations distinguish between AMPA and kainate receptor gating mechanisms. J. Physiol. *539*, 725–733.

Bowie, D. (2008). Ionotropic glutamate receptors & CNS disorders. CNS Neurol. Disord. Drug Targets *7*, 129–143.

Bowie, D. (2010). Ion-dependent gating of kainate receptors. J. Physiol. *588*, 67–81.

Bowie, D. (2012). Redefining the classification of AMPA-selective ionotropic glutamate receptors. J. Physiol. *590*, 49–61.

Cais, O., Herguedas, B., Krol, K., Cull-Candy, S.G., Farrant, M., and Greger, I.H. (2014). Mapping the interaction sites between AMPA receptors and TARPs reveals a role for the receptor N-terminal domain in channel gating. Cell Rep. *9*, 728–740.

Catterall, W.A., Goldin, A.L., and Waxman, S.G. (2005). International Union of Pharmacology. XLVII. Nomenclature and structure-function relationships of voltage-gated sodium channels. Pharmacol. Rev. *57*, 397–409.

Chen, S., and Gouaux, E. (2019). Structure and mechanism of AMPA receptor - auxiliary protein complexes. Curr. Opin. Struct. Biol. *54*, 104–111.

Chen, V.B., Arendall, W.B., 3rd, Headd, J.J., Keedy, D.A., Immormino, R.M., Kapral, G.J., Murray, L.W., Richardson, J.S., and Richardson, D.C. (2010). MolProbity: all-atom structure validation for macromolecular crystallography. Acta Crystallogr. D Biol. Crystallogr. *66*, 12–21.

Coleman, S.K., Möykkynen, T., Cai, C., von Ossowski, L., Kuismanen, E., Korpi, E.R., and Keinänen, K. (2006). Isoform-specific early trafficking of AMPA receptor flip and flop variants. J. Neurosci. *26*, 11220–11229.

Dawe, G.B., Musgaard, M., Andrews, E.D., Daniels, B.A., Aurousseau, M.R., Biggin, P.C., and Bowie, D. (2013). Defining the structural relationship between kainate-receptor deactivation and desensitization. Nat. Struct. Mol. Biol. *20*, 1054–1061.

Dawe, G.B., Aurousseau, M.R., Daniels, B.A., and Bowie, D. (2015). Retour aux sources: defining the structural basis of glutamate receptor activation. J. Physiol. *593*, 97–110.

Dawe, G.B., Musgaard, M., Aurousseau, M.R.P., Nayeem, N., Green, T., Biggin, P.C., and Bowie, D. (2016). Distinct structural pathways coordinate the activation of AMPA receptor-auxiliary subunit complexes. Neuron *89*, 1264–1276.

Díaz-Alonso, J., Sun, Y.J., Granger, A.J., Levy, J.M., Blankenship, S.M., and Nicoll, R.A. (2017). Subunit-specific role for the amino-terminal domain of AMPA receptors in synaptic targeting. Proc. Natl. Acad. Sci. USA *114*, 7136–7141.

Dingledine, R., Borges, K., Bowie, D., and Traynelis, S.F. (1999). The glutamate receptor ion channels. Pharmacol. Rev. *51*, 7–61.

Dürr, K.L., Chen, L., Stein, R.A., De Zorzi, R., Folea, I.M., Walz, T., Mchaourab, H.S., and Gouaux, E. (2014). Structure and dynamics of AMPA receptor GluA2 in resting, pre-open, and desensitized states. Cell *158*, 778–792.

Dutta, A., Krieger, J., Lee, J.Y., Garcia-Nafria, J., Greger, I.H., and Bahar, I. (2015). Cooperative dynamics of intact AMPA and NMDA glutamate receptors: similarities and subfamily-specific differences. Structure *23*, 1692–1704.

Elegheert, J., Kakegawa, W., Clay, J.E., Shanks, N.F., Behiels, E., Matsuda, K., Kohda, K., Miura, E., Rossmann, M., Mitakidis, N., et al. (2016). Structural basis for integration of GluD receptors within synaptic organizer complexes. Science *353*, 295–299.

Emsley, P., Lohkamp, B., Scott, W.G., and Cowtan, K. (2010). Features and development of Coot. Acta Crystallogr. D Biol. Crystallogr. *66*, 486–501.

Engel, A.G., Shen, X.M., Selcen, D., and Sine, S.M. (2010). What have we learned from the congenital myasthenic syndromes. J. Mol. Neurosci. *40*, 143–153.

Evans, P. (2006). Scaling and assessment of data quality. Acta Crystallogr. D Biol. Crystallogr. *62*, 72–82.

García-Nafría, J., Herguedas, B., Watson, J.F., and Greger, I.H. (2016). The dynamic AMPA receptor extracellular region: a platform for synaptic protein interactions. J. Physiol. *594*, 5449–5458.

Geisheker, M.R., Heymann, G., Wang, T., Coe, B.P., Turner, T.N., Stessman, H.A.F., Hoekzema, K., Kvarnung, M., Shaw, M., Friend, K., et al. (2017). Hotspots of missense mutation identify neurodevelopmental disorder genes and functional domains. Nat. Neurosci. *20*, 1043–1051.

Gielen, M., Siegler Retchless, B., Mony, L., Johnson, J.W., and Paoletti, P. (2009). Mechanism of differential control of NMDA receptor activity by NR2 subunits. Nature *459*, 703–707.

Greger, I.H., Akamine, P., Khatri, L., and Ziff, E.B. (2006). Developmentally regulated, combinatorial RNA processing modulates AMPA receptor biogenesis. Neuron *51*, 85–97.

Greger, I.H., Watson, J.F., and Cull-Candy, S.G. (2017). Structural and functional architecture of AMPA-type glutamate receptors and their auxiliary proteins. Neuron *94*, 713–730.

Hansen, K.B., Naur, P., Kurtkaya, N.L., Kristensen, A.S., Gajhede, M., Kastrup, J.S., and Traynelis, S.F. (2009). Modulation of the dimer interface at ionotropic glutamate-like receptor delta2 by D-serine and extracellular calcium. J. Neurosci. *29*, 907–917.

Hastie, P., Ulbrich, M.H., Wang, H.L., Arant, R.J., Lau, A.G., Zhang, Z., Isacoff, E.Y., and Chen, L. (2013). AMPA receptor/TARP stoichiometry visualized by single-molecule subunit counting. Proc. Natl. Acad. Sci. USA *110*, 5163–5168.

Henley, J.M., and Wilkinson, K.A. (2016). Synaptic AMPA receptor composition in development, plasticity and disease. Nat. Rev. Neurosci. *17*, 337–350.

Herguedas, B., García-Nafría, J., Cais, O., Fernández-Leiro, R., Krieger, J., Ho, H., and Greger, I.H. (2016). Structure and organization of heteromeric AMPA-type glutamate receptors. Science *352*, aad3873.

Herguedas, B., Watson, J.F., Ho, H., Cais, O., Garcia-Nafria, J., and Greger, I.H. (2019). Architecture of the heteromeric GluA1/2 AMPA receptor in complex with the auxiliary subunit TARP γ8. Science. Published online March 14, 2019. https://doi.org/10.1126/science.aav9011.

Herring, B.E., and Nicoll, R.A. (2016). Long-term potentiation: from CaMKII to AMPA receptor trafficking. Annu. Rev. Physiol. *78*, 351–365.

Horning, M.S., and Mayer, M.L. (2004). Regulation of AMPA receptor gating by ligand binding core dimers. Neuron *41*, 379–388.

Jackson, M.B. (1984). Spontaneous openings of the acetylcholine receptor channel. Proc. Natl. Acad. Sci. USA *81*, 3901–3904.

Jackson, M.B. (1986). Kinetics of unliganded acetylcholine receptor channel gating. Biophys. J. *49*, 663–672.

Jackson, A.C., and Nicoll, R.A. (2011). The expanding social network of ionotropic glutamate receptors: TARPs and other transmembrane auxiliary subunits. Neuron *70*, 178–199.

Jacobi, E., and von Engelhardt, J. (2017). Diversity in AMPA receptor complexes in the brain. Curr. Opin. Neurobiol. *45*, 32–38.

Jadey, S.V., Purohit, P., Bruhova, I., Gregg, T.M., and Auerbach, A. (2011). Design and control of acetylcholine receptor conformational change. Proc. Natl. Acad. Sci. USA *108*, 4328–4333.

Jin, R., Clark, S., Weeks, A.M., Dudman, J.T., Gouaux, E., and Partin, K.M. (2005). Mechanism of positive allosteric modulators acting on AMPA receptors. J. Neurosci. *25*, 9027–9036.

Kabsch, W. (2010). Xds. Acta Crystallogr. D Biol. Crystallogr. *66*, 125–132.

Kadowaki, T. (2015). Evolutionary dynamics of metazoan TRP channels. Pflugers Arch. *467*, 2043–2053.

Kim, K.S., Yan, D., and Tomita, S. (2010). Assembly and stoichiometry of the AMPA receptor and transmembrane AMPA receptor regulatory protein complex. J. Neurosci. *30*, 1064–1072.

Klein, R.M., and Howe, J.R. (2004). Effects of the lurcher mutation on GluR1 desensitization and activation kinetics. J. Neurosci. *24*, 4941–4951.

Kohda, K., Wang, Y., and Yuzaki, M. (2000). Mutation of a glutamate receptor motif reveals its role in gating and delta2 receptor channel properties. Nat. Neurosci. *3*, 315–322.

Koike, M., Tsukada, S., Tsuzuki, K., Kijima, H., and Ozawa, S. (2000). Regulation of kinetic properties of GluR2 AMPA receptor channels by alternative splicing. J. Neurosci. *20*, 2166–2174.

König, P., Engel, A.K., and Singer, W. (1996). Integrator or coincidence detector? The role of the cortical neuron revisited. Trends Neurosci. *19*, 130–137.

Krintel, C., Frydenvang, K., Olsen, L., Kristensen, M.T., de Barrios, O., Naur, P., Francotte, P., Pirotte, B., Gajhede, M., and Kastrup, J.S. (2012). Thermodynamics and structural analysis of positive allosteric modulation of the ionotropic glutamate receptor GluA2. Biochem. J. *441*, 173–178.

Krintel, C., Frydenvang, K., Ceravalls de Rabassa, A., Kaern, A.M., Gajhede, M., Pickering, D.S., and Kastrup, J.S. (2014). L-Asp is a useful tool in the purification of the ionotropic glutamate receptor A2 ligand-binding domain. FEBS J. *281*, 2422–2430.

Lane, J.R., May, L.T., Parton, R.G., Sexton, P.M., and Christopoulos, A. (2017). A kinetic view of GPCR allostery and biased agonism. Nat. Chem. Biol. *13*, 929–937.

Latorre, R., Castillo, K., Carrasquel-Ursulaez, W., Sepulveda, R.V., Gonzalez-Nilo, F., Gonzalez, C., and Alvarez, O. (2017). Molecular determinants of BK channel functional diversity and functioning. Physiol. Rev. *97*, 39–87.

Lipscombe, D., and Andrade, A. (2015). Calcium channel CaVα_1 splice isoforms—tissue specificity and drug action. Curr. Mol. Pharmacol. *8*, 22–31.

Matsuda, K., Budisantoso, T., Mitakidis, N., Sugaya, Y., Miura, E., Kakegawa, W., Yamasaki, M., Konno, K., Uchigashima, M., Abe, M., et al. (2016). Transsynaptic modulation of kainate receptor functions by C1q-like proteins. Neuron *90*, 752–767.

Mayer, M.L., and Armstrong, N. (2004). Structure and function of glutamate receptor ion channels. Annu. Rev. Physiol. *66*, 161–181.

McCoy, A.J., Grosse-Kunstleve, R.W., Adams, P.D., Winn, M.D., Storoni, L.C., and Read, R.J. (2007). Phaser crystallographic software. J. Appl. Cryst. *40*, 658–674.

Meyerson, J.R., Kumar, J., Chittori, S., Rao, P., Pierson, J., Bartesaghi, A., Mayer, M.L., and Subramaniam, S. (2014). Structural mechanism of glutamate receptor activation and desensitization. Nature *514*, 328–334.

Monyer, H., Seeburg, P.H., and Wisden, W. (1991). Glutamate-operated channels: developmentally early and mature forms arise by alternative splicing. Neuron *6*, 799–810.

Mosbacher, J., Schoepfer, R., Monyer, H., Burnashev, N., Seeburg, P.H., and Ruppersberg, J.P. (1994). A molecular determinant for submillisecond desensitization in glutamate receptors. Science *266*, 1059–1062.

Möykkynen, T., Coleman, S.K., Semenov, A., and Keinänen, K. (2014). The N-terminal domain modulates α-amino-3-hydroxy-5-methyl-4-isoxazolepropionic acid (AMPA) receptor desensitization. J. Biol. Chem. *289*, 13197–13205.

Nakagawa, T., Cheng, Y., Ramm, E., Sheng, M., and Walz, T. (2005). Structure and different conformational states of native AMPA receptor complexes. Nature *433*, 545–549.

Partin, K.M., Patneau, D.K., and Mayer, M.L. (1994). Cyclothiazide differentially modulates desensitization of alpha-amino-3-hydroxy-5-methyl-4-isoxazolepropionic acid receptor splice variants. Mol. Pharmacol. *46*, 129–138.

Partin, K.M., Bowie, D., and Mayer, M.L. (1995). Structural determinants of allosteric regulation in alternatively spliced AMPA receptors. Neuron *14*, 833–843.

Partin, K.M., Fleck, M.W., and Mayer, M.L. (1996). AMPA receptor flip/flop mutants affecting deactivation, desensitization, and modulation by cyclothiazide, aniracetam, and thiocyanate. J. Neurosci. *16*, 6634–6647.

Penn, A.C., Williams, S.R., and Greger, I.H. (2008). Gating motions underlie AMPA receptor secretion from the endoplasmic reticulum. EMBO J. *27*, 3056–3068.

Penn, A.C., Balik, A., Wozny, C., Cais, O., and Greger, I.H. (2012). Activity-mediated AMPA receptor remodeling, driven by alternative splicing in the ligand-binding domain. Neuron *76*, 503–510.

Plested, A.J., and Mayer, M.L. (2007). Structure and mechanism of kainate receptor modulation by anions. Neuron *53*, 829–841.

Purohit, P., and Auerbach, A. (2009). Unliganded gating of acetylcholine receptor channels. Proc. Natl. Acad. Sci. USA *106*, 115–120.

Quirk, J.C., Siuda, E.R., and Nisenbaum, E.S. (2004). Molecular determinants responsible for differences in desensitization kinetics of AMPA receptor splice variants. J. Neurosci. *24*, 11416–11420.

Regan, M.C., Grant, T., McDaniel, M.J., Karakas, E., Zhang, J., Traynelis, S.F., Grigorieff, N., and Furukawa, H. (2018). Structural mechanism of functional modulation by gene splicing in NMDA receptors. Neuron *98*, 521–529.e3.

Robert, A., Armstrong, N., Gouaux, J.E., and Howe, J.R. (2005). AMPA receptor binding cleft mutations that alter affinity, efficacy, and recovery from desensitization. J. Neurosci. *25*, 3752–3762.

Schneider, C.A., Rasband, W.S., and Eliceiri, K.W. (2012). NIH Image to ImageJ: 25 years of image analysis. Nat. Methods *9*, 671–675.

Schwarz, M.K., Pawlak, V., Osten, P., Mack, V., Seeburg, P.H., and Köhr, G. (2001). Dominance of the lurcher mutation in heteromeric kainate and AMPA receptor channels. Eur. J. Neurosci. *14*, 861–868.

Sekiguchi, M., Fleck, M.W., Mayer, M.L., Takeo, J., Chiba, Y., Yamashita, S., and Wada, K. (1997). A novel allosteric potentiator of AMPA receptors: 4–2-(phenylsulfonylamino)ethylthio–2,6-difluoro-phenoxyaceta mide. J. Neurosci. *17*, 5760–5771.

Shadlen, M.N., and Newsome, W.T. (1994). Noise, neural codes and cortical organization. Curr. Opin. Neurobiol. *4*, 569–579.

Shaikh, S.A., Dolino, D.M., Lee, G., Chatterjee, S., MacLean, D.M., Flatebo, C., Landes, C.F., and Jayaraman, V. (2016). Stargazin modulation of AMPA receptors. Cell Rep. *17*, 328–335.

Shepherd, J.D., and Huganir, R.L. (2007). The cell biology of synaptic plasticity: AMPA receptor trafficking. Annu. Rev. Cell Dev. Biol. *23*, 613–643.

Shi, Y., Lu, W., Milstein, A.D., and Nicoll, R.A. (2009). The stoichiometry of AMPA receptors and TARPs varies by neuronal cell type. Neuron *62*, 633–640.

Sobolevsky, A.I., Rosconi, M.P., and Gouaux, E. (2009). X-ray structure, symmetry and mechanism of an AMPA-subtype glutamate receptor. Nature *462*, 745–756.

Sommer, B., Keinänen, K., Verdoorn, T.A., Wisden, W., Burnashev, N., Herb, A., Köhler, M., Takagi, T., Sakmann, B., and Seeburg, P.H. (1990). Flip and flop: a cell-specific functional switch in glutamate-operated channels of the CNS. Science *249*, 1580–1585.

Soreq, H. (2015). Checks and balances on cholinergic signaling in brain and body function. Trends Neurosci. *38*, 448–458.

Sun, Y., Olson, R., Horning, M., Armstrong, N., Mayer, M., and Gouaux, E. (2002). Mechanism of glutamate receptor desensitization. Nature *417*, 245–253.

Suzuki, Y., Goetze, T.A., Stroebel, D., Balasuriya, D., Yoshimura, S.H., Henderson, R.M., Paoletti, P., Takeyasu, K., and Edwardson, J.M. (2013). Visualization of structural changes accompanying activation of N-methyl-D-aspartate (NMDA) receptors using fast-scan atomic force microscopy imaging. J. Biol. Chem. *288*, 778–784.

Taverna, F., Xiong, Z.G., Brandes, L., Roder, J.C., Salter, M.W., and MacDonald, J.F. (2000). The Lurcher mutation of an alpha-amino-3-hydroxy-5-methyl- 4-isoxazolepropionic acid receptor subunit enhances potency of glutamate and converts an antagonist to an agonist. J. Biol. Chem. *275*, 8475–8479.

Terwilliger, T.C., Grosse-Kunstleve, R.W., Afonine, P.V., Moriarty, N.W., Zwart, P.H., Hung, L.W., Read, R.J., and Adams, P.D. (2008). Iterative model building, structure refinement and density modification with the PHENIX AutoBuild wizard. Acta Crystallogr. D Biol. Crystallogr. *64*, 61–69.

Traynelis, S.F., Wollmuth, L.P., McBain, C.J., Menniti, F.S., Vance, K.M., Ogden, K.K., Hansen, K.B., Yuan, H., Myers, S.J., and Dingledine, R. (2010). Glutamate receptor ion channels: structure, regulation, and function. Pharmacol. Rev. *62*, 405–496.

Turrigiano, G.G. (2017). The dialectic of Hebb and homeostasis. Philos. Trans. R. Soc. Lond. B Biol. Sci. *372*, 20160258.

Twomey, E.C., Yelshanskaya, M.V., Grassucci, R.A., Frank, J., and Sobolevsky, A.I. (2016). Elucidation of AMPA receptor-stargazin complexes by cryo-electron microscopy. Science *353*, 83–86.

Twomey, E.C., Yelshanskaya, M.V., Grassucci, R.A., Frank, J., and Sobolevsky, A.I. (2017a). Channel opening and gating mechanism in AMPA-subtype glutamate receptors. Nature *549*, 60–65.

Twomey, E.C., Yelshanskaya, M.V., Grassucci, R.A., Frank, J., and Sobolevsky, A.I. (2017b). Structural bases of desensitization in AMPA receptor-auxiliary subunit complexes. Neuron *94*, 569–580.e565.

Ursby, T., Unge, J., Appio, R., Logan, D.T., Fredslund, F., Svensson, C., Larsson, K., Labrador, A., and Thunnissen, M.M. (2013). The macromolecular crystallography beamline I911-3 at the MAX IV laboratory. J. Synchrotron Radiat. *20*, 648–653.

Watson, J.F., Ho, H., and Greger, I.H. (2017). Synaptic transmission and plasticity require AMPA receptor anchoring via its N-terminal domain. eLife *6*, e23024.

Winn, M.D., Ballard, C.C., Cowtan, K.D., Dodson, E.J., Emsley, P., Evans, P.R., Keegan, R.M., Krissinel, E.B., Leslie, A.G., McCoy, A., et al. (2011). Overview of the CCP4 suite and current developments. Acta Crystallogr. D Biol. Crystallogr. *67*, 235–242.

Wong, A.Y., Fay, A.M., and Bowie, D. (2006). External ions are coactivators of kainate receptors. J. Neurosci. *26*, 5750–5755.

Yamazaki, M., Le Pichon, C.E., Jackson, A.C., Cerpas, M., Sakimura, K., Scearce-Levie, K., and Nicoll, R.A. (2015). Relative contribution of TARPs γ-2 and γ-7 to cerebellar excitatory synaptic transmission and motor behavior. Proc. Natl. Acad. Sci. USA *112*, E371–E379.

Yuan, H., Hansen, K.B., Vance, K.M., Ogden, K.K., and Traynelis, S.F. (2009). Control of NMDA receptor function by the NR2 subunit amino-terminal domain. J. Neurosci. *29*, 12045–12058.

Zhao, Y., Chen, S., Yoshioka, C., Baconguis, I., and Gouaux, E. (2016). Architecture of fully occupied GluA2 AMPA receptor-TARP complex elucidated by cryo-EM. Nature *536*, 108–111.

Zuo, J., De Jager, P.L., Takahashi, K.A., Jiang, W., Linden, D.J., and Heintz, N. (1997). Neurodegeneration in Lurcher mice caused by mutation in delta2 glutamate receptor gene. Nature *388*, 769–773.

STAR★METHODS

KEY RESOURCES TABLE

REAGENT or RESOURCE	SOURCE	IDENTIFIER
Antibodies		
Mouse monoclonal anti-hemagglutinin antibody	Covance, HA.11 clone 16B12	MMS-101P; RRID: AB_291259
Bacterial and Virus Strains		
E. coli Origami B (DE3)	Novagen	N/A
Chemicals, Peptides, and Recombinant Proteins		
Spermine tetrahydrochloride	Sigma-Aldrich	Cat#S2876 CAS#306-67-2
Cyclothiazide	Tocris Bioscience	Cat#0713 CAS#2259-96-3
BAPTA, tetrasodium salt	Thermo Fisher	Cat#B1214 CAS#126824-24-6
EGTA tetrasodium salt	Sigma-Aldrich	Cat#E9145 CAS#13368-13-3
D-APV	Abcam	Cat#ab120003 CAS# 79055-68-8
L-glutamic acid monosodium salt hydrate	Sigma-Aldrich	Cat#G1626 CAS#142-47-2
ATP disodium salt hydrate	Sigma-Aldrich	Cat#A2383 CAS#34369-07-8
Phenol red solution	Sigma-Aldrich	Cat#P0290 CAS#143-74-8
Penicillin-Streptomycin	Sigma-Aldrich	Cat#P4333
Polyethyleneimine	Sigma-Aldrich	Cat#764604 CAS#9002-98-6
Anti-hemagglutinin agarose	Sigma-Aldrich	Cat#A2095
Complete protease inhibitor cocktail	Sigma-Aldrich	Cat#11697498001
Biotechnology performance certified water	Sigma-Aldrich	Cat#W3513
CHAPS	Sigma-Aldrich	Cat#C9426 CAS#331717-45-4
Hemagglutinin peptide	Sigma-Aldrich	Cat#I2149 CAS#92000-76-5
L-α-phosphatidylcholine	Avanti Polar Lipids	Cat#840053C
1,2-dioleoyl-*sn*-glycero-3-phospho-L-serine	Avanti Polar Lipids	Cat#840035C
Fast Scan silicon AFM probes	Bruker	FASTSCAN-D
CNQX	Tocris Bioscience	Cat#0190 CAS#115066-14-3
Triton X-100	Sigma-Aldrich	Cat#93443 CAS#9002-93-1
Poly(ethylene glycol) 4,000	Sigma-Aldrich	Cat#81240 CAS#25322-68-3
Deposited Data		
Structure of GluA2o-N775S LBD (S1S2J) in complex with glutamate and RbBr, at 1.75 A	This paper	PBD: 6GIV
Structure of GluA2o LBD (S1S2J) in complex with glutamate and NaBr, at 1.95 A	This paper	PBD: 6GL4
Experimental Models: Cell Lines		
Human: HEK293T/17 cells (for electrophysiology)	ATCC	CRL-11268
Human: tsA201 cells (for AFM)	Suzuki et al., 2013	ECACC 96121229
Experimental Models: Organisms/Strains		
Mouse: C57/BL6J	The Jackson Laboratory	RRID: IMSR_JAX:000664
Recombinant DNA		
pRK5-ΔΔGluA1-flip	Dr. M. Mayer, NIH, Maryland, USA	Partin et al., 1995
pRK5-ΔΔGluA1-flop	This Paper	N/A
pRK5-GluA2(Q/R)-flip	Dr. P. Seeburg, Max Planck Institute for Medical Research, Heidelberg, Germany	N/A
pRK5-GluA2(Q/R)-flop	Dr. P. Seeburg, Max Planck Institute for Medical Research, Heidelberg, Germany	N/A

(*Continued on next page*)

Continued

REAGENT or RESOURCE	SOURCE	IDENTIFIER
pRK5-ΔΔGluA1-flip/γ2 tandem	This paper	N/A
pRK5-ΔΔGluA1-flop/γ2 tandem	This paper	N/A
pRK5-GluA2(Q/R)-flip/γ2 tandem	Dawe et al., 2016	N/A
pRK5-GluA2(Q/R)-flop/γ2 tandem	This paper	N/A
pRK5-GluA2(Q)-flip ΔNTD	This paper	N/A
pRK5-GluA2(Q)-flip ΔNTD-eGFP	This paper	N/A
pRK5-GluA2(Q)-flop ΔNTD-eGFP	This paper	N/A
pRK5-GluA2(Q)-L504A-flip	This paper	N/A
pRK5-GluA2(Q)-L504C-flip	This paper	N/A
pRK5-GluA2(Q)-T765N/P766A-flip	This paper	N/A
pRK5-GluA2(Q)-T765N/P766A/S775N-flip	This paper	N/A
pRK5-GluA2(Q)-S775N-flip	This paper	N/A
His_8-GluA2o-LBD, plasmid PET-22B(+)	Dr. M. Mayer, NIH, Maryland, USA	N/A
His_8-GluA2o- N775S-LBD, plasmid PET-22B(+)	Krintel et al., 2012	N/A
Software and Algorithms		
pCLAMP Software	Molecular Devices	https://www.moleculardevices.com
Origin 7.0 and OriginPro 8.5	OriginLab Corporation	https://www.originlab.com
NanoScope Analysis v1.5	Bruker	https://www.bruker.com
SigmaPlot	Systat Software Inc., San Jose, CA	https://systatsoftware.com/products/sigmaplot/
ImageJ	ImageJ, Schneider et al., 2012	https://imagej.nih.gov/ij/index.html
Adrian's FWHM Software (ImageJ Plugin)	ImageJ	https://imagej.nih.gov/ij/plugins/fwhm/
XDS	Kabsch, 2010	http://xds.mpimf-heidelberg.mpg.de/
CCP4i	Winn et al., 2011	https://www.ccp4.ac.uk/ccp4i_main.php
Coot	Emsley et al., 2010	https://www2.mrc-lmb.cam.ac.uk/personal/pemsley/coot/
Phenix	Adams et al., 2010	https://www.phenix-online.org/
PyMOL Molecular Graphics System	Version 1.7.4, Schrödinger, LLC	https://pymol.org/2/

CONTACT FOR REAGENT AND RESOURCE SHARING

Further information and requests for resources and reagents should be directed to and will be fulfilled by the Lead Contact, Derek Bowie (derek.bowie@mcgill.ca).

EXPERIMENTAL MODEL AND SUBJECT DETAILS

Cell Culture

Electrophysiology experiments: human embryonic kidney cells (HEK293T/17) were purchased from ATCC (CRL-11268). These cells constitutively express the simian virus 40 (SV40) large T-antigen and 17 refers to the clone number selected for its high transfectability. Cells were grown at 37°C under 5% CO_2 in Minimum Essential Medium with GlutaMAX (i.e., MEM GlutaMAX) supplemented with 10% fetal bovine serum. The sex of the cell line is not determined.

AFM experiments: tsA201 cells (a subclone of HEK293 cells stably expressing the SV40 large T-antigen, see Suzuki et al., 2013) were grown at 37°C under 5% CO_2 in Dulbecco's Modified Eagle's Medium (DMEM) supplemented with 10% fetal bovine serum, 100 μg/mL streptomycin and 100 units/mL penicillin. The sex of the cell line is not determined.

Mice

All experiments have been approved by the local authorities, were performed in accordance with the guidelines of the Canadian Council on Animal Care and were approved by the Animal Care Committee of McGill University. Wild-type mice with a C57BL/6J background were obtained from Jackson Laboratories (Bar Harbor, USA) and maintained as a breeding colony at McGill University. Both male and female wild-type mice were used for experiments and ranged from postnatal days 18 to 25.

METHOD DETAILS

Recombinant Electrophysiology

HEK293 cells were used to express recombinant GluA1 and/or GluA2 AMPAR subunits for outside-out patch recordings. For GluA2 homomers, the Q/R unedited flip and flop isoforms ($GluA2Q_i$ and $GluA2Q_o$) were used. For GluA1/A2 heteromers, the Q/R edited flip and flop isoforms of GluA2 ($GluA2R_i$ and $GluA2R_o$) were used. Residue numbering includes the signal peptide. Mutant receptors were generated using site-directed mutagenesis. External and internal recording solutions typically contained (in mM): 150 NaX (X = halide ion), 5 HEPES, 0.1 $CaCl_2$, 0.1 $MgCl_2$, and 2% phenol red at pH 7.4, and 115 NaCl, 10 NaF, 5 HEPES, 5 Na_4BAPTA, 0.5 $CaCl_2$, 1 $MgCl_2$, and 10 Na_2ATP at pH 7.4, respectively. For GluA1/A2 heteromer recordings, 30 μM spermine was included in the internal solution; data points were only included when the I/V plot was linear, typical of GluA2(R)-containing AMPARs (Partin et al., 1995) (see Figure S7). Sucrose was supplemented to maintain the osmotic pressure at 300 mOsm. L-Glu was typically applied at 10 mM and CTZ at 100 μM, unless otherwise indicated.

Recording pipettes were composed of borosilicate glass (3-5 MΩ, King Precision Glass, Inc.) coated with dental wax. The reference electrode was connected to the bath via an agar bridge of 3 M KCl. Agonist solutions were applied using a piezo-stack driven perfusion system, and measured solution exchange time was under 400 μs. Series resistances (3-15 MΩ) were routinely compensated by 95%. All recordings were performed using an Axopatch 200B amplifier (Molecular Devices, LLC). Current records were low-pass filtered by an 8-pole Bessel filter at 10 kHz and sampled at 25-50 kHz. Data were acquired using pClamp9 software (Molecular Devices, LLC) and illustrated using Origin 7 (OriginLab Corp.).

Slice Electrophysiology

Slice preparation

Mice were anesthetized with isoflurane and immediately decapitated. A block of cerebellar vermis was rapidly dissected from the mouse head and submerged in ice-cold cutting solution perfused with carbogen gas (95% O_2, 5% CO_2). Cutting solution contains (in mM): 235 sucrose, 2.5 KCl, 1.25 NaH_2PO_4, 28 $NaHCO_3$, 0.5 $CaCl_2$, 7 $MgCl_2$, 28 D-glucose, 1 ascorbic acid, 3 sodium pyruvate (pH 7.4; 305–315 mOsmol/L). The block of vermis was then fastened to a platform, transferred to the slicing chamber and again submerged in ice-cold cutting solution, bubbled with carbogen throughout the remainder of the procedure. Thin slices of cerebellar vermis (300 μm) were obtained with a vibrating tissue sectioner (Leica VT1200; Leica Instruments, Nussloch, Germany). The slices were transferred to oxygenated artificial cerebrospinal fluid (aCSF) and held at room temperature (21°C-23°C) for at least 1 h before recordings were performed. aCSF contained the following (in mM): 125 NaCl, 2.5 KCl, 1.25 NaH_2PO_4, 26 $NaHCO_3$, 2 $CaCl_2$, 1 $MgCl_2$, 25 D-glucose (pH of 7.4; 305–315 mOsmol/L).

Acute slice electrophysiology

Slice experiments were performed on an Olympus BX51 upright microscope (Olympus, Southall, UK) equipped with differential interference contrast/infrared optics. Recordings were made from either visually identified stellate or Purkinje cells in acute sagittal slices of cerebellar vermis. Patch pipettes were prepared from thick-walled borosilicate glass (GC150F-10, OD 1.5 mm, ID 0.86 mm; Harvard Apparatus Ltd, Kent, UK) and had open tip resistances of 3–6 MΩ when filled with an intracellular recording solution. Internal solution contained (in mM): 140 CsCl, 10 HEPES, 10 EGTA, 2 $MgCl_2$ and 60 μM spermine-HCl to examine rectification due to polyamine channel block (pH of 7.4; 295-305 mOsmol/L). Local agonist/antagonist applications were performed using a homemade flowpipe from theta tubing with a tip diameter of 300–400 μm. External solution was the same as described above with the addition of 10 μM D-APV to block NMDA receptors. Nucleated (stellate) or excised membrane (Purkinje) patches were placed near the mouth of a double-barreled flowpipe, which was rapidly jumped between control and solution containing 10 mM L-Glu (1 - 250 ms duration). Recordings were performed using a Multiclamp 700A amplifier (Molecular Devices, Sunnyvale, CA, USA). The bath was continuously perfused at room temperature (21–23°C) with aCSF at a rate of 1–2 mL/min. Currents were filtered at 5 kHz with an eight-pole low-pass Bessel filter (Frequency Devices, Haverhill, MA, USA) and digitized at 25 kHz with a Digidata 1322A data acquisition board and Clampex 10.1 (pClamp) software.

Crystallization

Wild-type $GluA2_o$ and N775S (flip-like) mutant ligand binding domains (LBDs) were expressed and purified as described previously (Krintel et al., 2012). Crystallization was performed using the vapor diffusion hanging drop method at 6°C. The crystallization drop consisted of 1 μL $GluA2_o$-LBD solution (8 mg/ml) or $GluA2_o$-LBD N775S mutant (4 mg/ml) in a buffer containing 10 mM HEPES, 20 mM NaCl, 1 mM EDTA (pH 7.0), and 1 μL of reservoir solution. Before setting up the crystallization drops, the protein solution was mixed with L-Glu to a final concentration of 2 mM L-Glu and 300 mM NaBr ($GluA2_o$-LBD) or 4 mM L-Glu and 250 mM RbBr ($GluA2_o$-LBD N775S). Crystals used for diffraction data collections were obtained at conditions consisting of reservoir solution: 25% PEG4000, 0.2 M Na_2SO_4, and 0.1 M CH_3COONa, pH 5.5 ($GluA2_o$) or 22%–24% PEG4000, 0.2-0.3 M Li_2SO_4 and 0.1 M cacodylate, pH 6.5 ($GluA2_o$-LBD N775S). Before data collection, the crystals were cryo-protected in reservoir solution containing 20% glycerol.

Data collection and structure determination

X-ray diffraction data on GluA2-LBD crystals were collected at the Max-Lab beamline I911-3 (Lund, Sweden) (Ursby et al., 2013) at 100 K. Diffraction images were processed in XDS (Kabsch, 2010). Data were scaled and merged using SCALA (Evans, 2006) within CCP4 (Winn et al., 2011) and the structures were solved by molecular replacement in Phaser (McCoy et al., 2007) using GluA2-LBD structures as search models (PDB: 3TDJ, molA for $GluA2_o$, (Krintel et al., 2012) and PDB: 4O3A, molA for $GluA2_o$-LBD N775S, (Krintel et al., 2014)). Initially, the structures were rebuilt in AutoBuild (Terwilliger et al., 2008) within Phenix (Adams et al., 2010). Structures were further improved using Coot (Emsley et al., 2010) and refinement in Phenix. Both structures displayed good quality indicators as calculated by MolProbity (Chen et al., 2010) within Phenix. Figures were prepared with the PyMOL Molecular Graphics System (Version 1.7.4, Schrödinger, LLC). For statistics on data collection and refinements, see Table S2.

AMPA receptor purification and AFM imaging

The following constructs were used, all with an HA tag at the N terminus and in the vector pRK5: rat $GluA2_i$ and $GluA2_o$ (Q/R site unedited), $GluA2_i$ with the point mutation S775N, ΔNTD-$GluA2_i$ (minus NTD), ΔNTD $GluA2_i$-GFP and ΔNTD $GluA2_o$-GFP. The HA tag contained the residues YPYDVPDYA, located after the first amino acid following the signal peptide (i.e., between residues 22 and 32).

Isolation of AMPARs

DNA (250 μg) was used to transfect 5 × 162 cm^2 flasks of tsA201 cells using polyethylenimine. After transfection, cells were incubated for 24-48 h at 37°C to allow expression of receptors. Proteins were isolated from transfected cells by immunoaffinity chromatography; all steps were carried out at 4°C. Cell pellets were resuspended in solubilization buffer [25 mM Tris-HCl, pH 7.5, 150 mM NaCl, 10 mM EDTA, 1% Triton X-100, 1 mM PMSF, and protease inhibitor cocktail (Roche), prepared in Biotechnology Performance Certified (BPC) water (Sigma)]. Precipitated DNA was removed by low-speed centrifugation, and the sample was then centrifuged in a 70 Ti rotor at 35,000 rpm for 1 h. Solubilized extracts were incubated with anti-HA-agarose beads (Sigma) for 3 h. The immunobeads bearing captured protein were then washed extensively with solubilization buffer containing 0.1% CHAPS (Sigma) instead of 1% (v/v) Triton X-100, and the bound protein was eluted with HA peptide (200 μg/mL). Protein purity was evaluated by silver staining and immunoblotting.

Integration of receptors into liposomes

Chloroform solutions of L-α-phosphatidylcholine (PC) and 1,2-dioleoyl-sn-glycero-3-phospho-L-serine (DOPS; Avanti Polar Lipids) were mixed at a molar ratio of 3:1. The chloroform was then evaporated under a stream of nitrogen gas, and the lipids were resuspended in HEPES-buffered saline (HBS; 150 mM NaCl, 20 mM HEPES, pH 7.6) containing CHAPS and mixed with purified receptor to give a final lipid concentration of 2 mg/mL and a final CHAPS concentration of 1% (w/v). The mixture was dialysed at 4°C against detergent-free buffer for 2 days, with several changes of buffer. To detect receptors, where appropriate, the dialysed sample was incubated for 12 h at 4°C with anti-HA antibody.

AFM imaging

A droplet (20 μL) of proteoliposome suspension was deposited onto the surface of a freshly cleaved mica disc (diameter, 1 cm), followed by incubation for 5 min at room temperature (20°C), during which time the proteoliposomes collapsed to form supported lipid bilayers containing integrated receptors. The mica surface was gently washed several times with HBS to remove unadsorbed proteoliposomes. AFM imaging under fluid was carried out at room temperature using a Bruker-AXS FastScan Dimension AFM instrument. The instrument was used in micro-volume fluid mode to facilitate the application of agonist, antagonist or ions directly while imaging. All images were collected in 'tapping' mode, using FastScan-D silicon probes (Bruker). The cantilevers (with a typical spring constant of 0.25 N/m) were tuned to a resonance frequency of between 90 and 140 kHz. The microscope was engaged with a 2 μm x 2 μm scan area and a 5 nm target amplitude to allow for tuning. The amplitude setpoint was adjusted to the highest setting that allowed imaging with little noise, to minimize the force applied to the sample. To measure receptor heights, images were captured at a scan rate of 20 Hz (25 s/frame) with 512 scan lines per area. Individual particles were identified, and particles with heights between 5 and 10 nm were taken to represent AMPARs.

To follow the dynamics of the NTDs, sequential high-magnification (120 nm x 120 nm) images of receptor-containing bilayers were captured at a frequency of 1 frame/second with a fixed integral gain of 2.5 and a target amplitude of 1 nm. The target amplitude was kept at 1 nm to exert minimum force on the receptor. Individual particles were identified, and particles with heights between 7 and 10 nm were taken to represent AMPARs. N.B. The particles were slightly taller when using target amplitude 1 nm instead of the conventional target amplitude of 5 nm. Movement of the two globular structures relative to each other was followed under various conditions. The centers of the structures were identified by using Gaussian fitting (ImageJ plug-in, Adrian's FWHM), and NTD mobility was expressed as the cumulative squared displacement (CSD):

$$CSD(t) = \sum_{i=1}^{t} (x_{i+1} - x_i)^2$$

where x is the distance between the centers of the globular structures.

Data analysis

Image analysis was performed using the Nanoscope analysis 1.5 software and ImageJ (Schneider et al., 2012). Data analysis was carried out using Microsoft Excel, OriginPro 8.5 or SigmaPlot 12.5. Histograms were drawn with bin widths chosen according to Scott's equation:

$$h = 3.5\sigma / n^{1/3}$$

where h is the bin width, σ is an estimate of the standard deviation and n is the sample size.

QUANTIFICATION AND STATISTICAL ANALYSIS

Additional details of data analysis and statistical analysis can be found in the Method Details, main and supplemental figures, supplemental tables, and corresponding legends.

Electrophysiological data

Electrophysiological data were analyzed using Clampfit 10.5 (Molecular Devices, LLC). To measure deactivation and entry into desensitization, current decay rates were fitted using 1st or 2nd order exponential functions of the form $y = A_i*\exp(-x/\tau_i)$. Where two exponential components were used, time constants are expressed as a weighted mean. To measure recovery from desensitization, a two-pulse protocol was delivered using variable interpulse intervals, and the peak amplitude of the second pulse was expressed as a fraction of the first peak. Recovery data were fitted with the Hodgkin-Huxley equation $y = N_0+(1-N_0)*(1-\exp(-k_{rec}*x))^n$, where N_0 is the equilibrium response at the end of the first pulse, k_{rec} is the recovery rate, and n is an exponent that reflects the number of kinetic transitions contributing to the recovery time course. The value of n was set to 2 (see Robert et al., 2005). Distributions were first evaluated using Kolmogorov-Smirnova test. Non-normally distributed data were analyzed using non-parametric tests such as the Mann-Whitney U test where indicated. Normally distributed data were compared using one-way ANOVA and unpaired two-tailed Student's t test. Significance is defined as $p < 0.05$. Data are presented as mean ± SEM, with n referring to individual patches.

Atomic force microscopy data

Data are presented as mean ± SEM, with n referring to individual receptors. Heights of individual AMPARs before and after either the addition of L-Glu or an anion switch were compared using a Student's paired, two-tailed t test. ATD mobility data for flip and flop AMPARs in the resting state, in the presence of L-Glu, and in the presence of L-Glu plus CNQX were compared using a one-way ANOVA, with a Fisher test. Combined ATD mobility data for flip and flop AMPARs in the resting state and in the presence of different concentrations of L-Glu were compared using a Mann-Whitney U test.

DATA AND SOFTWARE AVAILABILITY

The X-ray crystal structures of $GluA2_o$-LBD (PDB: 6GL4) and the flip-like mutant $GluA2_o$-LBD N775S (PDB: 6GIV) have been uploaded to the Protein Data Bank.

APPENDIX II:

Reprints of published chapters

Neuronal Excitability

Cerebellar Stellate Cell Excitability Is Coordinated by Shifts in the Gating Behavior of Voltage-Gated Na^+ and A-Type K^+ Channels

Ryan P.D. Alexander,[1,2] John Mitry,[3] Vasu Sareen,[3] Anmar Khadra,[3] and Derek Bowie[2]

https://doi.org/10.1523/ENEURO.0126-19.2019

[1]Integrated Program in Neuroscience, McGill University, Montréal, Quebec H3A 2B4, Canada, [2]Department of Pharmacology and Therapeutics, McGill University, Montréal, Quebec H3G 1Y6, Canada, and [3]Department of Physiology, McGill University, Montréal, Quebec H3G 1Y6, Canada

Abstract

Neuronal excitability in the vertebrate brain is governed by the coordinated activity of both ligand- and voltage-gated ion channels. In the cerebellum, spontaneous action potential (AP) firing of inhibitory stellate cells (SCs) is variable, typically operating within the 5- to 30-Hz frequency range. AP frequency is shaped by the activity of somatodendritic A-type K^+ channels and the inhibitory effect of GABAergic transmission. An added complication, however, is that whole-cell recording from SCs induces a time-dependent and sustained increase in membrane excitability making it difficult to define the full range of firing rates. Here, we show that whole-cell recording in cerebellar SCs of both male and female mice augments firing rates by reducing the membrane potential at which APs are initiated. AP threshold is lowered due to a hyperpolarizing shift in the gating behavior of voltage-gated Na^+ channels. Whole-cell recording also elicits a hyperpolarizing shift in the gating behavior of A-type K^+ channels which contributes to increased firing rates. Hodgkin–Huxley modeling and pharmacological experiments reveal that gating shifts in A-type K^+ channel activity do not impact AP threshold, but rather promote channel inactivation which removes restraint on the upper limit of firing rates. Taken together, our work reveals an unappreciated impact of voltage-gated Na^+ channels that work in coordination with A-type K^+ channels to regulate the firing frequency of cerebellar SCs.

Key words: A-type potassium channel; action potential; cerebellum; computational modeling; sodium channel; stellate cell

Significance Statement

The cerebellum is a brain region that fulfills critical roles in motor function in adults as well as being linked to neurodevelopmental disorders in the developing brain. Significant attention has been directed toward understanding connectivity within the cerebellum and how its neuronal circuits are regulated. Stellate cells (SCs) are inhibitory GABAergic interneurons that make-up neuronal circuits that control the output from the cerebellar cortex by regulating the firing properties of Purkinje cells. The strength of GABAergic inhibition of Purkinje cells is governed by the excitability of SCs which fire action potentials (APs) at a wide range of frequencies. Our study reveals an unappreciated role of voltage-gated sodium channels that work in coordination with A-type K^+-channels to establish SC firing rates.

Received April 1, 2019; accepted May 13, 2019; First published May 20, 2019.
The authors declare no competing financial interests.

Author contributions: R.P.D.A., J.M., A.K., and D.B. designed research; R.P.D.A., J.M., and V.S. performed research; R.P.D.A., J.M., and V.S. analyzed data; R.P.D.A., A.K., and D.B. wrote the paper.

Introduction

Cerebellar stellate cells (SCs) are GABAergic interneurons that exert inhibitory tone onto both Purkinje cells (PCs) and SCs to shape motor function in awake, behaving animals (Astorga et al., 2017; Gaffield and Christie, 2017). Investigations into the physiologic activity of SCs both *in vitro* and *in vivo* have estimated their action potential (AP) firing rates to be in the range of 5–30 Hz (Armstrong and Rawson, 1979; Midtgaard, 1992; Häusser and Clark, 1997; Carter and Regehr, 2002), with some studies reporting even lower spontaneous rates (Jörntell and Ekerot, 2003; Liu et al., 2014). SCs are also highly sensitive to minimal amounts of synaptic input (Carter and Regehr, 2002; Jörntell and Ekerot, 2003), suggesting that the excitability of SCs is finely tuned to ensure that their target cells receive robust and reliable feedforward inhibition.

Several molecular mechanisms have been shown to modulate the excitability of SCs. For example, elevations in cytosolic Ca^{2+} mediated by T-type voltage gated Ca^{2+} channels (VGCCs) have been shown to dynamically regulate the firing rates of SCs by modulation of somatodendritic A-type K^+ channels (Molineux et al., 2005; Anderson et al., 2013). Firing rates are further controlled by neurochemical transmission. The inhibitory tone of $GABA_A$ receptors constrains AP firing (Häusser and Clark, 1997) whereas the prolonged depolarization by NMDA-type ionotropic glutamate receptors (Liu et al., 2014) activates axonal VGCCs (Christie and Jahr, 2008) and promotes GABA release (Glitsch and Marty, 1999; Duguid and Smart, 2004; Liu and Lachamp, 2006). To complicate matters, the firing rates of SCs are also affected by patch-clamp recording conditions. The intrinsic excitability of SCs increases in a time-dependent manner in cell-attached recordings (Alcami et al., 2012). The molecular events that give rise to this increase in excitability are still not fully understood, although observations in other cell types have demonstrated that patch breakthrough during whole-cell recording can cause unintended changes to ion channel gating and activity, including an effect on voltage-gated Na^+ channels (Fenwick et al., 1982; Dani et al., 1983; Fernandez et al., 1984; Vandenberg and Horn, 1984; Townsend et al., 1997). Whether a similar mechanism accounts for increased firing in SCs in whole-cell recordings has yet to be investigated.

Here, we have elucidated the molecular events responsible for the increase in excitability of SCs in whole-cell recording conditions. Using a combination of brain slice patch-clamp electrophysiology and Hodgkin–Huxley modeling, we show that shifts in the gating properties of voltage-gated Na^+ channels cause an increase in SC excitability by promoting AP firing at more hyperpolarized potentials. These events occur concurrently with a hyperpolarizing shift in A-type K^+ channel gating which reduces the number of channels available for activation, and thus contributes to increased AP firing. Taken together, our data identify an unappreciated role of voltage-gated Na^+ channels that work in coordination with somatodendritic A-type K^+ channels to upregulate SC excitability on whole-cell recording.

This work was supported by the Canadian Institutes of Health Research Operating Grant MOP 142431 (to D.B.) and by a National Natural Sciences and Engineering Research Council of Canada (NSERC) Discovery Grant (A.K.). R.P.D.A. was supported by a NSERC CGS-D Doctoral Fellowship.

Acknowledgements: We thank members of the Bowie laboratory for comments on this manuscript and Z. Nusser for discussions on sodium channel expression patterns.

Correspondence should be addressed to Derek Bowie at derek.bowie@mcgill.ca.

https://doi.org/10.1523/ENEURO.0126-19.2019

Materials and Methods

Ethical approval

All experiments have been approved by the Animal Care Committee of McGill University and were performed in accordance with the guidelines of the Canadian Council on Animal Care.

Animals

Wild-type mice with a C57BL/6J background (RRID: IMSR_JAX:000664) were obtained from The Jackson Laboratory and maintained as a breeding colony at McGill University. Both male and female wild-type mice were used for experiments and ranged from postnatal day 18 to 30.

Slice preparation

Mice were anesthetized with isoflurane and immediately decapitated. A block of cerebellar vermis was rapidly dissected from the mouse head and submerged in ice-cold cutting solution perfused with carbogen gas (95% O_2, 5% CO_2). Cutting solution contains: 235 mM sucrose, 2.5 mM KCl, 1.25 mM NaH_2PO_4, 28 mM $NaHCO_3$, 0.5 mM $CaCl_2$, 7 mM $MgCl_2$, 28 mM D-glucose, 1 mM ascorbic acid, and 3 mM sodium pyruvate (pH 7.4; 305–315 mOsmol/l). The block of vermis is then fastened to a platform, transferred to the slicing chamber and again submerged in ice-cold cutting solution, bubbled with carbogen throughout the remainder of the procedure. Thin slices of cerebellar vermis (300 μm) were obtained with a vibrating tissue sectioner (Leica VT1200; Leica Instruments). The slices were transferred to oxygenated artificial CSF (aCSF) and held at room temperature (21°C–23°C) for at least 1 h before recordings were performed. aCSF contained the following: 125 mM NaCl, 2.5 mM KCl, 1.25 mM NaH_2PO_4, 26 mM $NaHCO_3$, 2 mM $CaCl_2$, 1 mM $MgCl_2$, and 25 mM D-glucose (pH 7.4; 305–315 mOsmol/l).

Electrophysiology

Slice experiments were performed on an Olympus BX51 upright microscope (Olympus) equipped with differential interference contrast/infrared optics. Whole-cell patch-clamp recordings were made from visually-identified stellate, granule or Purkinje cells in acute sagittal slices of cerebellar vermis. SCs were distinguished from misplaced or migrating granule, glial or basket cells by their small soma diameter (8–9 μm), location in the

outer two-thirds of the molecular layer and whole-cell capacitance measurement (4–12 pF). Granule cells (GCs) were identified based on location in the granule layer (immediately less superficial to the Purkinje layer), small soma size and whole-cell capacitance measurement (1–3 pF). Purkinje cells were identified based on large relative size, location in the Purkinje monolayer and whole-cell capacitance measurement (25–35 pF). Patch pipettes were prepared from thick-walled borosilicate glass (GC150F-10, OD 1.5 mm, ID 0.86 mm; Harvard Apparatus Ltd) and had open tip resistances of 4–7 MΩ when filled with an intracellular recording solution. Recordings were performed using a Multiclamp 700A amplifier (Molecular Devices) at a holding potential of –70 mV (stellate and Purkinje) or –80 mV (granule). Series resistance and whole-cell capacitance were estimated by cancelling the fast transients evoked at the onset and offset of brief (10 ms) 5-mV voltage-command steps. Access resistance during whole-cell recording (7–25 MΩ) was compensated between 60 and 80% and checked for stability throughout the experiments (~15% tolerance). Recordings where pipette offset changed by >3 mV were excluded. Liquid junction potential was not corrected for. The bath was continuously perfused at room temperature (21°C–23°C) with aCSF at a rate of 1–2 mL/min. Currents were filtered at 5 kHz with an eight-pole low-pass Bessel filter (Frequency Devices) and digitized at either 25 or 100 kHz with a Digidata 1322A data acquisition board and Clampex 10.1 (pClamp, RRID:SCR_011323) software. For voltage-clamp recordings, the online P/N leak-subtraction suite in Clampex 10.1 was used to assess voltage-gated responses.

For recording voltage dependence of activation of A-type K^+ current (I_A) a protocol was applied consisting of 500-ms steps evoked from a holding potential of –100 mV, ranging from –100 to +20 mV in 10-mV increments. An inactivation protocol was applied consisting of 500-ms prepulse steps ranging from –120 to –30 mV in 5-mV increments, followed by a probe step to –20 mV to assess channel availability. For recording voltage dependence of activation of delayed rectifier K^+ current (I_K), a protocol was applied consisting of 1-s steps evoked from a holding potential of –50 mV, ranging from –50 to +40 mV in 5-mV increments. The holding potential of –50 mV was chosen to selectively inactivate I_A, because of its relatively hyperpolarized $V_{1/2}$ inactivation, and study a more isolated I_K. For recording voltage dependence of activation of Na^+ current (I_{Na}), a protocol designed to circumvent space-clamp errors in neurons was used (Milescu et al., 2010) consisting of a 5-ms suprathreshold step from –80 to –35 mV to evoke an action current, followed by a ~1-ms step to –60 mV, followed by 100-ms steps ranging from –80 to +30 mV in 5-mV increments. To measure steady-state channel availability, an inactivation protocol consisting of 100-ms steps ranging from –110 to –20 mV in 5-mV increments, followed by a probe step to –20 mV.

Recording solutions

All chemicals were obtained from Sigma Aldrich unless otherwise indicated. Internal pipette solution for most current-clamp experiments as well as voltage-clamp experiments, both whole-cell and nucleated patch, examining I_K in SCs contained: 126 mM K-gluconate, 5 mM HEPES, 4 mM NaCl, 15 mM D-glucose, 0.05 mM $CaCl_2$, 1 mM $MgSO_4$, 0.15 mM K_4-BAPTA, 2 mM Mg-ATP, and 0.1 mM Na-GTP (adjusted to pH 7.4 with KOH, 300–310 mOsmol/l). I_K experiments had external aCSF supplemented with 100 nM tetrodotoxin (TTX) to block AP firing, as well as 5 mM 4-aminopyridine (4-AP) to limit the activity of I_A-mediating channels. In one set of experiments, all K-gluconate in this internal solution was substituted for K-methanesulfonate to examine the effect of different anions on intrinsic membrane properties. Pipette solution for voltage-clamp experiments, both whole-cell and nucleated patch, examining I_A contained: 140 mM KCl, 10 mM HEPES, 2.5 mM $MgCl_2$, and 0.15 mM K_4-BAPTA (adjusted to pH 7.4 with KOH, 300–310 mOsmol/l). For these experiments, the external aCSF was supplemented with 5 mM TEA-Cl and 2 mM CsCl to block non-I_A-mediating K^+ channels, and 100 nM TTX to block AP firing. Pipette solution for voltage-clamp experiments examining I_{Na} contained: 110 mM Cs-methanesulfonate, 5 mM HEPES, 4 mM NaCl, 15 mM D-glucose, 0.05 mM $CaCl_2$, 0.15 mM Cs_4-BAPTA, 4 mM Mg-ATP, 0.1 mM Na-GTP, 10 mM TEA-Cl, and 10 mM 4-AP (adjusted to pH 7.4 with CsOH, 300–310 mOsmol/l). Pipette solution for voltage-clamp experiments examining I_{Na} in excised membrane patches contained: 140 mM CsCl, 10 mM HEPES, 10 mM EGTA, 2 mM $MgCl_2$, and 2 mM Na_2-ATP (adjusted to pH 7.4 with CsOH, 300–310 mOsmol/l). Free Ca^{2+} concentration for all current-clamp internal solutions was calculated to be ~100 nM using MaxChelator freeware (Bers et al., 2010). For all experiments investigating I_{Na}, the external aCSF was supplemented with 100 μM $CdCl_2$ and 1 μM Mibefradil dihydrochloride (Tocris Bioscience) to block voltage-gated calcium channels. Additional current-clamp experiments were performed in the presence of hyperpolarization-activated cyclic nucleotide-gated channel (HCN) blocker ZD 7288 in the aCSF (20 μM; Tocris Bioscience). Except where indicated, all experiments were performed in the presence of fast excitatory and inhibitory synaptic blockers: NMDA receptor antagonist D-(-)-2-amino-5 phosphonopentanoic acid (D-APV; 10 μM), AMPA/kainate receptor antagonist 2,3-dioxo-6-nitro-1,2,3,4-tetrahydrobenzo[f]quinoxaline-7-sulfonamide (NBQX; 10 μM), and $GABA_A$ receptor antagonist bicuculline (BIC; 10 μM), all of which were purchased from Abcam.

Mathematical model

A modified Hodgkin–Huxley type model was adopted from Molineux et al. (2005) and Anderson et al. (2010). The model consists of five ionic currents, including I_{Na}, I_K, I_A, T-type Ca^{2+} current (I_T) and nonspecific leak current (I_L). The A-type K^+ and T-type Ca^{2+} current were added in Molineux et al. (2005) to capture biphasic first spike latency profile. The resulting voltage equation associated with this model is expressed as

$$C_m \frac{dV}{dt} = -[I_{Na} + I_K + I_A + I_T + I_L] + I_{app},$$

where C_m is the membrane capacitance per unit area and I_{app} is the applied current. The kinetics of the various ionic currents included in the model are as described below (Molineux et al., 2005; Anderson et al., 2010).

(1) Fast activating Na^+ current:

$$I_{Na} = \bar{g}_{Na} m_\infty^3 h(V - V_{Na}),$$

with maximum conductance $\bar{g}_{Na}$ and Nernst potential for Na^+ V_{Na}. Its gating is governed by both the steady state activation function

$$m_\infty = (1 + e^{-(V - v_m)/s_m})^{-1}$$

and the inactivation variable h satisfying the dynamic equation

$$\frac{dh}{dt} = \frac{h_\infty(V) - h}{\tau_h(V)},$$

where $h_\infty(V)$ is the steady state inactivation function given by

$$h_\infty = (1 + e^{(V - v_h)/s_h})^{-1}$$

and $\tau_h(V)$ is its time constant described by the Lorentzian function

$$\tau_h(V) = y_0 + \frac{2Aw}{4\pi(V - V_c)^2 + w^2}.$$

(2) Delayed rectifier K^+ current:

$$I_K = \bar{g}_K n^4 (V - V_K),$$

with maximum conductance $\bar{g}_K$ and Nernst potential for K^+ V_K. The gating of this current is governed by the activation variable n only, which satisfies the dynamic equation

$$\frac{dn}{dt} = \frac{n_\infty(V) - n}{\tau_n(V)},$$

where $n_\infty(V)$ is the steady state activation function given by

$$n_\infty = (1 + e^{-(V - v_n)/s_n})^{-1}$$

and $\tau_n(V)$ is its time constant defined by

$$\tau_n(V) = \frac{6}{1 + e^{(V+23)/15}}.$$

(3) A-type K^+ current:

$$I_A = \bar{g}_A n_A h_A (V - V_K)$$

with maximum conductance $\bar{g}_A$ and Nernst potential V_K. Its activation/inactivation kinetics are governed by the gating variables n_A and h_A, respectively, each satisfying the dynamic equations

$$\frac{dn_A}{dt} = \frac{n_{A,\infty}(V) - n_A}{\tau_{n_A}}$$

and

$$\frac{dh_A}{dt} = \frac{h_{A,\infty}(V) - h_A}{\tau_{h_A}}$$

where $n_{A,\infty}$ and $h_{A,\infty}$ are, respectively, the steady state activation and inactivation functions given by

$$n_{A,\infty} = (1 + e^{-(V - v_{n_A})/s_{n_A}})^{-1} \quad \text{and} \quad h_{A,\infty} = (1 + e^{(V - v_{h_A})/s_{h_A}})^{-1} \tag{1}$$

and τ_{n_A} and τ_{h_A} are their corresponding time constants that are independent of membrane voltage V.

(4) Fast activating T-type Ca^{2+} current:

$$I_T = \bar{g}_T m_{T,\infty} h_T (V - V_{Ca}),$$

with maximum conductance $\bar{g}_T$ and Nernst potential for Ca^{2+} V_{Ca}. Its gating is governed by the steady state activation function

$$m_{T,\infty} = (1 + e^{-(V - v_{m_T})/s_{m_T}})^{-1}$$

and the inactivation variable h_T satisfying the dynamic equation

$$\frac{dh_T}{dt} = \frac{h_{T,\infty}(V) - h_T}{\tau_{h_T}},$$

where $h_\infty(V)$ is the steady state inactivation function given by

$$h_{T,\infty} = (1 + e^{(V - v_{h_T})/s_{h_T}})^{-1}$$

and τ_{h_T} is its voltage-independent time constant.

(5) Non-specific leak current:

$$I_A = \bar{g}_L (V - V_L)$$

with constant maximum conductance $\bar{g}_L$ and Nernst potential V_L.

The model is thus described by a six-dimensional system representing the time-dependent membrane voltage V and the five time-dependent gating variables m, n, n_A, h_A, and h_T.

Model parameter values

Simulations of the model using parameter values listed in Molineux et al. (2005) and Anderson et al. (2010) produced cycles of APs in the (V, dV/dt) − plane that did not match the activities at either baseline (0 min) or the activities after the increase in excitability (data not shown). To capture the dynamics of the increase in excitability, we

Table 1. Parameter values of ionic currents included in the baseline and revised models whenever two values are provided for a given parameter, the first corresponds to the baseline model (before the increase in excitability at baseline) while the second shown between parentheses corresponds to the revised model (after the increase in excitability at 25 min)

Parameter	Value/units	Parameter	Value/units	Parameter	Value/units	Parameter	Value/units
C_M	1.50148 μF/cm^2	V_{Ca}	22 mV	w	46 mV	v_{m_T}	− 50 mV
$\bar{g}_{Na}$	3.4 μS/cm^2	V_L	− 38 mV	V_c	− 74 mV	s_{m_T}	3 mV
$\bar{g}_K$	9.0556 μS/cm^2	v_m	− 37 (− 44) mV	v_n	− 23 mV	v_{h_T}	− 68 mV
$\bar{g}_A$	15.0159 μS/cm^2	s_M	3 mV	s_n	5 mV	s_{h_T}	3.75 mV
$\bar{g}_T$	0.45045 μS/cm^2	v_h	− 40(− 48.5) mV	v_{n_A}	− 27(− 41) mV	τ_{n_A}	5 ms
$\bar{g}_L$	0.07407 μS/cm^2	s_h	4 mV	s_{n_A}	13.2 mV	τ_{h_A}	10 ms
V_{Na}	55 mV	y_0	0.1 ms	v_{h_A}	− 80(− 96) mV	τ_{h_T}	15 ms
V_K	− 80 mV	A	322 ms mV	s_{h_A}	6.5(9.2) mV		

first fitted the expressions of $n_{A,\infty}$ and $h_{A,\infty}$ to the steady state activation/inactivation kinetic data of I_A before and after the shift, then used the full model to manually fit its numerical simulations to baseline data before the increase in excitability. This was done in two sequential steps: (1) by first capturing all features of the AP cycles in the $(V, dV/dt)-$ plane at baseline, followed by (2) matching the firing frequency obtained from the temporal profiles of membrane voltage. We will refer to this model associated with baseline data as the "baseline" model. To capture all features of the AP cycle after the increase in excitability (i.e., after 25 min), we identified the list of all parameters that need to be adjusted to produce these features in the $(V, dV/dt)-$ plane and the higher firing frequency. Because our analysis revealed that the T-type Ca^{2+} current played a minor role in inducing the increase in excitability within the model, we left the kinetic parameters of activation/inactivation of I_T listed in Molineux et al. (2005) and Anderson et al. (2010) unchanged for both before and after the increase in excitability. The reversal potentials of Na^+, K^+ and Ca^{2+} were also left unchanged. As for the remaining parameters, they were estimated based on fitting and parsimony. The resulting model that produced the increase in excitability will be referred to hereafter as "revised" model. The list of all parameter values for the baseline and revised models are provided in Table 1. Simulations were run in Mathematica 11.2 (Wolfram Mathematica, RRID:SCR_014448).

Experimental design and statistical analysis

Paired *t* tests were used to compare electrophysiological data recorded at baseline and after 25 min (step-evoked AP frequency, AP threshold, AP cycle parameters, $V_{1/2}$ values for I_{Na}). In the cases of I_A and I_K gating properties, a two-way mixed design ANOVA was used with Tukey's *post hoc* test to compare patch configuration data (nucleated and whole-cell) between groups while comparing data over time (baseline and 25 min) within each group. For each experimental group, recordings from a minimum of five cells from a minimum of three animals were collected. Analysis was not blinded.

Voltage dependence of activation for all current types was analyzed by first calculating conductance (G) values from the peak currents elicited by each respective activation protocol using the formula:

$$G_x = \frac{I_x}{V_m - V_{rev_x}}$$

where I_x is the peak current of current type x (i.e., I_A, I_K, I_{Na}) evoked at membrane potential V_m, and V_{rev_x} is the reversal potential of current type x. Conductance-voltage relationships for each current type were then fit to a Boltzmann function using the formula:

$$G_x = \frac{G_{max}}{1 + \exp((V_{1/2} - V_m)/k)}$$

where G_x is the conductance at membrane potential V_m for current type x, G_{max} is the maximum conductance for current type x, $V_{1/2}$ is the membrane potential where G_x is 50% of G_{max}, and k is the slope factor. Boltzmann fits were performed for each time point in each cell to calculate normalized conductance values. Summary conductance-voltage relationships for each current type were calculated by averaging the normalized conductance values across all cells in the dataset. $V_{1/2}$ values reported in the Results section for each current type were calculated by fitting the normalized conductance averages.

Data are reported as mean ± SEM. Significance was denoted with $*p < 0.05$, $**p < 0.01$, and $***p < 0.001$. All fitting was performed with Origin 7.0 (Microcal Origin, RRID:SCR_002815). Statistical analyses were performed using SPSS 17.0 (SPSS, RRID:SCR_002865).

Results

AP firing in cerebellar stellate and GC (granule cell), but not Purkinje cells, increases during whole-cell recording

To examine time-dependent changes in membrane excitability, whole-cell patch-clamp recordings were obtained from three types of visually-identified cerebellar neurons, namely stellate, granule and Purkinje cells (Fig. 1*A–C*). After obtaining the whole-cell current-clamp configuration, negative current was injected into each neuron to maintain the membrane potential at –70 or –80 mV (see Materials and Methods). To assess membrane excitability following breakthrough, incremental depolarizing current steps were applied within the first minute (termed baseline), and then once every 5 min during a typical 25-min recording (Fig. 1*A–F*).

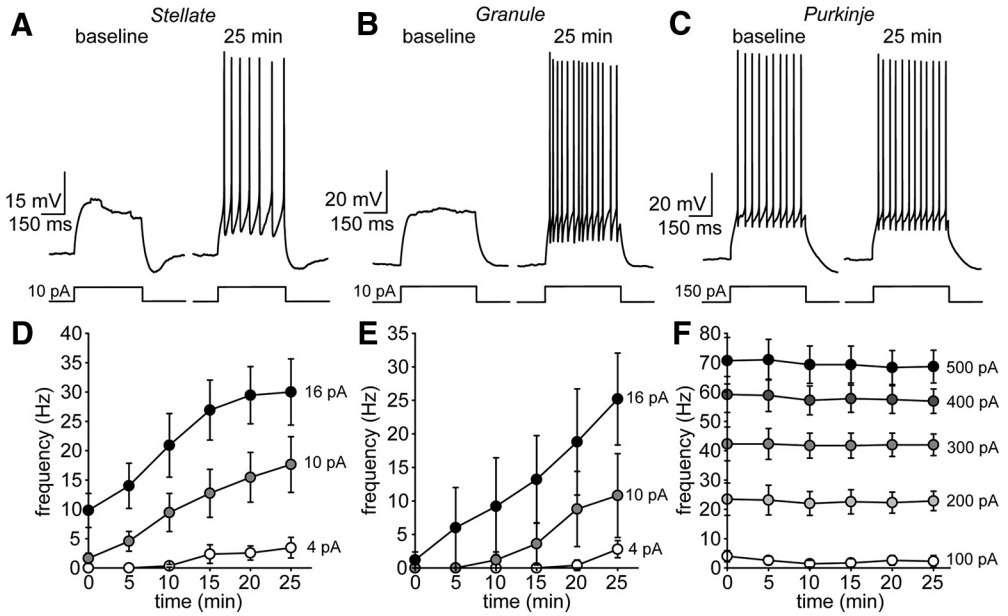

Figure 1. Stellate and GC (granule cell), but not Purkinje cells, exhibit excitability increases during whole-cell recording. ***A***, Example SC current-clamp recording (patch #150129p2) applying a 10-pA step protocol shortly following breakthrough and after 25 min. ***B***, ***C***, Same for GC (patch #150324p2) and Purkinje cell (patch #141010p5) examples using 10- and 150-pA current steps, respectively. ***D***, Summary SC AP frequency over 25-min recording for multiple step amplitudes (n = 11 cells). ***E***, ***F***, Same for granule (n = 6 cells) and Purkinje cells (n = 6 cells).

Under these conditions, both stellate and GCs fired many more APs at the 25-min time point (Fig. 1*D*,*E*). For example, in SCs, AP frequency evoked by a 16-pA current step at baseline was 9.8 ± 2.9 Hz versus 30.0 ± 5.6 Hz after 25 min (t = 4.73, p < 0.001; n = 11 cells; Fig. 1*A*,*D*). In contrast, firing rates in Purkinje cells remained stable throughout the recording (Fig. 1*C*,*F*) but required larger step depolarizations to elicit APs. For example, AP frequency evoked by a 400-pA step at baseline was 59.1 ± 6.1 Hz versus 56.9 ± 4.2 Hz after 25 min (t = −0.88, p = 0.41; n = 7 cells). The increase in AP frequency in SCs was not accompanied by a change in input resistance (1011 ± 148 MΩ at baseline vs 967 ± 137 MΩ at 25 min; t = −1.21, p = 0.26; n = 11 cells) or resting membrane potential (–50.6 ± 1.3 mV at baseline vs –52.2 ± 1.6 mV at 25 min; t = –1.33, p = 0.23; n = 7 cells) suggesting that the increase in membrane excitability was primarily due to changes in the activity of active membrane conductances (i.e., ion channels). In contrast, the increase in step-evoked AP frequency in GCs (16-pA step: 1.2 ± 1.2 Hz at baseline vs 25.2 ± 6.7 Hz at 25 min; t = 4.07, p = 0.015; n = 5 cells; Fig. 1*B*,*E*) was accompanied by a concurrent increase in membrane input resistance (44.5 ± 13.4% increase, n = 3 cells). Given this, we focused the rest of our study on SCs to pinpoint the molecular events that give rise to the increase in membrane excitability.

A closer examination of SC recordings revealed a decrease in spike latency in response to current injection (Fig. 2*A*) at all current step amplitudes tested (Fig. 2*B*). For example, the latency to first spike in response to a 16-pA current step at baseline was 89.9 ± 14.4 versus 37.1 ± 9.5 ms at 25 min (t = −6.68, p < 0.001; n = 11 cells). To measure the shift precisely, we used a 1-s current ramp protocol to monitor the membrane potential at the initiation of the AP upstroke. To ensure that the ramp protocol had no direct effect on spike threshold, the protocol began with a 5-pA ramp that increased five times in increments of 5 pA. The threshold for each cell was then calculated by averaging the value obtained at each ramp amplitude. For comparison, we also repeated these experiments on both granule (not shown) and Purkinje cells (Fig. 2*D*,*E*). As anticipated, SCs exhibited a shift in AP threshold starting at –39.7 ± 0.9 mV following breakthrough and hyperpolarizing to –48.2 ± 1.3 mV at 25 min (t = –15.74, p < 0.001; n = 12 cells; Fig. 2*C*,*E*). GCs exhibited an even more substantial hyperpolarizing shift in AP threshold (–35.9 ± 0.6 mV at baseline vs –52.5 ± 2.1 mV at 25 min; t = –7.31, p < 0.001; n = 6 cells) whereas the threshold in Purkinje cells remained constant (–48.5 ± 1.5 mV at baseline vs –49.5 ± 1.4 mV at 25 min; t = –0.073, p = 0.51; n = 5 cells; Fig. 2*E*).

To ensure that the excitability increase in SCs was present in physiologically relevant conditions, the temperature of the aCSF perfusion was raised to near-physiologic level (33°C–34°C) and current-clamp experiments were repeated. SCs at elevated ambient temperatures still exhibited hyperpolarizing AP thresholds that closely resembled those at room temperature (–37.4 ± 1.7 mV at baseline vs –47.4 ± 1.9 mV at 20 min; t = 10.04, p < 0.001; n = 5 cells). Lastly, since others have noted that internal anions can affect intrinsic membrane properties of neurons during whole-cell recording (Kaczorowski et al., 2007), we repeated current-clamp experiments in SCs using a K-methanesulfonate-based intracellular solution in place of the initial K-gluconate version. Although slightly hyperpolarized at baseline compared to gluconate, the pres-

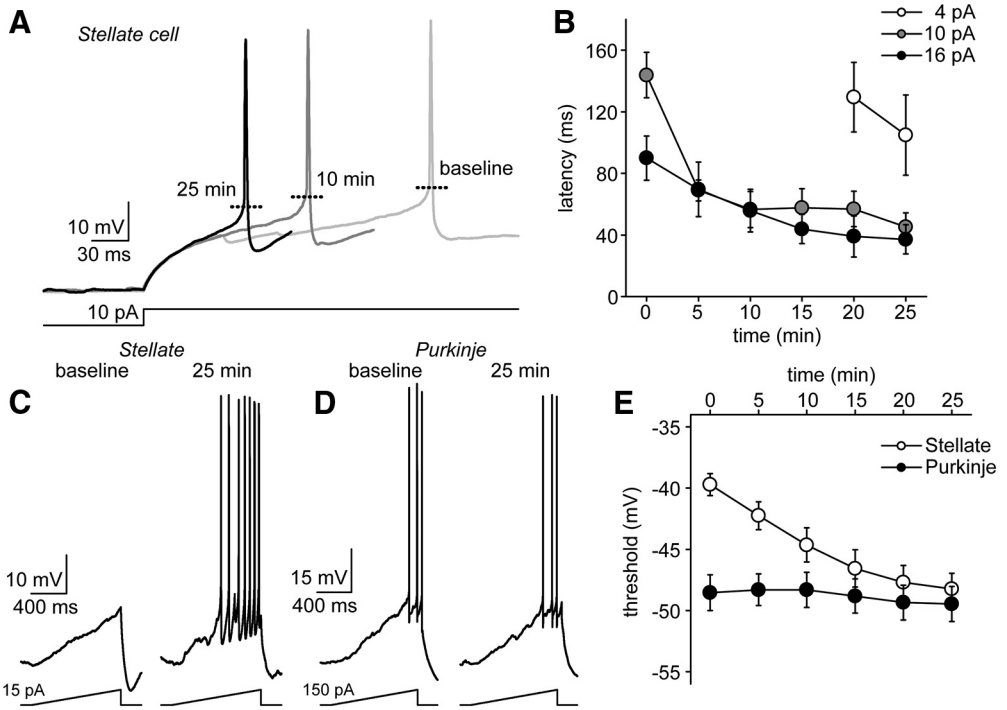

Figure 2. Excitability increase is underpinned by decrease in spike latency and hyperpolarization of AP threshold. ***A***, First APs fired by a SC in response to 10-pA current step at three different time points: 1, 10, and 25 min after breakthrough. The spike latency in response to the step decreases substantially over the course of the recording. ***B***, Summary plot of spike latencies for multiple step amplitudes over the course of a 25-min recording ($n = 11$ cells). ***C***, Example current-clamp responses evoked by ramp protocol at baseline (left) and after 25 min (right) in a SC (patch #150129p2). ***D***, Same for an example Purkinje cell (patch #141010p5). ***E***, Summary plot depicting change in AP threshold over time in stellate ($n = 11$ cells) and Purkinje cells ($n = 6$ cells).

ence of methanesulfonate did not prevent the decrease of AP threshold over the duration of patch-clamp recording (–42.8 ± 1.1 mV at baseline vs –51.0 ± 1.8 mV at recording endpoint; $t = 6.14$, $p < 0.001$; $n = 7$ cells).

Modified Hodgkin–Huxley model predicts a dominant role for voltage-gated Na^+ channels

To better understand the change in excitability of SCs, we used a modified Hodgkin–Huxley model to examine the potential impact of ion channels that are likely to be involved. The model was based on a previous study that included a voltage-gated Na^+ current (I_{Na}), a delayed rectifier K^+ current (I_K), an A-type K^+ current (I_A), a T-type Ca^{2+} current (I_T) and a leak current (I_L; Molineux et al., 2005). The A-type K^+ and T-type Ca^{2+} currents were specifically included in the model as they have been shown to play key roles in determining first spike latencies (Molineux et al., 2005; Anderson et al., 2010, 2013). The model parameters were then adjusted to match observations of spontaneous AP firing at the beginning of SC recordings (see Materials and Methods).

To provide an accurate experimental baseline to use as a template for modeling spontaneous AP firing, gap-free recordings from multiple SCs were made in the absence of injected current (Figs. 3, 4*A*). In line with the previous current step and ramp experiments, spontaneous AP firing in all SCs increased significantly over 25 min (12.5 ± 3.2 Hz at baseline vs 17.9 ± Hz at 25 min; $t = 2.60$, $p = 0.041$; $n = 7$ cells; Figs. 3*A*, 4*A*). The AP cycle, which was obtained from these data by taking the derivative of the measured voltage plotted against membrane potential (Figs. 3*A*, 4*B*), revealed two defining characteristics of time-dependent changes in AP shape: (1) a negative shift in AP upstroke, indicating the hyperpolarization of spike threshold (defined as dV/dt = 10 mV/ms; Fig. 3*B*, yellow box); (2) a reduction in the peak of the AP cycle where it intersects with the voltage-axis (Fig. 3*B*, green box). These measurements were compared over multiple SCs, demonstrating significant differences in AP threshold (–38.7 ± 1.3 mV at baseline vs –44.5 ± 1.7 at 25 min; $t = -11.25$, $p < 0.001$; $n = 7$ cells; Fig. 3*C*) as well as AP maximum (–2.7 ± 2.4 mV at baseline vs –11.5 ± 2.1 mV at 25 min; $t = -4.41$, $p = 0.0045$; $n = 7$ cells; Fig. 3*C*). The change in after-hyperpolarization (AHP) minimum (Fig. 3*B*, light blue box) was variable across cells (three examples in Fig. 3*A*), but this was not significant (–55.4 ± 1.3 mV at baseline vs –56.5 ± 1.5 mV at 25 min; $t = -0.88$, $p = 0.41$; $n = 7$ cells; Fig. 3*C*). Together, these findings identify three cardinal features that are observed during whole-cell recording from SCs: (1) an increase in spontaneous AP frequency, (2) a hyperpolarizing shift of AP threshold, and (3) a hyperpolarizing shift in the AP maximum.

To examine the potential impact of each ionic current, we systematically modified their activation and inactivation kinetic parameters in the baseline model and compared the resulting AP cycle with experimental data. For example, a symmetrical negative shift of both activation ($n_{A,\infty}$) and inactivation ($h_{A,\infty}$) functions of I_A, obtained by

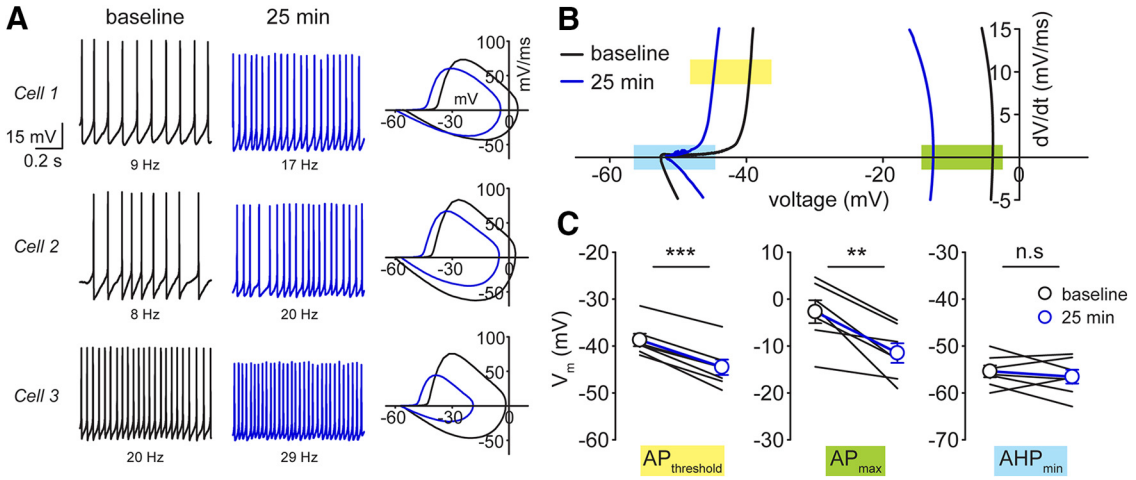

Figure 3. Defining the hallmark membrane features of SC excitability increase. ***A***, left panels, Spontaneous AP firing traces from three example SCs at baseline (black) and after 25 min (blue; patch #150129p2, #181111p6, #181109p3). Right panels, AP cycles for each cell calculated from voltage-time data at baseline (black) and 25 min (blue). ***B***, AP cycle plot of an example SC with *y*-axis expanded. Colored rectangles designate quantities of interest (yellow, AP threshold; green, AP maximum; light blue, AHP minimum). ***C***, Summary comparison of these three features measured from individual AP cycles ($n = 7$ cells). *** denotes $p < 0.001$, ** denotes $p < 0.01$, n.s denotes $p > 0.05$.

decreasing both v_{n_A} and v_{h_A} by –2.5 mV, yielded a ~50% increase in AP firing frequency but no change in the shape of the AP cycle (Fig. 4*C*). Likewise, shifts in either activation (Fig. 4*D*) or inactivation (Fig. 4*E*) functions of I_A separately showed substantial shifts in firing frequency without altering the AP cycle shape or threshold. A negative shift in the activation function (n_∞) of I_K, obtained by decreasing v_n by –2.5 mV, resulted in no change in AP firing frequency but produced a leftward extension of the AHP in the AP cycle (Fig. 4*F*). Shifting either the activation function $m_{T,\infty}$(Fig. 4*G*) or inactivation function $h_{T,\infty}$(Fig. 4*H*) of I_T, obtained by decreasing each v_{m_T} and v_{h_T} separately by –2.5 mV, had little effect on AP firing frequency (where only an ~20% increase in the former and a ~20% decrease in the latter were observed) and no effect on the AP cycle. Given this, we concluded that T-type Ca^{2+} channels are unlikely to contribute to the temporal increase in excitability of SCs. Although the A-type K^+ channel may contribute to the increase in AP firing rates, other ion channels must be responsible for the hyperpolarizing shift in AP threshold.

Modification of the model parameters defining I_{Na} had a substantial impact on AP firing and the AP cycle profile (Fig. 5). Identical negative shifts in both activation and inactivation parameters resulted in a concomitant shift in the AP cycle upstroke as well as an increase in AP firing frequency, although a reduction in the AP maximum was absent (Fig. 5*A*). Likewise, a differential left-shift in favor of the activation function (given by –5 mV for activation and –2.5 mV for inactivation) produced a ~80% increase in AP firing frequency, but was unable to generate a reduction in AP maximum (Fig. 5*B*). In contrast, a differential left-shift in favor of inactivation resulted in a ~100% increase in AP firing as well as reproducing the profile of the AP cycle similar to that observed experimentally (Fig. 5*C*). Taken together, the model suggests that hyperpolarizing shifts in the gating properties of I_{Na} alone can account for the increase in firing rate as well as the characteristic AP cycle changes exhibited by SCs during patch-clamp recording.

SC excitability is accompanied by gating shifts in I_A but not I_K

To directly test the prediction of the model, we used customized activation and inactivation voltage-clamp protocols to isolate two subtypes of K^+ current, I_A and I_K (Figs. 6, 7; see Materials and Methods). Since it can be problematic to accurately measure voltage-gated ion channel activity in highly ramified structures such as neurons, we repeated experiments in nucleated patches where a more faithful voltage-clamp control can be achieved. In whole-cell recordings, we observed a significant time-dependent shift in the voltage dependence of both activation and inactivation of I_A (Fig. 6*B*,*D*). From Boltzmann fits of conductance-voltage relationships, $V_{1/2}$ activation of I_A shifted from –25.8 ± 2.4 mV at baseline to –39.1 ± 2.6 mV after 25 min ($F = 7.07$, $p < 0.001$, Tukey's *post hoc* test; $n = 7$ cells), while $V_{1/2}$ inactivation changed from –80.7 ± 2.8 mV at baseline to –95.3 ± 4.6 mV at 25 min ($t = -11.91$, $p < 0.001$; $n = 7$ cells). Plotting the normalized changes in $V_{1/2}$ measurements between baseline and after 25 min for individual cells yielded a comparable result ($\Delta V_{1/2}$ activation: –15.7 ± 2.7 mV; $\Delta V_{1/2}$ inactivation: –16.2 ± 1.5 mV; Fig. 6*E*). Since the changes in $V_{1/2}$ activation and $V_{1/2}$ inactivation are very similar, this produced a hyperpolarizing shift in the window current of about –11 mV with the midpoint moving from –62.5 to –73.5 mV (Fig. 6*F*). Interestingly, the shift in the voltage dependence of activation of I_A was completely lost in nucleated patches suggesting that the time-dependent change in the gating properties of I_A is probably mediated by a cytoplasmic signaling pathway, such as phosphorylation (Fig. 6*G*,*H*). The $V_{1/2}$ activation was –19.6 mV at baseline and –19.3 mV after 25 min of recording ($F = 0.07$,

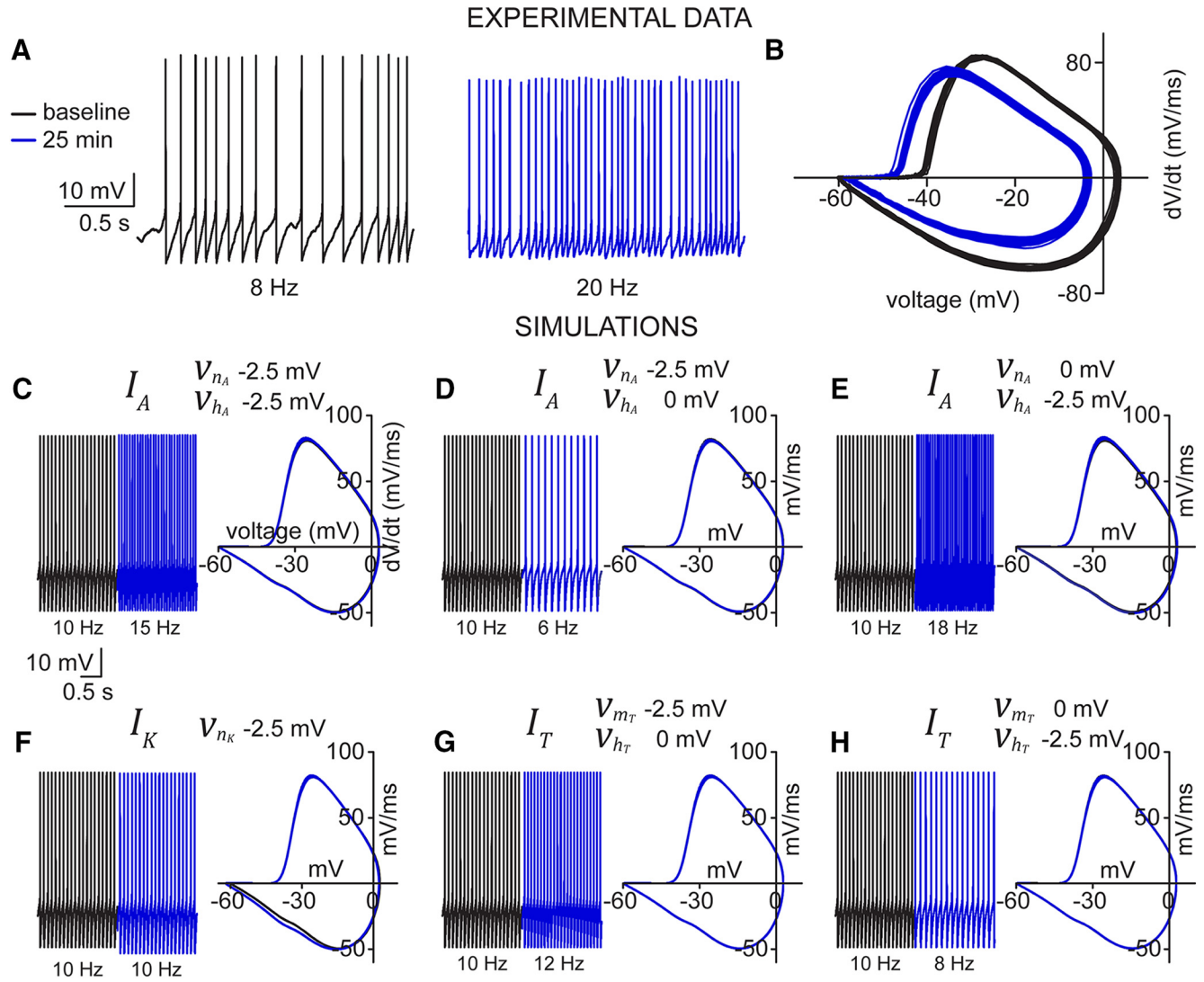

Figure 4. Simulating I_A, I_K, and I_T shifts predicts little contribution to excitability increase. ***A***, Example SC current-clamp recording depicting spontaneous AP firing at baseline (black) and after 25 min (blue; patch #181111p5). ***B***, AP cycle calculated from current-clamp data from ***A*** at baseline (black) and 25 min (blue). ***C–E***, Simulated spontaneous firing and AP cycle from baseline model (black) and after making symmetric and asymmetric shifts in v_{n_A} and v_{h_A}(blue). ***F***, Same for I_K after shifting v_{n_K}(blue). ***G***, ***H***, Same for I_T after shifting either v_{m_T} or v_{h_T}.

$p = 0.96$, Tukey's *post hoc* test; $n = 6$ patches), which was slightly more depolarized than measurements in whole-cell recordings ($F = 3.31$, $p = 0.038$, Tukey's *post hoc* test; Fig. *6H*), possibly reflecting the improvement in voltage-clamp control.

In contrast to I_A, there was no significant time-dependent change in the voltage dependence of I_K activation in whole-cell recording, nor in nucleated patches ($F = 3.88$, $p = 0.081$, two-way mixed design ANOVA; Fig. 7*A–D*). In whole-cell configuration, $V_{1/2}$ activation at baseline was –17.7 mV compared to –17.5 mV at 25 min ($n = 8$ cells), while the voltage dependence of activation in excised patches ($n = 6$) was –3.6 mV at baseline compared to +2.6 mV at 25 min. There was, however, a significant difference in $V_{1/2}$ values between measurements made in whole-cell and nucleated patches ($F = 23.42$, $p < 0.001$, two-way mixed design ANOVA), suggesting that the recording configuration (whole-cell vs patch) affects I_K gating.

I_{Na} exhibits hyperpolarizing shifts in both activation and inactivation

Because of space clamp issues, it is not possible to record the fast gating of I_{Na} in SCs with conventional voltage-clamp protocols. The main problem is the inability to accurately record Na^+ channel activity in distant processes such as axons. To circumvent this, we adapted a protocol using a depolarizing prepulse step to inactivate Na^+ channels distant from the recording electrode which was followed shortly afterward with a second test step to record Na^+ channels close to the cell soma (Milescu et al., 2010). Using this approach, we reliably resolved well-clamped, albeit smaller, I_{Na} responses in SCs to profile their activation and inactivation properties (Fig. 8*A–D*). Performing this protocol over a 25 min period revealed that SC Na^+ channels undergo a hyperpolarizing shift of –7.8 mV in their activation (–32.4 ± 1.5 mV at baseline vs –40.2 ± 1.6 mV at 25 min; $t = –9.10$, $p < 0.001$; $n = 11$

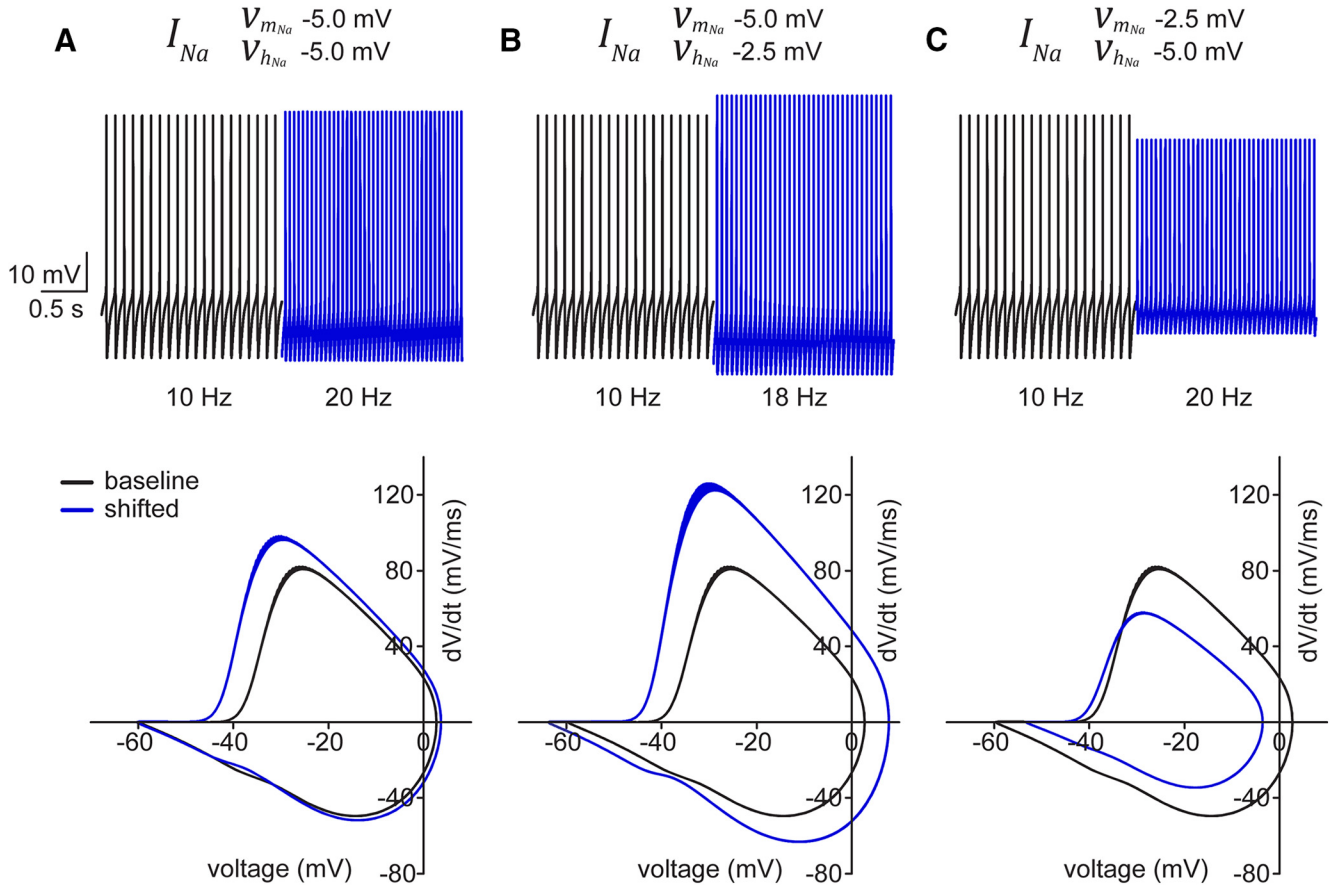

Figure 5. Simulated I_{Na} shifts suggest primary role for sodium channel in excitability increase. Simulated spontaneous firing (upper panels) and AP cycles (lower panels) from baseline model (black) and after either symmetric (***A***) or asymmetric (***B***, ***C***) shifts in $v_{m_{Na}}$ and $v_{h_{Na}}$.

cells; Fig. 8*A*,*B*) and a similar hyperpolarizing shift in steady-state inactivation (–49.3 ± 0.7 mV at baseline to –57.4 ± 1.0 mV at 25 min; $t = -8.95$, $p < 0.001$; $n = 11$ cells; Fig. 8*C*,*D*). This finding is in agreement with the hyperpolarizing shift in Na^+ channel gating predicted by the modified Hodgkin–Huxley model applied to stellate AP firing (Fig. 5).

Interestingly, we also observed a reduction in peak I_{Na} current density that developed over the duration of the experiment (–75.5 ± 8.4 pA/pF at baseline vs –45.1 ± 6.7 pA/pF at 25 min; $t = 6.64$, $p < 0.001$; $n = 11$ cells; Fig. 8*E*). To test whether this was due to a reduction in I_{Na} current density or a consequence of the hyperpolarizing shift in inactivation, we compared peak currents from the first step of the inactivation protocol (–110- to –20-mV probe; Fig. 8*F*). At this voltage, all SC Na^+ channels are available for activation both at baseline and after a 25-min recording. According to this measure, there is no difference between Na^+ current density before and after 25 min and this reduction reflects the shift in steady-state inactivation alone (peak current: –2012.3 ± 149.1 pA at baseline vs –1984.5 ± 162.8 pA at 25 min; $t = 0.43$, $p = 0.68$; $n = 11$ cells; Fig. 8*F*,*G*).

Pharmacological block of K^+, Ca^{2+}, or HCN channels has no effect on AP threshold

To test the hypothesis that the shift in Na^+ channel gating is primarily responsible for the increase in SC excitability, we examined whether pharmacological block of I_A with 4-AP attenuates the hyperpolarizing shift in AP threshold. As expected, block of I_A with bath application of 2 mM 4-AP resulted in a more depolarized inter-spike membrane potential at baseline compared to control cells (Fig. 9*B*). 4-AP, however, did not attenuate the shift in AP threshold (Fig. 9*A*) which hyperpolarized from –40.7 ± 0.9 mV at baseline to –48.6 ± 0.9 mV after 25 min ($t = -9.37$, $p < 0.001$; $n = 5$ cells). Interestingly, 2 mM 4-AP also attenuated the AHP of the AP (Fig. 9*B*) which may reflect pharmacological block of delayed rectifier K^+ channels. In keeping with this, block of I_K with 2 mM external tetraethylammonium (TEA) had the expected effect on AP shape at baseline but did not attenuate the shift in AP threshold (Fig. 9*C*,*D*). AP threshold observed in 2 mM TEA hyperpolarized from –37.2 ± 0.4 mV at baseline to –47.5 ± 1.4 mV after 25 min of recording ($t = -8.99$, $p < 0.001$; $n = 5$ cells; Fig. 9*C*,*D*). Since hyperpolarization-activated cyclic nucleotide-gated (HCN) channels (which mediate the mixed cation current I_h) and voltage-gated Ca^{2+} channels (VGCCs) have also been shown to affect excitability of molecular layer interneurons (MLIs; Saitow and Konishi, 2000; Anderson et al., 2010, 2013), we tested the effect of the selective I_h blocker, ZD 7288 (20 μM) and nonselective VGCC blocker $CdCl_2$ (200 – 300 μM) on AP threshold (Fig. 9*E–H*). In each case, the hyperpolarizing shift in AP threshold was unaffected by either ZD 7288 or $CdCl_2$. The AP threshold with 20 μM ZD 7288 was –38.2 ± 1.3 mV at

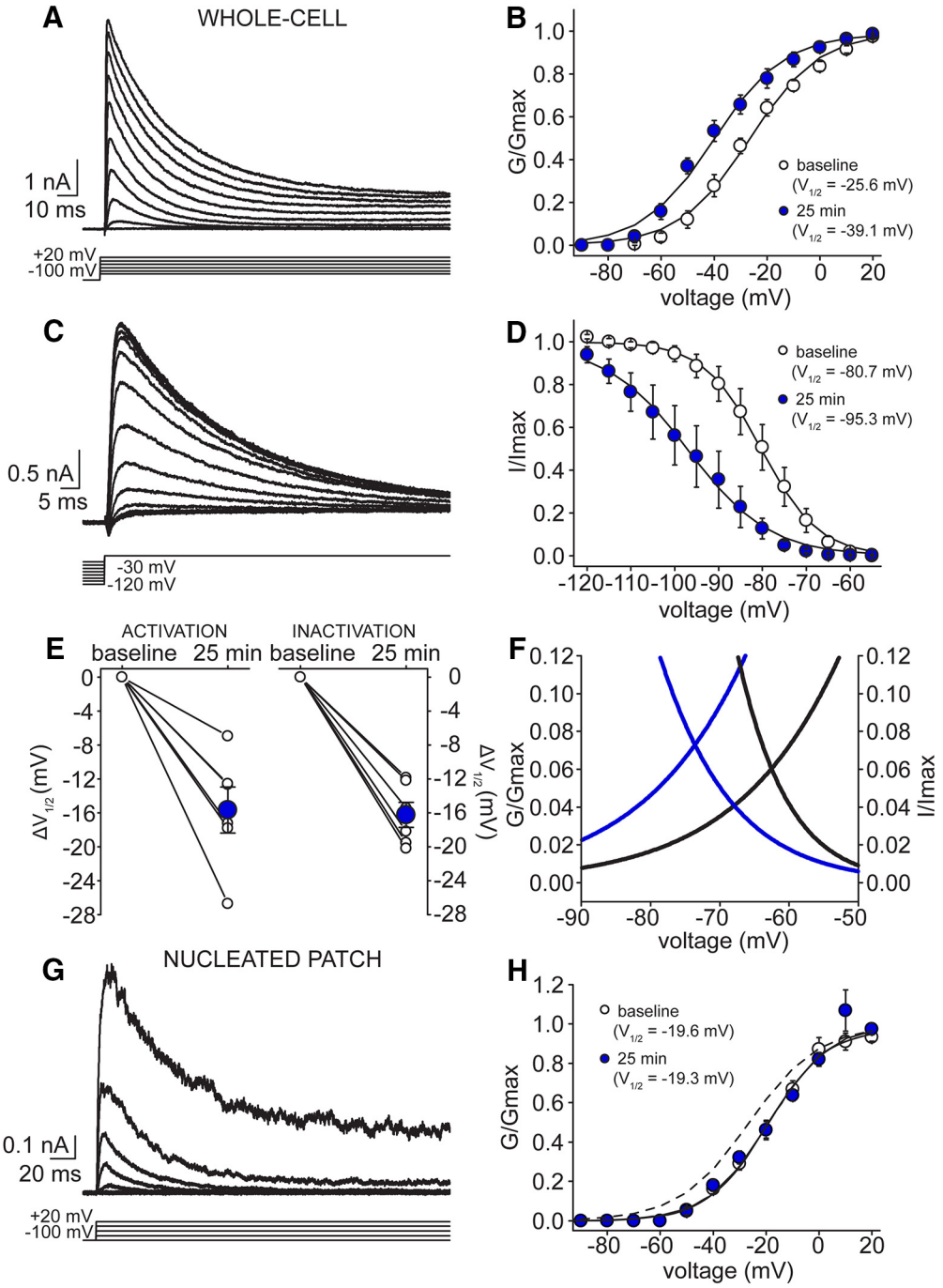

Figure 6. I_A exhibits shifts in both activation and inactivation during 25-min recording. ***A***, Example voltage-clamp traces of I_A currents at baseline during activation protocol (patch #171024p3). ***B***, Summary plot of voltage dependence of activation of I_A at baseline (white circles) and after 25 min of recording (blue circles; $n = 7$ cells). ***C***, Example voltage-clamp traces of I_A currents evoked during inactivation protocol (patch #171127p3). ***D***, Summary plot of voltage dependence of inactivation of I_A at baseline (white circles) and after 25 min of recording (blue circles; $n = 7$ cells, same as in ***B***). ***E***, Normalized $V_{1/2}$ activation (left) and inactivation (right) compared to delta shift after 25-min recording for each cell (white circles), along with summary mean delta for each measure (blue circles). ***F***, Zoom-in of Boltzmann fits for both voltage dependence of activation and inactivation at baseline (black lines) and at 25 min (blue lines) from ***B***, ***D***, respectively, depicting symmetrical translocation of I_A window current. ***G***, Example voltage-clamp traces of I_A currents during activation protocol observed in a SC nucleated patch (patch #180510p3). ***F***, Summary plot of voltage dependence of activation of I_A at baseline (white circles) and 25 min (blue circles; $n = 6$ patches). Dashed line depicts baseline activation curve measured in whole-cell configuration from ***B***.

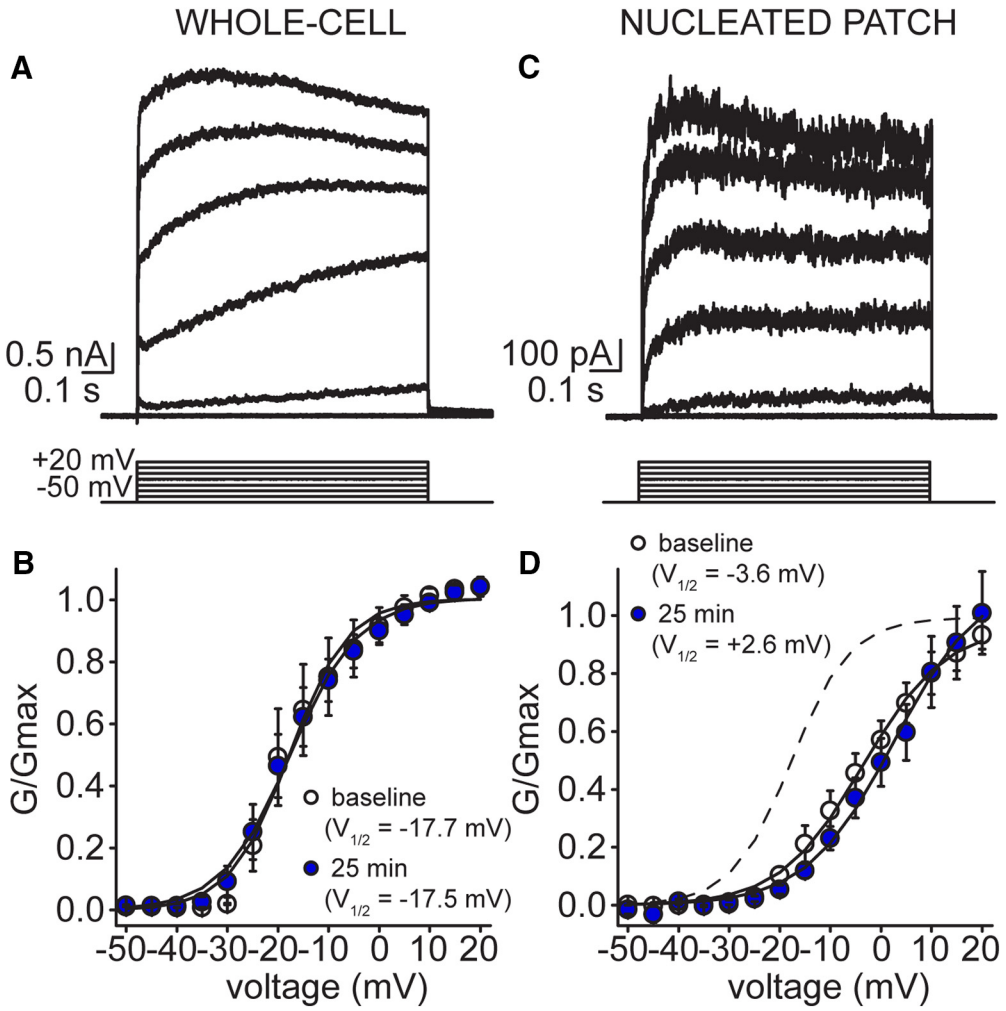

Figure 7. I_K voltage dependence of activation remains stable over patch-clamp recording in both whole-cell and nucleated patch configurations. ***A***, Example whole-cell voltage-clamp traces of delayed rectifier K^+ current at baseline during activation protocol evoked from –50-mV holding potential (5-mV increments, up to +20 mV; patch #180521p2). ***B***, Summary plot of voltage dependence of activation of delayed rectifier K^+ current at baseline (white circles) and after 25 min of recording (blue circles; $n = 8$ cells). ***C***, Example voltage-clamp traces after excising a nucleated patch of delayed rectifier K^+ current at baseline during activation protocol evoked from –50-mV holding potential (5-mV increments, up to +20 mV; patch #180510p3). ***D***, Summary plot of voltage dependence of activation of delayed rectifier K^+ current at baseline (white circles) and after 25 min of recording (blue circles; $n = 6$ cells). Dashed line depicts baseline activation curve measured in whole-cell configuration from ***B***.

baseline and hyperpolarized to −46.8 ± 1.3 mV at 25 min ($t = –10.13$, $p < 0.001$; $n = 6$ cells). Likewise, the threshold shifted from –38.1 ± 0.8 mV at baseline with $CdCl_2$ to −47.7 ± 1.3 mV after 25 min of recording ($t = –7.69$, $p = 0.0015$; $n = 5$ cells). Taken together, these data demonstrate that I_A, I_K, I_h and VGCCs do not contribute to the hyperpolarization of AP threshold of SCs, consistent with our hypothesis that the primary mechanism for the shift is mediated by Na^+ channels.

Revised Hodgkin–Huxley model recapitulates the increase in SC excitability

Based on the voltage-clamp data, we revised the Hodgkin–Huxley model to match the observed changes in I_{Na} and I_A (see Materials and Methods). To do this, we targeted only their activation/inactivation properties without altering their conductances. Specifically, $v_{m_{Na}}$ was shifted by –7 mV and $v_{h_{Na}}$ by –8.5 mV, while v_{n_A} was shifted by –14 mV and v_{h_A} by –16 mV (Table 1), which reproduced well the observed increase in excitability of SCs (Fig. 10*A–D*). With respect to the changes in the AP cycle described earlier (Fig. 3), the revised model captures all the cardinal features seen in the experimental recordings (Fig. 10*A*,*B*). Specifically, the AP threshold of the revised model hyperpolarized by –5.8 mV from –38.7 to –44.5 mV, which agrees well with the –6.0-mV hyperpolarization observed experimentally. The simulated AP maximum hyperpolarized by –8.4 mV from 3.9 to –4.5 mV, which is comparable to the hyperpolarization of –8.8 mV measured experimentally. Finally, the AHP minimum observed in the revised model depolarized by +1.8 mV from –60.1 to –58.3 mV, which is within the margin of error of the experimental results (Fig. 3*C*). The fact that these specific adjustments are able to closely capture the dynamics observed exper-

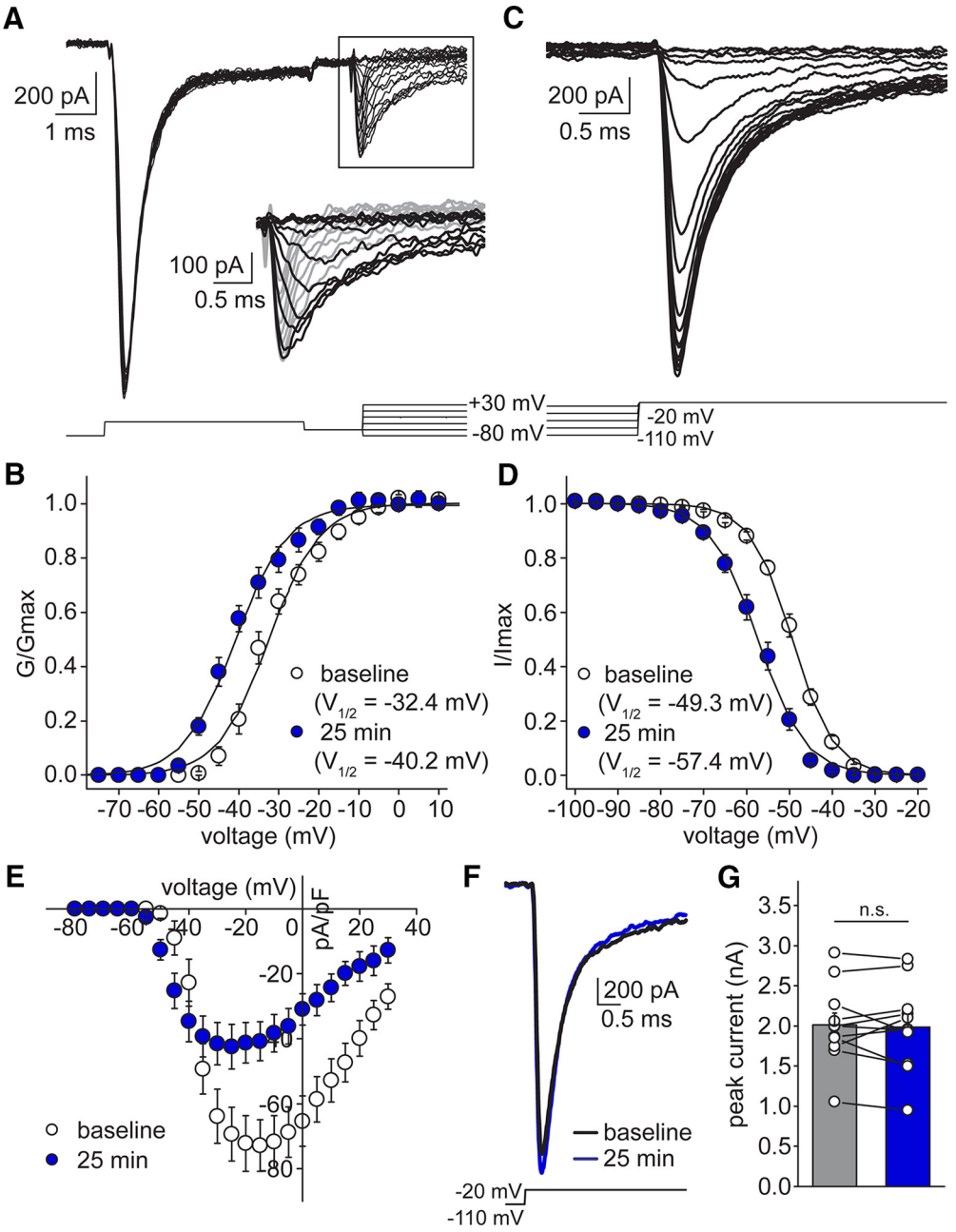

Figure 8. Na^+ current SCs exhibits shift in both activation and inactivation properties, but not current density. ***A***, Example voltage-clamp traces of Na^+ currents evoked with a prepulse protocol (patch #170222p4). Inset, Zoom-in of portion of traces depicting strong voltage-clamp of Na^+ currents evoked after prepulse. ***B***, Summary plot of voltage dependence of activation of Na^+ current at baseline (white circles) and at 25 min (blue circles; $n = 11$ cells). ***C***, Example traces from a Na^+ inactivation protocol (patch #170222p4). ***D***, Summary plot of voltage dependence of inactivation at baseline (white circles) and at 25 min (blue circles; $n = 11$ cells). ***E***, Summary current density-voltage plot (data used to construct conductance-voltage plots in ***B***, ***D***, of sodium responses at baseline (white circles) and at 25 min (blue circles). ***F***, Example peak sodium current traces evoked by a –110 to –20 mV probe at baseline (black) and at 25 min (blue; patch #171108p3). ***G***, Summary graph of peak sodium currents evoked from a holding potential of –110 mV at baseline (gray) and at 25 min (blue). n.s. denotes $p > 0.05$.

imentally further supports the dominance of I_{Na} in driving the increase in SC excitability, with an additional role for I_A in further modulating AP firing.

Discussion

The present study advances our understanding of the neurophysiology of cerebellar SCs in two important ways. First, we identify a predominant role of voltage-gated Na^+ channels in upregulating the excitability of cerebellar SCs following membrane patch breakthrough. Under these conditions, the threshold for AP initiation is shifted to more hyperpolarized membrane potentials due to changes in the activation and inactivation properties of Na^+ channels. Since similar shifts in gating behavior are observed in other central neurons by physiologic stimuli, such as

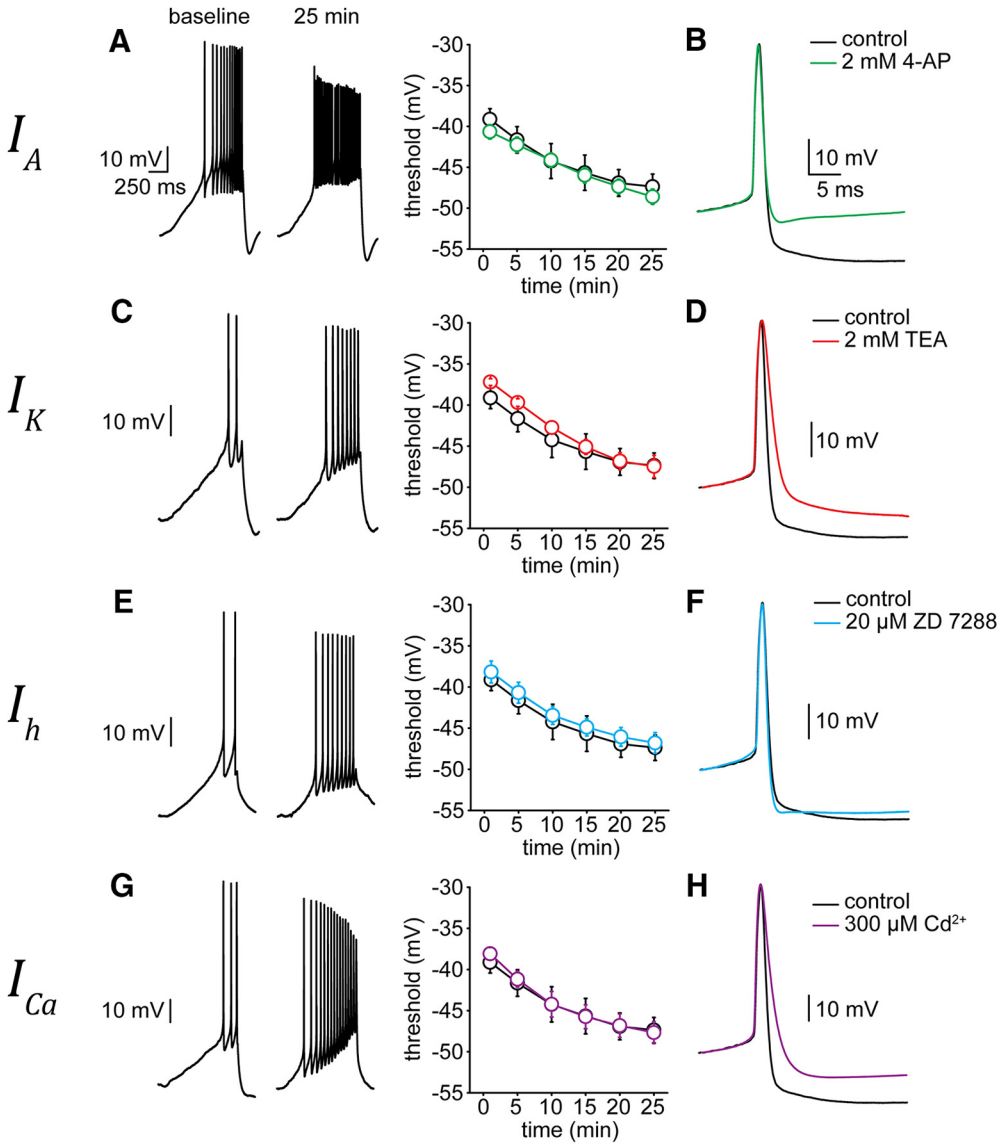

Figure 9. AP threshold hyperpolarization persists with pharmacological blockade of I_K, I_A, I_{Ca} and I_h. ***A***, left panel, Example traces recorded at baseline and after 25 min of APs evoked by a current ramp protocol (25 pA over 1 s) in a SC. Right panel, Summary AP threshold data for control conditions (black open circles; $n = 6$ cells) and in the presence of 2 mM TEA in the aCSF (red open circles; $n = 5$ cells). ***B***, Superimposed first APs evoked by ramp protocol in control (black) and external TEA (red) conditions. TEA scaled to control (patch #181008p8). ***C***, ***D***, Same as ***A***, ***B***, but in the presence of 2 mM 4-AP (green lines; $n = 5$ cells; patch #181015p7). ***E***, ***F***, Same as ***A***, ***B***, but in the presence of 20 μM ZD 7288 (blue lines; $n = 6$ cells; patch #181018p2). ***G***, ***H***, Same as in ***A***, ***B***, but in the presence of 200–300 μM $CdCl_2$ (purple lines; $n = 5$ cells; patch #181024p4).

NMDA receptor activation (Xu et al., 2005), it is possible that Na^+ channels are targeted in a comparable manner in SCs to upregulate AP firing. Second, we report hyperpolarizing shifts in both the activation and inactivation properties of A-type K^+ channels that contribute to the time-dependent increase in firing rates observed in SCs but do not participate in the hyperpolarizing shift in AP threshold. Previous work has established that depolarizing shifts in A-type K^+ channel inactivation are triggered by elevations in cytosolic Ca^{2+} due to T-type Ca^{2+} channel activity in SCs (Molineux et al., 2005; Anderson et al., 2010, 2013). Given this distinction with the present study, it is likely that different signaling events are at play to regulate the gating behavior of A-type K^+ channels in cerebellar SCs.

Increased membrane excitability following whole-cell recording is not unique to SCs

SCs are not the only neuronal cell type that undergo functional changes after the establishment of the whole-cell patch-clamp configuration. In fact, early patch clamp studies of voltage-gated ion channels noted time-dependent changes in both activation and inactivation properties including changes to voltage-gated Na^+ channels (Fenwick et al., 1982; Fernandez et al., 1984; Vandenberg and Horn, 1984; Marty and Neher, 1985). The

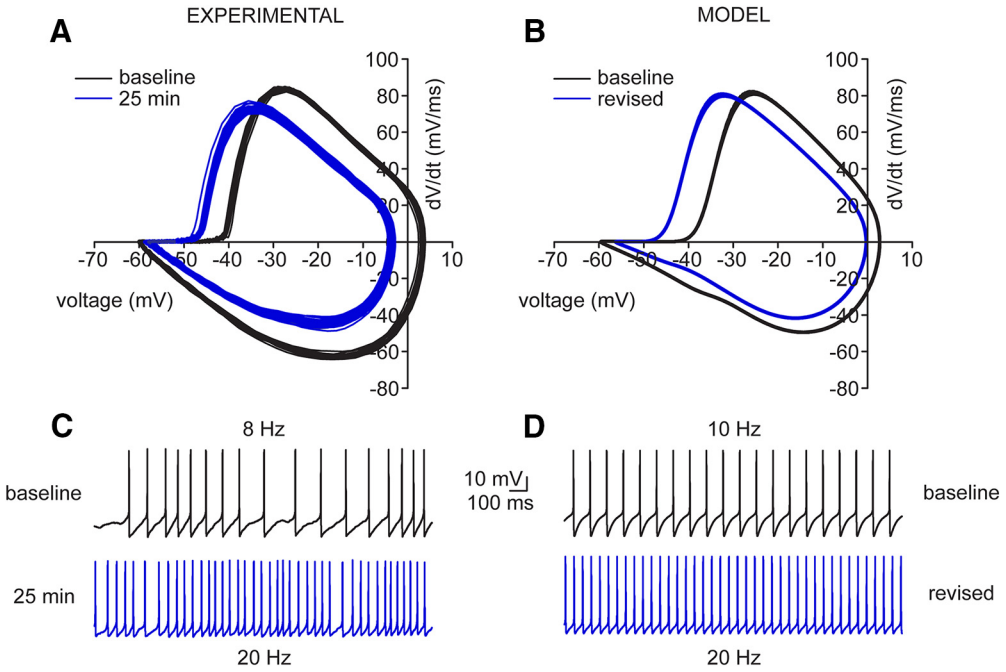

Figure 10. Voltage-clamp-informed model recapitulates the dynamics of current-clamp experimental data. ***A***, AP cycle calculated from experimental SC current-clamp recording at baseline (black) and 25 min (blue). ***C***, Same current-clamp recording data as above, presented as voltage versus time at baseline (black) and 25 min (blue). ***B***, Simulated AP cycle of baseline (black) and revised (blue) models after modifying all gating parameters based on values measured experimentally in voltage-clamp in SCs. ***D***, Simulated firing properties of baseline (black) and revised (blue) models.

mechanism(s) underlying these changes has remained largely unexplored and thus ignored - as has been the case for cerebellar SCs. In the cerebellum, the increased firing rate we have observed in GCs (compare Fig. 1) may be attributed to the cell's buffering capacity for cytosolic Ca^{2+} which is further compromised when GCs lack the calcium binding protein, calretinin (Gall et al., 2003). Similarly, Alcami and colleagues also linked a rise in intracellular Ca^{2+} to an increase in firing rates of SCs (Alcami et al., 2012) suggesting that there may be overlapping signaling pathways at play in both cell types (see below). A distinction with SCs, however, is that we have observed an increase in the input resistance of GCs following patch breakthrough. Whether the change in membrane leak is due to the activity of other ion channels, such as TASK-1 (Millar et al., 2000) or HCN channels (Zúñiga et al., 2016), in GCs remains to be studied. Why the excitability of SCs and GCs increases after patch breakthrough whereas Purkinje cells remain stable is not clear. It is tempting to speculate that the smaller soma of SCs makes their subcellular Ca^{2+} stores more susceptible to perturbation during whole-cell recording compared to Purkinje cells. It is also possible that SCs are mechanosensitive which is in keeping with the observation that SC excitability increases during cell-attached recordings, particularly in recordings with a tight seal (Alcami et al., 2012). As discussed below, the events that are initiated by membrane patch breakthrough suggest that voltage-gated Na^+ channels may be impacted by several endogenous signaling pathways in SCs.

Expression and regulation of Na^+ channels in cerebellar SCs

Cerebellar MLIs are thought to express several Na^+ channel pore-forming subunits that include Nav1.1, Nav1.2, and Nav1.6 (Schaller and Caldwell, 2003); however, more recent data suggest that the Nav1.2 protein is expressed only on presynaptic terminals of GCs (Jarnot and Corbett, 2006; Martínez-Hernández et al., 2013). This latter finding agrees with our experiments using the Nav1.2-selective inhibitor, Phrixotoxin-III, which has negligible pharmacological effect on SC excitability (Alexander and Bowie, unpublished observation). Based on antibody staining, both Nav1.1 and Nav1.6 subunits are expressed in MLIs (Kalume et al., 2007); however, their subcellular distribution is distinct (Lorincz and Nusser, 2008). The Nav1.6 subunit is almost exclusively expressed at the axon initial segment (AIS), a region of the axon close to the cell body where APs are initiated. In contrast, Nav1.1 is expressed throughout the axon, although it is also found in the proximal AIS (Lorincz and Nusser, 2008). Given this arrangement, both Nav1.1 and Nav1.6 subunits may contribute to the Na^+ channel currents we have recorded from SCs. Whether these subunits are also expressed in the dendrites has not be formally investigated, although SC dendrites are apparently devoid of Na^+ channels (Myoga et al., 2009). It is curious that the expression pattern of the delayed rectifier K^+ channel subunits, Kv1.1 and Kv1.2, overlap with Nav1.6 subunits, but yet, are not subject to modulation following patch breakthrough (compare Fig. 9). This observation suggests that the signaling pathway(s) that promotes gating shifts in Na^+

channels is tightly compartmentalized from other ion channels, such as Kv1.1 and Kv1.2, even within the AIS.

Gating shifts in Na^+ channel activation and inactivation, as observed in the present study (compare Fig. 8), may, in principle, be mediated by a number of mechanisms that include direct binding by cytosolic Ca^{2+}, binding of the Ca^{2+}-calmodulin complex and/or changes in the phosphorylation state of the Na^+ channel (Cantrell and Catterall, 2001; Van Petegem et al., 2012). Regulation of recombinant Nav1.6 channels has primarily focused on the effect of channel phosphorylation where protein kinase A (PKA) stimulation (Chen et al., 2008) and p38 mitogen-activated protein kinase (Wittmack et al., 2005) both cause a reduction in peak Na^+ channel current. In the latter case, the reduction in current density did not affect channel gating (Wittmack et al., 2005), unlike the present study (compare Fig. 8) but was due to the internalization of Nav1.6 channels (Gasser et al., 2010). In contrast, inhibition of glycogen-synthase kinase 3β (GSK3β) causes a decrease in recombinant Nav1.6 responses (Scala et al., 2018) suggesting that phosphorylation sustains channel activity in HEK 293 cells. Likewise, in medium spiny neurons of the nucleus accumbens, regulation of GSK3β activity impacts firing rates in a Nav1.6-dependent manner (Scala et al., 2018) suggesting that phosphorylation and dephosphorylation events may be critical in fine-tuning neuronal output. Much less is known about the regulation of Nav1.1 channels, although, earlier recombinant studies and more recent proteomic work has identified putative phosphorylation sites which often overlap with sites identified for Nav1.2 channels (Smith and Goldin, 1998; Berendt et al., 2010). Interestingly, forskolin activation of PKA causes a hyperpolarizing shift in both the activation and inactivation curves for recombinant Nav1.1 (Liu and Zheng, 2013) as observed in the present study on cerebellar SCs. An identical gating shift is observed in hippocampal CA1 pyramidal cells, probably mediated by Nav1.2 channels, that is triggered by NMDA receptor activation and the activity of CaM kinase II (Xu et al., 2005). Given the similarity in how Nav1.1 and Nav1.2 channels are regulated by phosphorylation, it would be interesting to test if a NMDA receptor-mediated signaling pathway could induce a similar shift in the gating behavior of Na^+ channels in cerebellar SCs. Likewise, experiments using dynamic clamp to test the effect of a Nav channel gating model on SC excitability would be interesting to test in future studies.

Multiple families of voltage-gated ion channels control SC excitability

Although SCs express a variety of voltage-gated ion channels, somatodendritic A-type K^+ channels are an important regulator of their firing rates (Molineux et al., 2005; Anderson et al., 2010, 2013). Specifically, AP firing rates are regulated by Kv4.2/4.3 subunits whose basal activity is fine-tuned by elevations in cytosolic Ca^{2+} mediated by the Ca^{2+} channel subunits, Cav3.2 and Cav3.3 (Anderson et al., 2010). Both ion channel families form a signaling complex through the modulatory protein, KChIP3, which contains an E-F hand and thus is able to act as a Ca^{2+} sensor that couples the activity of Ca^{2+} channels to the regulation of K^+ channels (Pongs and Schwarz, 2010). Elevations in intracellular Ca^{2+} selectively promote depolarizing shifts in steady-state inactivation of A-type K^+ channels and, in doing so, attenuate membrane depolarization and AP firing (Anderson et al., 2010, 2013). In contrast, our data establish that A-type K^+ channels contribute to an increase in AP firing of SCs via a hyperpolarizing shift in channel activation and inactivation (compare Fig. 6). Although the formation of the whole-cell recording is likely to elevate cytosolic Ca^{2+} in SCs, as discussed above, the shifts A-type K^+ channel gating observed in this study are probably not reliant on KChIP3 modulation. Finally, although other voltage-gated ion channels may be involved in controlling SC excitability, pharmacological block of many of these channels (Fig. 9) reveals that they do not impact AP threshold. Consequently, our work identifies a predominant role of voltage-gated Na^+ channels in upregulating the firing rates of cerebellar SCs.

References

Alcami P, Franconville R, Llano I, Marty A (2012) Measuring the firing rate of high-resistance neurons with cell-attached recording. J Neurosci 32:3118–3130.

Anderson D, Mehaffey WH, Iftinca M, Rehak R, Engbers JD, Hameed S, Zamponi GW, Turner RW (2010) Regulation of neuronal activity by Cav3-Kv4 channel signaling complexes. Nat Neurosci 13:333–337.

Anderson D, Engbers JD, Heath NC, Bartoletti TM, Mehaffey WH, Zamponi GW, Turner RW (2013) The Cav3-Kv4 complex acts as a calcium sensor to maintain inhibitory charge transfer during extracellular calcium fluctuations. J Neurosci 33:7811–7824.

Armstrong DM, Rawson JA (1979) Activity patterns of cerebellar cortical neurones and climbing fibre afferents in the awake cat. J Physiol 289:425–448.

Astorga G, Li D, Therreau L, Kassa M, Marty A, Llano I (2017) Concerted interneuron activity in the cerebellar molecular layer during rhythmic oromotor behaviors. J Neurosci 37:11455–11468.

Berendt FJ, Park KS, Trimmer JS (2010) Multisite phosphorylation of voltage-gated sodium channel alpha subunits from rat brain. J Proteome Res 9:1976–1984.

Bers DM, Patton CW, Nuccitelli R (2010) A practical guide to the preparation of Ca(2+) buffers. Methods Cell Biol 99:1–26.

Cantrell AR, Catterall WA (2001) Neuromodulation of Na+ channels: an unexpected form of cellular plasticity. Nat Rev Neurosci 2:397–407.

Carter AG, Regehr WG (2002) Quantal events shape cerebellar interneuron firing. Nat Neurosci 5:1309–1318.

Chen Y, Yu FH, Sharp EM, Beacham D, Scheuer T, Catterall WA (2008) Functional properties and differential neuromodulation of Na(v)1.6 channels. Mol Cell Neurosci 38:607–615.

Christie JM, Jahr CE (2008) Dendritic NMDA receptors activate axonal calcium channels. Neuron 60:298–307.

Dani JA, Sanchez JA, Hille B (1983) Lyotropic anions. Na channel gating and Ca electrode response. J Gen Physiol 81:255–281.

Duguid IC, Smart TG (2004) Retrograde activation of presynaptic NMDA receptors enhances GABA release at cerebellar interneuron-Purkinje cell synapses. Nat Neurosci 7:525–533.

Fenwick EM, Marty A, Neher E (1982) Sodium and calcium channels in bovine chromaffin cells. J Physiol 331:599–635.

Fernandez JM, Fox AP, Krasne S (1984) Membrane patches and whole-cell membranes: a comparison of electrical properties in rat clonal pituitary (GH3) cells. J Physiol 356:565–585.

Gaffield MA, Christie JM (2017) Movement rate is encoded and influenced by widespread, coherent activity of cerebellar molecular layer interneurons. J Neurosci 37:4751–4765.
Gall D, Roussel C, Susa I, D'Angelo E, Rossi P, Bearzatto B, Galas MC, Blum D, Schurmans S, Schiffmann SN (2003) Altered neuronal excitability in cerebellar granule cells of mice lacking calretinin. J Neurosci 23:9320–9327.
Gasser A, Cheng X, Gilmore ES, Tyrrell L, Waxman SG, Dib-Hajj SD (2010) Two Nedd4-binding motifs underlie modulation of sodium channel Nav1.6 by p38 MAPK. J Biol Chem 285:26149–26161.
Glitsch M, Marty A (1999) Presynaptic effects of NMDA in cerebellar Purkinje cells and interneurons. J Neurosci 19:511–519.
Häusser M, Clark BA (1997) Tonic synaptic inhibition modulates neuronal output pattern and spatiotemporal synaptic integration. Neuron 19:665–678.
Jarnot M, Corbett AM (2006) Immunolocalization of NaV1.2 channel subtypes in rat and cat brain and spinal cord with high affinity antibodies. Brain Res 1107:1–12.
Jörntell H, Ekerot CF (2003) Receptive field plasticity profoundly alters the cutaneous parallel fiber synaptic input to cerebellar interneurons in vivo. J Neurosci 23:9620–9631.
Kaczorowski CC, Disterhoft J, Spruston N (2007) Stability and plasticity of intrinsic membrane properties in hippocampal CA1 pyramidal neurons: effects of internal anions. J Physiol 578:799–818.
Kalume F, Yu FH, Westenbroek RE, Scheuer T, Catterall WA (2007) Reduced sodium current in Purkinje neurons from Nav1.1 mutant mice: implications for ataxia in severe myoclonic epilepsy in infancy. J Neurosci 27:11065–11074.
Liu H, Zhao SN, Zhao GY, Sun L, Chu CP, Qiu DL (2014) N-methyl-d-aspartate inhibits cerebellar Purkinje cell activity via the excitation of molecular layer interneurons under in vivo conditions in mice. Brain Res 1560:1–9.
Liu S, Zheng P (2013) Altered PKA modulation in the Na(v)1.1 epilepsy variant I1656M. J Neurophysiol 110:2090–2098.
Liu SJ, Lachamp P (2006) The activation of excitatory glutamate receptors evokes a long-lasting increase in the release of GABA from cerebellar stellate cells. J Neurosci 26:9332–9339.
Lorincz A, Nusser Z (2008) Cell-type-dependent molecular composition of the axon initial segment. J Neurosci 28:14329–14340.
Martínez-Hernández J, Ballesteros-Merino C, Fernández-Alacid L, Nicolau JC, Aguado C, Luján R (2013) Polarised localisation of the voltage-gated sodium channel Na(v)1.2 in cerebellar granule cells. Cerebellum 12:16–26.
Marty A, Neher E (1985) Potassium channels in cultured bovine adrenal chromaffin cells. J Physiol 367:117–141.
Midtgaard J (1992) Membrane properties and synaptic responses of Golgi cells and stellate cells in the turtle cerebellum in vitro. J Physiol 457:329–354.
Milescu LS, Bean BP, Smith JC (2010) Isolation of somatic Na+ currents by selective inactivation of axonal channels with a voltage prepulse. J Neurosci 30:7740–7748.
Millar JA, Barratt L, Southan AP, Page KM, Fyffe RE, Robertson B, Mathie A (2000) A functional role for the two-pore domain potassium channel TASK-1 in cerebellar granule neurons. Proc Natl Acad Sci USA 97:3614–3618.
Molineux ML, Fernandez FR, Mehaffey WH, Turner RW (2005) A-type and T-type currents interact to produce a novel spike latency-voltage relationship in cerebellar stellate cells. J Neurosci 25:10863–10873.
Myoga MH, Beierlein M, Regehr WG (2009) Somatic spikes regulate dendritic signaling in small neurons in the absence of backpropagating action potentials. J Neurosci 29:7803–7814.
Pongs O, Schwarz JR (2010) Ancillary subunits associated with voltage-dependent K+ channels. Physiol Rev 90:755–796.
Saitow F, Konishi S (2000) Excitability increase induced by beta-adrenergic receptor-mediated activation of hyperpolarization-activated cation channels in rat cerebellar basket cells. J Neurophysiol 84:2026–2034.
Scala F, Nenov MN, Crofton EJ, Singh AK, Folorunso O, Zhang Y, Chesson BC, Wildburger NC, James TF, Alshammari MA, Alshammari TK, Elfrink H, Grassi C, Kasper JM, Smith AE, Hommel JD, Lichti CF, Rudra JS, D'Ascenzo M, Green TA, et al. (2018) Environmental enrichment and social isolation mediate neuroplasticity of medium spiny neurons through the GSK3 pathway. Cell Rep 23:555–567.
Schaller KL, Caldwell JH (2003) Expression and distribution of voltage-gated sodium channels in the cerebellum. Cerebellum 2:2–9.
Smith RD, Goldin AL (1998) Functional analysis of the rat I sodium channel in xenopus oocytes. J Neurosci 18:811–820.
Townsend C, Hartmann HA, Horn R (1997) Anomalous effect of permeant ion concentration on peak open probability of cardiac Na+ channels. J Gen Physiol 110:11–21.
Van Petegem F, Lobo PA, Ahern CA (2012) Seeing the forest through the trees: towards a unified view on physiological calcium regulation of voltage-gated sodium channels. Biophys J 103:2243–2251.
Vandenberg CA, Horn R (1984) Inactivation viewed through single sodium channels. J Gen Physiol 84:535–564.
Wittmack EK, Rush AM, Hudmon A, Waxman SG, Dib-Hajj SD (2005) Voltage-gated sodium channel Nav1.6 is modulated by p38 mitogen-activated protein kinase. J Neurosci 25:6621–6630.
Xu J, Kang N, Jiang L, Nedergaard M, Kang J (2005) Activity-dependent long-term potentiation of intrinsic excitability in hippocampal CA1 pyramidal neurons. J Neurosci 25:1750–1760.
Zúñiga R, González D, Valenzuela C, Brown N, Zúñiga L (2016) Expression and cellular localization of HCN channels in rat cerebellar granule neurons. Biochem Biophys Res Commun 478:1429–1435.